



BINDING SERVICES
Tel +44 (0)29 2087 4949
Fax +44 (0)29 20371921
e-mail bindery@cardiff.ac.uk

**On The Possibility Of Layered Mantle Convection
-
Numerical Simulations In A Spherical Geometry**

**David N. Oldham
Supervisor: Dr J. H. Davies**

Thesis

**Submitted in partial fulfilment for the
degree of Doctor of Philosophy**

February 2004

The School of Earth, Ocean and Planetary Science

Cardiff University

UMI Number: U584645

All rights reserved

INFORMATION TO ALL USERS

The quality of this reproduction is dependent upon the quality of the copy submitted.

In the unlikely event that the author did not send a complete manuscript and there are missing pages, these will be noted. Also, if material had to be removed, a note will indicate the deletion.



UMI U584645

Published by ProQuest LLC 2013. Copyright in the Dissertation held by the Author.
Microform Edition © ProQuest LLC.

All rights reserved. This work is protected against
unauthorized copying under Title 17, United States Code.



ProQuest LLC
789 East Eisenhower Parkway
P.O. Box 1346
Ann Arbor, MI 48106-1346

Acknowledgments

I would like thank Dr. Huw Davies for his help and encouragement throughout my PhD. Dr. Andy Heath (Uni. of Liverpool) for the development of MantleVis (the parallel visualisation tool used to generate many of the cross sections in this thesis), Alan McCormack for doing an excellent job administrating NESSC, Prof. Peter Bunge (Princeton University) and Dr. John Baumgardner (Los Alamos) for providing the TERRA source code, Dr. Ian Thomas for administrating Helix, and Rhodri Davies for helpful comments and guidance. I also acknowledge the current support of the School of Earth, Ocean and Planetary Science at Cardiff University and the earlier support of the Department of Earth Sciences at the University of Liverpool. Thanks to HEFCE (JREI) for NESSC and HEFCW (SRIF) for Helix, the cluster super computers used to perform these calculations.

Abstract

We investigate the possibility of a deep, dense layer in Earth's mantle. For this purpose we have developed a tool to simulate stratified layered convection in three-dimensional spherical geometry. This was achieved by making alterations to a well-established parallel convection code. The chemical boundary is represented by markers distributed as a surface in the computational grid. These markers are advected by the velocity field, allowing the chemical boundary to deform, and the correct buoyancy forces to be calculated. This method was tested and verified.

This method was used to simulate a number of layered cases with an Earth-like geometry. We investigated the effects of varying the depth of the boundary, the density contrast across the boundary, the heating mode used to power convection and the Rayleigh number (Ra) of the system.

We found that the stability of the layer is strongly dependent on the buoyancy ratio B ($B = \Delta\rho / \rho\alpha\Delta T$ where $\Delta\rho$ is the chemical density increase across the boundary, ρ is the density in the upper layer, α is the thermal expansivity and ΔT is the radial temperature difference across the whole system) with a dense layer becoming unstable when B becomes less than some critical value, B_c . B_c is weakly dependent on Ra , the depth of the interface, and the heating mode used. We find $B_c \approx 0.5$, which is consistent with other work.

As the Rayleigh number increases the system moves from viscous to thermal coupling. We present a relationship between the surface area of the interface and the buoyancy ratio, which is useful in defining the critical buoyancy ratio. We investigate the constraints provided by seismic reflection studies on layered convection.

Seismic free oscillations suggest a density increase of less than 0.4% in the lower mantle. Assuming a thermal steady-state, we estimate the temperature increase across a thermo chemical boundary layer needed to produce Earth-like surface heat flux. We find that a deep layer with an intrinsic density contrast of 2% may be both dynamically stable and consistent with seismic observations.

The presence of layering is expected from our work, to produce large lateral variations of temperature, density and seismic velocity at the depth of the interface between the layers. Current seismic tomography studies do not show such a feature in the lower mantle away from the core mantle boundary, suggesting that layering is unlikely.

An introduction to the formatting of this thesis

Appendix A contains a glossary that defines many of the terms and variables used in this thesis. Variables are used throughout this thesis as they are defined in this glossary except for in section 4.4[†]. Important equations are also included in the glossary and have the reference number that they were assigned when they are first used in the main text of this thesis. References to equations that are in the glossary are in **bold**.

When the TERRA code is being discussed, variables within the code are printed in `courier font`. This is used mainly in chapter 3 and to a lesser extent in chapter 4.

Sections of text and equations that are contained within square brackets (like the one below) are sections that are superfluous to the arguments in the main body of the text.

A reader who is skimming through the thesis or looking for a particular important point can therefore ignore these sections.

An example of a time when a square bracketed section would be used is when a value such as the mass of the mantle is quoted in the main body of the text. The calculation used to arrive at this figure including all parameters used such as the density of the mantle and radius of the CMB would then be shown in the square bracketed section.

Important points and summaries are often displayed in bordered sections. These normally appear at the end of a section and contain summary of the conclusions reached. Bordered sections are also used to highlight important reference information that any student working on the marker code developed as part of this thesis may need to find within the text and is therefore highlighted in the spirit of saving them time.

Important summaries and reference information are displayed in bordered sections like this.

[†] Here we are commenting on the work of Davaille [1999a] and so we use her notation to allow an easy comparison of the two works.

Content

Declaration	I
Acknowledgments	II
Abstract	III
An introduction to the formatting of this thesis	IV
Content	V
1 Introduction	1
1.1 Objectives	1
1.2 Methodology	3
1.3 The structure of this thesis	4
2 Mantle convection	5
2.1 The structure of the mantle	6
2.2 The Rayleigh Ra and Nusselt Nu numbers	8
2.3 The need for a chemical reservoir in Earth's mantle	9
2.3.1 Geochemical arguments	9
2.3.1.1 Helium and Argon abundances in the atmosphere	10
2.3.1.2 Heat budget arguments	10
2.3.2 Seismic and geodynamic arguments	11
2.3.2.1 The fate of subducting slabs	11
2.3.2.2 The distribution, fixity and source of plumes	14
2.3.2.3 Mega plumes	15
2.3.3.4 Lateral variations in tomography inversions	18
2.3.3.5 Topography	21
2.4 Suggested locations of the mantle reservoir and the Kellogg layer	23
2.5 Estimates of the rate of radiogenic heating in a chemically enriched layer	25
2.6 Mixing - do we need a chemical reservoir?	29
2.7 The behaviour of a layered convecting system	30
2.7.1 The stability of a layered system	31
2.7.2 Entrainment and the lifespan of layered convection	38
2.7.3 Other characteristics of layered convection	41
2.8 Thermal expansion and its variance with depth	44
2.9 Summary	46
3 The marker method	47
3.1 An introduction to the concept of parallel computing	48
3.1.1 NESSC	49
3.1.2 NESSC specifications	50
3.1.3 Helix specifications	50
3.2 An introduction to the TERRA program	50
3.2.1 The governing equations and assumptions used	51
3.2.2 The computational method	52
3.2.3 The finite element method	53
3.2.4 The multigrid	54
3.2.5 The icosahedron grid used in TERRA	54
3.2.6 Indexing conventions employed by TERRA	56

3.2.7	Domain decomposition in TERRA	59
3.3	Implementation of the marker method in the TERRA program	60
3.3.1	Overview of the marker code	61
3.3.2	Preliminaries, allan-keys and prisms	64
3.3.2.1	How are the markers stored?	64
3.3.2.2	Initialising the markers	65
3.3.3	Updating the positions of the markers	66
3.3.4	The halo region and boundary swapping	70
3.3.5	Controlling the population of the markers	73
3.3.5.1	Moving markers to new allan-keys	75
3.3.5.2	Conditions for creating new markers	75
3.3.5.3	Conditions for deleting markers	76
3.3.6	Controlling the number of markers	77
3.4	Adding buoyancy forces associated with the dense layer	78
3.5	Analyzing the deformable surface and the layered system	79
3.5.1	The temperature in the layers	79
3.5.2	Calculating the surface area of the boundary defined by the markers	79
4	Analysis of the marker method	81
4.1	Verification tests	81
4.1.1	Velocity interpolations: up and down method	81
4.1.2	Marker generation and destruction: round and round	83
4.2	Parallel program performance	85
4.2.1	What is the best number of processors to use?	87
4.2.2	The effect of the marker code on the performance of TERRA	90
4.3	Resolution test	90
4.4	Entrainment	95
4.4.1	The plan-form of entrainment	100
4.4.2	The effects of viscous coupling	101
4.4.3	Other assumptions	106
4.4.4	Comparing predicted entrainment with a numerical example	108
4.4.5	A simple constraint on entrainment from a deep layer	111
5	The effect of the heating mode on layered convection	112
5.1	Producing initial cases for layered convection models	112
5.2	Changes in the interfacial area once the system has reached a quasi steady state	114
5.3	Cases studied	117
5.4	The thermal evolution of layered convection	120
5.5	Results	124
5.6	The relationship between the buoyancy ratio B and the non-dimensional area parameter ϕ	139
5.6.1	Characterising the B - ϕ relationship	140
5.6.2	Is depth a factor in the $\phi = a \div (B^\alpha - b^\alpha)$ relationship?	142
5.7	Internally heated cases with accelerated heating rates	144
5.8	Summary	150
6	The effects of Rayleigh number on stability of a layered mantle	151
6.1	Cases investigated	151
6.2	The thermal evolution of the layered system	153

6.3	Is heat balanced in the layered system?	159
6.4	Stability of the layering	162
6.5	Coupling between the layers	167
6.6	Changing the viscosity structure	170
7	Implications for the Earth	173
7.1	Using entrainment to constrain the density contrast across the deformable interface	173
7.2	Coupling between the two layers	179
7.3	Plan form of convection	182
7.4	Lateral temperature variations	185
7.4.1	Lateral variations in the thermal structure with chemical effects removed	187
7.4.2	Lateral variations in the seismic velocity structure inferred from a linear combination of thermal and chemical effects	189
7.5	Four types of buoyancy ratio	194
7.5.1	Comparing different buoyancy ratios	197
7.6	Seismic constraints on the density contrast across a layer	200
7.6.1	The inclination of the boundary and its effect on seismic imaging	201
7.7	Stability and the density contrast in a deep layer	207
7.8	The temperature increase across the boundary	213
7.9	The effective density contrast of a lower layer	221
7.10	Summary	223
8	Conclusions and summary	225
9	References	229
	Appendix	
A	Glossary	242
B	The halo swap process	252
B.1	Position of a subdomain within a diamond	254
B.2	Knowing which diamond we are sending data to	255
B.3	Parallel communication – but where to?	257
B.4.1	Saving data in the left-hand side of the subdomains	259
B.4.2	Parallel communication to the left	261
B.4.3	Saving the right edge data into the halo region	262
B.5.1	Saving data in the right-hand side of the subdomains	265
B.5.2	Parallel communication to the right	266
B.5.3	Saving the left edge data into the halo region	268
C	Communicating the top and bottom corners beyond the halo region	270
C.1	Configuring parallel communication	271
C.2	An overview of the top and bottom exchange code	272
C.3	How do we know which processor to send the top and bottom data to?	273
C.4	And which data to send?	275
C.5	Parallel communication: how do we know where to save the data?	276
C.6	Storing the received data: has the data moved into a new diamond?	277

D	Template for the icosahedron model	279
E	Benchmarking TERRA programs on NESSC	282
E.1	Aim	282
E.2	Introduction	282
E.3	Method	283
E.4	Results	284
E.4.1	Heterogeneous behaviour	285
E.5	Discussion	285
E.6	Conclusions	286
F	Calculating the Rayleigh and Nusselt numbers	287
G	Solving $\varphi = a \div (B^a - b^a)$	288
H	Solutions to Davaille's equations with Earth-like parameters	290

1 Introduction

1.1 Objectives

Convection in Earth's mantle is driving plate tectonics. This process is responsible for generating most of the geological processes we see on Earth's surface: earthquakes, mountain building, volcanism and continental drift. Despite the importance of mantle convection and continued multidiscipline research there are still some basic aspects of the mantle that are not understood.

A series of geochemical observations suggest the presence of a chemically isolated reservoir in the mantle [e.g. Hoffman 1997]. However, geodynamical investigations suggest the mantle to be well mixed and it is expected that convection over the lifetime of Earth would homogenise the mantle [e.g. van Keken et al. 2002]. These two apparently conflicting observations have led to the suggestion that the mantle has a layered structure, with the upper and lower layers convecting independently and there being only very limited material exchange between the two layers. Historically, it has been suggested that the interface between these two layers is at a depth of 670km since this coincides with a seismic discontinuity. Recent improvements to seismic imaging techniques have allowed the imaging of subducting plates passing through the 670km discontinuity [van der Hilst et al. 1997; Grand et al. 1997]. A new model of mantle dynamics that allows material to flow over the 670km discontinuity has been suggested by Kellogg et al. [1999]. A chemically isolated reservoir is placed in a deeper layer in the mantle with the interface between the two layers at a depth of 1500-2000km. The interface between the deep layer and the upper mantle is suggested to be deformable with cold subducted material pushing it down and hot uplifted regions. See figure 1.1.

The behaviour of layered convecting systems such as that suggested by Kellogg et al. [1999] is not well understood [see Davaille et al. 2003 for a review]. Such a dense layer would require a sufficiently high-density contrast to be dynamically stable. In contrast, it must also have a sufficiently low-density contrast to explain its weak (or absent) seismic signal. There are very few simulations of convection in a three-dimensional (3D) spherical geometry and few dimensions of the parameter space likely to affect layering in Earth's mantle have been investigated.

The objectives of this thesis are to:

1. Develop a technique that will allow the modelling of a dense deformable layer in a 3D spherical geometry.
2. Determine the thermal structure of a layered convecting system and establish the contribution from convection taking place in a 3D spherical geometry as opposed to a Cartesian geometry.
3. Establish the density contrast needed to keep a layer dynamically stable and determine if the depth of the layer and the heating mode used to power convection affects this.
4. Determine how the stability of a layer is affected by the vigour of convection, allowing results to be extrapolated to Earth-like values.

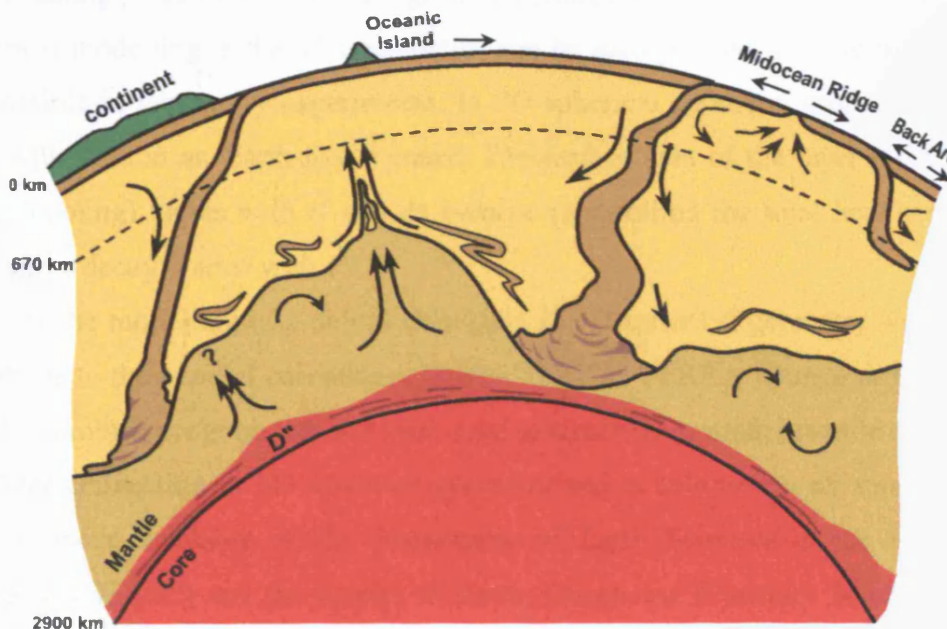


Figure 1.1

Diagram illustrating the possible dynamics of an intrinsically dense layer in the lower mantle. Depth to the top of the layer ranges from ~1600km to near the CMB, where it is deflected by downwelling slabs. Internal circulation within the layer is driven by internal heating and by heat flow across the CMB. A thermal boundary layer develops at the interface, and plumes arise from local high spots, carrying recycled slab and some primordial material.

Reproduced from Kellogg et al. 1999

1.2 Methodology

Previous investigations of layered convection have used a variety of methods including numerical modelling [Montague & Kellogg 2000, Tackley 1998], laboratory tank experiments [Richter & Johnston 1974, Davaille 1999a], and analytical methods [Sleep 1988]. Laboratory methods have contributed significantly to the current understanding of the behaviour of layered convecting systems. This method allows the depth of the layering, the density and the viscosity contrast between the layers to be altered. However it is limited to a Cartesian geometry and cannot incorporate radiogenic heating and depth dependent properties.

Previous numerical models have been limited to two-dimensions (2D) [Montague & Kellogg 2000] and/or a Cartesian geometry [Tackley 1998], with only very recent models taking place in 3D spherical geometry [Stegman et al. 2002a]. The advantage of numerical modelling is that characteristics can be incorporated into the model that are not possible in laboratory experiments. In 3D spherical geometry properties of a deep layer will scale in an Earth-like manner. The surface area of the layer (controlling its rate of cooling) varies with r^2 and its volume (controlling the total heat generated by radioactive decay) varies with r^3 .

To allow the modelling of a deformable layer in 3D spherical geometry we have made alterations to the parallel computer program TERRA. TERRA [Bunge & Baumgardner 1995] is a robust program that has been used extensively to model mantle convection. It simulates convection in 3D spherical geometry and is able to run on super computers such as those available in the Department of Earth Sciences at the University of Liverpool (NESSC) and the School of Earth, Ocean and Planetary Science at Cardiff University (Helix). We choose to develop a method that could be added to the existing TERRA program.

1.3 The structure of this thesis

In chapter 2 we introduce mantle convection and the arguments used for and against mantle layering. We also review the previous work on layered convection and summarise our current understanding of layered systems.

In chapter 3 we introduce the problem of numerically simulating mantle convection and describe the approach used by TERRA. We then describe the alterations made to TERRA to introduce a dense layer. Verification and performance of this method are then discussed in chapter 4.

We present the results of a number of simulations in which the depth and density contrast across the interface between two layers, and the heating mode used to drive convection are varied in chapter 5. This work has been submitted to G-cubed and accepted subject to revision [Oldham & Davies 2004]. In chapter 6 we present simulations in which the density increase across the boundary and the Rayleigh number Ra are varied. We then use these results to scale up earlier results to Earth-like Rayleigh number Ra .

The behaviour of layer convection within the parameter space investigated in chapters 5 and 6 are then discussed in chapter 7. The implications for convection in Earth's mantle are then discussed. The possibility of a layered mantle in Earth and a summary of our findings are presented in chapter 8.

2 Mantle Convection

The internal structure of Earth can be divided into several distinct layers. These layers appear to be concentric and so allow us to produce a one-dimensional model of Earth's internal structure, see figure 2.1. The inner core is comprised of solid iron and surrounds the liquid outer core that is comprised of iron and a lighter diluent (probably oxygen or sulfur [Fowler 1990, p113]). Convection is taking place in the outer core and being driven by a number of processes. The time scale of this convection is thought to be relatively rapid (in geological terms) around 10^4ms^{-1} †. The combination of convection and electrical currents in the outer core is responsible for generating Earth's magnetic field, though this process is not fully understood and is currently one of the most challenging problems in Earth science.

The mantle (German for coat) makes up the region between the brittle crust and the liquid outer core. The mantle is comprised of solid silicate material and is able to transmit both longitudinal (P) and transverse (S) seismic waves. There are some small regions of liquid material in the very upper mantle caused by the adiabatic decompression of material rising towards Earth's surface. Despite the apparently solid behavior of the mantle over short period its behavior over longer timescales is quite different with thermal and chemical buoyancy forces able to drive slow deformation. Over geological time, mantle material is able to convect with cold subducted material sinking downwards and hot buoyant material rising upward. The timescale of this process is estimated to be hundreds of Ma [Bunge et al. 1998; Tackley 2000]. The thin crust is only tens of kilometers thick and has a very different rheology to the mantle, with deformation processes ranging from brittle failure to viscous creep [Tackley 2000].

† This is probably an upper end estimate and comes from projecting the westwards drift velocity of the geomagnetic field to the core-mantle boundary.

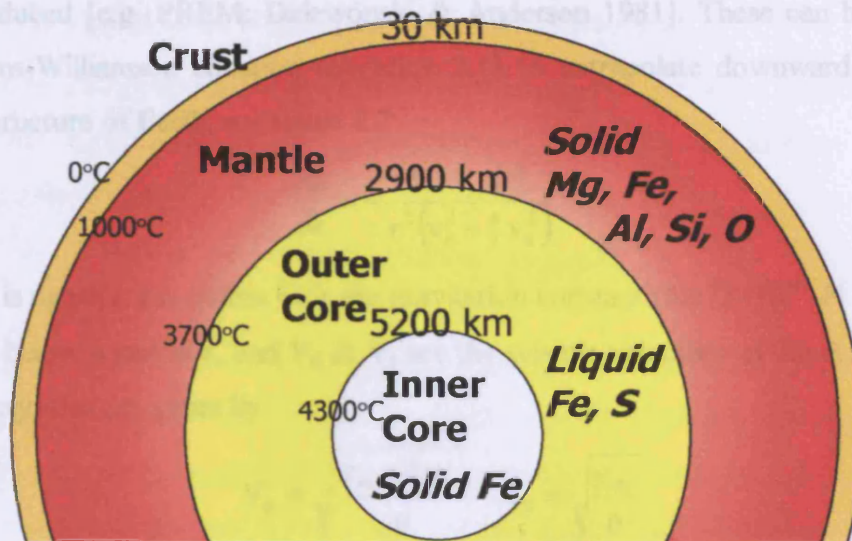


Figure 2.1

An overview of Earth's internal structure.

Reproduced from Univ. of Oregon Tremors Student Earthquake Research website

2.1 The structure of the mantle

Our knowledge of the composition of the mantle comes from various sources. Meteorites are thought to represent the composition of material from which Earth (and the other terrestrial planets) formed. Chondritic meteorites and comets represent the 'dust cloud' from which the solar system formed. Other meteorites such as irons, stony-irons and stones, probably represent a proto-planet that was broken apart by a large impact early in the solar system and suggest that stone meteorites have a composition similar to Earth's mantle. Other methods of determining the composition of the mantle come from solar spectroscopy from which we can determine the mineral abundances in the Sun and by studying other terrestrial bodies such as Mimas (a moon of Saturn) where a large impact has exposed the mantle and even sections of the core.

Direct measurements of mantle material are possible where mantle rocks (xenoliths) are brought to the surface in fast moving magma bodies. E.g. Kimberlite pipes have a source around 150km deep and often contain xenoliths. Two common types of xenoliths are spinel and garnet lherzolite that are ultramafic rocks and contain at least 40% olivine.

Lateral variations in seismic wave speeds are significantly smaller than the radial variations and so many one-dimensional models of the Earth's seismic structure have

been produced [e.g. PREM: Dziewonski & Anderson 1981]. These can be used with the Adams-Williamson equation (equation 2.1) to extrapolate downward to find the density structure of Earth, see figure 2.2.

$$\frac{d\rho}{dr} = -\frac{GM_r\rho(r)}{r^2\left(v_p^2 - \frac{4}{3}v_s^2\right)} \quad (2.1)$$

Where ρ is density, r is radius, G is the gravitation constant ($6.672 \times 10^{-11} \text{ N m}^2 \text{ kg}^{-2}$), M_r the mass below a radius r , and V_p & V_s are the seismic velocities of the P and S waves respectively, that are given by

$$V_p = \sqrt{\frac{\kappa_m + \frac{4}{3}\mu_m}{\rho}} \quad V_s = \sqrt{\frac{\mu_m}{\rho}} \quad (2.2)$$

Where κ_m is the bulk modulus and μ_m is rigidity modulus.

Phase transformations of mantle material can be studied using high pressure experiments on representative minerals e.g. olivine $(\text{MgFe})_2\text{SiO}_4$ [Ringwood & Major 1970]. Olivine transforms to a spinel structure at 410km. Between 410 and 670km two high-pressure phases exist; a spinel structure, ringwoodite and a distorted spinel structure, wadsleyite (sometimes called the intermediate or β -phase). At 670km a final phase change takes place to perovskite.

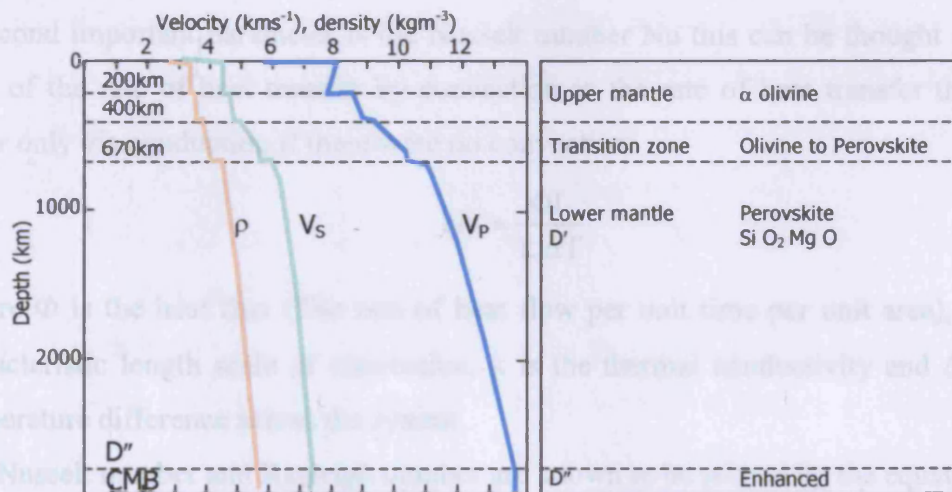


Figure 2.2

Estimates of the distributions with depth of seismic properties from the classic PREM model [Dziewonski & Anderson 1981].

2.2 The Rayleigh Ra and Nusselt Nu numbers

An important parameter that controls the nature of convection is the Rayleigh number. This is a non-dimensional parameter that represents the ratio of buoyancy to viscosity forces (for a derivation see Davies 1999, p217).

$$Ra = \frac{\text{buoyancy forces}}{\text{viscous forces}} = \frac{\alpha g \rho \Delta T L^3}{\kappa \eta} \quad (2.3)$$

Where α is the thermal expansivity, g is the gravitational constant, ρ is the density, ΔT is the temperature difference across the system, L is the characteristic length scale of convection, κ is the thermal diffusivity and η is the dynamic viscosity. For small values of Ra a system will not convect and heat will be transported only by conduction. For values of Ra greater than a critical value (the critical Rayleigh number Ra_c) convection will be present in the system, with more vigorous convection for increasing values of Ra .

There are numerous non-dimensional parameters in the field of fluid dynamics: Prandtl number [section 3.3.1], Ekman number [section 3.3.1], the buoyancy ratio [section 2.7.2 & 7.4]. The Rayleigh number can also be defined in a number of different ways. Each definition is dealt with as it arises in this thesis, but see appendix A (the glossary) for a summary.

A second important parameter is the Nusselt number Nu this can be thought of as the ratio of the rate of heat transfer by convection to the rate of heat transfer the would occur only via conduction if there were no convection.

$$Nu = \frac{\Phi L}{k \Delta T} \quad (2.4)$$

Where Φ is the heat flux (The rate of heat flow per unit time per unit area), L is the characteristic length scale of convection, k is the thermal conductivity and ΔT is the temperature difference across the system.

The Nusselt number and Rayleigh number are known to be related by the equation...

$$Nu = \left(\frac{Ra}{Ra_c} \right)^\beta \quad (2.5)$$

Where the values of Ra_c for Earth range from 82 to 1000 and β from 0 to 0.33 [M^cNamara & van Keken 2000].

2.3 The need for a chemical reservoir in Earth's mantle

Until the mid 1990's there were two (main) conflicting models of the mantle. The classic geochemical model had two-layers with the boundary between the layers placed at a depth of 670km. The depth of the interface between the two layers was chosen to agree with a known seismic discontinuity and because it agrees with some geochemical predictions of the relative volumes of the two layers, see figure 2.10a. The classic geodynamic model (figure 2.10b) places a deep reservoir at the base of the mantle and has single layer convection with the source of plumes at the Core Mantle Boundary (CMB). In this section we will summarize the geochemical arguments for the presence of a primitive reservoir in the mantle and the geodynamic and seismic arguments for whole mantle convection. We shall see that improving seismic methods have made the classic geochemical model unlikely. In response there have been a number of other models suggested [for a review see Hoffmann 1997 & Tackley 2000] each with their own merits and limitations.

2.3.1 Geochemical arguments

The geochemical arguments for multiple isolated chemically distinct reservoirs in the mantle are outlined in Hoffmann [1997] and Helffrich & Wood [2001].

Geochemical arguments are based on the assumption that Chondritic meteorites can represent the composition of Earth and that these meteorites form the building blocks of the terrestrial planets in our solar system. Once the iron has been removed from a Chondritic composition (as would happen during core formation) the remaining chemical abundances are often referred to as the Bulk Earth and are thought to represent the mantle and crust.

The composition of mantle rocks is altered when they melt and incompatible elements enter the magma and compatible elements remain in the solid mantle. As regions of the mantle are melted and transported to the surface through magmatic processes compatible elements are left in the mantle while incompatible elements are added to the crust. This process is especially effective for very highly incompatible elements, e.g. more than half the world's Th and U are now contained in continental crust [Hoffmann 1997]. This process leaves the upper mantle with low abundances of the incompatible elements, which it is said to be depleted, while the crust is described as enriched.

It is possible to sample the composition of the upper mantle by studying Mid Ocean Ridge Basalts (MORB). These are found to be depleted and so suggest the upper mantle as a whole is also depleted. Ocean Island Basalts (OIB) are thought to sample material from deep in the mantle. The plume model [Morgan 1971] suggests that hot buoyant plumes rising through the mantle and impacting on the lower surface of the crust cause hot spots. OIB are found to be less depleted than MORB and even enriched in some trace elements. The fact that material from the shallow mantle is depleted while material thought to represent or sample the deeper mantle is less depleted has led to the argument that in the deep mantle there is a homogenous region of enriched material. Also the uniform composition of MORB compared to the more varied composition of OIB is used as evidence that the upper mantle is well stirred with the enriched reservoir being less well mixed.

For a critique of the interpretation of MORB and OIB compositions see Anderson [2000a, 2000b & 2001] and Meibom & Anderson [2003].

2.3.1.1 Helium and Argon abundances in the atmosphere

The abundance of noble gas isotopes particularly Helium and Argon in Earth's atmosphere is another popular geochemical argument for the presence of a deep isolated reservoir. ^4He and ^{40}Ar are produced by the decay of U and Th, and ^{40}K and are degassed into the atmosphere. The flux of ^4He into the atmosphere and the amount of ^{40}Ar in the atmosphere should be predictable from surface heat flow and the amount of U, Th, and ^{40}K in the bulk Earth. There is around 50% of the ^{40}Ar that is thought to have been produced in Earth's history in the atmosphere and the flux of ^4He is a fraction of that expected [e.g. Craig & Lupton 1976; Hoffmann 1997 and Helffrich & Wood 2001]. This leads to the suggestion that there is a reservoir of material in the lower mantle where the ^4He and ^{40}Ar produced is chemically but not thermally isolated from the upper mantle. The high $^3\text{He}/^4\text{He}$ ratio in hotspot lavas also suggests that their source region is enriched compared to that of MORB [van Keken et al. 2002]. We note that, mechanisms have been suggested that can explain the ^4He and ^{40}Ar anomalies without a chemical reservoir [van Keken et al. 2001b; Anderson 2001].

2.3.1.2 Heat budget arguments

“At present Earth is losing heat at a rate of 44 TW. This heat loss must be balanced by radiogenic heat production and cooling. If the Bulk Earth has the same rate of

radiogenic heat production as chondritic meteorites then 31 TW would be generated. This would leave 13TW to be produced by cooling and would require cooling of 65K per 10^9 years. However, MORB are depleted in heat production and if (nearly) the entire mantle were made up of MORB then only 2 to 6 TW would be produced. The crust is observed to have enriched heat production and produces 6 TW. This leaves a deficit of 32 TW to be balanced by cooling. This needs a cooling rate of 175 K per 10^9 years, which requires unrealistically high temperatures in the Archaean.” paraphrased from Kellogg et al. [1999]; also see Davies [1999, p192].

2.3.2 Seismic and geodynamic arguments

The length scale of plate boundaries suggests that the scale of convection driving plate motions is of the order of 1000’s km. This favours a scale of mantle convection across the whole mantle as opposed to within a shallow layer. The bulk of the geophysical evidence comes from seismic investigations of the mantle structure and in particular images of subducting plates that extend deep into the mantle. The source regions of plumes and their apparently static motions also place limitations on any successful model of the mantle’s structure.

2.3.2.1 The fate of subducting slabs

Until the mid 1990’s there was some limited evidence that subducting material was able to penetrate the 670km discontinuity. The advancement of seismic tomography methods made possible by increasing computer power created the ‘break-through’ papers: Grand et al. [1997] and van der Hilst et al. [1997]. For the first time, cross sections of subducted material extending into the lower mantle were produced in both P and S wave images from different data sets. Images show seismic anomalies extending across 670km [van der Hilst et al. 1997; figure 2.3], and also some slower moving slabs ‘sticking’ at the 410km and 670km discontinuities but all extended into the lower mantle eventually [e.g. Hall & Spakman 2002]. The agreement of seismic tomography imaging of cold slow anomalies with the expected position of subducted plates [Richards & Engebretson 1992] and those predicted by mantle circulation models [Bunge et al. 1998; Bunge & Grand 2000; Bunge & Davies 2001] further suggest that subducted slabs do indeed extend to a depth of at least 2000km. Unfortunately plate motion histories are only reliably known for the last 100-120 Myr and this limits the depth to which we can trace plates using the circulation models. This limit is at a depth

of around 2000km that (annoyingly) coincides with the depth at which plates disappear in some tomography models.

Although there is some variation in the angle of descent of fast anomalies in tomographic models [Megnin & Romanowicz 2000] there is convincing evidence that subducting material does penetrate the 670km discontinuity and extends to a depth of at least 2000km in some locations. We can only speculate as to what happens below this depth. Both increasing viscosity and decreasing thermal expansivity will hinder the downward march of subducted material. There is some geochemical evidence to suggest that as subducted material descends to a depth of around 2000km it becomes neutrally buoyant [Ono et al. 2001; Niu & O'Hara 2003]. These factors may be sufficient to decrease a slab's descent to such a slow pace that it will thermally dissipate before it reaches the CMB. The increasing thermal conductivity with depth [e.g. Hofmeister 1999] will not directly impede a slab but will increase the rate at which it is absorbing heat from the surrounding mantle. This will make the slab more buoyant and also harder to image with seismic methods. Subducted material could reach the top of a deep layer and remain there and so explain the apparent disappearance of slabs at around 2000km. Folding of the subducted material such as those modeled by McNamara et al. [2001 & 2002] (this is a possible source of seismic anisotropy) could produce layers of hot and cold material that may be difficult to resolve using seismic tomography. It is also noted by the author that the models of McNamara et al. [2001] do bear some similarity to the tomography results of Ritsema & van Heijst [2000], see figure 2.3. A final reason for the disappearance of slabs between 1500 and 2000km depth is suggested by Fukao et al. [2001]. They suggest that a flushing event occurred around 45 M years ago. Such a sudden exchange of material between the upper and lower mantle could have caused the apparent gap in the tomographic images of subducting material and also caused a reorganization of global plate motions.

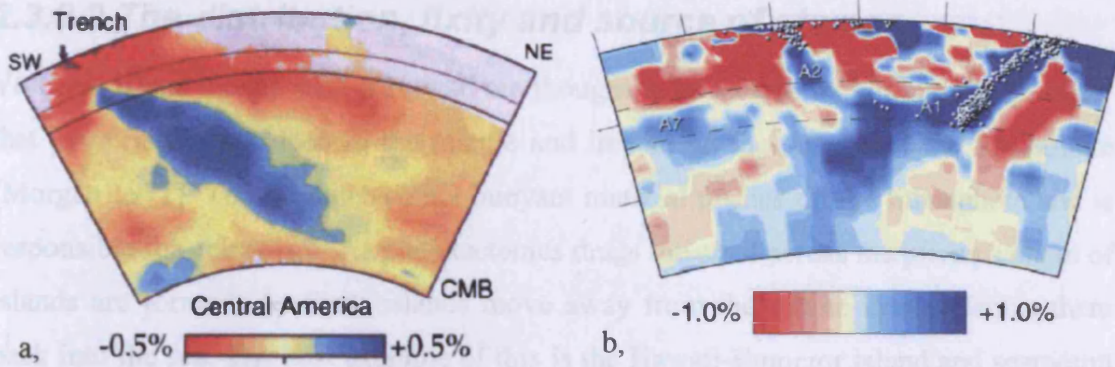


Figure 2.3

Tomography sections showing a subducting slab passing through the 670km discontinuity and a case in which the slab appears to stick at the discontinuity before continuing into the lower mantle.

a, Vertical mantle section through a global P-wave model from the Earth's surface to the CMB across the convergent margin in Central America. The word trench marks the location at the surface of the Middle American trench. Thin lines represent the depths 410 and 670km.

Taken from van der Hilst et al. 1997

b, Vertical section through the tomographic model of Bijwaard & Spakman [2000] to a depth of 1500 km on great circle segments of 30°, the section shown cuts across the Tonga trench. Colors denote the anomalous P-wave velocity structure.

Taken from Hall & Spakman 2002

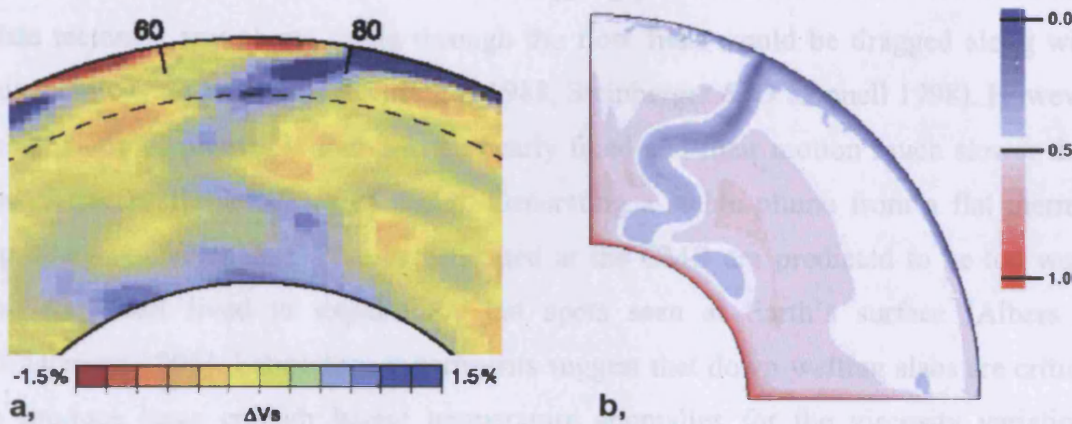


Figure 2.4

A comparison of the folding structures seen in seismic tomography models (a) and those simulated in numerical experiments (b).

a, Tomography model S20RTS across Japan's subduction zone [Ritsema & van Heijst 2000]. The continuous high seismic velocity anomaly extending from the subduction zone to the CMB is most consistent with subduction of oceanic lithosphere into the lower mantle, clear down to the core mantle boundary.

Taken from Tan et al. 2001

b, Snapshot of a simulation. There is greater convective vigor in the lower mantle. The temperature field is shown in non-dimensional units.

Taken from McNamara et al. 2001

2.3.2.2 The distribution, fixity and source of plumes

Volcanic island chains such as Hawaii are thought to be caused by hot buoyant plumes[†] that have risen from deep in the mantle and impact on the bottom of the lithosphere [Morgan 1971]. The presence of hot buoyant material pushes up the lithosphere and is responsible for volcanism. As plate tectonics drags the crust across the plume a chain of islands are formed. As these islands move away from the plume isostasy sinks them back into the sea. The best example of this is the Hawaii-Emperor island and seamount chain. The origin of plumes is a critical part of any dynamic or chemical model of the mantle, see figure 2.10. Hotspots are distributed irregularly, although their positions are not thought to be random. Hotspots appear to prefer locations close to spreading centres and dislike locations close to subduction zones [Weinstein & Olson 1989]. The location of hotspots also seems to preferentially coincide with regions of long wavelength geoid highs [Richards et al. 1988].

In a whole layer mantle model, such as the classic geodynamic model (figure 2.01b), there is no reason why plumes (and hence hotspots) should remain stationary. If we consider a mantle in which convection is dragging plates around the surface and driving plate tectonics any plume rising through the flow field would be dragged along with this mantle wind [Richards & Griffiths 1988, Steinberger & O'Connell 1998]. However the position of plumes is found to be nearly fixed and their motion much slower than the characteristic velocities of plates. Generating a stable plume from a flat thermal boundary is challenging. Plumes generated at the CMB are predicted to be too weak and too short lived to explain the hot spots seen at Earth's surface [Albers & Christensen 1996]. Laboratory experiments suggest that down-welling slabs are critical to produce large enough lateral temperature anomalies for the viscosity variations needed to produce plumes. So large headed plumes are perhaps a feature of planets with plate tectonics [Jellinek et al. 2002; Fougler & Natland 2003]. The inclusion of a dense viscous layer aids the stability of plumes by adding a stable base from which the plumes form and rise [Jellinek & Manga 2002, Davaille et al. 2002].

Imaging of plumes below hot spots can be achieved using a number of seismic methods with tomography being the most frequent [for a review see Nataf 2000]. Iceland is

[†] This assumption has recently been challenged, the attack being directed by Don Anderson, see Anderson [2003] (and other articles in the same issue) for a summary of his arguments.

frequently chosen as the site for detailed investigations mainly because the large landmass of Iceland (compared to Hawaii) provides a larger base line for seismic receivers. Initial work imaged the plume only in the shallow mantle (<400km) [Wolfe et al. 1997]. The more recent work of Bijwaard & Spakman [1999]; Maclennan et al. [2001] & Shen et al. [1998] all found evidence that the Iceland plume originates below the 670km discontinuity; although there are other results that suggest the Iceland plume is only present in the upper mantle [Fouger et al. 2001].

Other global surveys suggest that multiple hotspots extending into the lower mantle are consistent with seismic travel times data [e.g. Rhodes & Davies 2001] and some convincing images produced using finite frequency tomography appear to follow a plume from the CMB to the surface below Hawaii [DePaolo & Manga 2003]. There is a correlation between hot anomalies at the CMB and the location of hotspots on Earth's surface [Williams et al. 1998]. Slow seismic anomalies associated with plumes feeding the Hawaiian & Iceland plumes have been imaged throughout the full depth of the mantle [Zhao 2001]. The gravity anomaly associated with hotspots can be reproduced by numerical simulations of a plume spreading out below a lithosphere [Ride & Christensen 1999].

2.3.2.3 Mega plumes

Seismic imaging of the deep mantle has revealed two large slow anomalies in the deep mantle that extend from the CMB to at least a depth of 2000km [Su & Dziewonski 1991, van der Hilst et al. 1997, Ritsema et al. 1999]. These two anomalies are present below Tonga and South West Africa. They have a broad base that thins [Bréger et al. 2001] and then expands into large plume heads [e.g. Kárason & van der Hilst 2001], giving them a mushroom shape and often referred to as 'megaplumes' [Matyska et al. 1994]. A thermal anomaly alone is not thought to be sufficient to generate these features [Forte & Mitrovica 2001] especially at their bases [Romanowicz 2003]. It is speculated that there must be some compositional contribution to their seismic structure. Seismic investigations show the African super plume to have a 3% drop in S-wave velocity associated with it and a base that is around 1200km wide [Ni & Helmberger 2003]. Geological evidence (joint inversions) suggests that the center of this feature is buoyant with a 0.2% density decrease compared to the surrounding mantle and is more viscous than the upper mantle (10^{22} PaS) [Gurnis et al. 1999].

It has been speculated that these mega-plumes structures are responsible for Super-swells: areas of Earth's surface that contain a high density of hotspots [e.g. Courtillot et al. 2003]. Super-swells are observed in Western Africa and Polynesia; both are directly above the seismically observed mega-plumes. Plumes rising from above, what could be chemically distinct reservoirs, could be enriched by the reservoirs and so have a different chemical signature to plumes from other sources. This, it is claimed (in part) explains the variation in plume geochemistry [Courtillot et al. 2003]. Evidence that the mantle below super swells is chemically enriched [Janney et al. 2000] further supports leakage from a primitive mega-plume. The presence of two diametrically opposed super swells with corresponding megaplumes has led to the suggestion that the mantle is convecting in a two-cell pattern [Forte & Mitrovica 2001]. Courtillot et al. [2003] proposed three distinct types of hotspot sources: plumes from the CMB, plumes from the top of super swells and from local fracturing of the lithosphere. These last two models mentioned are summarized in figure 2.5.

2.3.3.4 Lateral variations in tomography inversions

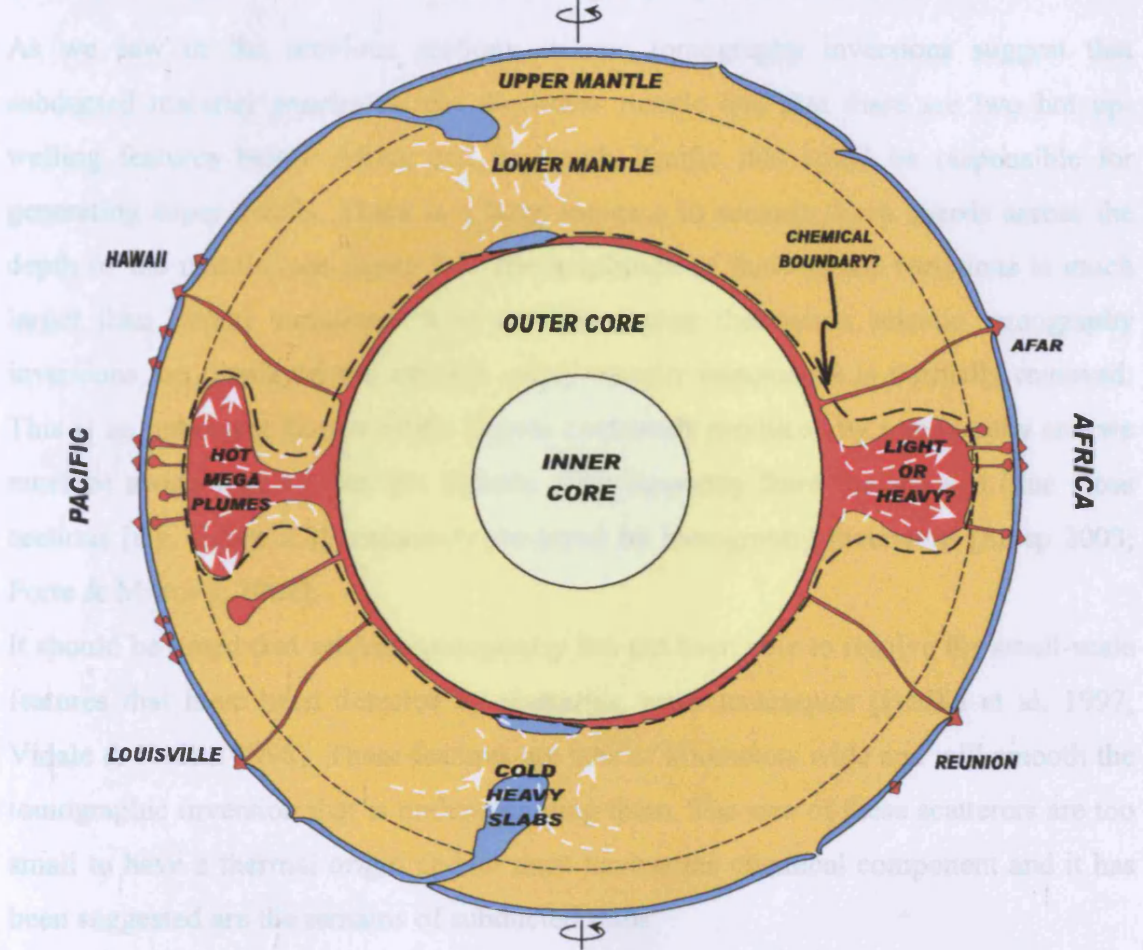


Figure 2.5

A schematic cross section showing (in the opinion of the author) one of the more currently accepted models of Earth's mantle. Convection is divided into two cells. The center of the cells containing hot mega plume structures that may be chemically distinct and form a primitive reservoir. Separating the two cells is a series of subduction zones. Plumes form on top of the mega plumes and the CMB, with other plumes being generated by local fracturing of the lithosphere.

This is a combination of figures from Courtillot et al. 2003 and Forte & Mitrova 2001 (in the supplementary section).

2.3.3.4 Lateral variations in tomography inversions

As we saw in the previous sections seismic tomography inversions suggest that subducted material penetrates into the lower mantle and that there are two hot upwelling features below Africa and the south Pacific that could be responsible for generating super swells. There is a large increase in seismic wave speeds across the depth of the mantle, see figure 2.2. The amplitude of these radial variations is much larger than lateral variations. It is for this reason that when seismic tomography inversions are displayed the average radial velocity component is normally removed. This is an important feature of the figures commonly produced by tomography and we must be aware that we can not directly infer buoyancy from the red and blue cross sections [e.g. figure 2.3] commonly produced by tomography inversions [Sleep 2003; Forte & Mitrovic 2001].

It should be noted that seismic tomography has not been able to resolve the small-scale features that have been detected by scattering wave techniques [Hedlin et al. 1997; Vidale & Hedlin 1998]. These features are tens of kilometers wide and will smooth the tomographic inversion that is under-sampling them. The size of these scatterers are too small to have a thermal origin and so must have some chemical component and it has been suggested are the remains of subducted slabs.

The variance of seismic wave speeds at a given depth contains information about the amplitude of temperature and chemical variations in mantle structure at that depth. This variance can be represented by the root-mean-square (RMS) of the inverted seismic wave speeds and can be calculated for all the depths. An example RMS wave speed with depth is shown in figure 2.6, here a large RMS wave speed can be interpreted as representing a radius in the mantle where there are large lateral variations in temperature and/or chemistry. The most heterogeneous regions are found to be at the surface and the very bottom of the mantle where there are thought to be large thermal boundaries. By using the angular correlation tomographic inversions it is also possible to study the wavelength of lateral variations seismic wave speeds [Helffrich & Wood 2001], see figure 2.7. The higher amplitude RMS velocities and longer wavelength of the angular correlations at the surface and D'' regions can be explained. In the upper mantle heterogeneities are determined by the presence of continental and oceanic material. The varying thickness and age of the crust causes variations in the temperature of the underlying mantle, the hottest regions being hot spots and the

coldest areas tectosphere below cratons. In the D'' region there is expected to be some chemical variations that would contribute to the high lateral variations seen. However, a deep deformable layer would cause large lateral variations in both the temperature and chemical structure of the mid-mantle. It is expected that these variations would cause equally large variations in the wave speed that are simply not seen. This is a common argument against a deep layer [e.g. Tackley 2000; Forte et al. 2002]. Simulations of layered mantle convection have been unsuccessful in producing a deformable layer in which the chemical and thermal structure of the layer cancel out in such a way that seismic wave speeds show little variance [Tackley 2002a].

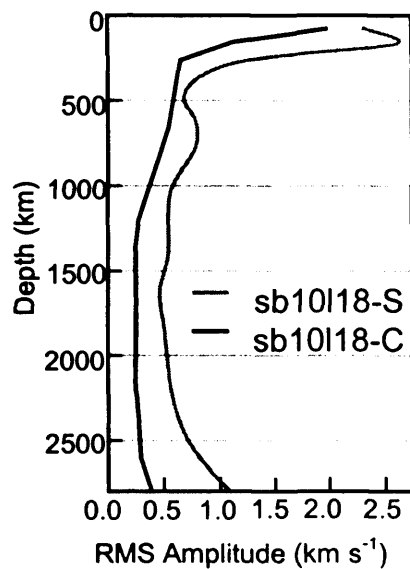


Figure 2.6
Depth variation of the RMS amplitude of S wave velocity and bulk sound speed from a recent tomographic model [SB10L18].
Reproduced from Masters et al. 2000

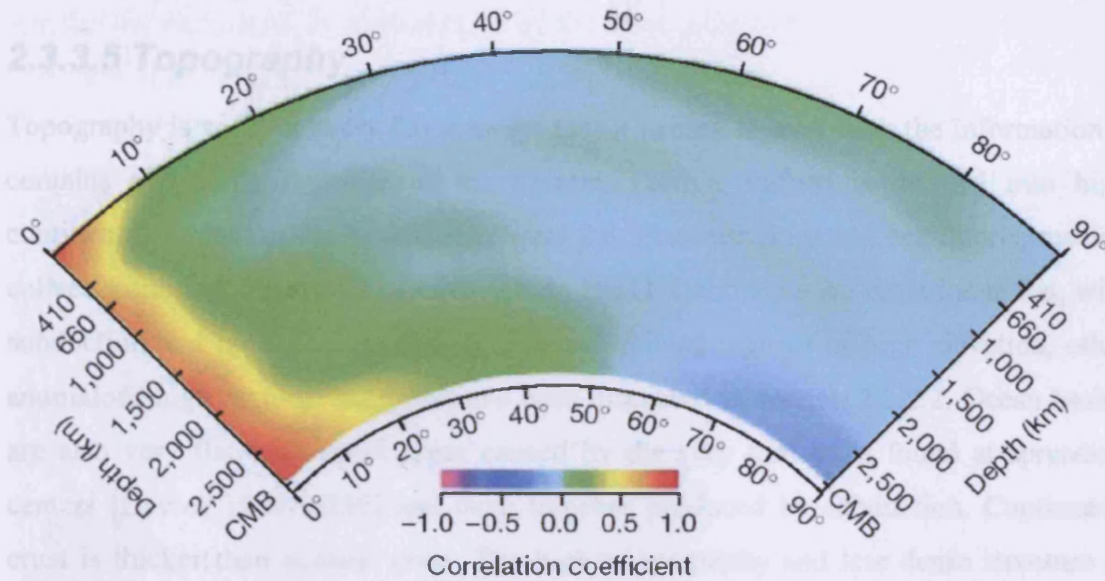


Figure 2.7

Angular correlation function of a shear-wave tomographic mode [Grand 1994] as a function of depth. This characterizes the similarity of wave speed of two points at the same depth in the mantle separated by some angular distance. Every point in the mantle is perfectly correlated with itself, resulting in the maximum correlation for points separated by zero distance (left side of figure). A drop of e^{-1} , or about 0.4, indicates a significant correlation decrease (the yellow band). Blue colors representing zero or negative correlations arise at large separations, and a degree-two pattern at the mantle's base is made evident by the maximum negative correlation at $\sim 90^\circ$. The correlation length is greatest in the upper mantle and in D". In the upper mantle, this probably corresponds to continent/ocean differences [Su & Dziewonski 1997], while the structure in D" possibly reflects the pattern of heat flow out of the core into the mantle. In the lower mantle above D" the correlation length is approximately constant, indicating no reorganization of heterogeneity scale length in the mid-lower mantle.

Taken from Helffrich & Wood 2001

2.3.3.5 Topography

Topography is such an every day concept that it is easy to over look the information it contains about the structure of the mantle. Earth's surface is divided into high continents and low ocean basins, see figure 2.8. Plate tectonics and sea floor spreading collects continental material together [Dietz 1961]. Continents are remarkable flat, with subduction and mountain building producing isolated regions of high elevation, other anomalous high regions: hotspots have been discussed in section 2.3.2.2. Ocean basins are also very flat with uplift areas caused by the very thin crust found at spreading centers [Davies 1999, p236] and deep trenches produced by subduction. Continental crust is thicker than oceanic crust. The higher topography and less dense structure of the continental material needs to penetrate deeper into the denser mantle material to balance the buoyancy forces acting, a process call isostatic equilibrium.

Isostatic equilibrium is not only affected by crustal material. In the arguments above we have considered the effects on topography of thickness and density of the overlying crust and have assumed the mantle to have a uniform structure. A buoyant 'blob' in the mantle will cause an increase in topography, with the amplitude of the topography being larger and the wavelength shorter as the 'blob' is nearer to the surface. Hot plumes are thought to be responsible for hotspots such as Hawaii and are speculated to be less dense than the surrounding mantle and so require large uplifted features to be in isostatic equilibrium. Similarly, a dense subducting slab would produce a depression or trench above it. Numerical models of plate scale convection have been able to produce similar topography to that observed when convection takes place across the whole mantle [Davies 1999 p279, Davies 1989a] but when convection was layered with a rigid boundary at 670km depth topography was much larger than Earth's [Davies 1988]. The increased topography was caused by the large thermal boundary needed at 670km to provide sufficiently high heat flux and the high temperature anomalies this produces. When a low viscosity layer is included in the upper mantle the amplitude of topography decreases slightly [Davies 1989b], but we should note that the layer in the case quoted here is not a boundary to flow, only a radial viscosity structure. A deep denser and deformed layer would be expected to contribute to topography. The amplitude of the topography would be greater for shallower, denser and more deformed layers. The wavelength of the topography will increase for a deeper layer and depend

on the wavelength of the deformation of the layer. Due to time constraints this is one behavior of layering that we have been unable to explore.

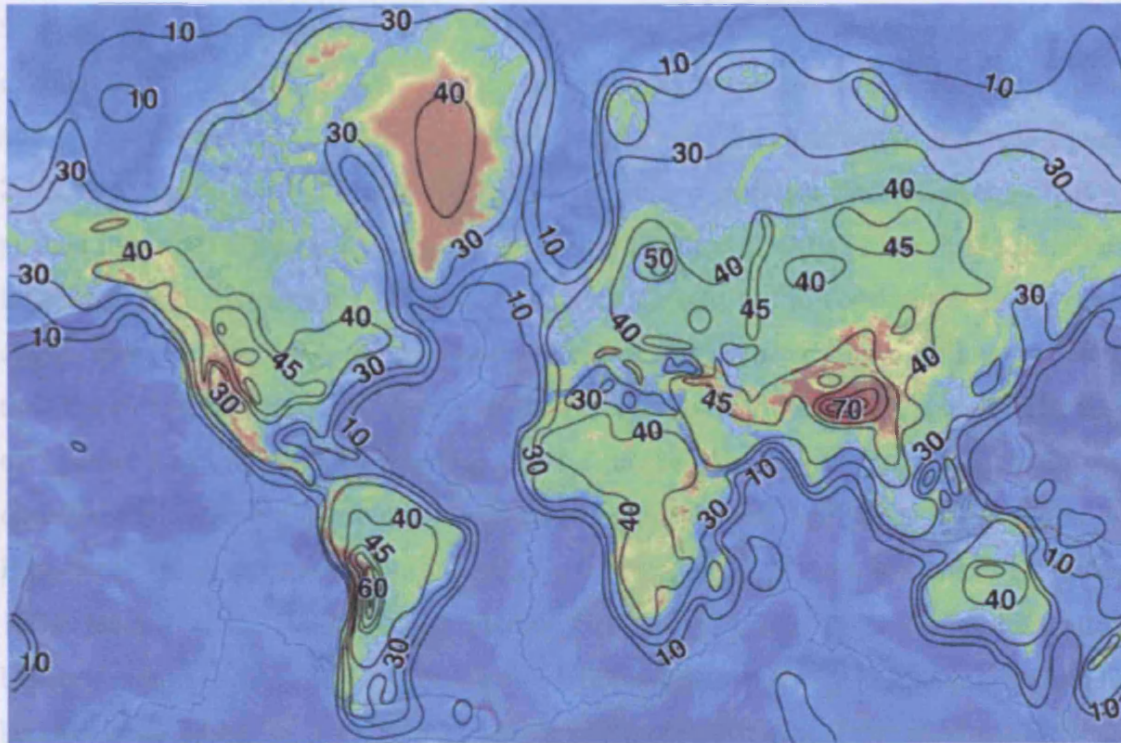


Figure 2.8 Earth's crustal thickness and topography. The high continents (green) and low ocean basins (blue) dominate. The more elevated continental crust is composed of a thicker crust.

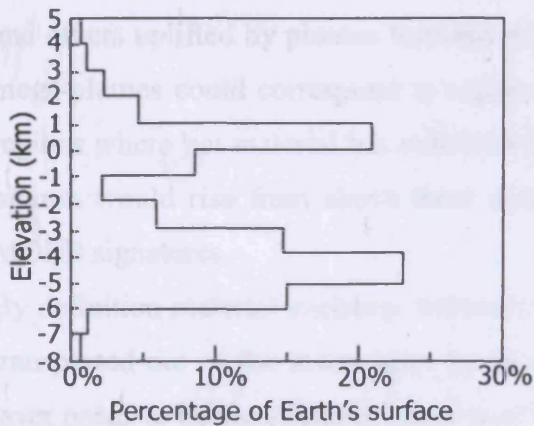


Figure 2.9 The distributions of the elevation of Earth's surface. There are two clear peaks, the higher continental material and the deeper oceanic material.

2.4 Suggested locations of the mantle reservoir and the Kellogg layer

Suggested locations of the non-MORB enriched chemical reservoir are almost exclusively in the deep mantle, though the structure suggested does vary. Piles, blobs and a 'deep' layer are the three most commonly considered arrangements, see figure 2.10. Pile structures would form as viscous, dense and enriched material at the CMB is pushed into high plateaus by subducted material [Tackley 2000]. These would form tall large sharp-sided structures that could extend high into the lower mantle. These piles could correspond to the two mega-plumes observed. They would be significantly hotter than the surrounding mantle because of bottom heating from the CMB and a higher rate of internal heating. Plumes forming on top of the piles could possibly sample the enriched pile by entrainment and cause a heterogeneous OIB and MORB signatures. A Blob model places the reservoirs in lumps of varying sizes in the lower mantle [Davies 1984; Becker et al. 1999]. Rising plumes interfere with the blobs and are deflected becoming enriched in the process. The two observed seismically fast anomalies could be two large blobs. In a layered system it is suggested that the chemical reservoir is contained in a dense layer that surrounds the core. The depth of the interface between the layers has been suggested to be between 1500km and 2000km [Kellogg et al. 1999]. The boundary between the lower mantle and the 'deep' layer would be deformable with undulations, see figure 1.1. Some areas would be pushed down by subducting material and others uplifted by plumes forming in the deep layer at the CMB. In this model the mega-plumes could correspond to regions of uplift in the deep layer. These would be regions where hot material has collected and uplifts the layer. As with the piles model, plumes would rise from above these domes and could cause heterogeneous OIB and MORB signatures.

By definition material exchange between two layers is limited and so heat can only be transported out of the lower layer by thermal conduction. As a consequence the deep layer needs to be significantly hotter than the upper mantle and a large thermal gradient is required at the interface between the layers. It has been suggested that the temperature contrast over this thermal boundary would be too large to remain unnoticed by seismic investigations [Tackley 2002a & 2002b]. Evidence to support a deep layer comes from investigations that show that a deep layer (if a common feature

of terrestrial planets) would have been critical in controlling the cooling rate of the early Luna core and maintaining the Luna-dynamo [Stegman et al. 2002a].

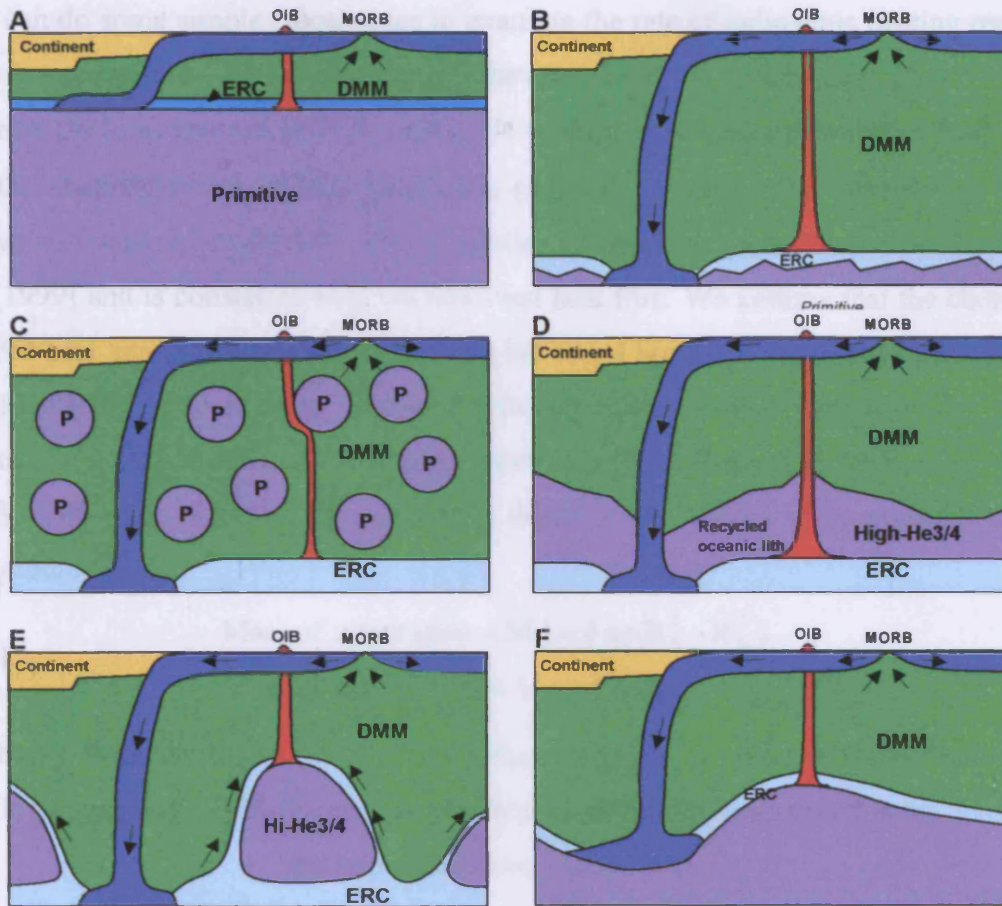


Figure 2.10

Some possible locations of mantle reservoirs and relationships to mantle dynamics. Convective features: blue, oceanic plates; red, hot plumes. Geochemical reservoirs: dark green, Depleted MORB Mantle (DMM); purple, high $^3\text{He}/^4\text{He}$ ("primitive"); light green, enriched recycled crust (ERC). (A) Typical geochemical model layered at 670km depth [Hoffman 1997]. (B) Typical geodynamic model: homogeneous except for some mixture or ERC and primitive material at the base. (C) Primitive blob model [Becker et al. 1999] with an added ERC layer. (D) Complete recycling model [Albarède 1998; Coltice & Ricard 1999], (E) Primitive piles model [developed from Kellogg et al. 1999]. (F) Deep primitive layer [Lithgow-Bertelloni & Silver 1998]

Reproduced from Tackley 2000

2.5 Estimates of the rate of radiogenic heating in a chemically enriched layer

We can do some simple calculations to examine the rate of radiogenic heating required in a layered mantle. We assume Earth to have a chondritic composition [Anders 1977; Wänke 1981; Ringwood 1977 & 1979]. We multiply the mass of Earth (5.972×10^{24} kg) by the chondritic rate of heat generation ($4\text{-}6 \times 10^{-12}$ Wkg⁻¹) [Davies 1999, p193] to arrive at a value of 24-36 TW. This is similar to the value quoted above by Kellogg et al. [1999] and is consistent with the observed heat flux. We assume that the chondritic rate of heat generation is correct for Earth but is not homogeneous throughout Earth or the mantle. We now consider a layered system. We assume that there is no radioactive heating in the Core and that the crust generates 6 TW [Kellogg et al. 1999]. This leaves 19-30 TW to be produced by radioactive decay in the mantle. If we consider a layer with radius R_K ...

$$\text{Mass of upper layer} = M_u = \frac{4}{3} \pi \rho (R_S^3 - R_K^3)$$

$$\text{Mass of upper lower} = M_l = \frac{4}{3} \pi \rho (R_K^3 - R_{CMB}^3)$$

Where ρ is the density of the mantle, R_S , R_K & R_{CMB} is the radius of Earth's surface, a Kellogg layer and the CMB respectively. We make the simplification that the density in the upper and lower layers is equal.

$$\text{Heat generated in the upper layer} = Q_u = M_u q_u = \frac{4}{3} \pi \rho (R_S^3 - R_K^3) q_u$$

$$\text{Heat generated in the lower layer} = Q_l = M_l q_l = \frac{4}{3} \pi \rho (R_K^3 - R_{CMB}^3) q_l$$

Where q_u & q_l are the rate of radiogenic heat production in the upper and lower layers respectively.

$$Q_u + Q_l = Q_{\text{Chondritic}}$$

Where $Q_{\text{Chondritic}}$ is the total heat produced in the mantle suggested by chondritic meteorites having a value of 19-30 TW.

$$\frac{4}{3} \pi \rho \left\{ (R_S^3 - R_K^3) q_u + (R_K^3 - R_{CMB}^3) q_l \right\} = Q_{\text{Chondritic}}$$

$$q_l = \left\{ \frac{3 Q_{\text{Chondritic}}}{4 \pi \rho} - (R_S^3 - R_K^3) q_u \right\} \div (R_K^3 - R_{CMB}^3) \quad (2.6)$$

The results of this can be seen in figure 2.11. The rate of heat generation required in the lower layer for layering at 670km is 6-13 p W/kg. For a Kellogg interface at 1500km the range of possible values is 11-24 p W/kg. When this layer is placed deeper in the mantle at 2000km this increases to 18-43 p W/kg. For a D'' layer the values are 81-198 p W/kg. Interestingly this is an order of magnitude larger than the rate of heat generation in oceanic crust and does not add weight to the suggestion that D'' is a graveyard for subducted material. If this were the case then a second enriched reservoir is required.

Region	Concentration of U	Power (pWkg ⁻¹)	Density (Mgm ⁻³)	Power (nWm ⁻³)
Upper continental crust	5 μ g/g	1000	2.6	2600
Oceanic crust	20 n g/g	10	2.9	30
Upper mantle	5 n g/g	1	3.3	3
Chondritic meteorites [†]	20 n g/g	4-6	3.3	12-18

Table 2.1

Radiogenic heat production rates (assuming Th/U = 4 kg/kg, K/U = 10⁴ kg/kg). † With K/U = 2-6 × 10⁴ kg/kg

Taken from Davies 1999, p193

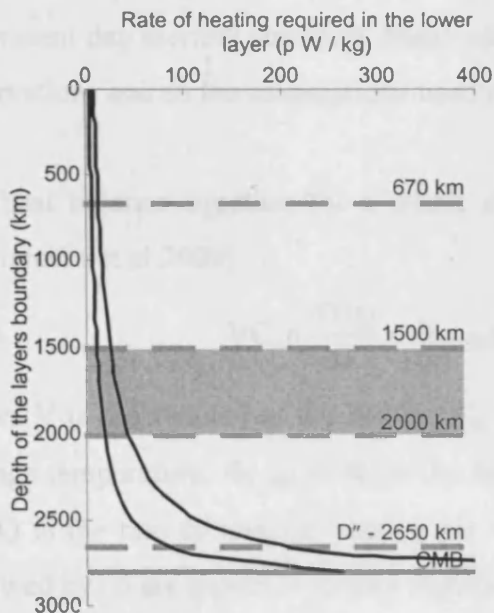


Figure 2.11

The rate of heating required in a lower layer to produce chondritic values of heat production across the whole Earth. The two black lines show the possible values calculated with the upper and lower suggested values of the chondritic concentration of U. The dashed horizontal lines show the depth at which layering has been suggested. The grey box corresponds to the suggested depths of the interface between the mantle layers.

By balancing the rate of heat production from radioactive decay in Chondritic meteorites and the observed heat production in the crust and upper mantle we estimate the rate of heat production in a lower layer. We find that an interface with a depth between 1500km and 2000km has a range of possible values of 11-43 p W kg⁻¹.

These arguments are however based on the assumption that Earth has a Chondritic composition. This may not be valid. Drake & Righter [2002] comment that no meteorite or comet has been found to have a chemical composition similar to that of Earth's mantle. They suggest that Earth accreted in part from hydrous material that is not present in Chondritic meteorites. There is a gap in the literature for estimates of the rate of heat production in an enriched lower mantle. For this reason we must consider the rate of radiogenic heat production in a lower layer to be part of parameter space and in need of further investigation. Becker et al. [1999] used the relative abundances of radiogenic elements for the bulk Earth from McDonough & Sun [1995] and combined them with the heat generation values quoted in Stacey [1992] to arrive at a figure of $5.1 \times 10^{-12} \text{ Wkg}^{-1}$ for the rate of internal heating in an enriched reservoir.

The Chondritic heat generation argument presented above is not the only constraint that heat flux can place on our understanding of the mantle. Heat balance of the mantle over its thermal history can be calculated. A number of assumptions are used in these calculations such as the heating mode and the rate of internal heating. The parameterized convection equations are started 4.2 billion years ago and integrated to the present day thermal structure. Many calculations yield results that do not agree with observations and so the assumptions used in these calculations can be rejected.

The heat balance equation for a whole mantle convection system can be written as [M^cNamara et al 2000]...

$$VC_p\rho \frac{dT(t)}{dt} = \Phi_{\text{CMB}}(t) - \Phi_S(t) + Q(t)V \quad (2.7)$$

Where V is the volume of the mantle, C_p is the specific heat, ρ is the density, T is the average temperature, Φ_{CMB} & Φ_S is the heat flux at the CMB and surface respectively and Q is the rate of internal heating per unit volume from radioactive decay. Values followed by (t) are expected to vary significantly during the mantle's history.

To calculate the heat flux at the CMB and the surface, the size of the thermal boundary layers (ΔZ) must be found. This is done using the following relationship...

$$\Delta Z = L \left(\frac{Ra_c}{Ra} \right)^\beta \quad (2.8)$$

Where: $87 < Ra_c < 1100$; $0 < \beta < 0.3$ for Earth's mantle [M^cNamara & van Keken 2000]

Where L is the length scale of convection, Ra is the Rayleigh number; Ra_c is the critical Rayleigh number (the point at which convection starts) and β is a constant. This relationship can be used in any constant viscosity fluid [Schubert et al. 1979] however the temperature dependent viscosity in the mantle can cause the lower boundary layer to be thinner than the surface boundary layer [Daly 1980]. The values of both Ra_c and β are not well constrained for Earth's mantle. The critical Rayleigh number is estimated to be between 87 and 1100 whilst β (important in controlling the Rayleigh Ra – Nusselt Nu number relationship) is expected to be between 0 and 0.3

Consequently the heat flux can be expressed as...

$$\Phi_{CMB} = \Phi_S = k \frac{\Delta T}{\Delta Z} = k \frac{\Delta T}{L} \left(\frac{Ra}{Ra_c} \right)^\beta \quad (2.9)$$

However to calculate the value of Ra throughout Earth's history we also need to know how the dynamic viscosity will vary. The cooling of the mantle and viscosity's temperature dependence means that some formulation of this relationship must be used...

$$\eta = \eta_0 \exp\left(\frac{E}{RT}\right) \quad (2.10)$$

Where η is the viscosity, η_0 is the minimum viscosity, E is the activation energy, R is the gas constant and T is the average temperature in the layer.

Equations 2.7, 2.9 & 2.10 have been solved (most recently) by M^cNamara & van Keken [2000] by assuming that the CMB was insulating ($\Phi_{CMB}=0$). They repeated the results of Spohn & Schubert [1982] and found that whole mantle convection is more efficient at removing heat from Earth's interior than layered convection. Spohn & Schubert looked at layered convection at 670km and found that for a layered system to have realistic thermal values in the Archaean and present day they required a depleted lower layer. This is in contrast with suggestion that a lower layer would be chemically enriched. M^cNamara & van Keken [2000] studied a layer at 1600km and found that very few cases ended with a thermal structure like the present day Earth's.

2.6 Mixing – do we need a chemical reservoir?

Mixing is the process of stirring that will homogenise a fluid's structure with sufficient time. If mixing in Earth's mantle is inefficient then there could be homogeneous sections that might not be sampled by MORB. A suggested location for such an unsampled region is in the center of convecting cells [Davies 1984]. This removes the need for a dynamically isolated reservoir, but is based on the assumption that the mantle is poorly mixed. Determining whether the mantle is efficiently or poorly mixed would therefore constrain whether there is a need for a chemical layer. Readers interested in an overview of this topic are directed towards van Keken et al. [2002 & 2003] with the latter being the more comprehensive.

Increasing viscosity has been suggested a mechanism for reducing mixing efficiency [Gurnis & Davies 1986], but has been shown to have limited effect [van Keken & Ballentine 1998; Hunt & Kellogg 2001; Stegman et al. 2002b]. The inclusion of phase boundaries, depth dependent diffusivity and thermal expansivity [van Keken & Ballentine 1999] does not suggest a poorly mixed mantle.

Simulations in three dimensions [Schmalzl et al. 1996] produce more effective mixing than those in two dimensions [Hoffman & McKenzie 1985] and the inclusion of a toroidal component to the flow field can produce areas of limited mixing [Ferrachat & Ricard 1998; van Keken & Zhong 1999]. In the mantle toroidal flow is generated by plate tectonics (specifically transform faults) and so moving plate boundaries make it unlikely that any isolated unmixed regions exist in the mantle [van Keken & Zhong 1999]

It is convenient to divide a field B in a spherical geometry in terms of its poloidal B_S and toroidal B_T components...

$$B_S = \nabla \times \nabla \times rS$$

$$B_T = \nabla \times rT$$

Where S and T are scale functions of (r, θ, ϕ) ; so B_T has no radial component.

“It is unlikely that a large chemical heterogeneity could remain unmixed in whole mantle convection over the lifetime of the earth” van Keken et al. 2002[†].

[†] When making this statement van Keken et al. references Ferrachat & Ricard 2001, Hunt & Kellogg 2001, and personal communications with Paul Tackley and Geoff Davies

2.7 The behaviour of a layered convecting system

It is unclear under what conditions a chemically distinct reservoir would have formed in the deep mantle. In their proposal of a deep layer Kellogg et al. [1999] merely state that “Such a layer could develop during the early differentiation of Earth, by processes associated with a deep magma ocean, or by formation and recycling of mafic crust in the Archean”. This clearly advocates that a deep layer would be primordial having formed during the initial differentiation of Earth or else very early in Earth history. A layer would have formed probably while the mantle was melted and so will have survived mixing and entrainment over a time scale of around 4.2 billion years. Consequently, any layered system present in Earth’s mantle must not only be stable in the present mantle but must also have sustained itself throughout Earth’s history.

Conditions in the early Earth such as higher rates of internal heating and hotter temperatures in the mantle may have been less favorable for a deep layer to exist in a stable state. Understanding the conditions needed to keep a deep layer stable in the present day mantle will place constraints on the possible structure of such a layer. These can then be compared with the limitations that can be placed on a deep layer by other considerations such as the entrainment from the deep layer [section 4.4 & Gonnermann et al. 2002], the topography produced by such a layer [Davies 1988], seismic reflection investigations [section 7.6 & e.g. Castle & van der Hilst 2003a], seismic tomography [section 7.4 & Tackley 2002a], and free oscillations [section 7.9 & Masters & Gubbins 2003].

In the case of a D" layer possible origins are: “a, primordial; b, an iron rich layer [Knittle & Jeanoz 1989]; or c, the segregated residuum component of oceanic slabs (a kind of slab graveyard)” [Tackley 1998].

“If the lower mantle was acting as a hot abyssal layer its density excess would have to be less than 0.4%. Whether such a layer would be dynamically stable remains to be seen” Masters & Gubbins [2003].

“It is important to ascertain what form a deep, dense layer could take, and how this would explain the geothermal and seismological observations” Tackley [2000].

2.7.1 The Stability of a layered system

One of the most important parameters controlling the nature of layered convection is the buoyancy ratio. This is defined as the ratio of the chemical buoyancy forces to the thermal buoyancy forces and is often given the notation B^\dagger .

$$\text{Buoyancy Ratio} = B = \frac{\text{Chemical Buoyancy}}{\text{Thermal Buoyancy}} = \frac{\Delta\rho/\rho_0}{\alpha\Delta T} \quad (2.11)$$

Where $\Delta\rho$ is the difference between the two intrinsic chemical densities in the system, ρ_0 is the reference density, α the thermal expansivity and ΔT is a temperature contrast. The definition of B does vary from paper to paper with the most common variations being the value of ΔT used. This is explored in more detail in section 7.5, where we conclude that the best value of ΔT to use is the temperature contrast radially across the whole system.

It is desirable to know how a layered system will behave when it has a given set of input parameters. Characteristics of convection such as the amplitude and wavelength of undulations on the interface between the two layers could then be predicted over the range of possible input parameters for Earth's mantle and the present state of a deep layer compared to observations. The most important characteristic we would like to be able to predict of a layered convecting system is whether it is stable. There is however a large parameter space that needs investigating: The buoyancy ratio B [chapters 5 & 6; e.g. Davaille 1999a], the Rayleigh number Ra of the system [chapter 6; e.g. Le Bars & Davaille 2002], the ratio of the viscosities in the two layers [e.g. Davaille 1999b, Le Bars & Davaille 2004], and the depth of the interface between the two layers [chapter 5; Davaille et al. 2003], have been investigated so far. Each of these will now be discussed in turn. It is important to note that while understanding the behaviour of a layered system with these parameters is a useful tool we must be careful when we extend them to Earth's mantle since we cannot predict the effect of changing other parameters.

Davaille et al. [2003] summarises the published investigations into layered convection within the Ra and B domain in figure 2.12. The results shown here do not all have the same parameters outside of the Ra and B domain and most significantly the ratio of the viscosities in the upper and lower layers does vary significantly between the cases and so affects the mode of convection. Even with these constraints some useful trends can

[†] The Buoyancy ratio is also sometimes given the notation $R\rho$ though this tends to be in older papers.

be seen, the system moves from a stable (squares) to unstable (circles) state as the buoyancy ratio falls below a particular value. This is called the critical buoyancy ratio B_c and estimates of its value are as small as 0.3. [Davaille et al. 2003] and as high as 1.0 [Montague & Kellogg 2000]. These variations are caused by B_c 's dependence on other parameters [Montague & Kellogg 2000]. Davaille et al. [2003] describe two modes of convection in a layered system. In the thermal mode, convection is driven by small-scale plumes that form at the thermal boundary at the bottom of the system. In the thermo-chemical mode large scale convection and deformation of the interface between the two layers is driven by the interaction between the unstable thermal gradient and the stable chemical density gradient. A third mode of convection is seen in which an initially stratified system develops into a whole layer system as the temperature increases in the lower layer (crosses). These cases tend to have $B > B_c$ and have varying Ra . We shall see that this mode is controlled by the viscosity ratio between the two layers.

As the Rayleigh number increases the system moves from a regime in which there is no convection, to a convecting system in which only the thermo-chemical mode is present (open symbols), to a convecting system in which both the thermo-chemical mode and the thermal mode are present (closed symbols). This happens as Ra increases above a value of around 10^5 .

Davaille et al. [2003] present a summary of the behaviour of layered systems within the Ra and B parameter space (see figure 2.13). Whole mantle convection is included below Ra_c since at lower Ra the layered problem can be solved analytically and its behaviour can be predicted [Le Bars & Davaille 2002, Richter & McKenzie 1981]. The value of B at which the system moves from stratified to whole layer convection B_c is a function of Ra . However the dependence of B_c with Ra becomes less significant when Ra is large. Davaille et al. [2003] quotes a value of \bar{B}_c of 0.33. \bar{B}_c is the value of B_c when the system has the critical Rayleigh number Ra_c . B_c is a function of the Rayleigh number and other parameters including the viscosity ratio and depth of the interface [Le Bars & Davaille 2002]. B_{lim} corresponds to the point at which a chemical layer becomes too negatively buoyant to be reversed by any thermal effects and like \bar{B}_c is function of other parameters [Le Bars & Davaille 2002].

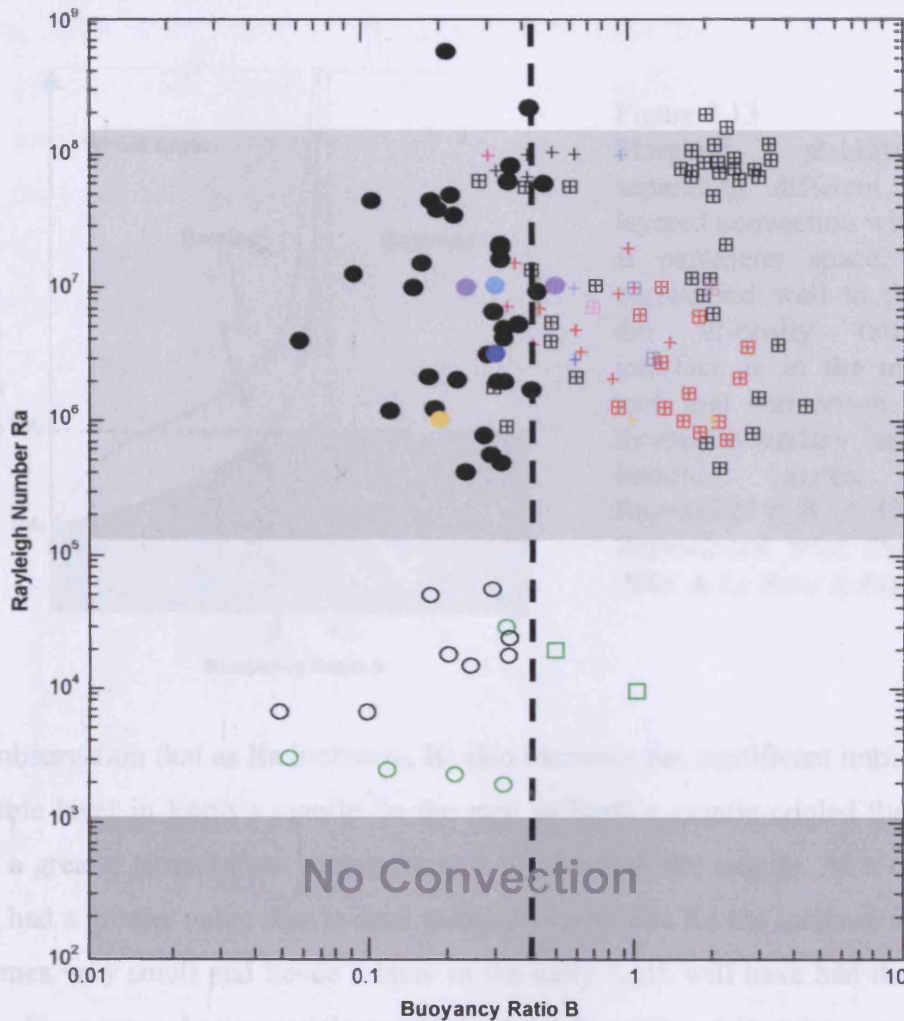


Figure 2.12

Different regimes of thermochemical convection as a function of Rayleigh number and buoyancy ratio. Circles: whole layer regime; squares: stratified regime throughout the whole duration of the experiment; crosses: convection initially stratified with strong deformation of the interface, which eventually becomes unstable (the doming regime). Open symbols designate experiments where only one scale of convection (thermochemical mode) is observed, while filled symbols stand for experiments where the purely thermal mode is superimposed on the thermochemical mode. In green, numerical data by Schmelting [1988], in purple by Tackley [1998 & 2002a], in pink by Samuel and Farnetani [2001], in light blue Kellogg et al. [1999] and Montague & Kellogg [2000], in orange by Hansen and Yuen [2000]; in red, lab experiments by Richter and McKenzie [1981], in dark blue by Olson and Kincaid [1991], in black, by Davaille et al. [1999a, 1999b, & 2002] and Le Bars [2002, & 2004]; in dark grey, the parameter space where convection does not occur. The light-grey shaded area represents the domain of parameters relevant for the Earth's mantle.

Reproduced from Davaille et al. 2003

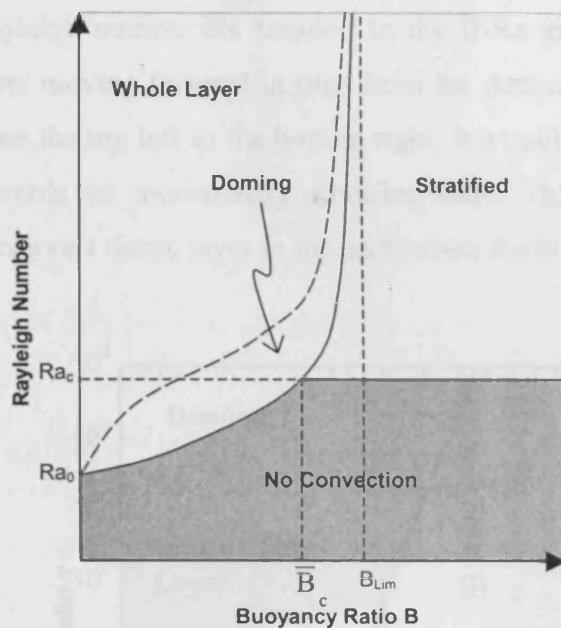


Figure 2.13
Marginal stability curves separating different regimes of layered convection within the $Ra - B$ parameter space. The curves correspond well to the case with the viscosity ratio=6.7, the interface is in the middle of the tank and convection is driven by thermal boundary on the top and bottom plates, $Ra=5430$, $Ra_c=38227$ & $B_c=0.302$
Reproduced from Davaille et al. 2003 & Le Bars & Davaille 2002

The observation that as Ra increases, B_c also increases has significant implications for a possible layer in Earth's mantle. In the past as Earth's mantle cooled there will have been a greater temperature increase across the depth of the mantle. As a result Ra will have had a greater value than it does today. At Earth-like Ra the increase of B_c with Ra becomes very small and hence a layer in the early Earth will have had the same value of B_c . However, a hotter mantle would decrease the value of B and so any layer would have been more unstable in the past. This is contrary to the results of Montague & Kellogg [2000] who found that for a D" layer increasing Ra decreased the value of B_c and so reached an opposing conclusion...

"At this [increasing] Ra the transition to a stable layered structure occurs at a lower value of the buoyancy number. This suggests that it may have been easier to preserve a dense layer in D" in the past when Earth was hotter" Montague & Kellogg 2000.

The author does not agree with the comment above. While it may be true that Montague & Kellogg [2000] observed a decrease in B_c as the Rayleigh number increased there is no evidence that they considered how a change in the Rayleigh number would affect the value of B . Consider a layer present in the mantle during the Archean. As we move forward in time to the present, the mantle will cool. The temperature contrast across the mantle, ΔT , will decrease. The fall in ΔT will have two

effects, firstly it will make the buoyancy ratio B larger and secondly, it will make the Rayleigh number Ra smaller. In the B - Ra graph shown in figure 2.13 we see how a layer moving forward in time from the Archean to the present would move diagonally, from the top left to the bottom right. It would move away from the whole layer domain towards an increasingly stratified state. This suggests it may have been harder to preserve a dense layer in the past (when Earth was hotter).

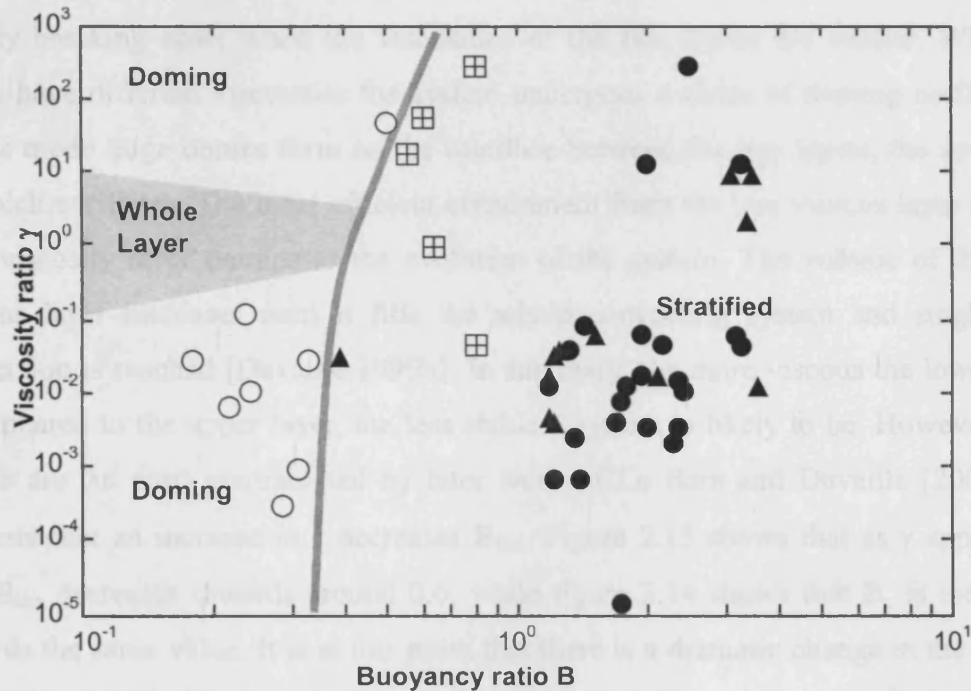


Figure 2.14

Different convecting regimes as a function of the buoyancy ratio B and the viscosity ratio γ . The thick line separates the oscillatory doming modes from the strictly stratified regime (B_c). In grey is the domain in which domes form but break up and mix within one cycle. Each symbol represents an experiment; open circles: domes involving the whole tank; filled circles: two-layer convection with hotspot formation; triangles: one layer too thin to convect and hot spot formation; patterned squares: hybrid regime with high interfacial topography and hotspots.

Reproduced from Davaille 1999a

Other regions of parameter space that have been investigated are the effect of varying the viscosities of the upper and lower layers. This is normally expressed by a non-dimensional parameter call the viscosity ratio γ , where...

$$\gamma = \frac{\nu_l}{\nu_u} \quad (2.12)$$

ν_l & ν_u are the kinematic viscosities of the lower and upper layers respectively. The results of Davaille [1999] are shown in figure 2.14. Increasing γ also increases the value of B at which a layered system moves from a stratified state to an unstable state (B_c) and so a more viscous lower layer would need a larger density contrast to be stable. The mode of the unstable system is affected by the value of γ with the layering rapidly breaking apart when the viscosities of the two layers are similar. When the layers have different viscosities the system undergoes a series of doming oscillations. In this mode large domes form on the interface between the two layers, the amplitude of which oscillates. The most efficient entrainment from the less viscous layer into the high viscosity layer dominates the evolution of the system. The volume of the more viscous layer increases until it fills the whole convecting system and single layer convection is reached [Davaille 1999b]. In summary, the more viscous the lower layer is compared to the upper layer, the less stable a system is likely to be. However these results are (in part) contradicted by later work of Le Bars and Davaille [2002] that suggests that an increase in γ decreases B_{lim} . Figure 2.15 shows that as γ approaches 10^3 , B_{lim} decreases towards around 0.6, while figure 2.14 shows that B_c is increasing towards the same value. It is at this point that there is a dramatic change in the style of convection and a sharp increase in the value of B_{lim} . For small γ ($<10^3$) an unstable layer is pulled apart by doming features that form on the interface between the two layers. These domes oscillate vertically and tend to be longer-lived the greater the values of γ [Davaille 1999a]. For $\gamma >10^3$ these domes no longer have a simple up and down motion, but also have a horizontal component.

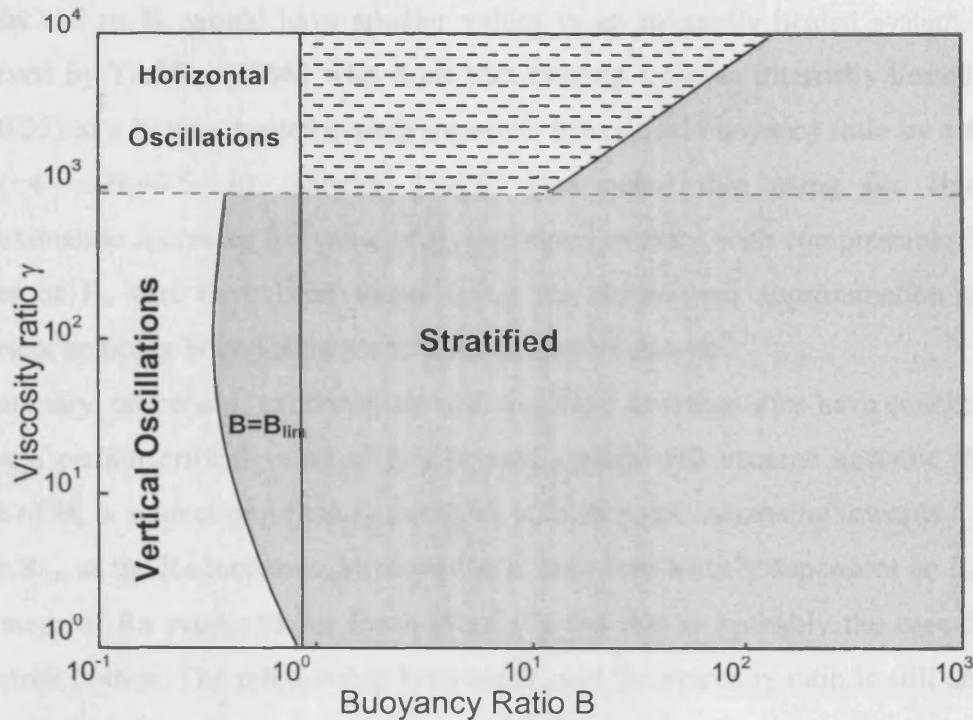


Figure 2.15

B_{lim} as a function of the viscosity ratio for the depth ratio $a=0.75$; the white domain corresponds to oscillations with an unstable whole-layer density profile ($B < a$ or $B < 1-a$) and the hatched domain to oscillations with a stable whole-layer density profile ($B > a$ and $B > 1-a$). In the grey domain oscillations are impossible.

In the grey and hatched areas there is stable stratified convection while in the white area convection is unstable.

Reproduced from Le Bars & Davaille 2002

It has also been noted that the heating mode may have a significant effect on the stability of a layered system. With a thermal gradient at the lower boundary, plumes will form that control convection and the length scale of thermal features in the lower layer. It follows that the plumes will control deformations of the interface between the two layers and by delivering hot material to the interface are crucial in controlling the thermal gradient at the boundary. In contrast the absence of plumes in a lower layer in convection driven only by internal heating will result in cooler material below the interface between the layers and a smaller thermal boundary across the interface. Since the stability of a layered system is determined by the battle fought out between the unstable thermal gradient and the stable chemical gradient [Davaille et al. 2003] it follows that an internally heated system would be more stable than a bottom heated

system and so B_c would have smaller values in an internally heated system. This is observed by Tackley [1998] who finds that moving from an internally heated system ($B_c=0.25$) to a bottom heated system increases the critical buoyancy ratio by a factor of 2 to 4 ($B_c=0.5-1.0$). Tackley [1998] also noted that using the Buossinesq approximation increases the value of B_c compared to cases with compressible fluid. So values of B_c that have been found using the Buossinesq approximation probably represent an upper bound estimate to those in Earth's mantle.

In summary, numerical, experimental and analytical investigations have concluded that below a certain critical value of B a layered system will become unstable (B_c). The value of B_c is a function of many variables with its value increasing towards a limiting value B_{lim} as the Ra increases. However B_c is only very weakly dependent on Ra within the range of Ra proposed for Earth ($Ra>10^6$) and this is probably the case for most terrestrial bodies. The relationship between B_c and the viscosity ratio is still an area of research, though in the opinion of the author a less viscous lower layer would increase the value of B_c [†]. For a deep layer, values of B_c between 0.4 and 0.6 are most frequently quoted in the literature though values as low as 0.3 and as high as 1.0 have been suggested.

2.7.2 Entrainment and the lifespan of layered convection

Aside from the stability of a layered mantle other constraints can be placed on the properties of a deep layer by considering entrainment of material between the two layers [see section 4.4]. A certain amount of entrainment is expected between the two layers in a convecting system with the rate of entrainment varying with the density contrast of the two layers, the viscosity ratio and other parameters. Constraints can be placed on the layer by considering that a layer present today must have existed throughout Earth's history and so entrainment must be such that the layer was not completely entrained away. When considering a D" layer this condition may not be valid since it is possible that the layer may be sustained by the influx of subducted oceanic plates or iron from the core.

Early work on the entrainment from a deep layer used the assumption that a denser layer is entrained into the upper layer as schlieren material captured viscously inside a plume originating in the lower thermal boundary layer of the upper layer. Sleep [1988]

[†] This comment is based on personal communication with Dave Stegman.

found that the magnitude of the entrainment is controlled by the buoyancy ratio with a denser layer (larger B) producing less entrainment. Gonnerman et al. [2002] and Davaille [1999a] carried on from the work of Sleep to derive the following equation (see section 4.4)...

$$E = \frac{\rho C_p}{k} \frac{CH^{-1}B^{-2}Ra^{1/3}}{1 + \gamma B^{-1}} \quad (2.13)$$

Where, E is the entrainment rate (upward + downward volume flux), C is an experimentally derived constant with a value of 0.2, k is Thermal diffusivity, C_p is Specific heat, ρ is density, H is the total fluid depth, Ra is the Rayleigh number of the whole system and B is the buoyancy ratio. Gonnermann et al. then time integrate this equation to calculate the values of B needed to maintain a D'' for 4.5 G years, the results are shown in figure 2.16. A thicker layer requires a smaller B since it contains more material and can therefore tolerate a higher rate of entrainment and still survive over the life span of Earth's mantle. Increasing Ra increases the rate of entrainment and so also the thickness of a possible lower layer that could survive. Zhong & Hager [2003] showed that the work of Sleep [1988] and so Davaille [1999a, 1999b] and Gonnermann et al. [2002] constitutes the maximum rate of entrainment and so we must consider the values shown in figure 2.16 as the maximum possible values of B to maintain a layer.

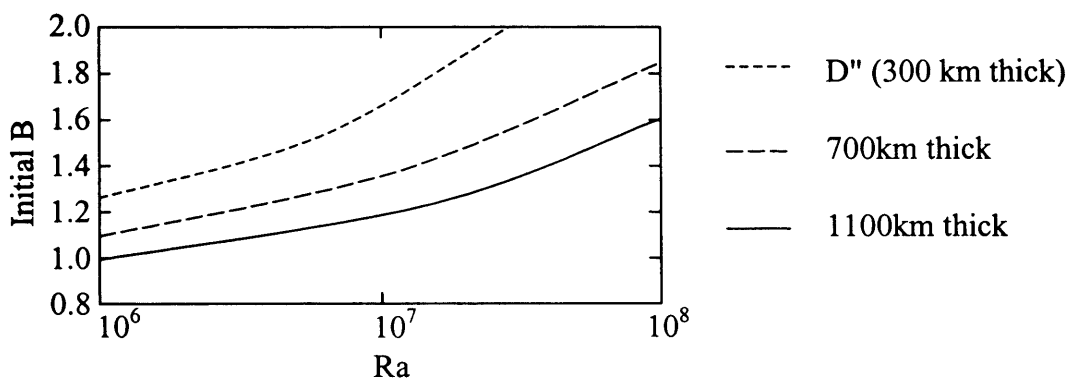


Figure 2.16

The buoyancy ratio required to maintain a layered mantle (for 4.5 G years) for three cases as the Rayleigh number increases.

Taken from Gonnermann et al. 2002

The assumption used by Sleep [1988] & Gonnermann et al. [2002] that entrainment is always upwards is probably valid for a layer deep in the mantle, however the direction of entrainment could depend upon both the viscosity ratio and the depth of the

interface. Layered convection in tank experiments is seldom stable over long periods and as convection and entrainment continues the volume of the layers change. The boundary between the two layers moves either up or down until the system convects as a single layer. Early investigations suggested this migration of the boundary always takes place such that the more viscous layer increases in volume until it fills the whole system [Davaille 1999b]. This suggests that entrainment from a less viscous into a more viscous layer is more efficient than entrainment from a more viscous into a less viscous layer. A lower layer in Earth's mantle is expected to be more viscous and so from these results it is expected that entrainment would be from the upper layer into the lower layer.

This work is followed up by a more detailed study [Le Bars & Davaille 2004] in which the dependence of the direction of entrainment is studied as a function of the depth of the interface and the viscosity ratio.

The depth of the interface between the two layers is often described by a non-dimensional parameter called the depth ratio and denoted by 'a'.

$$a = \frac{h_0}{H} \quad (2.14)$$

Where h_0 is the thickness of the lower layer and H is the thickness of the whole system. Le Bars & Davaille [2004] note that as the interface is placed at shallower depths the direction of dominant entrainment changes from upward to downward. This suggests that at the interface of a deep layer, cusps leads to entrainment would point upward (in a manner assumed by Sleep [1988]), however as the boundary is placed at shallower depths these cusp structures start to point downward. The viscosity structure also affects the direction of entrainment with an increasing γ moving the system from downwards to upwards entrainment. See figure 2.17. Applying these results to Earth's mantle in which γ is thought to be 10^1 to 10^2 we see that a layer in the deep mantle would entrain upwards into the overlying mantle producing a marble cake pattern and also hot plumes that could be responsible for OIB signatures by entrainment.

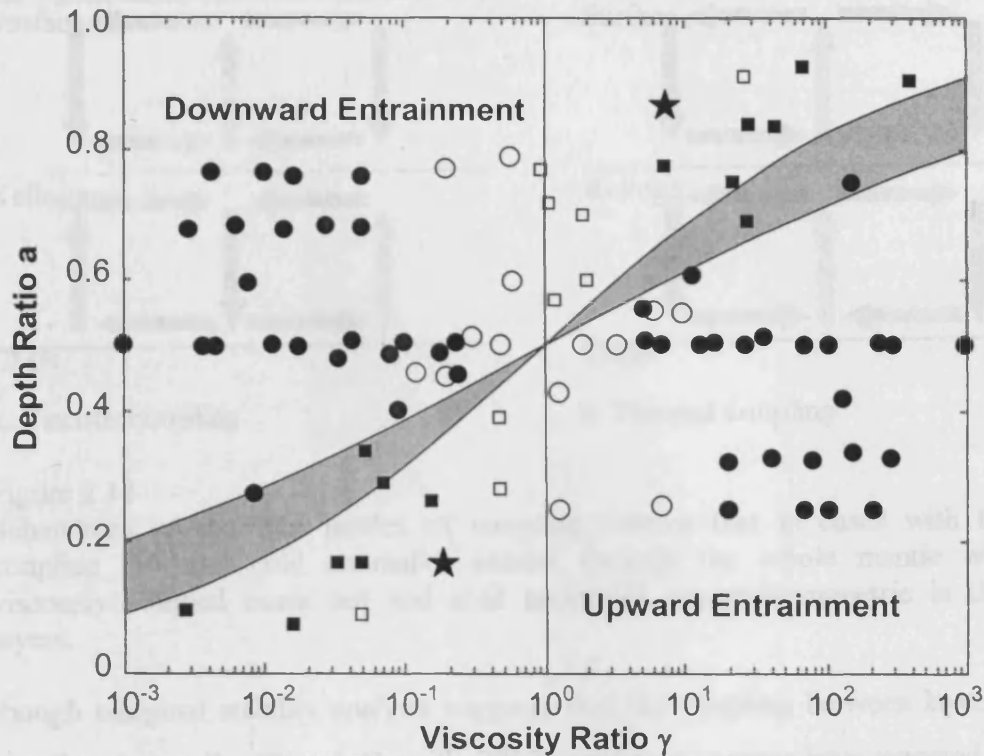


Figure 2.17

Spouting direction as a function of γ and a . Circles: experiments where more viscous diapirs invade a less viscous mantle; squares: experiments where less viscous diapirs invade a more viscous mantle. Filled symbols designate cases where at least two pulsations were observed. The stars designate experiments with sugar syrup.

Above the grey region there is downwards entrainment and below there is upward entrainment.

Reproduced from Davaille et al. 2003

2.7.3 Other Characteristics of layered convection

The nature of coupling between two layers will have a significant effect on the planform of convection in both layers. There are two possible modes. Firstly, viscous coupling: here the viscosity forces dominate the coupling. The velocity structure at the boundary is symmetrical in both layers. Consequently hot anomalies in the lower mantle are overlain by cold anomalies and vice versa cold anomalies in the lower layer are overlain by hot anomalies. Secondly, thermal coupling: where the heat transfer over the deformable boundary dominates. In this mode both hot and cold anomalies will extend through the whole mantle.

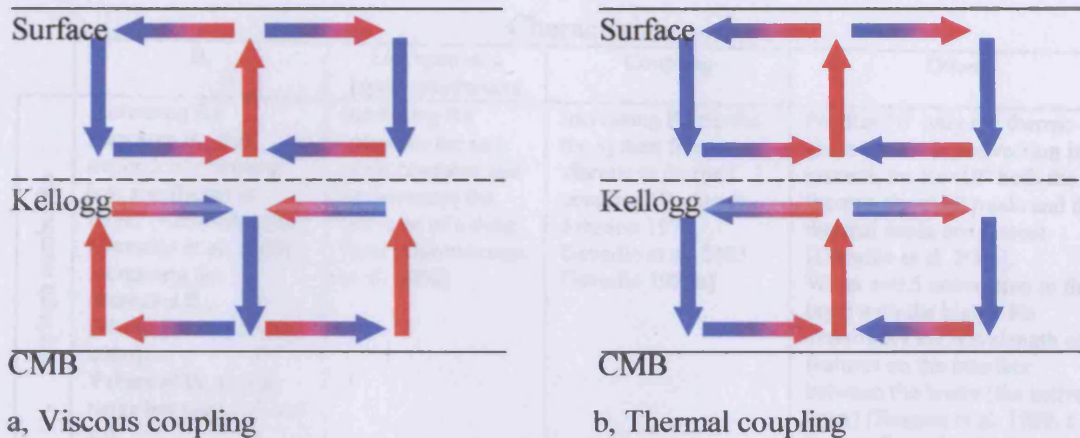


Figure 2.18

Schematics of the two modes of coupling. Notice that in cases with thermal coupling hot and cold anomalies extend through the whole mantle while in viscously coupled cases hot and cold anomalies are anti-symmetric in the two layers.

Although marginal stability analysis suggests that the coupling between layers should always be viscous [Le Bars & Davaille 2002] numerous sources have reported seeing a change from viscous to thermal coupling as the Rayleigh number increases [e.g Richter & Johnson 1974, Davaille et al. 2003]. The reasons for this change in the state of convection is discussed in more detail in section 7.2.

The viscosity ratio also affects the mode of coupling between the two layers. Glatzmaier & Schubert [1993] modeled layered convection in a 3D spherical geometry with an undeformable interface at 670km. They found that increasing γ moved the coupling between the layers from viscous to thermal coupling. Rasenat et al. [1989] quantified this and found that for $\gamma > 5$ the two layers are thermally coupled.

A summary of the parameter space that has been investigated and the effect of certain input parameters on the characteristics of layered convection are summarized in table 2.2.

Parameter	Characteristic			
	B_c	Life span of a layer/ entrainment	Coupling	Other
Rayleigh number Ra	Increasing Ra increases B_c , this dependence become less significant at larger (Earth-like) Ra [Davaile et al. 2003]. Increasing Ra decreases B_c , [Montague & Kellogg 2000]. Values of B_c quoted range between 0.3 and 1.0.	Increasing Ra increases the rate of entrainment and so decreases the life span of a deep layer [Gonnermann et al. 2002]	Increasing Ra moves the system from viscous to thermal coupling [Richter & Johnson 1974, Davaile et al. 2003, Davaile 1999b]	For $Ra < 10^5$ only the thermo-chemical mode convection is present, for $Ra > 10^5$ both the thermo-chemical mode and the thermal mode are present [Davaile et al. 2003]. When $a=0.5$ convection in the layer with the higher Ra determines the wavelength of features on the interface between the layers (the active layer) [Rasenat et al. 1989, Le Bars & Davaile 2002]
Viscosity ratio γ	Increasing γ increases B_c . For $\gamma < 10^{-2}$ there is little change in B_c [Davaile 1999a]. Increasing γ decreases B_{lim} [Le Bars & Davaile 2002].	Increasing γ moves entrainment's spouting direction from upwards to downwards [Davaile et al. 2003].	For $\gamma=1$ a 670km type layer is viscously coupled. Increasing γ moves the system towards thermal coupling [Glatzmaier & Schubert 1993]. For $\gamma > 5$ a layer is thermally coupled [Rasenat et al. 1989].	Increasing γ moves a system from having an 'active' upper layer to an 'active' lower layer [Le Bars & Davaile 2002].
Depth ratio a	There is a complex relationship between a and B_c but for $\gamma=1$ increasing a will decrease B_c [Le Bars & Davaile 2002].	Increasing a moves entrainment from downwards to upwards [Davaile et al. 2003]. For a D'' type layer increasing a (i.e. making D'' thicker) prolongs the lifetime of the layer [Davaile et al. 2002].		Increasing a moves a system from having an 'active' upper layer to an 'active' lower layer. The wavelength of convective motion is proportional to the depth of thickness of the active layer. The other layer is passive with convection being driven by coupling between the layers [Le Bars & Davaile 2002].
B		Increasing B increases the life span of a deep layer [e.g. Sleep 1988].		For $B > B_{lim}$ the behaviour of the stratified regime is independent of B [Le Bars & Davaile 2002].
Heating mode	For bottom heated case $B_c=0.5-1.0$, For internally heated cases $B_c=0.25$ [Tackley 1998]		The wavelength of the thermal structure of a layer is greater in a bottom heated system than internally heated system [Houseman 1988]	Increasing the rate of internal heating increases heat conducted across the interface and suppresses convection in the lower layer [Montague & Kellogg 2000].

Table 2.2

A summary of the parameter space investigated in previous work.

Lab experiments: Davaile et al. 2003 & 2002, Davaile 1999a & 1999b, Richter & Johnson 1974, Gonnermann et al. 2002

3D spherical, numerical, non-deformable interface: Glatzmaier & Schubert 1993

2D Cartesian, numerical (D''): Montague & Kellogg 2000, Houseman 1988

2D & 3D Cartesian, numerical, with the Boussinesq approximation and compressible convection: Tackley 1998b

Analytical: Sleep 1988, Rasenat et al. 1989

2.8 Thermal expansion and its variance with depth

The volume coefficient of thermal expansion (thermal expansivity, α) is a measure of the increase in a material's volume as its temperature is increased. It is defined as the fractional increase in volume V per unit temperature T at constant pressure P .

$$\alpha = \frac{1}{V_0} \left(\frac{dV}{dT} \right)_P \quad (2.15)$$

Where V_0 is a reference volume normally having a value of one unit volume.

The change in the values of α across the mantle would affect the buoyancy of the deep mantle. The formation of plumes and other instabilities will also be affected by changing α . A decreasing α with depth hinders the formation of upwelling features that could affect the plan-form of these plumes, and aiding the stability of a deep layer.

Early studies [D. L. Anderson 1967[†]] of the variation of thermal expansivity in the mantle suggested that α is independent of temperature and is related to density by.

$$\frac{\alpha}{\alpha_0} = \left(\frac{\rho}{\rho_0} \right)^{-\delta_T} \quad (2.16)$$

$$\delta_T = -\frac{1}{\alpha \kappa_m} \left(\frac{\partial \kappa_m}{\partial T} \right)_P \quad (2.17)$$

Where δ_T is the Anderson-Grüneisen constant having a value of 0.55 [Schmeling et al. 2003], ρ the density, T the temperature, κ_m the isothermal bulk modulus and P is pressure.

Chopelas & Boehler [1989] measured the pressure dependence of thermal expansivity of MgO and forsterite in a diamond anvil experiment and found δ_T to remain constant in the mantle and concluded that α has a uniform value throughout the depth of the mantle. However, later work [Sharma & Gupta 1975, O. L. Anderson et al. 1990, Chopelas & Boehler 1992] find that δ_T is a function of both pressure and temperature and reevaluate D. L. Anderson's [1967] equations without making this assumption. This reevaluation of α revealed that it would decrease by a factor 5 to 10 across the mantle [Hansen et al. 1993].

[†] We are using the initials here to distinguish between D. L. Anderson and O. L. Anderson.

Previous modeling that has incorporated depth dependent thermal expansivity, α , have used a range of formulae to calculate α . Depth dependence of α is of the form [Zhao & Yuen 1987]...

$$\alpha(z_d) = \left(\frac{m+1}{(m(z_d+1)+1)} \right)^3 \alpha(0) \quad (2.18)$$

Where z_d is the non-dimensional depth, $\alpha(0)$ is the value of α at the surface and 'm' is a non-dimensional parameter that controls the increase of α with depth. The variation of α with depth described by equation 2.18 is shown in figure 2.19 for a range of values of m. We can express the decrease $\alpha(0)/\alpha(1)$ in terms of m...

$$\frac{\alpha(0)}{\alpha(1)} = \left(\frac{2m+1}{m+1} \right)^3 \quad (2.19)$$

For $m=0$ $\alpha(0)/\alpha(1)=1$ and α remains constant throughout the depth of the mantle. Taking the limit as m tends towards infinity, $\alpha(0)/\alpha(1)$ tends towards 8. So the maximum decrease possible in the thermal expansivity across the mantle is eightfold and the minimum decrease is 0. Matyska & Yuen [2000] continue on from this work and use the simplification that $m=1$ reducing the above equation 2.18 to...

$$\alpha(z_d) = \frac{8\alpha(0)}{(2+z_d)^3} \quad (2.20)$$

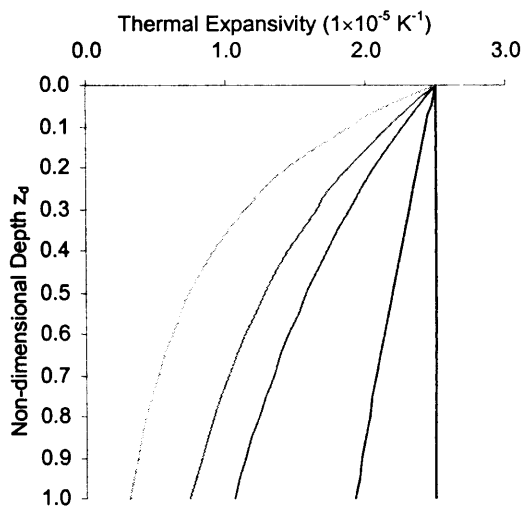


Figure 2.19

The variation of thermal expansivity α with depth as defined by equation 2.18, with the surface value of α set to 2.5×10^{-5} . For a range of values of m; $m=0$, α remains constant with depth; $m=\infty$, α decreases by a factor of 8 across the mantle.

- $m=0.0$
- $m=0.1$
- $m=0.5$
- $m=1.0$
- $m=\text{inf}$

2.9 Summary

We have developed a picture of the mantle in which slow deformation over millions of years is driving many processes observed at Earth's surface. Despite the importance of mantle convection we are still unsure of whether convection is taking place across the whole depth of the mantle, or in a layered structure. An interface between layers in the top 1000km is unlikely. Geochemical observations seem to require some kind of chemically distinct reservoir. Given that the mantle is well mixed this reservoir must be dynamically isolated from the upper mantle and so suggests a layered mantle.

One of the limitations of previous investigations of the behaviour of a layered system is that it has been confined to either a Cartesian geometry or two dimensions (with one notable exception [Stegman et al. 2002a]). Characterising layered convection in a 3D spherical geometry is the primary aim of this thesis.

3 The marker method

We considered using a number of methods to model a layered system in a 3D spherical co-ordinate system. In the past, three methods have been used to model thermochemical convection; particles, a marker chain and field methods [van Keken 1997]. Particles would be an ideal method to use and have been added to TERRA [see the proceeding section 3.2] by Stegman at Berkeley [Stegman 2002a]. This method works by placing a series of particles (sometimes called tracers) at all places in the grid being used. The number of particles is normally around one order of magnitude higher than the number of nodes in the grid. The particles are moved around with the velocity field and report back to their nearest node, information, such as density. This information can then be used when solving the buoyancy equation. Particle population has to be controlled to maintain a good distribution. This is achieved by combining particles in regions of particle surplus and splitting in regions of low concentrations.

The marker method uses a similar approach to the particle method. A series of 'markers' are used to define the interface between two chemically distinct regions. The markers positions are updated in the same manner as in the particle method. Reporting information back to the nodes is done on the basis of which side a node is of the marker defined interface. Like the particle method, marker population needs to be controlled to maintain a good distribution.

The final method considered: the Eulerian field method works by adding a field similar to the temperature field for the chemical composition. This is then solved using standard methods.

van Keken [1997] ran comparison tests for all three of these methods and his results can be summarised as....

Particles: Works well and is flexible, but the number of particles needed has to be high to limit spurious diffusion. It also suffers from statistical noise.

Markers: The most accurate method for nondiffusional problems. It is not suited to cases in which long term mixing is taking place.

Field: Works quite well and is very economical.

We rejected the field method because of concerns about the accuracy and considered further the marker and tracer methods. A disadvantage of the particle method is the high number of particles that would need to be added to the calculation and the RAM this would use up. The addition of particles to a TERRA calculation would increase the

RAM used by an order of magnitude. This would limit the grid size that could be used and consequently the Rayleigh number that could be investigated.

The disadvantage that the marker method would not work for cases with any major entrainment was not thought to be significant since we were only interested in studying cases in which there was stratified layering and so limited entrainment [see section 4.4]. The marker chain method has only previously been employed in 2D calculations [Christensen & Yuen 1984; Schott et al 2002]. Applying a marker method in 3D is more complex. The term ‘chain’ is no longer accurate and ‘marker net’ is, perhaps a less misleading terminology. The significance of moving from a chain to a net is that markers are not stored in a linear array and it is not trivial to find the appropriate neighbour to each marker. Consequently a new method has to be devised to control the marker distributions and populations.

3.1 An introduction to the concept of parallel computing

Modelling mantle convection with TERRA at high resolutions requires the use of parallel computers. A parallel computer uses more than one processor to work on a particular problem at any one time. By dividing the computational task over a collection of processors the calculation can be performed more quickly than on a single processor.

Historically supercomputers have been extremely expensive and have been built of specially made parts. The growth in the PC industry has allowed the development of a new kind of supercomputer. These use off-the-shelf parts and so are very cost effective. Called cluster computers or Beowulf machines, they cannot match the performance of a purpose built supercomputer, however in terms of floating point operations per pound they out perform classical supercomputers such as Crays.

The definition of a Beowulf machine is not rigid. My personal favourite is that a Beowulf machine is a cluster computer whose components can be bought entirely from within the pages of a computer shopper magazine. Most definitions however agree that Beowulf machines are a collection of high performance desktop machines that are connected using a regular Ethernet connection. We can think of Beowulfs as a micro-computing lab without monitors or keyboards attached to the PC’s.

3.1.1 NESSC

At the Department of Earth Sciences at the University of Liverpool there is a parallel computer (Beowulf machine) called NESSC (Networked Earth Sciences Supercomputing Cluster). NESSC was designed almost exclusively to run the mantle convection code TERRA. There are two main limiting factors that control the resolution at which TERRA can be run. The first of these is the speed of the machine being used. The amount of wall clock time required could severely limit the resolution at which a simulation can be run. A TERRA simulation run at the maximum resolution possible, with 84 million points in the grid, will take months to simulate a billion years of convection. This speed problem can be overcome in part by having access to a machine for long periods. This is one way in which NESSC was designed for this problem, since NESSC is used exclusively by the Department of Earth Sciences. This allows simulations to be left running for weeks, which is not the case for Cray machines; these are normally shared by a large number of users. The second limiting factor is the amount of RAM available. Each simulation needs to save a number of parameters for each node. These include temperature, pressure, velocity, position, and so on; there are up to 10 floating point numbers to be saved in RAM per node. TERRA uses double precision floating point that use 64 bits per floating point. This means a total RAM of $64 \times 10 \times 83,886,080 = 53.7 \times 10^9$ Bytes = 53.7 GB is needed. For this reason TERRA was built with 100GB of RAM.

A series of benchmarking tests were run on NESSC using the TERRA code to compare the machines to performance to a similar yet older machine at Princeton University. The results can be seen in Appendix E.

3.1.2 NESSC Specifications

Motherboard	Tyan Tiger 133 (S1834) - Dual Slot 1 Pentium III Motherboard (100MHz & 133MHz FSB) using VIA 694X chipset ATX form factor, AGP, 6 x PCI, 1 x ISA, 2 x USB, UDMA 66 4 x DIMM sockets (PC100 or PC133) - 005-070002
Processor	2 x Intel Pentium III 733hz
Memory	3 x 256MB PC133 ECC DIMM
Hard Disks EIDE	20.4GB Maxtor Titan VL EIDE- Ultra DMA
Floppy Drive	3.5" 1.44Mb floppy disk drive
Graphics Card	Videologic 410 2Mb PCI Graphics Card
Network Card	Intel®Pro/100+ Management Adapter Card PCI.

3.1.3 Helix Specifications

Motherboard	Supermicro P4DPE motherboard
Processor	Two Pentium Xeon processors (54 of the nodes have 2.2 GHz, 18 have 2.4 GHz)
Memory	1.5 GB RAM (one node has 2 GB)
Hard Disks	80 GB hard-drive
Network Card	On-board Ethernet LAN (100 Mbit/s) Dolphin Wulfkit SCI (Scalable Coherent Interface) network card. The Dolphin Wulfkit forms a 2D grid (torus).

3.2 An introduction to the TERRA program

In this thesis we use the computer program TERRA to simulate mantle convection. TERRA models mantle convection in a three dimensional spherical geometry and is written in the Fortran and MPI (message passing interface) programming languages. TERRA was first developed by John R Baumgardner as part of his PhD at the University of California Los Angeles in 1983 [Baumgardner 1983]. TERRA was edited by Hans-Peter Bunge to allow it to run on parallel computers as part of his PhD at the University of California Berkeley in 1996 [Bunge 1996]. More recent alterations made to TERRA have been to include variable viscosity [Yang 1997; Yang & Baumgardner 2000], the inclusion plate-like surface velocities on the upper shell [Bunge et al. 1998], and the introduction of tracer particles [Stegman 2002a].

3.2.1 The governing equations and assumptions used

Over short time scales the mantle behaves as a solid and is able to transmit P & S-waves. Its behaviour over long time scales is quite different with the effects of thermal and chemical buoyancy causing creep of mantle rocks. The Rayleigh number of the mantle (between 10^6 and 10^8) is several orders of magnitude higher than the estimated value of the critical Rayleigh number of the mantle [McNamara & van Keken 2000]. This creep of mantle rocks allows us to treat Earth's mantle as a viscous fluid over geological time scales [Yang 1997].

This physical problem is described by three equations that describe the conservation of mass, momentum and energy. A constitutive law relates the stress and velocity fields [Bunge 1996].

Three assumptions are used to simplify the three conservation equations. The inertial forces within the fluid are ignored. Here we assume that the Prandtl number Pr is infinite. Pr is the approximate ratio of viscous forces to inertial forces is described by...

$$Pr = \frac{\text{viscous forces}}{\text{inertial forces}} = \frac{\nu}{\kappa} \quad (3.1)$$

Where ν is the Kinematic viscosity and κ the thermal diffusivity. Pr is expected to have a value of around 10^{24} which is sufficient to justify the assumption that Pr is infinite.

Using the definition of the dynamic viscosity η ($\eta = \nu\rho$) and the thermal diffusivity κ ($\kappa = k \div \rho C_p$) where ρ is density, k is thermal conductivity and C_p is the specific heat capacity, then we can write Pr as...

$$Pr = \frac{\nu}{\kappa} = \frac{\rho\eta C_p}{k}$$

Using values of $\eta=10^{21}$, $C_p=1000$, $\rho=5000 \text{ kg m}^{-3}$ and $k=5 \text{ W m}^{-1} \text{ K}^{-1}$ (thought to be about right for Earth's mantle) $Pr= 10^{27}$.

The mantle is also assumed to be a Newtonian fluid; this assumes that there is a linear relationship between stress and strain rate. The final assumption used is that changes in density are unimportant and can be neglected save for in the buoyancy term of the momentum equation. This is known as the Boussinesq approximation [Boussinesq 1903]. Free slip boundary conditions are applied at both the upper and lower boundary. The effect of Earth's rotation is also ignored. The Ekman number Ek is the ratio of viscous forces to the Coriolis force (the inertial force produced by the Earth's rotation) and given by...

$$Ek = \frac{\text{viscous forces}}{\text{coriolis force}} = \frac{\nu}{2\Omega L^2 \sin\theta} \quad (3.2)$$

Where Ω is the angular velocity, L is the radius and θ is the latitude. For Earth Ek is of the order 10^7 or larger [Yang 1997].

For the Earth: $\nu = \eta / \rho = 10^{21} / 5 \times 10^3 = 2 \times 10^{17} \text{ m}^2 \text{ s}^{-1}$; $\Omega \approx 2\pi / 1 \text{ day} = 2\pi / 86400 \text{ s} = 7 \times 10^{-5} \text{ rad s}^{-1}$; $L = 6370 \times 10^3 \text{ m}$

$$Ek = \frac{\nu}{2\Omega L^2 \sin\theta} = \frac{2 \times 10^{17}}{2 \times 7 \times 10^{-5} \times (6370 \times 10^3)^2} = 3.4 \times 10^7$$

These three assumptions allow the mass, momentum and energy conservation equations to be written as...

$$\text{Mass} \quad \nabla \cdot \underline{v} = 0 \quad (3.3)$$

$$\text{Momentum} \quad \frac{1}{\rho} \nabla P = \nu \nabla^2 \underline{v} - \alpha g \Delta T \quad (3.4)$$

$$\text{Energy} \quad \frac{\partial T}{\partial t} + \underline{v} \cdot \nabla T = \kappa \nabla^2 T + \frac{J}{\rho C_p} \quad (3.5)$$

Where the momentum equation is also known as the Navier-Stokes equation [e.g. Ranalli 1995] and J is the rate of internal heat generation per unit volume.

3.2.2 The computational method

The system is solved by starting with an initial temperature field T . This is used with the momentum equation 3.4 to find the velocity field \underline{v} . This velocity field is then used with the energy equation 3.5 to find the rate of change of the temperature field $\partial T / \partial t$. This rate of change can then be used to move the system forward a time step by calculating the new temperature field.

However, this is a simplification of how TERRA actually updates the temperature field. A first order Runge-Kutta method is used to move the temperature field forward by a time Δt . The method outlined above is used to find the rate of change of the temperature field at time t $(\partial T / \partial t)_t$. This is then used to find the temperature field at time $t + \frac{1}{2} \Delta t$ $T_{t+\frac{1}{2}\Delta t}$. The method above is then used to find the rate of change of the temperature field using the temperature field $T_{t+\frac{1}{2}\Delta t}$, $(\partial T / \partial t)_{t+\frac{1}{2}\Delta t}$. This rate of change at time $t + \frac{1}{2} \Delta t$ is then used to update the temperature field at time t T_t . See equation 3.6...

$$T_{t+\Delta t} = T_t + \left(\frac{\partial T}{\partial t} \right)_{t+\frac{1}{2}\Delta t} \Delta t \quad (3.6)$$

The size of the time step Δt has a maximum value of the largest velocity in \underline{v} divided by the minimum length of an element. In this way it is impossible for feature (i.e. a particle) in the icosahedral grid to move further than the next node in a time step. The size of the time step is also controlled by the multigrid, see section 3.2.4. The energy equation is solved using a finite volume approach and a method known as the donor cell.

3.2.3 The finite element method

The starting point of any finite element method is to divide the domain over which the equations are going to be solved into a number of elements. These elements are defined by a series of nodes that make up the vertices of the elements. In the case of TERRA, elements connect together to form prisms, and nodes are defined by the icosahedral grid (or mesh) used by TERRA, see section 3.2.5. A series of independent equations is used to approximate fields such as velocity $\underline{v}(\mathbf{r})$ and pressure $p(\mathbf{r})$ for each element. Whatever the form of this approximation the total number of unknowns is always identical to the total number of equations. These equations can then be solved simultaneously to find the unknowns (this problem normally reducing to the need to invert a matrix).

The velocity $\underline{v}(\mathbf{r})$ and pressure $p(\mathbf{r})$ are of interest when solving the momentum equation and are represented at each node by...

$$\underline{v}_i = (v_{i1}, v_{i2}, v_{i3}) \ \& \ p_i \quad (3.7)$$

...where i is the node number. So that...

$$\begin{aligned} \underline{v}_l(\mathbf{r}) &= N_i(\mathbf{r})v_{il} \quad (l = 1,2,3) \\ p(\mathbf{r}) &= N_i(\mathbf{r})p_i \end{aligned} \quad (3.8)$$

Where $N_i(\mathbf{r})$ are the finite element basis functions. The basis functions used in this thesis were piecewise linear functions, though TERRA can use quadratic or cubic functions [Yang 1997]. For a comprehensive guide to the finite element method see Zienkiewicz & Taylor [2000].

3.2.4 The multigrid

As we saw in the preceding section the problem of solving the momentum equation can be reduced to a series of simultaneous equations...

$$Ax = y \quad (3.9)$$

The normal method to solve such an equation would be to invert the matrix A so that: $x=A^{-1}y$. However the rank of the matrix A that needs to be solved in TERRA is very large (4055238 for $nt=64$ [Yang 1997]). For such a large matrix a direct inversion is either impractical or impossible. Instead an iterative method is normally used. A solution of x , x_0 is approximated, and residual value r is defined as...

$$r = Ax_0 - y \quad (3.10)$$

An iterative method such as the as Jacobi method (e.g. the Harvard CMT method uses the Jacobi method) is used to minimise the value of r . Once r has fallen below a tolerable value or once the iterative method being used has stopped converging the values of x_0 are used. TERRA uses a multigrid method [Brandt 1977] to converge on solutions of x_0 . The advantage of the multigrid method is that it can be applied over a range of grid sizes. By relaxing the refinement of the grid to coarser levels longer wavelength errors in x_0 can be removed.

3.2.5 The icosahedron grid used in TERRA

TERRA uses an icosahedron grid to discretise the spherical shell [Williamson 1968; Baumgardner & Frederickson 1985]. The advantage of an icosahedron grid over a latitude-longitude grid is that the distribution of the nodes over the spherical surface remains (almost) even and there is no bunching of points at the poles. This bunching is undesirable since having nodes close together normally decreases the time-step needed to keep the numerical system stable. In grids in which nodes are extremely bunched the decrease of the time step makes the code become impractical.

The grid works by projecting an icosahedron (a 20 sided shape made up of equally sized equilateral triangles) onto the spherical surface. This divides the surface into twenty equilateral triangles. Each of these triangles can then be subdivided into four triangles to divide the surface into 80 triangles; these triangles can also be subdivided. In this way the grid can be continuously refined to a finer and finer mesh. See figure 3.1.

Nodes are defined to be points at the corners of these triangles. So in the original grid there are only 12 data points. Within the TERRA code, refinements to the grid are referred to by “the number of data points along the edge of one of the primary triangles”. This value is labelled mt and is defined in `size.h`. The value of mt defines the number of data points present in the TERRA grid and the resolution of a case. As mt increases the TERRA program will need more RAM but will be able to model more vigorous convection. The number of data points on a spherical surface is therefore given by $(10 \times mt^2) + 2$. The grid is extended radially by placing layers of these spherical shells one on top of one another. The number of radial layers is set to be half the number of data points along the edge of a primary triangle. The number of radial layers is referred to as nr within the TERRA program; so we can say: $nr = \frac{1}{2}mt$. A layer is considered to be the region between two spherical shells that contain nodal points. So the total number of shells containing nodes is $nr+1$ or $\frac{1}{2}mt+1$.

A limitation of this method is that the density of the spherical shell grid used is the same at the upper and lower shells, consequently the lateral grid spacing is smaller in the lower mantle and not constant throughout the grid. Viscosity is thought to increase in the lower mantle so if any thing a larger grid spacing could be used there.

The size of the grid used by TERRA is defined by the parameter mt . Where mt is the number of grid points along the edge of a primary triangle that make up the icosahedron grid. mt must have a value that is a power of two

$$\left\{ \begin{array}{l} \text{Total number} \\ \text{of data points} \end{array} \right\} = (10mt^2 + 2) \left(\frac{1}{2}mt + 1 \right) \quad (3.11)$$

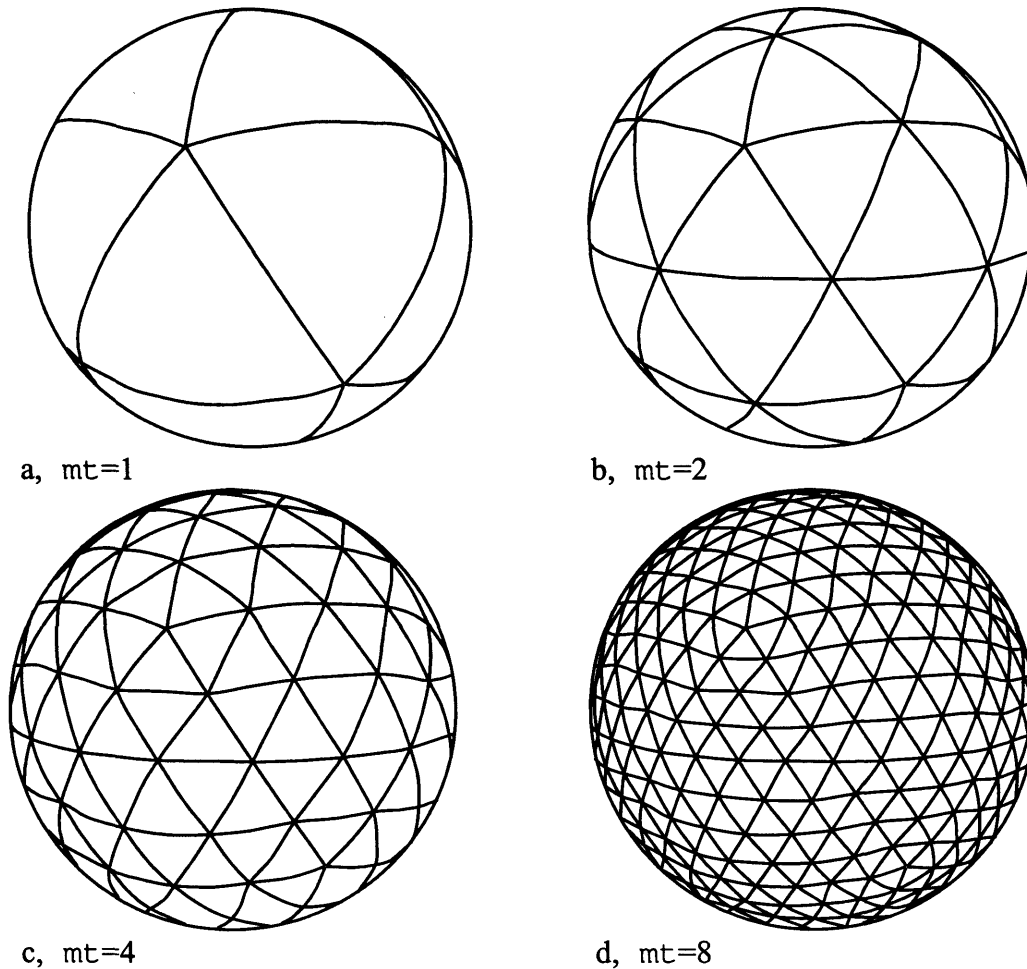


Figure 3.1

Dyadic refinements of the icosahedron grid. a, the original grid ($mt=1$); b, the second refinement ($mt=2$); c, the third refinement ($mt=4$); the fourth refinement ($mt=8$)

Reproduced from Baumgardner 1983.

3.2.6 Indexing conventions employed by TERRA

The icosahedron grid breaks a spherical shell volume up into a well-spaced mesh. However the method used to refer to each grid point uniquely is not obvious and needs some explanation.

As stated earlier the original grid is divided into twenty equilateral triangles. These twenty triangles are grouped into pairs to form ten diamonds. These diamonds are indexed as shown in figure 3.2. Within the TERRA program the diamond number is referred to as *id*.

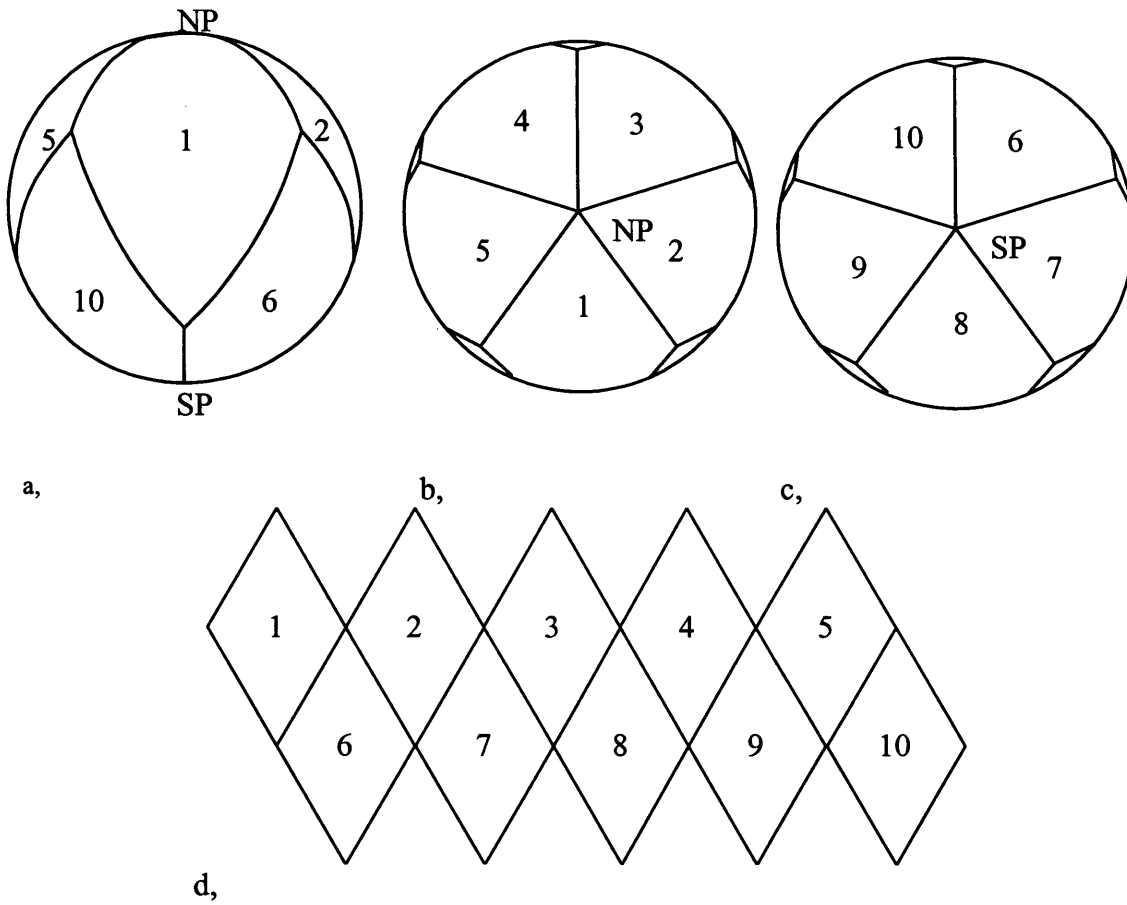


Figure 3.2
 The numbering convention for the diamonds
 a, Viewed from the equator.
 b, Viewed from the North Pole (NP).
 c, Viewed from the South Pole (SP).
 d, With the diamonds projected onto a flat plane.
a,b,c reproduced from Baumgardner 1984.

The data points within each diamond (or more accurately each subdomain – see the next section) are indexed by the placing of axes along the edges of the diamond running away from the data point at the pole. Nodes along these axes are labelled i_1 and i_2 . See figure 3.3.

Finally, the radial layers are indexed by i_r . This ranges between 0 (the surface) and n_r+1 (the CMB).

We can refer to any point in the TERRA grid using four components: i_1 , i_2 , i_d and i_r . Where i_1 and i_2 are axes running along the edge of the diamond away from the pole, i_d is the diamond number, i_r is the radial layer number. i_1 varies between 0 and m_t , i_2 between 1 and m_t+1 , i_d between 1 and 10 and i_r between 0 and $\frac{1}{2}m_t+1$

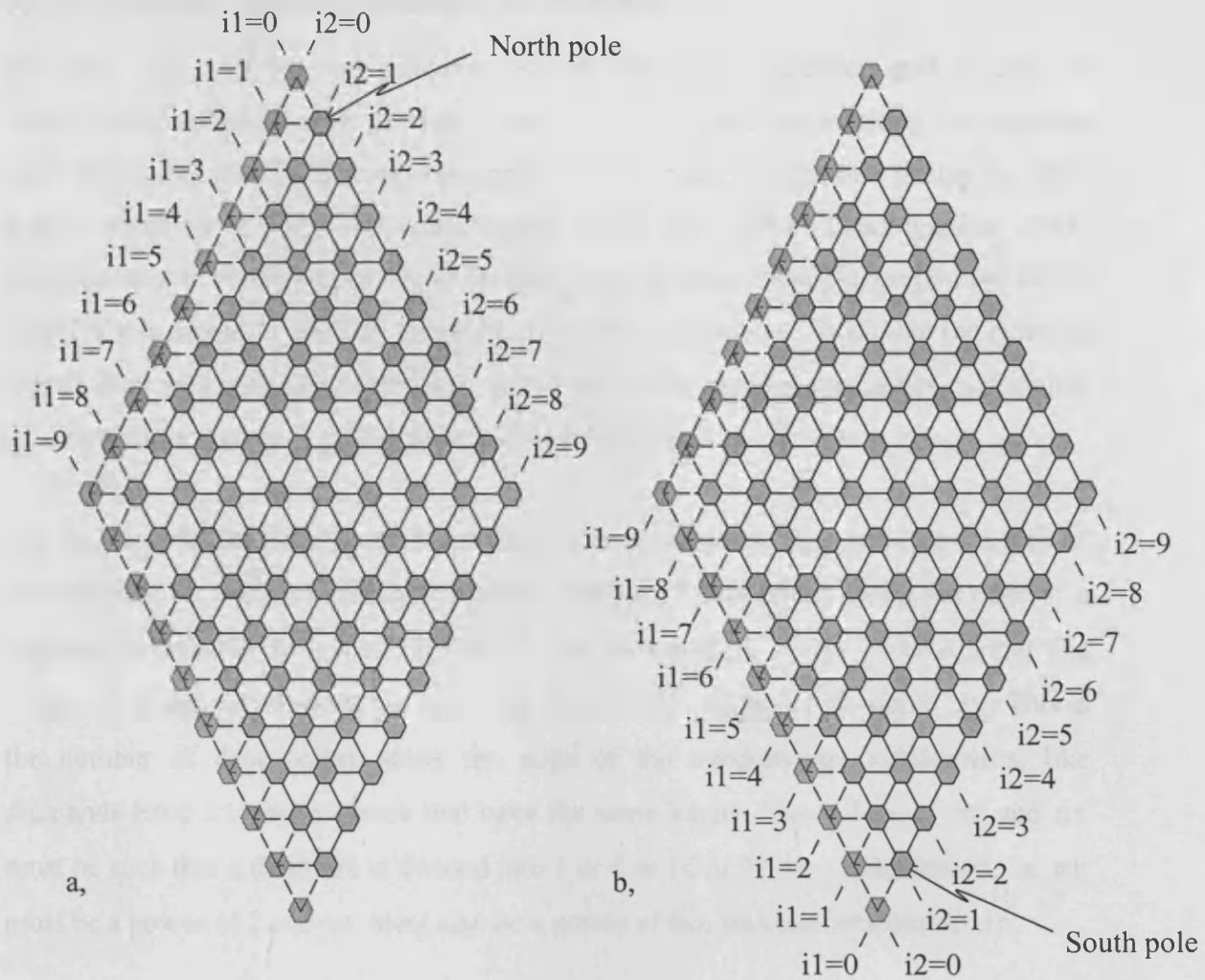


Fig 3.3

The indexing convention for diamonds for the $mt=8$ case. a, northern hemisphere diamonds b, southern hemisphere diamonds. Hexagons represent data points. Solid grey hexagons represent data points that are owned by the diamond while transparent grey hexagons are data points that while they do form part of this diamond are on the edge of the diamond and so are considered to be owned by the adjacent diamond.

Reproduced from Baumgardner 1984.

3.2.7 Domain decomposition in TERRA

We have shown in the two previous sections how an icosahedron grid is used to discretise the spherical shell geometry used by TERRA and the indexing conventions used within this grid. This work was performed by John Baumgardner during his PhD at the University of California, Los Angeles in the early 1980's [Baumgardner 1983, Baumgardner & Frederickson 1985]. In later work by Hans Peter Bunge [Bunge 1996] TERRA was edited to allow it to be run on parallel computers. To do this the existing icosahedron grid was subdivided and spread across the parallel processors performing the calculation, a process called domain decomposition.

The first step in the domain decomposition is to divide each diamond into a series of subdomains. As we have already stated the number of data points along the edge of a diamond is referred to as m_t in TERRA and is specified in the TERRA input file `size.h`. A second parameter is used to define the size of the subdomains: n_t . This is the number of data points along the edge of the subdomains. Subdomains, like diamonds have i_1 and i_2 axes that have the same length. The values of m_t and n_t must be such that a diamond is divided into 1 or 4 or 16 or 32 or... subdomains, i.e. m_t must be a power of 2 and n_t must also be a power of two less than or equal to m_t .

Decomposition is then continued by selecting how many subdomains each processor will own. This is defined by the parameter n_d in `size.h`, where n_d is the number of diamonds from which subdomains will be mapped onto the processors and can have a value of either 5 or 10.

If the number of diamonds is set to 5 then only northern hemisphere diamonds are mapped on the first half of the processors used and southern hemisphere diamonds to the last half. If n_d is set to 10 then each processor owns one subdomain from each of the ten diamonds. An example of both of these cases is shown in figure 3.4. Subdomains extend throughout the radial dimension. This does have some disadvantages, and can lead to long thin shaped subdomains that have large surface area. This is undesirable since the large surface area has to be communicated with neighbouring subdomains on different processors. This can lead to excessive message passing that can limit the performance of the program.

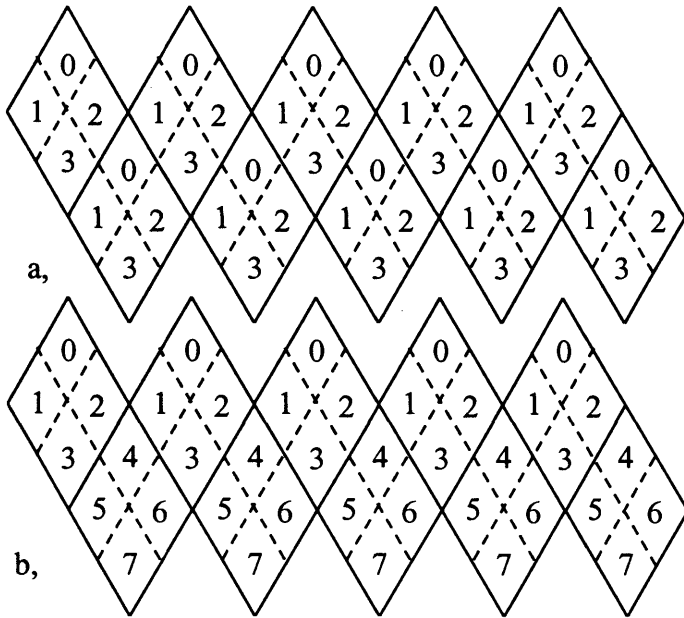


Figure 3.4
 The domain decomposition
 for a TERRA case in which
 $mt/nt=2$
 a, $nd = 10$
 b, $nd = 5$
 The diamonds have been
 projected on to a flat
 surface and solid black lines
 define their boundaries. The
 dashed lines show the
 divisions of the
 subdomains. The number is
 the MPI rank of the
 processor to which the
 subdomain is mapped.

$$\left\{ \begin{array}{l} \text{Number of} \\ \text{processors} \end{array} \right\} = \left(\frac{mt}{nt} \right)^2 \left(\frac{nd}{10} \right) \quad (3.12)$$

3.3 Implementation of the marker method in the TERRA program

In the following section I shall outline in some detail the method used to add markers in the TERRA code.

The markers' positions are updated within the Runge-Kutta (R-K) scheme used by TERRA. The velocity field is solved, the markers are advanced half a time step and the velocities used to do this for each marker are saved. The velocity field is then solved again. The markers are moved back by half a time step using the saved velocities and then moved forward one full time step. The choice to use a first order R-K time step was made purely on the basis that this was the scheme already used by TERRA. To implement a higher order Runge-Kutta scheme would mean making substantial alterations to the TERRA code and more importantly would require more data to be stored in RAM that could mean that TERRA would not be able to run at high resolutions.

Subroutine advance

```

c... Use a second-order Runge-Kutta scheme to update the
temperature.

    call usolve

    call energy(tdot(1,1))

    call markers(1)           ! Dave Oldham

    do ii=1,nv
        temp(ii) = temp(ii) + 0.5*tstep*tdot(ii,1)
    end do

    call usolve

    call energy(tdot(1,2))

    call markers(2)           ! Dave Oldham

    do ii=1,nv
        temp(ii) = temp(ii) + tstep*(tdot(ii,2) - 0.5*tdot(ii,1))
    end do

```

Passive markers are markers that advance with the velocity field and do not feed back any data into TERRA. It is not necessary to use the Runge-Kutta (R-K) scheme for passive markers; the same results would be obtained by advancing one full time step after the R-K scheme had been used to solve the velocity field. It is only necessary to include the advancement of the marker positions within the R-K time step when the markers are 'active' and feed back parameters such as buoyancy forces into the code that are used to solve the temperature and velocity fields.

3.3.1 Overview of the marker code

The marker code used in thesis can be separated into 4 distinct sections. There is the initialisation code. This is called before the main do loop that loops over the iterations being performed. This contains a number of subroutines that initialise the positions of the markers within the marker array. Within the Runge-Kutta time step [see section 3.2.2] the positions of the markers are updated to their new positions. Parallel communication is then used to allow markers to migrate to neighbouring processors, and finally the marker population is controlled. Marker population is controlled by creating and destroying markers such that their distribution remains even over the spherical surface.

In figure 3.5 there is a complete overview of the marker code used to advance the markers within the R-K time step. This is displayed by breaking the code down into the

subroutines used and showing their nested structure within the code. A brief description of the purpose of each subroutine is also included.

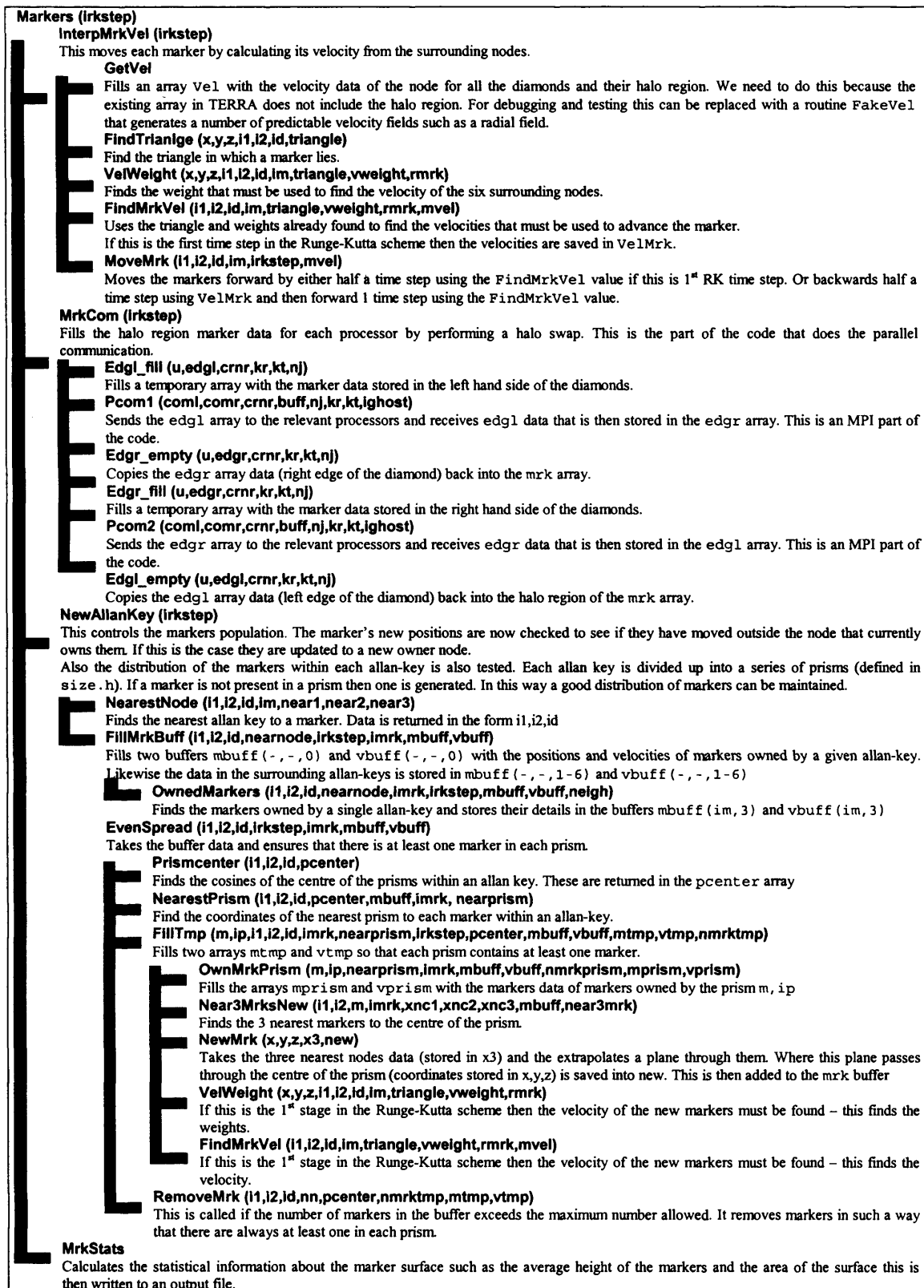


Figure 3.5

A summary of the subroutines employed by the code used to advance the markers within the Runge-Kutta scheme.

3.3.2 Preliminaries, allan-keys and prisms

The distribution of markers is closely tied into the icosahedron grid used by TERRA. This is discussed in section 3.2.5, however it makes sense to explain several aspects of the grid here.

The icosahedron grid divides the surface of a sphere into a series of hexagonal areas. At the centre of each of these areas is a data point in the grid (or node). The grid is extended radially by stacking these layers one on top of the other. A hexagonal area stretched from the CMB to Earth's surface forms a volume that shall be referred to as an allan-key. If we now consider the hexagonal area projected onto a sphere, we can divide this into a series of triangles whose volume when stretched radially we shall refer to as a prism. See figure 3.6.

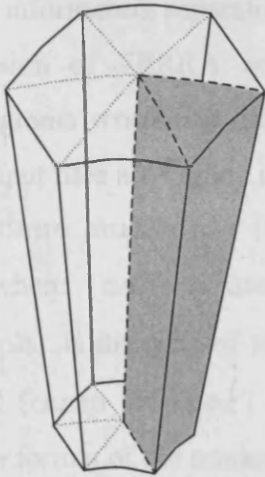


Figure 3.6

An illustration of an allan-key and a prism. The icosahedron grid employed by TERRA divides a spherical surface into a series of hexagonal areas. These are then extended radially to form a volume that is referred to as an allan-key. Each allan-key is divided into six volumes referred to as prisms. The volume defined by a solid black wire frame is an allan-key. The grey shaded volume is a prism.

3.3.2.1 How are the markers stored?

Marker and information used by the marker code are stored in a number of common blocks. The main block is `/mrk/` this contains three arrays. `mrk (i1, i2, id, im, 3)` contains the positions of the markers in Cartesian coordinates (x_1, x_2, x_3) , in units of meters relative to an origin at the centre of the Earth; `velmrk (i1, i2, id, im, 3)` contains the velocity of the markers in the first time step Runge-Kutta scheme, these are also stored in Cartesian coordinates and units of meters per second; `nmrk (i1, i2, id, im, 3)` is an integer array that contains the number of markers present in each allan-key. Where `i1, i2, id` are the common coordinates used in the TERRA icosahedron grid; see section 3.2.5; and `im` is the individual marker number of each marker in an allan-key.

3.3.2.2 Initialising the markers

When TERRA is started the position of the markers needs to be put into the marker array. There are two ways in which this can be done: by generating a new marker surface or by loading in an old one.

A new marker surface is initialised by placing the markers on a spherical surface at the depth requested in the TERRA input parameter file: `interra`. This is done in the subroutine `mrkinit`. This activates six markers in each allan-key and places them at the centre of the prisms owned by the allan-key.

Writing marker positions to files is performed by the subroutine `mrkout`. This produces one file per processor. It would have been possible to add the marker output into the standard output files used by TERRA. However there are advantages to storing the information separately. This makes it possible to create initial cases with the regular version of TERRA and gives our layered output more compatibility with other programs written to handle TERRA code, such as visualisation code like `mantlevis`. Output files are named in a similar manner to TERRA dump files...

`m[case number].[MPI rank].[dump number]`

...where `[case number]` is a three digit number specified in `interra`; `[MPI rank]` is the rank of the processor outputting the file (note that this starts at 0 not 1) and `[dump number]` is the number of times output files have been dumped.

The format of the marker dump files is as follows...

`m000.0000.01` -- the format of a dump file

`mt, nt, nm, mv` – A header: this allows us to check that the run using the markers dump file had the same set up as the run that created it.

`nmrk(i1, i2, id)` – The number of markers in the allan-key `i1, i2, id`

`mrk(i1, i2, id, im, 1), mrk(i1, i2, id, im, 2), mrk(i1, i2, id, im, 3)` – The Cartesian coordinates of the marker `i1, i2, id, im` in units of meters. This is then repeated for all the markers in the allan-key, and then for all the allan-keys owned by the processor, this includes the halo region.

Reading in marker information from these dump files is done by the `mrkin` subroutine. This effectively reverses the above process, i.e. reads from the files rather than writing to them.

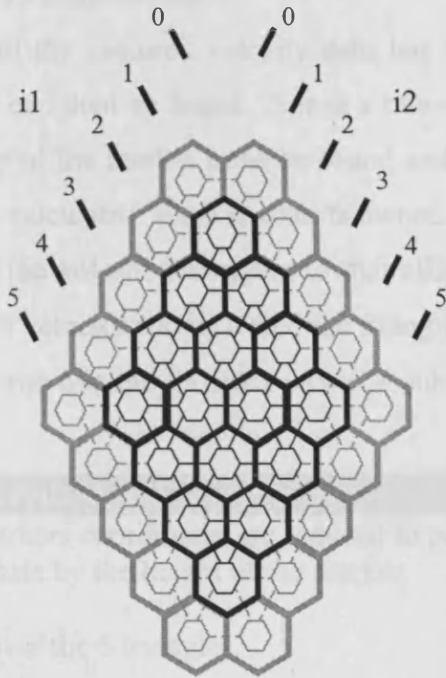


Figure 3.7

The areas owned by nodes in a subdomain. The black hexagons represent nodes unique to the subdomain while the grey hexagons show the nodes in the halo region. These are the nodes that are owned by the surrounding subdomains (on different processors). Some markers at the edge of the subdomain will require information about the velocity in the halo region to update their positions.

3.3.3 Updating the positions of the markers

It is only necessary to calculate the new position of markers owned by a processor and not those in the halo region. However to evaluate a marker's velocity we need to know the velocities at the six nodes surrounding a marker. For markers at the very edge of the subdomain this will include nodes in the halo region. See figures 3.7 and 3.8. The velocity array in the normal version of TERRA is stored in the `/velo/` common block however it only has a range of `u(0:nt, nt+1, nd, 3, nr+1)` which falls short of the `(0:nt+1, 0:nt+1)` range needed by the markers. There are a number of possible ways to overcome this problem. The size of the velocity array in `/velo/` could be increased to include the extra nodes. However this would require substantial revisions to a number of subroutines within TERRA. Instead I opted to use a second array `vel(0:nt+1, 0:nt+1, nd, 3, nr+1)` that is stored in the `/velhalo/` common block. The data from the `/velo/` array is copied into this array and the 'missing' data is filled in by using the halo-swap subroutines. This is done in the `GetVel` subroutine.

An artificial velocity field can be placed in the `vel()` array by calling the `FakeVel` subroutine instead of `GetVel`. Currently this can add a number of velocity fields that rotates the markers around one of the Cartesian axes or a purely radial field that moves the markers up and down. These artificial velocity fields are used as a debug tool and as part of a validation test.

Once all the required velocity data has been found the individual velocities of each marker can then be found. This is a two-stage process: the nodes that contribute to the velocity of the marker must be found and then the weights of these contributions must also be calculated. Each marker is owned by a particular allan-key and so we know that it is in the volume belonging to that allan-key. To find which nodes contribute to the markers velocity we must find the triangle that contains the marker, see figure 3.8. This is performed in the `findtriangle` subroutine. The pseudo code is below...

Pseudo code for the `findtriangle` subroutine

The markers coordinates are reduced to points on a unit sphere by dividing each coordinate by the height of the marker.

Loop over the 6 triangles.

Find the coordinates of the two nodes of the outer corners of each triangle.

Find the coordinates of the point midway between these two nodes.

Calculate the distance from the marker to this point.

Check to see if this distance is smaller than for previous triangle & if necessary update.

End loop over the 6 triangles.

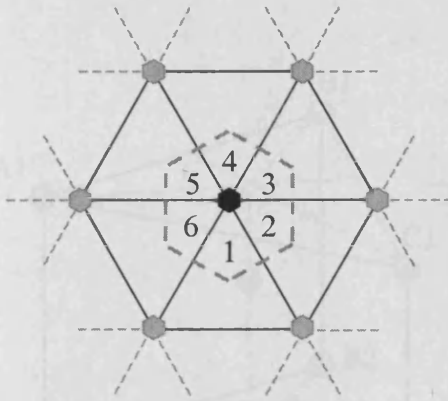


Figure 3.8

The triangles around a node. It is necessary to find which triangle a marker is in to calculate its velocity. Filled hexagons represent nodes, solid black lines and light grey dotted lines represent the icosahedron grid and the thick grey dashed line represents the area owned by the node. The numbers within each triangle are their numbers as defined within TERRA.

The triangle information can then be used as part of the `Velweight` subroutine. This calculates the contribution of each of the nodes surrounding the marker to its velocity. These weights are defined by the shape function employed in the TERRA method and are defined as follows.

$$W_{A1} = \left(\frac{a'}{a+a'} \right) \left(\frac{f-e}{f} \right) \quad W_{B1} = \left(\frac{b'}{b+b'} \right) \left(\frac{f-e}{f} \right) \quad W_{C1} = \left(\frac{c'}{c+c'} \right) \left(\frac{f-e}{f} \right) \quad (3.13)$$

$$W_{A2} = \left(\frac{a'}{a+a'} \right) \left(\frac{e}{f} \right) \quad W_{B2} = \left(\frac{b'}{b+b'} \right) \left(\frac{e}{f} \right) \quad W_{C2} = \left(\frac{c'}{c+c'} \right) \left(\frac{e}{f} \right)$$

Where a , a' , b , b' , c & c' are distances defined in figure 3.9.

The lengths a , a' , b , b' , c & c' are calculated from the positions of the nodes which are stored in Cartesian coordinates in meters in the `/xnex/` common block in the `xne (-1:nt+1, 0:nt+2, nd, 3)` array.

The markers velocities are then found by the `FindMrkVel` subroutine. The marker's position is updated in the subroutine in a manner defined by the Runge-Kutta scheme.

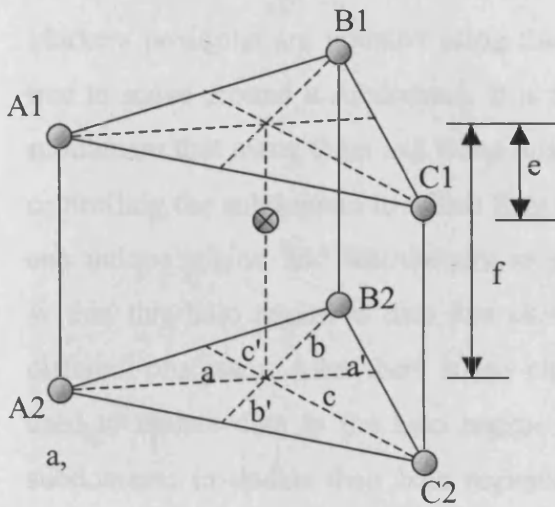


Figure 3.9

The lengths a , a' , b , b' , c & c' are used to calculate the weighting coefficients of each marker in equation 2. These are used to interpolate properties of markers such as its velocity from the six surrounding nodes.

Pseudo code for the `MoveMrk` subroutine

If this is the 1st time step in R-K then...

Update the position of the markers by half a time step

1

Store the velocity of the marker in `/mrk/ velmrk(i1,i2,id,im,2)`

3

Else if this is the 2nd time step in the R-K scheme

Move the marker backwards half a time step using the velocity stored in `/mrk/`

1

`velmrk(i1,i2,id,im,2)`

3

Move the marker forward one full time step.

End if

3.3.4 The halo region and boundary swapping

Markers positions are updated using the velocity field and consequently markers are free to move around a subdomain. It is also possible for markers to move outside the subdomain that owns them and when this happens they must be passed to the processor controlling the subdomain to which they have moved. To do this each subdomain owns one unique region and additionally an area surrounding it known as a halo region. Within this halo region is data that exists in a neighbouring subdomain owned by a different processor. After there is any change to the values, parallel communication is used to update data in the halo region. Likewise data must be sent to neighbouring subdomains to update their halo regions. This process is known as halo or boundary swapping. This concept is illustrated in figure 3.10 and discussed in some detail in appendix B.

Applying a halo region to the grid used by TERRA: the region $i1=1,nt$ & $i2=1,nt$ is unique to the subdomain and is surrounded by a halo region. This region is displayed in figure 3. 11. During a boundary swap each subdomain must pass edge-information to six processors.

A boundary swap is performed in three stages. First the correct data is put into common blocks. Then it is sent to the relevant processors. At the same time information is received, that is then copied into the halo region. Data is copied in to a common block before being sent so that it is stored in one common location in memory; this speeds up sending the data. One consequence of using MPI send and receive commands is that a send command must be accompanied by a receive command and the data received must equal the amount being sent. In the case of a boundary swap this is not an unreasonable requirement, indeed if we do not get back the same amount of data as we send then we would not have enough to fill the halo region. However the unusual distribution of subdomains in the icosahedron grid complicates matters. At the edge of diamonds subdomains do not align with one another in the same manner as they do within a diamond, this complicates which processors the data should be stored in. Boundary swapping is performed left to right and then right to left, with left being defined as in a westwards direction and right in a eastward direction. Left to right: data from the left hand side of the subdomain is copied into the correct arrays and then sent to the correct

processors. Data is received and copied into the correct sections of the right side of the halo region. Right to left: this is repeated with the right side of the subdomain being sent and the left side of the halo region being received.

The halo swap method is discussed in more detail in Appendix B. In particular the complications arising from the applying the method on an icosahedron grid are discussed in some detail.

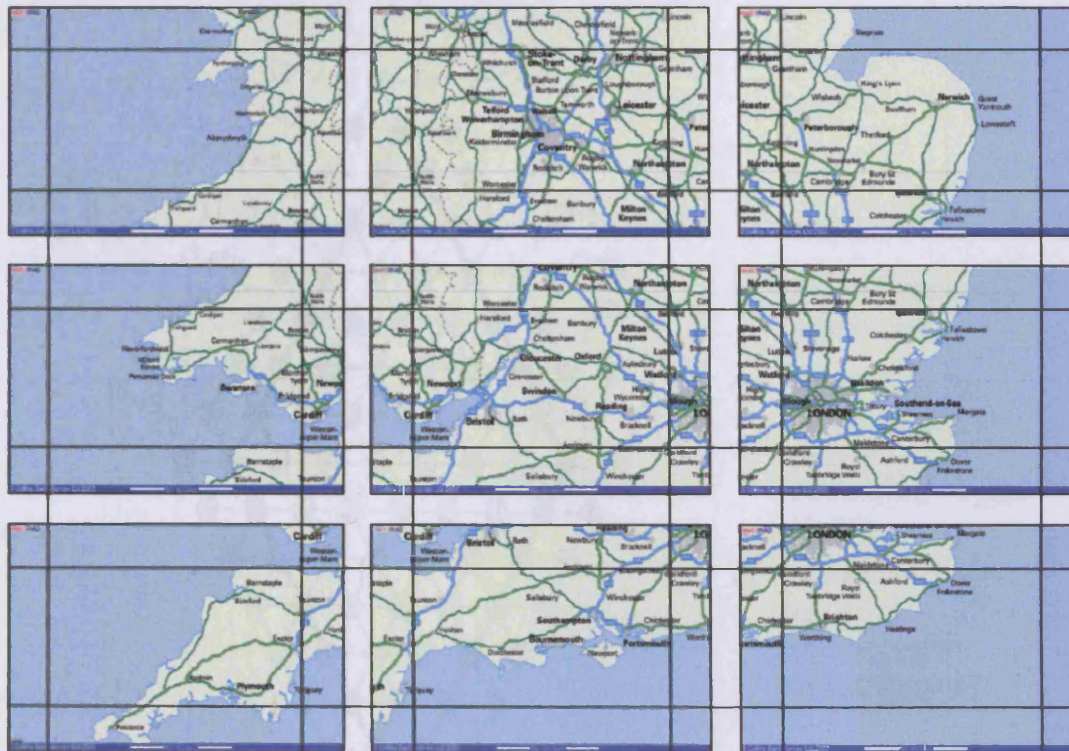


Figure 3.10

A concept of halo swapping. Each processor owns one region unique to itself. It is surrounded by a halo region that contains data owned by a neighbouring node. Routinely in the calculation halo regions are swapped. This information can then be used by the local processor to continue its calculations

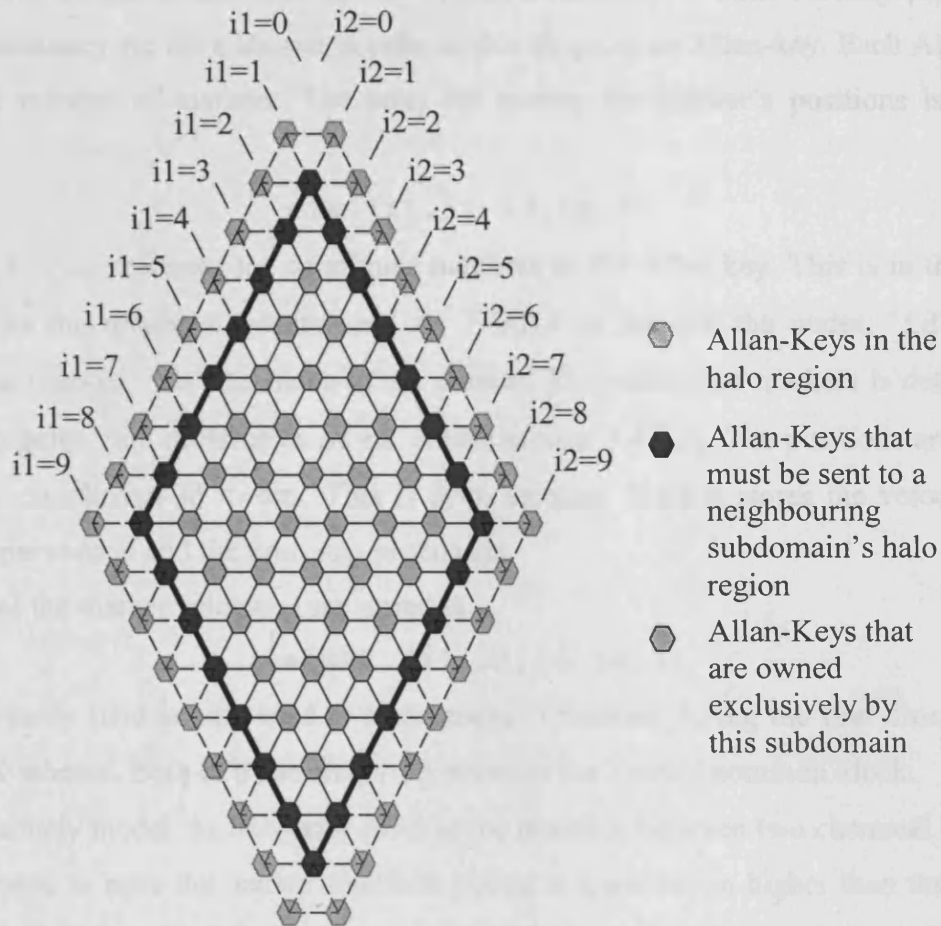


Fig 3.11
 The region owned by a subdomain for the $nt=8$ case. Notice the halo region that surrounds the subdomain does not include nodes $0,0$ and $nt+1,nt+1$

3.3.5 Controlling the population of the markers

As described in section 3.2.5 each radial layer of the icosahedron grid is composed of a collection of nodes. Each node has 6 neighbours¹ and a hexagonal region around it that can be thought of as being ‘owned’ by the node. See figure 3.8.

The region owned by the node can be extended vertically to form a hexagonal prism. For consistency we have chosen to refer to this shape as an Allan-key. Each Allan-key owns a number of markers. The array for storing the marker’s positions is in the form...

```
mrk (i1,i2,id,im,3)
```

Where $i1, i2$ represent the coordinate numbers of the Allan key. This is in the same format as the reference system used by TERRA to number the nodes. ‘id’ is the diamond number, ‘im’ the index of the marker. The number of markers is defined by the parameter ‘nm’ declared in `size.h` (see section 3.4.2.2). The positions are stored in x,y,z coordinates in meters. This is done because TERRA stores the velocities in meters per second and the time step in seconds.

Likewise the marker velocities are stored in ...

```
velmrk (i1,i2,id,im,3)
```

This velocity field is only used to store marker velocities during the first time step of the R-K scheme. Both of these arrays are stored in the `/mrk/` common block.

To accurately model the buoyancy force at the interface between two chemical layers it is desirable to have the marker interface placed at a resolution higher than that of the force field. To make this the case in our method we force there to be at least six markers in each allan-key. This means that the number of markers in a simulation is higher than the number of data points on the lateral icosahedron grid of the next order of refinement to the one being used. A demonstration of this is shown below.

If we consider a single subdomain, where the number of data points in one radial layer is N_p and the number of markers is N_m then when the order of refinement with mt N_p and N_m are given by....

$$N_p(mt) = mt^2 ; N_m(mt) = 6mt^2$$

So at the next order of refinement on the grid ($2mt$) the number of data points is...

$$N_p(2mt) = (2mt)^2$$

¹ With the exception of the ten pentagon nodes which are present at the points where three diamonds join and at the poles.

We compare this to the number of markers at a lower order of refinement...

$$\begin{aligned} N_p(2mt) : N_m(mt) \\ (2mt)^2 : 6mt^2 \\ 4mt^2 : 6mt^2 \\ 4 < 6 \end{aligned}$$

So the number of markers is always higher than the number of data points (in a radial layer) at a higher order of refinement of the icosahedron grid

The purpose of the markers is to resolve the boundary between two chemical layers so that buoyancy forces can be calculated. To do this the ratio of the volume of the layers owned by each node must be found. It is desirable to have not just a high number of markers but also a good distribution of markers within each allan-key. To do this each allan-key is divided up into the six prisms (see section 3.4.2). By specifying that each prism must contain at least one marker we can maintain a good distribution of markers throughout each allan-key.

To enforce this condition after each time step in the R-K scheme we call the `Newallankey` subroutine. This serves two purposes. The new positions of the new or updated markers are checked to see if they have moved to a new allan-key, if this is the case then they are moved to this allan-key. The distribution of the markers within each allan key and the one marker-per-prism condition is enforced.

A logical question is “why is it necessary to do this after the first stage in the R-K scheme”? Once a marker’s position has been updated it may have moved to a new prisms and a new allan-key. To find the markers new velocity we need to know its new allan-key and prism. It is possible to do this without moving the markers to new allan-keys. However if the marker has moved into the halo region the velocity array will not contain the data needed to calculate its new velocity. So to ensure that the new marker velocity can be found we must move markers to their new owner allan-keys. The number of markers that migrate into an allan-key may exceed the maximum number that can be stored within the `mrk` array forcing us to remove some markers. The simplest way to do this is by applying the marker population controls. Once we are forced to move markers to a new allan-key we are also committed to controlling marker population since the number of markers that can be owned by each allan-key is limited.

3.3.5.1 Moving markers to new allan-keys

Once the position of the markers has been updated a boundary swap is performed. The new positions of the markers are then checked to see if they have moved to new allan-keys.

The time step used by TERRA is determined such that a marker can (at most) move to a neighbouring allan-key during each time step. This means that only the surrounding allan-keys to those currently owning the marker need checking.

Pseudo code to find new owner allan-keys

Loop over allan keys

Loop over markers currently in the allan-key, and the surrounding allan-keys

Calculate the distance from the marker to the centre of the allan-key and the neighbouring allan-keys. If this is the nearest allan-key add the marker info to the arrays: `mbuff()`, and `vbuff()`

Control marker population in the buffers

End Loop over markers currently in the allan-key, and the surrounding allan-keys

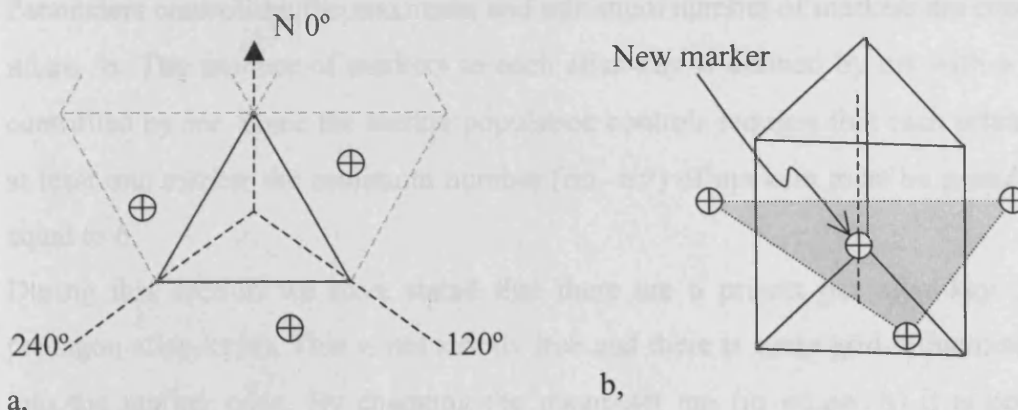
End loop over allan keys

3.3.5.2 Conditions for creating markers

Marker population is controlled an allan-key at a time. Before new markers are created or old ones destroyed all the markers owned by an allan-key are copied into a buffer: `mbuff((nm+mv)*7, 3, 0:6)`. The size of `mbuff` is such that it can contain 7 times the maximum number of markers allowed in each allan-key. In this way we can ensure that if all the markers owned by this allan-key and the neighbouring allan-keys are now owned by this node that there will be room for them in the buffer. The buffer also contains the markers owned by the six neighbouring nodes. Each prism is checked to see if it contains a marker. If no marker is present in the prism a new one is created. A plane is projected through three existing markers. The new marker is placed at the intercept of this plane and the centre of the prism. The three markers used are found with the condition that they are...

1. The nearest marker to the centre of the prism between 0° and 120° .
2. The nearest marker to the centre of the prism between 120° and 240° .
3. The nearest marker to the centre of the prism between 240° and 0° .

Where we have taken 0° to be the vector pointing to the North Pole on the spherical surface. This process is illustrated in figure 3.12.



a,
Figure 3.12

The method used to generate new markers.

a, A prism containing no markers. The region around the prism is divided up into three sections (between 0° - 120° ; between 120° - 240° & between 240° - 0°). The three nearest existing markers to the centre of each of the three regions are found.

The black triangle represents the base of the prism with no marker in it, other prisms are represented by grey dotted lines. Black dotted lines are the boundary of the regions in which we choose the nearest markers. These regions are taken from the bearing they make with the centre of the prism from north.

b, A plane is projected through the three nearest markers and a new marker placed where this bisects the centre of the prism. The black lines show a wire mesh of the prism, the grey transparent surface is the plane through the three existing markers; the black dotted line is the line through the centre of the prism.

3.3.5.3 Conditions for deleting markers

Once the buffer containing markers in an allan-key has been treated such that there is at least one marker per prism markers can be deleted. It is necessary to delete markers since there is a maximum number of markers that can be stored in each allan-key. Markers are only deleted if the number is greater than the allowed maximum. Markers are deleted by looping over the prisms in the allan key and deleting one random marker from each prism (a marker is not deleted if it would mean that there would be no markers left in the prism) until there are the maximum number of allowed markers. Markers are deleted in the `removeMrk()` subroutine.

3.3.6 Controlling the number of markers

Parameters controlling the maximum and minimum number of markers are contained in `size.h`. The number of markers in each allan-key is defined by `nm` with a variance controlled by `mv`. Since the marker population controls requires that each prism contain at least one marker the minimum number ($nm - mv$) of markers must be greater than or equal to 6.

During this section we have stated that there are 6 prisms per allan-key (or 5 for pentagon allan-keys). This is not strictly true and there is some grid refinement written into the marker code. By changing the parameter `mp` (in `size.h`) it is possible to change the refinement of the marker surface. `mp` defines the number of prism along the edge of a spoke. So the total number of prisms in each allan-key is give by $6 \times mp^2$. See figure 3.13.

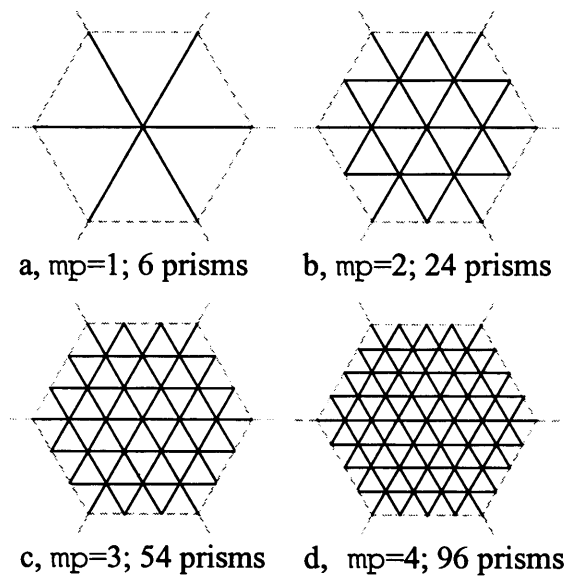


Figure 3.13

Grid decompositions within the allan-keys. The number of prisms can be changed by altering the parameter `mp` in `size.h`.

In all the cases used in this paper `mp` was set to 1. There has been only limited debugging of the marker code with `mp` set to any value other than 1. Running TERRA with a more refined grid for the markers is currently an untested procedure and could result in errors.

3.4 Adding buoyancy forces associated with the dense layer

The density contrast ($\Delta\rho$) associated with the boundary is introduced in the buoyancy term of the force equation.

$$\frac{1}{\rho} \nabla P = \nu \nabla^2 \mathbf{v} - \mathbf{g} \left(\alpha \Delta T + \frac{\Delta \rho}{\rho} \right) \quad (3.14)$$

Where P is the non-lithostatic pressure, ρ is the density, ν is the kinematic viscosity, \mathbf{v} is the velocity, \mathbf{g} is the gravitational force per unit mass, α is the coefficient of thermal expansion and ΔT is the temperature anomaly relative to the radial reference temperature profile.

The contribution of the density at each node is defined by the position of the node relative to markers i.e. whether the node is above or below the boundary. For nodes whose volume contains one or more markers the density is taken to be the average of the densities in the two layers weighted by the volume of each layer associated with the node. The volume ratio is found by subdividing the hexagonal volume horizontally into a series of triangular prisms. The average height of the markers in each prism is then used to calculate the volume of each layer within the prism. This is then repeated for all six prisms and the results are summed to give the volume of the upper and lower layer associated with the node. See figure 3.14.

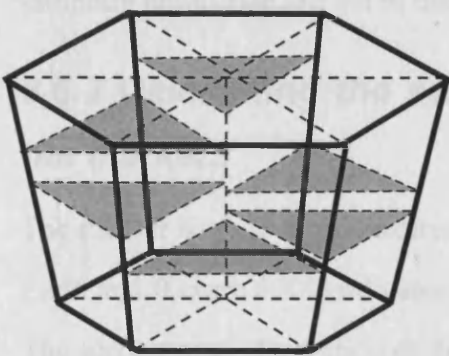


Figure 3.14

An example of the method used to find the ratio of the upper and lower layer volumes associated with each node. The hexagonal region 'owned' by a node is divided into six triangular prisms. The average height of the markers present in each prism is used to divide the prism into two. The sum of the individual prisms volumes are used to give the total volumes associated with each layer and hence the ratio of the two.

3.5 Analyzing the deformable surface and the layered system

There is little point in modelling a layered system if we are not going to analyse its behaviour in any way. Modifications were made to TERRA to add output specific to the layered case. Many of these are calculated and outputted in an obvious manner. For example the method to calculate the standard deviation of the marker's heights does not need explaining. However some output data needs more discussion.

3.5.1 The temperature in the layers

A number of methods were considered to calculate a representative temperature for the upper and lower layers. The first was to average the temperature of all the nodes present in a layer. This was rejected because it would sample thermal boundary layers. A second method considered was to (i) take the average height of the deformable boundary, (ii) use this to find the depth at the middle of the layer, (iii) then the average temperature of nodes at this depth could then be used to find the temperature in the layer. However, if the layer is deforming then we could be sampling temperature in the other layer. Finally the method used was to take the average temperature of nodes at the midpoints between the marker surface and the upper and lower surface to get the temperature in the upper or lower layer respectively. By using this method we avoid sampling temperatures in the boundary layers (unless the layer gets too thin). We do not use points where the layer has pressed against the surface or CMB and so avoid sampling points that are not in the layer.

3.5.2 Calculating the surface area of the boundary defined by the markers

The marker surface can be expressed as $r(\theta, \phi)$ where r is the radius from the centre of Earth and θ, ϕ are the coordinates in a spherical geometry.

The surface area of a section of this surface can then be given as [Garboczi 2002]...

$$ds = r \left[\left(\frac{\partial r}{\partial \phi} \right)^2 + \left(\frac{\partial r}{\partial \theta} \right)^2 \sin^2(\theta) + r^2 \sin^2(\theta) \right]^{\frac{1}{2}} \quad (3.15)$$

...and so the total surface area is...

$$S = \int_{\phi=0}^{2\pi} \int_{\theta=0}^{\pi} r \left[\left(\frac{\partial r}{\partial \phi} \right)^2 + \left(\frac{\partial r}{\partial \theta} \right)^2 \sin^2(\theta) + r^2 \sin^2(\theta) \right]^{\frac{1}{2}} d\theta d\phi \quad (3.16)$$

We can then apply this to the marker surface...

$$S = \sum_{\substack{\text{All radial} \\ \text{spokes}}} r \left[\left(\frac{\Delta r_{\phi}}{\Delta \phi} \right)^2 + \left(\frac{\Delta r_{\theta}}{\Delta \theta} \right)^2 \sin^2(\theta) + r^2 \sin^2(\theta) \right]^{\frac{1}{2}} \quad (3.17)$$

Where r is the average height of the markers in each radial spoke. Within the TERRA grid this equation can be written more completely as...

$$S = \sum_{id=1}^{nd} \sum_{i1=1}^{nt} \sum_{i2=1}^{nt} r_{i1,i2,id} \left[\left(\frac{\Delta r_{\phi}}{\Delta \phi} \right)^2 + \left(\frac{\Delta r_{\theta}}{\Delta \theta} \right)^2 \sin^2(\theta) + r_{i1,i2,id}^2 \sin^2(\theta) \right]^{\frac{1}{2}} \quad (3.18)$$

Where...

$$\Delta r_{\phi} = \frac{1}{2} (r_{i1+1,i2-1,id} - r_{i1-1,i2+1,id}) \quad (3.19)$$

$$\Delta r_{\theta} = \frac{1}{4} (r_{i1,i2-1,id} - r_{i1-1,i2,id} + r_{i1+1,i2,id} - r_{i1,i2+1,id}) \quad (3.20)$$

$$\Delta \phi = \frac{1}{2} \left(\tan^{-1} \left(\frac{x_{i1+1,i2-1,id}}{y_{i1+1,i2-1,id}} \right) - \tan^{-1} \left(\frac{x_{i1-1,i2+1,id}}{y_{i1-1,i2+1,id}} \right) \right) \quad (3.21)$$

$$\Delta \theta = \Delta \phi \quad (3.22)$$

4. Analysis of the marker method

4.1 Verification tests

The methods used to validate different components of the marker code are outlined as well as the results of these tests. These give an overview of the errors in the marker method.

4.1.1 Velocity interpolation: up and down method

Velocity interpolation is the simplest element of the code to validate. It has been tested by applying a radial field to the markers i.e. the markers are moved up and down with no tangential component to their motion.

Validation is achieved by describing the position of the markers with a simple equation. This is then differentiated to give the velocity field that is calculated in TERRA at each of the nodes. The velocity of the markers is then interpolated from the velocity of the six surrounding nodes during the Runge-Kutta time step.

So if we describe the position $r(x, y, z)$ of each marker as...

$$r = A \sin(\omega t) \hat{r} \quad (4.1)$$

Where \hat{r} is the radial unit vector $\hat{r} = (\underline{x}, \underline{y}, \underline{z})$ & $\omega = 2\pi/T$ T is the period of the oscillation of the markers and A is the amplitude, then this can be differentiated to give us the velocity...

$$v = \omega k \cos(\omega t) \hat{r} \quad (4.2)$$

So by applying this velocity field we know four values about a marker at each point in the calculation. These four values are...

1. The velocity is interpolated from the six surrounding nodes. $v_{TERRA} (v_{Tx}, v_{Ty}, v_{Tz})$
2. The real velocity is calculated for the marker with the velocity equation (4.2)

$$v_{Real} (v_{Rx}, v_{Ry}, v_{Rz})$$

$$v_{Rx} = A \omega \cos(\omega t) \underline{x} \quad (4.3)$$

$$v_{Ry} = A \omega \cos(\omega t) \underline{y} \quad (4.4)$$

$$v_{Rz} = A \omega \cos(\omega t) \underline{z} \quad (4.5)$$

3. The position of the marker is calculated by advancing it with a Runge-Kutta scheme

$$r_{\text{TERRA}}(x_T, y_T, z_T).$$

4. The position of the marker can be found from equations 4.6, 4.7 & 4.8

$$r_{\text{real}}(x_R, y_R, z_R)$$

$$x_R = A \sin(\omega t) \underline{x} \quad (4.6)$$

$$y_R = A \sin(\omega t) \underline{y} \quad (4.7)$$

$$z_R = A \sin(\omega t) \underline{z} \quad (4.8)$$

The errors are defined as the difference between the expected and observed ...

$$\text{ERROR}_{\text{Velocity}} = \sqrt{\frac{(v_{Rx} - v_{Tx})^2 + (v_{Ry} - v_{Ty})^2 + (v_{Rz} - v_{Tz})^2}{V_{Rx}^2 + V_{Ry}^2 + V_{Rz}^2}} \times 100\% \quad (4.9)$$

$$\text{ERROR}_{\text{Position}} = \sqrt{\frac{(x_R - x_T)^2 + (y_R - y_T)^2 + (z_R - z_T)^2}{\{\text{Total distance moved}\}}} \times 100\% \quad (4.10)$$

The test was run for an $\omega t = 32$ case on 32 processors. 'A' was set to 1,000km and T to 40 Billion years. The time step was controlled by TERRA and the imposed velocity field was applied only to the markers. The markers were not active (there was no density contrast associated with the boundary). The markers were initialised at a spherical shell at 1500km depth and the run performed 20,000 iterations. The markers completed seven cycles. The size of the velocity error associated with interpolating the markers velocity from the surrounding nodes had its largest values when the markers were at the maximum and minimum of their oscillation where the velocity was smallest. Figure 4.1 shows the results for an example marker though it should be noted that all markers showed very similar results.

The velocity error has its largest values of 0.1% when the imposed velocity field tends towards zero. The position error has an oscillatory nature with largest values at the maximum and minimum of the oscillations. The decay in the markers position errors is caused by the increase in total distance travelled by the marker with the marker consistently being 5km from its predicted position at the maximum of an oscillation.

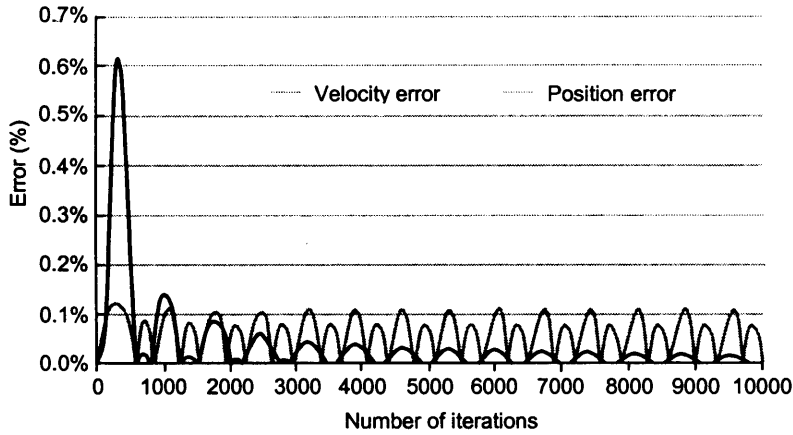


Figure 4.1

An imposed radial velocity field was employed with a time scale of 40 Billion years and an amplitude of 1000km for an $mt=32$ run. The data shown is the errors for a marker in the 1st subdomain. The x-axis shows the number of iterations and the y-axis the error as a percentage.

4.1.2 Marker generation and destruction: round and round

Testing the successful passing of markers from allan key to allan key and from subdomain to subdomain is done using an identical method to that used by Stegman et al. [2002a] to test his particle code. Markers are initialised in such a way that they all lie on a spherical shell at a given radius. A tangential field is applied to the markers and they rotate as a fixed body around the pole. It is not possible to check the position of individual markers since markers will be generated and destroyed by the marker population controls described in section 3.3.6. Controlling the population of the markers. Instead the average height of the markers and their standard deviation are used to judge if the markers are being created and destroyed in a successful manner.

The fake velocity field applied is given by...

$$\mathbf{v} \begin{pmatrix} x \\ y \\ z \end{pmatrix} = \begin{pmatrix} -\Omega y \\ \Omega x \\ 0 \end{pmatrix} \quad (4.11)$$

Where $\Omega=2\pi/T_r$ and T_r is the time for one complete revolution. The fake velocity field is only applied to the markers and TERRA solves the conservation equations (3.3, 3.4 & 3.5) in the usual manner (see section 3.3.2). The size of the time step is controlled by this processes and so we must make sure that the angular velocity applied to the markers is not too large and requires them to move beyond a neighbouring allan key in one time step.

The code was run for 20000 iterations for an $m_t=32$ case on 32 processors with $T=5$ Billion years. The total time simulated was 61.34 Billion years, achieving just over 12 rotations. One of the fundamental assumptions of the marker code is that markers only migrate to neighbouring allan keys during a time step. This is normally enforced in TERRA by altering the size of the time step by measuring the largest velocity. For the imposed velocity field this condition is not imposed and the markers could migrate across multiple cells during a single time step. We shall now use some simple calculations to validate that the angular velocity used for the imposed velocity is not too large. The grid used is $m_t=32$ so the number of allan keys around the pole is $32 \times 5 = 160$. It takes 970 to 400 iterations for a marker to migrate completely around the polar axis. The average number of iterations for a marker lying on the equator of the rotation to pass through an allan key is $400 \div 160 = 2.5$.

The results of the calculations can be seen in figure 4.2. Just over 12 rotations are achieved during the run with the average height of the markers falling by 28.826km and the standard deviation reaching 29.165km. The trend for the surface to edge inwards is thought to be caused by the numerical rounding in the code used to calculate the imposed velocity field. This can be verified by looking at the output of runs in which a different value of T is used to rotate the markers. The rate of descent of the markers does not vary with the speed at which they are rotated or the size of the time-step used by TERRA. It remains consistent at ~ 14 m per iteration. The size of the standard deviation increases linearly with the distance the markers have moved from their starting point. If we take the size of the standard deviation to be representative of the error in moving the markers and compare this to the distance moved by the markers $(6370-1500) \times 2\pi \times 12 = 367,189$ km then we see an error of $(29 \div 367,189) \times 100\% \approx 0.0079\%$ which per iteration works out to be $0.0079\% \div 4000 \approx 0.000002\%$. This is consistent with the results found from the up and down test and suggests that the markers are being migrated, generated and destroyed in an acceptable manner.

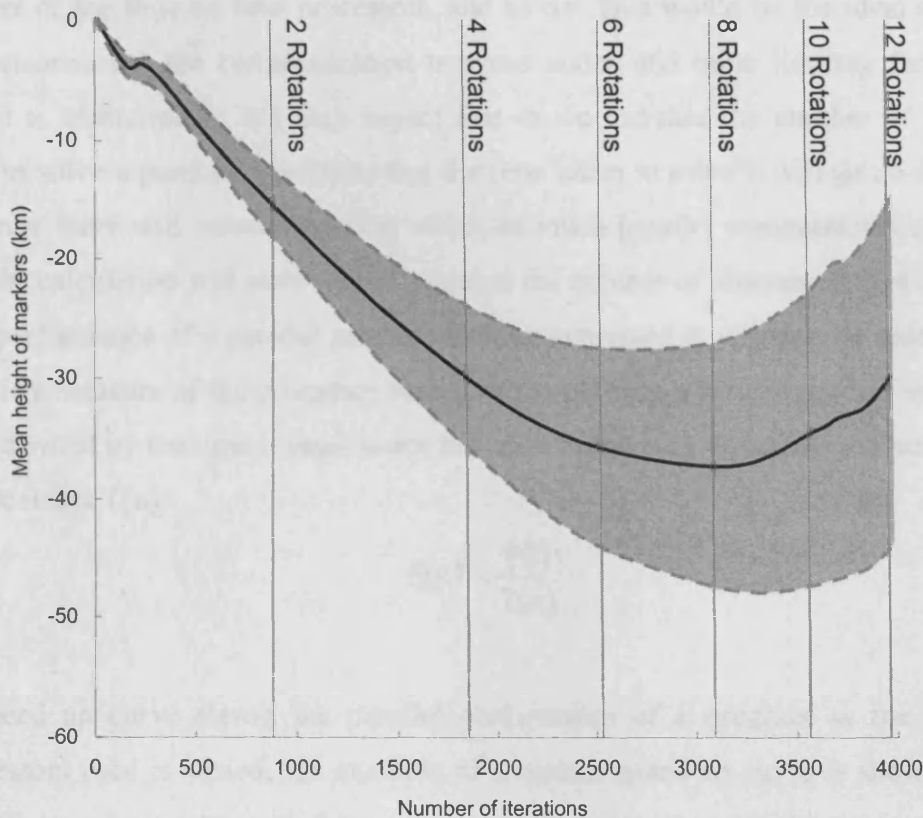


Figure 4.2

The results of a rotation verification test. The x-axis shows the number of iterations & the y-axis the height in km. The line shows the average height of the markers. The error bars show the size of the standard deviation of the markers heights.

4.2 Parallel program performance

It is only worth all the effort of writing a computer program to run on parallel computers if there is some advantage in doing so. Normally the desired purpose is to make the program run faster. In the case of TERRA and many other parallel programs it could equally be argued that the purpose of parallelising the program is to allow it to run on machines with more RAM than can be offered by a single workstation.

If this were sole reason then we would expect the program to be written so that it could run on a shared memory machine rather than distributed memory machine.

The increase in performance of a parallel program is normally measured in reference to its performance when it is run on a single processor (i.e. not in parallel). If the program

is then run on two processors we would hope that it may take half as long and take a quarter of the time on four processors, and so on. This would be the ideal increase in performance but the communication between nodes and other limiting factors mean that it is unattainable. We may expect that as we increase the number of processors used to solve a particular problem that the time taken to solve it will go on decreasing, however there will come a point at which so much parallel communication is needed that the calculation will start to take longer as the number of processors used increases. The performance of a parallel program is often expressed in terms of its speed-up $S(n)$. This is a measure of the processor time taken to perform a benchmark test on one node $T(1)$ divided by the time it takes when the same benchmark calculation is performed on n processors $T(n)$...

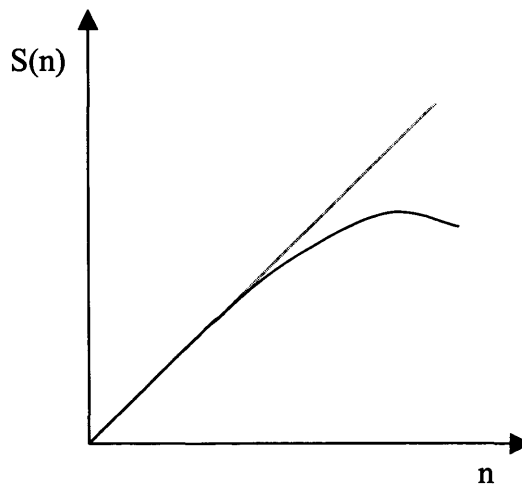
$$S(n) = \frac{T(1)}{T(n)} \quad (4.12)$$

A speed up curve shows the parallel performance of a program as the number of processors used is varied. An example of a normal speed up curve is shown in figure 4.3. We use these curves to choose how many processors to run the program on. Once the speed up curve has become level there is no advantage to using more processors. Normally we would choose a smaller number of processors.

Figure 4.3

An example of the normal speed up curve for a parallel program. The x-axis is the number of processors n , while the y-axis shows the speed up.

For few processors there is almost ideal speed up (the grey line), as the number of processors increases the performance decreases until we reach a point where the speed up decreases.



A second parameter: the parallel efficiency $E(n)$...

$$E(n) = \frac{S(n)}{n} = \frac{T(1)}{nT(n)} \quad (4.13)$$

...contains very similar information to the speed up. $E(n)$ has values between zero and one, the closer $E(n)$ is to one the more efficient the program.

4.2.1 What is the best number of processors to use?

To find the optimum number of processors on which to run the marker code a number of benchmark tests were run on the Helix and NESSC supercomputing clusters. These tests were performed on a range of number of processors and grid sizes. The results can be seen in table 4.1 and figure 4.4.

The speed up curves shown in figure 4.4 show that the performance of the program increases as the number of points in the grid increases. We see almost perfect speed up for $mt=128$ cases. It is most probable that the performance of marker program will decrease when it is run on a higher number of processors than 128, however since we do not have access to a machine with this many nodes it is not a concern.

In summary I would suggest that for the best performance I would run $mt=32$ cases on 8 or 16 nodes; $mt=64$ on 32 or 64 nodes and $mt=128$ on as many nodes as are available.

Computer	mt	np	Total Time	Speed up	Peff
NESSC	32	4	422.53	4.00	1.00
NESSC	32	8	194.09	8.70	1.09
NESSC	32	16	129.58	13.04	0.82
NESSC	32	32	65.69	25.72	0.80
NESSC	64	4	3375.72	4.00	1.00
NESSC	64	8	1571.66	8.59	1.07
NESSC	64	16	886.44	15.23	0.95
NESSC	64	32	399.12	33.83	1.06
NESSC	64	64	282.96	47.72	0.75
NESSC	64	128	158.53	85.17	0.67
NESSC	128	16	6754.44	16.00	1.00
NESSC	128	32	3241.83	33.33	1.04
NESSC	128	64	1856.96	58.19	0.90
NESSC	128	128	851.78	126.87	0.99
Helix	32	4	223.45	4.00	1.00
Helix	32	8	115.57	7.73	0.97
Helix	32	16	70.42	12.69	0.79
Helix	32	32	40.28	22.18	0.69
Helix	64	4	1493.8	4.00	1.00
Helix	64	8	798.19	7.48	0.94
Helix	64	16	462.88	12.90	0.81
Helix	64	32	240.58	24.83	0.78
Helix	128	32	1688.56	32.00	1.00
Helix	128	64	868.39	62.22	0.97

Table 4.1

Performance of the marker code on the NESSC and Helix super computers. The benchmark test had minimum input and output and was run for 100 iterations.

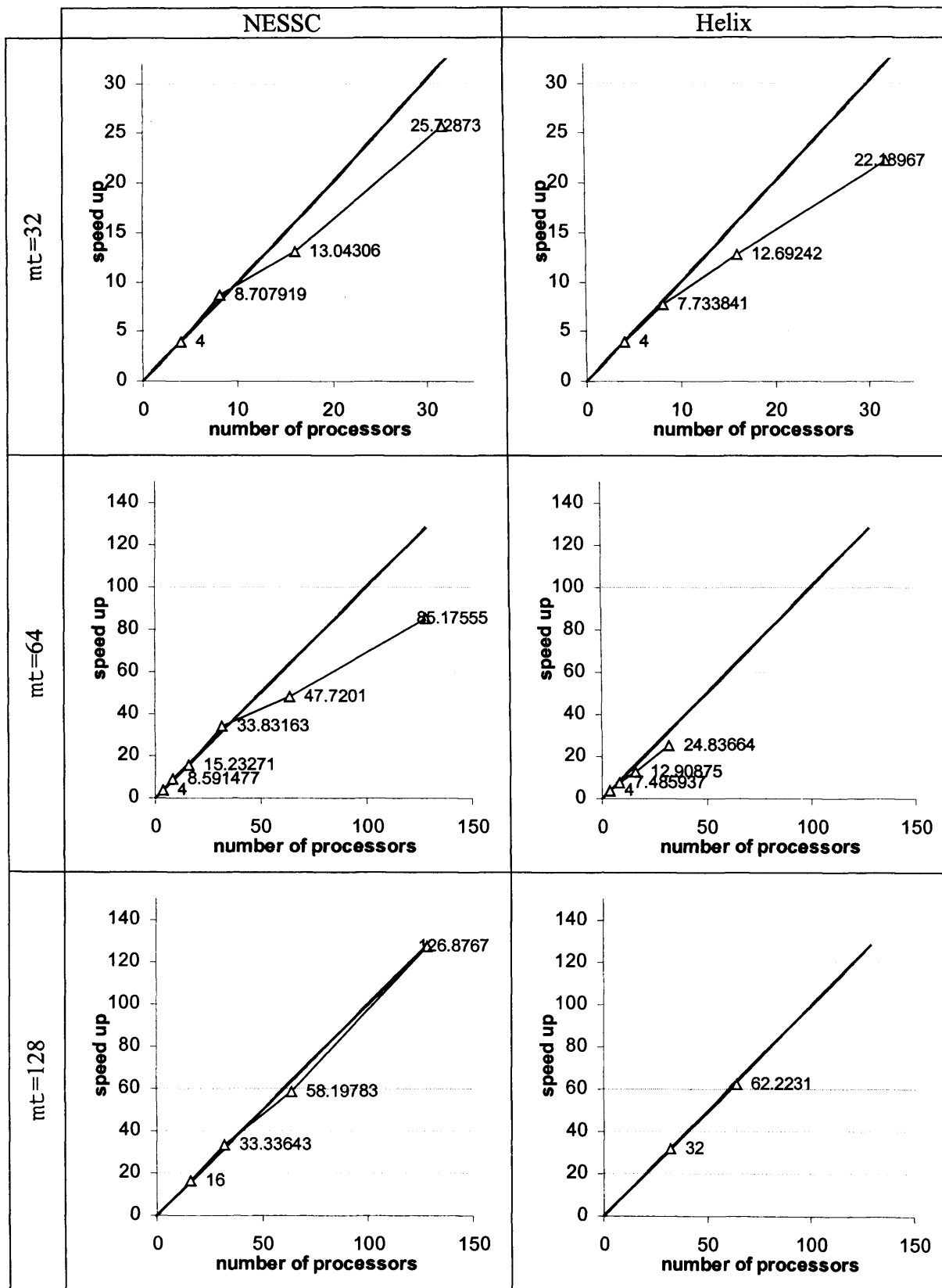


Figure 4.4
 The speed up graph for a range of grid sizes run on the two super computers available. Increases in mt represent an increase in the grid size used and hence the size of the problem being solved.

4.2.2 The effect of the marker code on the performance of TERRA

To investigate the increased computation time added by the marker code to TERRA three benchmark tests were performed. The first benchmark test was the default TERRA code with no markers, while second test was the TERRA code with passive markers (no density contrast) and third test used active markers (a 2% contrast over the boundary). All cases were run for 500 iterations on a TERRA grid size that contained 1,310,720 nodes ($mt=64$) that were divided over 8 processors. The results are shown in table1. We see that the advancement of the markers adds little overhead to the calculation (around 30%). However, the addition of buoyancy forces does decrease the performance of the code with a slowdown of more than 100%. The overhead is incurred in the greater effort required to solve the velocity field.

Run	Wall clock time (hours: minutes: seconds)	Total run time (s)	No. of micro seconds used by the move marker code	No. of micro seconds used by the marker buoyancy code
1	1:21:26	3766.130	0.000	0.000
2	1:42:18	4946.910	4310.000	0.000
3	2:35:39	7524.890	4750.000	520.000

Table 4.2

The effects of the markers on the performance of the marker code. Run one is the default TERRA code, run two passive markers & run three active markers. The performance is significantly compromised when the markers are activated with passive markers having little effect on the performance.

4.3 Resolution test

When we perform a run using TERRA we need to ensure that the spacing of the grid being used is sufficiently small to resolve features in the calculation. To check that this is the case it is usual to run a test case where a calculation is repeated with a finer grid spacing. It is desirable that the two runs are identical in every way save the resolution of the grid on which they are performed. The results are then compared and if they are significantly different then this suggests that at least in the case with the coarser grid spacing the system is unresolved.

A resolution test was run with grid spacing of $mt=64$ and 128 (see section 3.2.5). The system had both bottom and internal heating. The viscosity structure within the system varied with depth. Parameters used can be seen in table 4.2.

Parameter		Value
Depth of marker surface	D_k	1500 km
Temperature of surface	T_s	1060 K
Temperature of CMB	T_{CMB}	3000 K
ρ upper layer	ρ_0	5.00×10^3 kg
ρ lower layer	ρ_1	5.20×10^3 kg
$\Delta\rho/\rho$		4 %
Dynamic viscosity η	η	4.000×10^{23} Pa s (with radial layering)
Rate of internal heating	Q_{rad}	4.50×10^{-12} W kg ⁻¹
Volume coefficient of thermal expansion	α	2.0×10^{-5} K ⁻¹
Specific heat at constant volume	C_v	1×10^3 J kg ⁻¹ K ⁻¹
Rayleigh number	Ra_T	8.4×10^4

Table 4.3

The parameters used in the convergence test. The Rayleigh number presented in this table was calculated by TERRA using the method outlined in Appendix F.

The initial condition used was generated using the normal method of allowing the system to convect with whole mantle convection from an initial spherical harmonic temperature field. The interface for the layered convection was introduced as a flat surface at 1500km depth. The initial thermal structure was identical to that used in chapter 6.

To transfer the initial case from a lower grid to a higher resolution grid, code written by Prof. Peter Bunge (Munich) was used. This uses a linear (first order) interpolation method to find the value of the temperature field at the new grid points. This is not an ideal method of interpolating; since we assume that the initial temperature field is resolved at the lower grid spacing, Shannon sampling theory [Gonzalez & Wood 1992] states that the field should be over sampled and that the ‘true’ values of the temperature field at any point can be found. However the calculation to do this becomes very expensive and the order of the interpolation is equal to the number of points within the grid. The first order method is probably sufficient but since the true values of the temperature field have not been found the two initial cases cannot be thought of as perfectly identical. This train of thought can be continued. If a TERRA calculation is resolved then it will be over sampled, if it is unresolved it will be under sampled. A Fourier investigation of the thermal structure may be able to detect which of these two cases the system is in by identifying any aliasing in the power spectrum. The advantage

of this method is that it could be run automatically at the beginning or end of each calculation and be part of the standard output.

The $mt=64$ and $mt=128$ were run for 77.278 billion years; this corresponds to 17 over turns of the system. Figure 4.5 shows mantlevis images of the two cases at the end of the runs. The two final cases are similar – but not identical. The plan form of upwelling features in the lower layer is similar in both case and this figure does not suggest that the lower resolution case might be unresolved. A more detailed description of the state of the two simulations is shown in table 4.4. This compares a series of parameters outputted during the simulations. These all agree to within one percent and suggest that the system is resolved. However the area parameters do not agree well. Further investigation how parameters vary with time in the calculation are displayed in figure 4.6. The variation of the thermal structure and the Nusselt number with time show good agreement. However the non-dimensional area variable is consistently larger in the case with a higher grid resolution, however the shape of the variations is consistent. We suggest that this discrepancy is caused by using a different scale to measure the surface area. If this is the case then the $mt=128$ surface area is around 1.3 times that of the $mt=64$ surface area.

Variable	$mt=64$	$mt=128$	% Difference
Rms surface velocity	0.1219 cm/year	0.1230 cm/year	-0.902 %
Mean surface heat flux	0.006313 Wm^{-2}	0.006308 Wm^{-2}	0.079 %
Nusselt number	7.089±0.025	7.067±0.022	-0.167 %
Area Variable	0.3370±0.0212	0.4262±0.0147	-26.491 %
Temperature of upper layer	1275.485±1.010K	1281.427±1.026K	-0.466 %
Temperature of lower layer	2405.611±2.152K	2429.268±3.068K	-0.983 %
Total			

Table 4.4

Output parameters of the convergence test. In cases with errors quoted the value of the parameter is the average value of the parameter in the calculation between 50 and 70 G years in the simulation. The errors quoted are the standard deviation of the parameter during the same time.

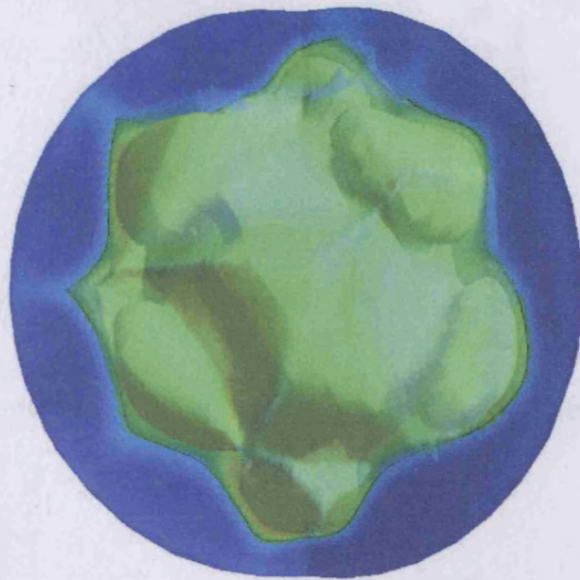
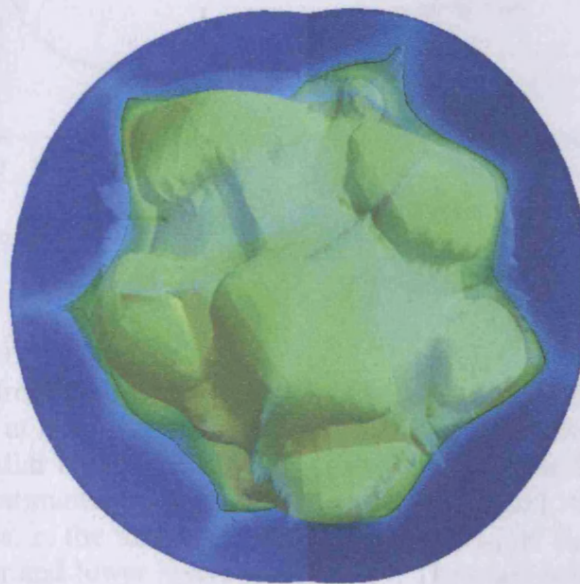
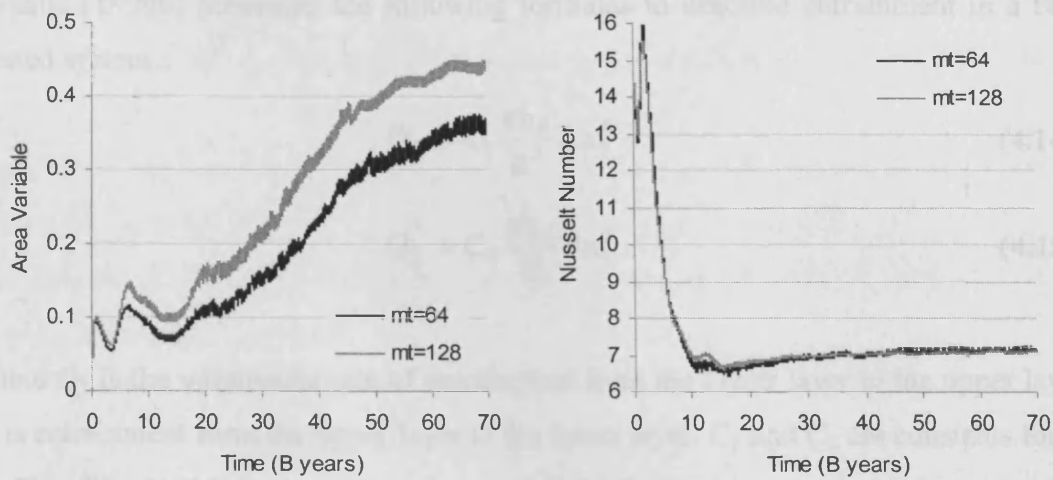
a, $mt = 64$ b, $mt = 128$

Figure 4.5

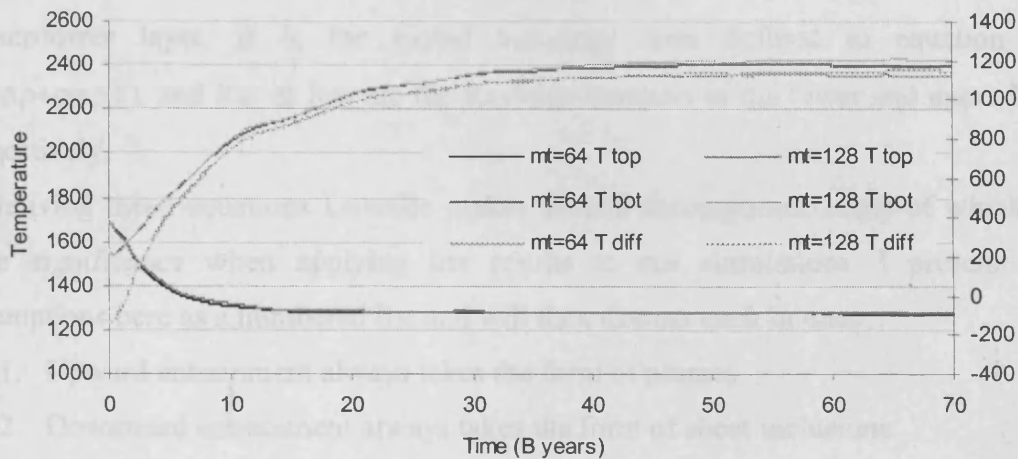
The same but different. Shown are mantlevis images of the layered structure of identical cases but run with a grid resolutions of a, $mt=64$ (1,351,680 node points) b, $mt=128$ (10,649,600 node points). The deformable boundary is represented by a semi transparent surface and an isosurface at 2000K is shown.

4.4 Entrainment



a,

b,



c,

Figure 4.6

Results from the resolution test. a, The area of the deformable boundary during the runs at both resolutions. The manner in which the area changes in time is very similar however the scale of the area is larger for the cases in which its area is estimated on a higher resolution scale grid. b, The Nusselt number of both runs. c, the thermal structure of runs. T_{top} & T_{bot} are the temperatures of the upper and lower layers respectively. These are both plotted on the left axis. T_{diff} is the difference between the temperature in the upper and lower layers. It is plotted on the secondary axis on the right.

4.4 Entrainment

Davaille [1999b] presented the following formulas to describe entrainment in a two-layered system...

$$Q_{\uparrow} = C_1 \frac{\kappa h_0}{B^2} Ra_2^{1/2} \quad (4.14)$$

$$Q_{\downarrow} = C_2 \frac{\kappa h_0}{B} Ra_1^{1/2} \quad (4.15)$$

Where Q_{\uparrow} is the volumetric rate of entrainment from the lower layer to the upper layer, Q_{\downarrow} is entrainment from the upper layer to the lower layer, C_1 and C_2 are constants found by Davaille [1999b] to have values of 0.0012 ($\pm 32\%$) and 0.0481 ($\pm 17\%$) respectively. κ is the thermal diffusivity, h_0 is the vertical length scale in the denser/lower layer, B is the global buoyancy ratio defined in equation 2.10 ($B = \Delta\rho / \rho\alpha\Delta T$), and Ra_1 & Ra_2 are the Rayleigh numbers in the lower and upper layers respectively.

In deriving these equations Davaille makes several assumptions, many of which will have significance when applying her results to our simulations. I present these assumptions here as a numbered list and will then discuss each in turn...

1. Upward entrainment always takes the form of plumes.
2. Downward entrainment always takes the form of sheet inclusions.
3. The layout of the cells is as shown in figure 4.7. A square cell of half width L has two edges of sheet-like downward entrainment; the centre of the cell contains a plume of width δ_p which has a velocity of W_p in its centre. The plume is fed by a hot region of radius 'a' below the cell.
4. Entrainment requires viscous coupling between the two layers.
5. The viscosity force has negligible effect on entrainment and buoyancy forces dominate.
6. The temperature difference across the whole system ΔT is equal to the interfacial horizontal temperature difference ΔT_B . ΔT_B is defined [Davaille 1997b, page236] as the difference between the temperature at the interface at points of downward entrainment and upward entrainment.



7. The radius 'a' of the heat source for a plume is directly proportional to the size of the viscous cell half width L of the plan form of entrainment on the interface. See figure 4.7.

8. The Boussinesq approximation for an incompressible fluid is applicable to the mantle.

Davaille's equations are derived in detail in Davaille [1999b] and in the two following bracketed sections.

Throughout this section I have used the same syntax as Davaille [1998b] to allow an easy comparison of our work.

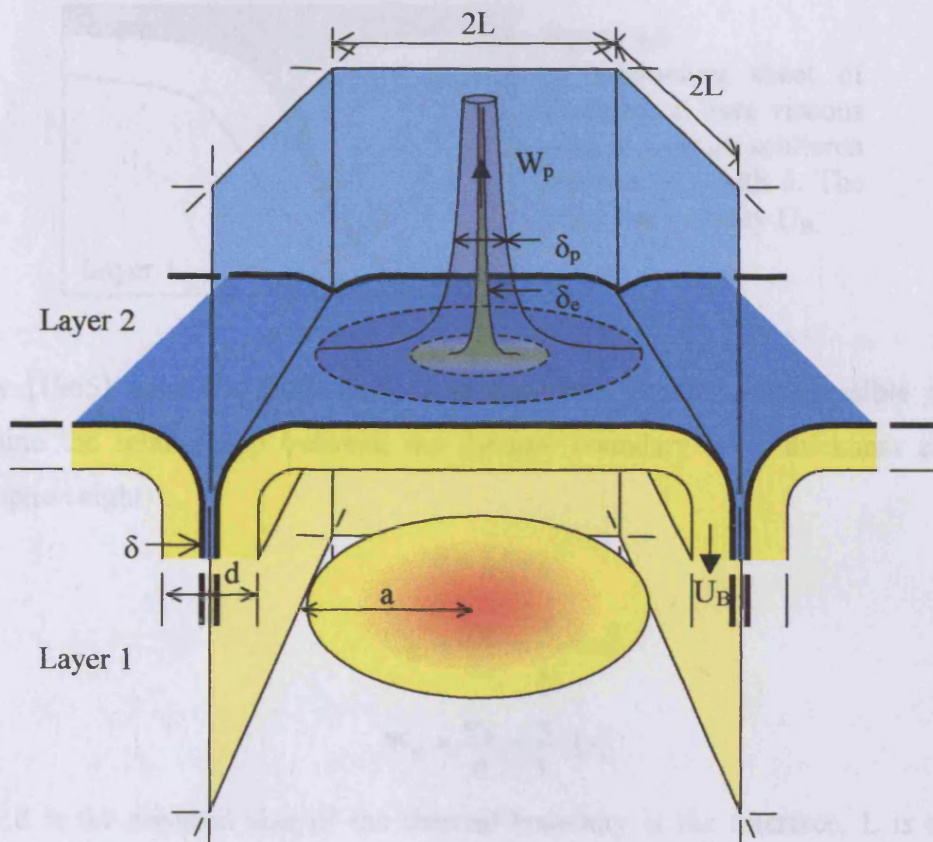


Figure 4.7

The plan-form of entrainment as described by Davaille [1999b]. A cell of half width L is bound on two sides by down going sheets of width d . Viscous drag entrains upper layer material into these sheets. The width of the schlieren material is δ . The down going sheets have velocity U_B .

In the centre of the cell is an up going plume that is fed by an anomalously hot region of width 'a'. The plume has width δ_p and via viscous drag captures a tendril of schlieren material of width δ_e . The plume has a velocity of W_p .

Material in the upper layer (layer 2) is shown in blue. Material from the lower layer (layer 1) is shown in yellow. The thick black line represents the boundary between the two layers.

Rates of entrainment from a 2D sheet

The build up of hot material below the interface and cold material above it produces a high horizontal temperature variation. The amplitude of these temperature variations ΔT_B is defined [Davaille 1997b, page236] as the difference between the temperature at the interface at points of downward entrainment and upward entrainment.

We consider entrainment of a thin sheet of schlieren material within a larger sheet that is captured by viscous drag forces. See figure 4.8

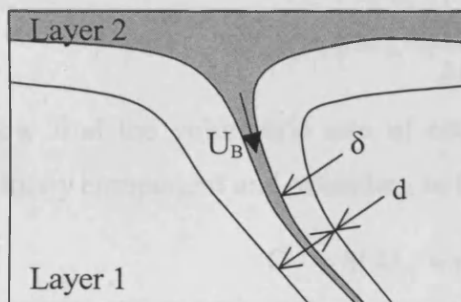


Figure 4.8

A subducting sheet of thickness d uses viscous drag to capture schlieren material of width δ . The sheet has velocity U_B .

Rossby [1965] used the Boussinesq approximation for an incompressible fluid to determine the relationship between the thermal boundary layer thickness and Ra_B (assumption eight)...

$$d = L Ra_B^{-1/2} \quad (4.16)$$

$$U_B \approx \frac{\psi_B}{L} = \frac{\kappa}{L} Ra_B^{2/5} \quad (4.17)$$

$$W_B \approx \frac{\psi_B}{d} = \frac{\kappa}{L} Ra_B^{1/5} \quad (4.18)$$

Where d is the physical size of the thermal boundary at the interface, L is the half width of the cell, Ra_B is the Rayleigh number based on ΔT_B , U_B and W_B are the horizontal and vertical velocity components at the boundary respectively, ψ_B is the stream function at the interface, and κ is the thermal diffusivity. Ra_B is given by...

$$Ra_B = \frac{\alpha g \rho \Delta T_B L^3}{\kappa \eta_1} \quad (4.19)$$

Viscous coupling at the interface forces a thin sheet upper layer material of thickness δ to be entrained into the lower layer (assumption four and two). By assuming that the viscous drag is balanced by buoyancy forces...

$$\alpha \Delta T_B g d - \frac{\Delta \rho}{\rho} g \delta \approx \frac{\eta_1}{\rho} \frac{W_B}{d} \approx \frac{\eta_1 \kappa}{\rho L^2} Ra_B^{2/5} \quad (4.20)$$

Substituting equation (4.16) into equation (4.20) ...

$$\alpha \Delta T_B g L Ra_B^{-1/5} - \frac{\Delta \rho}{\rho} g \delta \approx \frac{\eta_1 \kappa}{\rho L^2} Ra_B^{2/5} \quad (4.21)$$

And by taking the leading order Davaille drops the viscosity term (assumption five) to give:

$$\alpha \Delta T_B g L Ra_B^{-1/5} = \frac{\Delta \rho}{\rho} g \delta \quad (4.22)$$

$$\delta \approx L \frac{\alpha \rho \Delta T_B}{\Delta \rho} Ra_B^{-1/5} \quad (4.23)$$

We can now find the volumetric rate of entrainment Q_l by multiplying this by the vertical velocity component and extending to the 3rd dimension...

$$Q_{\downarrow} = \delta L U_B \approx \kappa L \frac{\alpha \rho \Delta T_B}{\Delta \rho} Ra_B^{1/5} \quad (4.24)$$

We need to remove several unknowns from this equation. Davaille sets $\Delta T_B = \Delta T$ (assumption six); $a \propto L$ (assumption seven) and sets the characteristic length scale L to be equal to the depth of the most viscous (lower) layer h_0 ...

$$Q_{\downarrow} = C_2 \frac{\kappa h_0}{B} Ra_1^{1/5} \quad (4.15)$$

Rates of entrainment from a plume

We consider a plume at the centre of a cell fed by a hot region with radius 'a' (see figure 4.7), a thin region of schlieren material is captured by viscous drag and is carried in the centre of the plume. See figure 4.9.

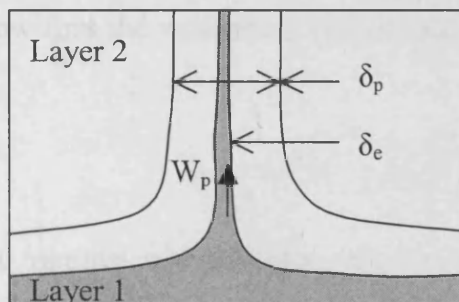


Figure 4.9
A plume of diameter δ_p uses viscous drag to capture schlieren material of diameter δ_e . The plume has velocity W_p .

This situation has already been studied by Singer [1986] and Olson et al [1993]. They found that the plume width δ_p and the velocity at the centre of the plume W_p are given by...

$$\delta_p \approx aRa_a^{-1/6} \quad (4.25)$$

$$W_p \approx \frac{\kappa}{a} Ra_a^{2/3} \quad (4.26)$$

Where κ is the thermal diffusivity and Ra_a is the Rayleigh number using the interfacial horizontal temperature variation ΔT_B (see the preceding boxed section) and the length scale 'a' of the hot anomaly feeding the plume.

$$Ra_a = \frac{\alpha g \rho \Delta T a^3}{\kappa \eta_2} \quad (4.27)$$

Where η_2 is the dynamic viscosity of the upper layer.

Balancing the buoyancy forces with the viscous forces...

$$\alpha \Delta T g \delta_p - \frac{\Delta \rho}{\rho} g \delta_e = \frac{\eta_1}{\rho} \frac{W_p}{\delta_p} \quad (4.28)$$

Substituting in equations 4.26 & 4.28...

$$\alpha \Delta T_B g a Ra_a^{-1/6} - \frac{\Delta \rho}{\rho} g \delta_e \approx \frac{\eta_1 \kappa}{\rho a \delta_p} Ra_a^{2/3} \quad (4.29)$$

And by taking the leading order of this Davaille drops the viscosity term (assumption five) to give:

$$\alpha \Delta T g a Ra_a^{-1/6} = \frac{\Delta \rho}{\rho} g \delta_e \quad (4.30)$$

$$\delta_e = a \left(\frac{\alpha \Delta T_B \rho}{\Delta \rho} \right) Ra_a^{-1/6} \quad (4.31)$$

We can now find the volumetric rate of entrainment Q_\uparrow and substituting in equation 4.26...

$$Q_\uparrow = \pi \delta_e^2 W_p \approx \kappa a \left(\frac{\alpha \rho \Delta T_B}{\Delta \rho} \right)^2 Ra_a^{1/3} \quad (4.32)$$

We need to remove several unknowns from this equation. Davaille sets $\Delta T_B = \Delta T$ (assumption six); $a \propto L$ (assumption seven) and sets the characteristic length scale to be equal to the depth of the most viscous (lower) layer h_0 ...

$$Q_{\uparrow} = C_1 \frac{\kappa h_0}{B^2} Ra_2^{1/2} \quad (4.14)$$

Taken from Davaille 1999b

4.4.1 The plan-form of entrainment

We shall now examine the assumptions used to produce equations 4.14 & 4.15. Assumptions 1 and 2 are not particularly troublesome for the equations in the form that Davaille presents them. In this form there are two equations: one describing sheet-like entrainment and the other plume-like entrainment. However, Gonnermann et al. [2002] uses equations 4.14 & 4.15 and the work of Sleep[1998] with assumptions 1 & 2 to create equation 4.33 in which the total entrainment from over the deformable interface is found.

$$Q = \frac{\rho C_p}{k} \frac{CH^{-1}B^{-2}Ra^{1/2}}{1 + \gamma B^{-1}} \quad (4.33)$$

Where, Q is the entrainment rate (upward + downward volume flux), C is an experimentally derived constant with a value of 0.2.

For $B > 0.2$ $C = 0.2$ [Davaille 1999b], k is the thermal diffusivity, C_p is specific heat, ρ is density, H is the total fluid depth, B is the buoyancy ratio as defined by Davaille [1999a], Ra is the Rayleigh number and γ is viscosity ratio (equal to one in our calculations).

If assumptions 1 & 2 are not valid then it casts doubts over the validity of equation 4.33.

In the cases that Davaille and Gonnermann et al. study the bottom layer is nearly always more viscous. Since our calculations are isoviscous it is not possible to rigorously test the plan form they suggested. However, for the simulations of bottom heated convection presented in chapter 5 we see a trend of the plan form of entrainment changing with the depth of the interface. When the boundary between the two layers is shallow in the mantle the upward entrainment is in the form of plumes and the downward entrainment is sheet-like. As the boundary is moved to deeper depths this changes with the upward entrainment becoming sheet-like and downward entrainment taking the form of cylindrical downwellings.

A consequence of this is that Davaille's formulae are only applicable to our cases when the layer is placed at shallow depths and in cases where there is viscosity increase at the same depth as the interface.

The overall plan-form of entrainment suggested by Davaille of a 2D sheet extended into the 3rd dimension and a plume in the centre of the cell does to some extent agree with the observations we see in our bottom heated calculations. For shallow layers we see a convection cell system like that in figure 4.7. However, rather than the square system we see a range of cell shapes. These vary from triangular to hexagonal. This may have an effect on the effectiveness of the sheet like entrainment compared to the cylindrical entrainment and the value of C_2 may be different in a spherical geometry.

4.4.2 The effects of viscous coupling

Davaille [1999b] describes the mechanism for generating entrainment in her tank experiments. Convection begins in both of the layers, the plan form of which is induced by the small thermal heterogeneities at the interface. Coupling between the two layers is viscous. Consequently flow in both layers converges at lines on the interface and cusps form. The viscous drag at the interfaces is sufficient to overcome buoyancy and entrain material from one layer to the other. However, when Davaille comes to derive her equations for entrainment she drops the viscous term from the equations (see equations 4.14 & 4.15 in section 4.4. We shall check this assumption by repeating Davaille's calculations without dropping the viscosity terms.

Sheet-like entrainment

We consider the case of a sheet of width d which is capturing a sheet of entrained material of width δ . We start with equation 4.21 that balances the buoyancy and viscous forces of the plume.

$$\alpha \Delta T_B g L Ra_B^{-1/2} - \frac{\Delta \rho}{\rho} g \delta \approx \frac{\eta_1 \kappa}{\rho L^2} Ra_B^{1/2} \quad (4.34)$$

Where α is the thermal expansivity, ΔT_B the interfacial horizontal temperature variation, g the gravitational constant, $\Delta \rho$ the density contrast across the chemical interface, Ra_B is Rayleigh number based on ΔT_B , ρ is the reference density, κ is the thermal diffusivity, η_1 the dynamic viscosity of the lower layer and L is the half width of the cell.

$$\delta \approx \frac{\rho}{\Delta\rho} \alpha \Delta T_B L Ra_B^{-1/5} - \frac{\rho}{\Delta\rho} \frac{\eta_1 \kappa}{\rho g L^2} Ra_B^{2/5} \quad (4.35)$$

We can now find the volumetric rate of entrainment Q_\downarrow and substituting in equation 4.17 ($U_B \approx \kappa Ra_B^{1/5} \div L$)

$$Q_\downarrow = \delta L U_B \approx \frac{\kappa \rho}{\Delta\rho} \left(\alpha \Delta T_B L Ra_B^{-1/5} - \frac{\eta_1 \kappa}{\rho g L^2} Ra_B^{2/5} \right) Ra_B^{1/5} \quad (4.36)$$

$$Q_\downarrow \approx \frac{\rho \alpha \Delta T_B}{\Delta\rho} \kappa L Ra_B^{1/5} - \frac{\eta_1 \kappa^2}{\Delta\rho g L^2} Ra_B^{3/5} \quad (4.37)$$

We now use some simplifications: $\Delta T_B = \Delta T$ (assumption six) and set the characteristic length scale to be equal to the depth of the most viscous (lower) layer $h_0 \dots$

$$Q_\downarrow = C_2 \left\{ \frac{\kappa h_0}{B} Ra_1^{1/5} - \frac{\eta_1 \kappa^2}{\Delta\rho g h_0^2} Ra_1^{3/5} \right\} \quad (4.38)$$

Plume-like entrainment

We consider the case of a plume of width δ_p that is capturing a tendril of entrained material of width δ_e . We start with equation 4.29 that balances the buoyancy and viscous forces of the plume.

$$\alpha \Delta T_B g a Ra_a^{-1/5} - \frac{\Delta\rho}{\rho} g \delta_e \approx \frac{\eta_2 \kappa}{\rho a \delta_p} Ra_a^{2/5} \quad (4.39)$$

Where α is the thermal expansivity, ΔT_B the interfacial horizontal temperature variation, g the gravitational constant, a the radius of the source region of the plume, $\Delta\rho$ the density contrast across the chemical interface, Ra_a is Rayleigh number of the source region of the plume, ρ is the reference density, κ is the thermal diffusivity, η_2 the dynamic viscosity of the upper layer.

$$Ra_a = \frac{\alpha g \rho \Delta T a^3}{\kappa \eta_2} \quad (4.40)$$

To remove the δ_p unknown from equation 4.39 we substitute in equation 4.25 ($\delta_p \approx a Ra_a^{-1/5}$)

$$\alpha \Delta T_B g a Ra_a^{-1/5} - \frac{\Delta\rho}{\rho} g \delta_e \approx \frac{\eta_2 \kappa}{\rho a^2} Ra_a^{2/5} \quad (4.41)$$

Rearranging we arrive at...

$$\delta_e \approx \frac{\rho\alpha\Delta T_B}{\Delta\rho} aRa_a^{-1/6} - \frac{\eta_2\kappa}{\Delta\rho g a^2} Ra_a^{5/6} \quad (4.42)$$

We can now find the volumetric rate of entrainment Q_\uparrow and substituting in equation

$$4.26 (W_p \approx \kappa Ra_a^{2/3} \div a) \dots$$

$$Q_\uparrow = \delta_e^2 W_p \approx \frac{\kappa}{a} \left\{ \frac{\rho\alpha\Delta T_B}{\Delta\rho} aRa_a^{-1/6} - \frac{\eta_2\kappa}{\Delta\rho g a^2} Ra_a^{5/6} \right\}^2 Ra_a^{2/3} \quad (4.43)$$

$$Q_\uparrow \approx \frac{\kappa}{a} \left\{ \frac{\rho\alpha\Delta T_B}{\Delta\rho} aRa_a^{1/6} - \frac{\eta_2\kappa}{\Delta\rho g a^2} Ra_a^{5/6} \right\}^2 \quad (4.44)$$

We now use some simplifications: $\Delta T_B = \Delta T$ (assumption six); $a \propto L$ (assumption seven) and set the characteristic length scale to be equal to the depth of the most viscous (lower) layer h_0 ...

$$Q_\uparrow = C_1 \frac{\kappa}{h_0} \left\{ \frac{h_0}{B} Ra_2^{1/6} - \frac{\eta_2\kappa}{\Delta\rho g h_0^2} Ra_2^{5/6} \right\}^2 \quad (4.44)$$

Note that C_1 will not have the same value as that derived by Davaille.

The two equations describe the rate of volumetric entrainment ($m^3 s^{-1}$) from a single cell that considers both buoyancy and viscous forces.

$$Q_\uparrow = C_1 \frac{\kappa}{h_0} \left\{ \frac{h_0}{B} Ra_2^{1/6} - \frac{\eta_2\kappa}{\Delta\rho g h_0^2} Ra_2^{5/6} \right\}^2 - \text{Plumes} \quad (4.44)$$

$$Q_\downarrow = C_2 \left\{ \frac{\kappa h_0}{B} Ra_1^{1/3} - \frac{\eta_1\kappa^2}{\Delta\rho g h_0^2} Ra_1^{2/3} \right\}^2 - \text{Sheets} \quad (4.38)$$

Where...

$$Ra_1 = \frac{\alpha_1 \rho g \Delta T h_0^3}{\kappa \eta_1} \quad (4.45)$$

$$Ra_2 = \frac{\alpha_2 \rho g \Delta T (H - h_0)^3}{\kappa \eta_2} \quad (4.46)$$

Where Ra_1 and Ra_2 are the Rayleigh numbers of the lower and upper layers respectively, η_1 and η_2 are the dynamic viscosities of the lower and upper layers

respectively, h_0 is the depth of the more viscous/lower layer and H is the depth of the whole system.

We calculate the values of the terms in equations 4.38 and 4.44 for the earth-like values quoted in table 4.5.

Sheet-like entrainment

$$\text{Buoyancy term } \kappa h_0 \text{Ra}_1^{1/5} \div B = 5.827 \quad \text{m}^3 \text{s}^{-1} \text{ per cell}$$

$$\text{Viscosity term } \eta_1 \kappa^2 \text{Ra}_1^{4/5} \div \Delta \rho g h_0^2 = 0.076 \quad \text{m}^3 \text{s}^{-1} \text{ per cell}$$

Plume-like entrainment

$$\text{Buoyancy term } \kappa h_0 \text{Ra}_2^{1/6} \div B^2 = 11.90 \quad \text{m}^3 \text{s}^{-1} \text{ per cell}$$

$$\text{Viscosity term } \eta_2^2 \kappa^3 \text{Ra}_2^{7/3} \div \Delta \rho^2 g^2 h_0^5 = 9278 \quad \text{m}^3 \text{s}^{-1} \text{ per cell}$$

For sheet-like entrainment the viscosity term is two orders of magnitude smaller than the buoyancy term and can be neglected. However, for plume-like entrainment the viscous term is two orders of magnitude larger than the buoyancy term. In this case it is not valid to abandon the viscosity term. This suggests that the chemical buoyancy force is not sufficient to stop sheet-like entrainment in Earth's mantle, and that viscous forces play a dominant role in driving plume-like entrainment.

We repeat these calculations for the parameters used in the entrainment calculation presented later in this section.

Sheet-like entrainment

$$\text{Buoyancy term } \kappa h_0 \text{Ra}_1^{1/5} \div B = 19.07 \quad \text{m}^3 \text{s}^{-1} \text{ per cell}$$

$$\text{Viscosity term } \eta_1 \kappa^2 \text{Ra}_1^{4/5} \div \Delta \rho g h_0^2 = 0.062 \quad \text{m}^3 \text{s}^{-1} \text{ per cell}$$

Plume-like entrainment

$$\text{Buoyancy term } \kappa h_0 \text{Ra}_2^{1/6} \div B^2 = 10.49 \quad \text{m}^3 \text{s}^{-1} \text{ per cell}$$

$$\text{Viscosity term } \eta_2^2 \kappa^3 \text{Ra}_2^{7/3} \div \Delta \rho^2 g^2 h_0^5 = 1.951 \quad \text{m}^3 \text{s}^{-1} \text{ per cell}$$

So in this case the viscosity term is sufficiently small for it to be neglected.

It is desirable to perform these calculations using the parameters in Davaille's experiments. However, this is not possible because she does not quote the parameters shown in table 4.5 for her experiments. It is likely that for her experiments the magnitude of the viscosity term is much smaller than the buoyancy terms.

Parameter		Value
Dynamic viscosity of the upper layer	η_2	1×10^{21} Pa s
Dynamic viscosity of the lower layer ($\eta_1 = \eta_2 \times 100$ [Davies 1999, p268])	η_1	1×10^{23} Pa s
Gravitational acceleration g		10 m s^{-1}
Volume coefficient of thermal expansion in the upper layer	α_2	$5.0 \times 10^{-5} \text{ K}^{-1}$
Volume coefficient of thermal expansion in the lower layer [Chopelas & Boehler, 1992]	α_1	$1.0 \times 10^{-5} \text{ K}^{-1}$
Thermal diffusivity	κ	$4.8 \times 10^{-7} \text{ m}^2 \text{ s}^{-1}$
Temperature difference across the mantle	ΔT	2000 K
Reference density	ρ	$5 \times 10^3 \text{ kg m}^{-3}$
Density contrast	$\Delta \rho$	$0.1 \times 10^3 \text{ kg m}^{-3}$ (2%)
Depth of the lower layer	h_0	1300 km
Depth of the interface of the layers	$H - h_0$	1500 km
Depth of the mantle	H	2800 km
Buoyancy ratio ($B = \Delta \rho \div \rho \alpha \Delta T$)	B	1.0
Rayleigh number of the upper layer	Ra_2	3.5×10^7
Rayleigh number of the lower layer	Ra_1	5.5×10^4

Table 4.5

Parameters used to calculate the buoyancy and viscosity terms for an Earth-like case.

The assumption that viscous forces are negligible compared with buoyancy forces is valid for an Earth-like system when sheet-like entrainment is taking place, but not for plume-like entrainment. In the case of our numerical experiments (and most likely Davaille's tank experiments) ignoring the viscous terms in interpreting our results is valid.

We test the significance of the assumption that viscosity forces can be neglected from equations 4.14 & 4.15 by calculating the entrainment in an Earth-like case using equations 4.14 & 4.15 (no viscous terms), and equations 4.38 & 4.44 (include viscous terms) with values from table 4.5. The results of these calculations are shown in table 4.6.

	With no viscosity term	With the viscosity term
Upward (plumes) volumetric flux	0.26 m ³ s ⁻¹ per cell	8.00 m ³ s ⁻¹ per cell
Downward (sheets) volumetric flux	0.28 m ³ s ⁻¹ per cell	0.28 m ³ s ⁻¹ per cell
Mean depth of an interface initially at 1500km after 4.2 B years	1498 km	2121 km

Table 4.6

Predictions of the amount of entrainment for an earth-like system. For the final row in which an estimate is made of the change of depth of an interface initially placed at 1500km, we assume there are 159 cells. We arrive at this value by assuming that the size of each cell is the same as the depth of the lower layer and calculating how many cells could fit on to a spherical surface at the depth of the interface.

We use Davaille's equation to predict that within the lifetime of Earth a layer initially at 1500km would be entrained upwards at a rate of 40.1 km³ year⁻¹, with downward entrainment at a rate of 1.4 km³ year⁻¹. So in total the layer would retreat at a rate of 2 km G years⁻¹.

4.4.3 Other assumptions

Davaille's assumption that the temperature structure across the mantle is equal to the interfacial temperature difference ($\Delta T_B = \Delta T$; assumption six) contradicts a statement she makes earlier in the same paper. She states that $\Delta T_B = [0.38 \pm 0.06] \times \Delta T$ and has no clear dependence on the Rayleigh number or the buoyancy ratio of the two layers, see figure 4.10. However Davaille could equally have made the assumption that $\Delta T_B \propto \Delta T$ and any constant would have been absorbed into C_1 & C_2 . Consequently while Davaille shows that assumption 6 is not valid, her use of it does not affect the validity of her scaling calculations.

Assumption seven that the radius of the heat source is proportional to the cell half width $a \propto L$ is not easily checked from the output of our calculations. It does not seem unreasonable.

And finally, assumption eight (the Boussinesq approximation for an incompressible fluid) is certainly applicable to our calculations since we use the same assumption.

Sleep [1988] assumed viscous and buoyancy forces balance in entrained tendrils in a plastic medium and used a 1D approximation to show that sheet-like entrainment is much more effective than plume-like entrainment. This is in agreement with Davaille and shows that we would expect the interface to move upwards as more entrained material (from sheets) enters than leaves from it (via plumes).

Sleep also found cases in which the entrainment is downward into the denser layer (though he was not interested in this case). He found that this has to do with the ratio of the thickness of the entrained sheet to the width of the whole sheet, and is affected by the Buoyancy ratio (using the temperature difference between the centre of the entrained material and the temperature in the upper layer). The larger the buoyancy ratio the smaller the ratio of entrained width to sheet width for downwards entrainment to take place.

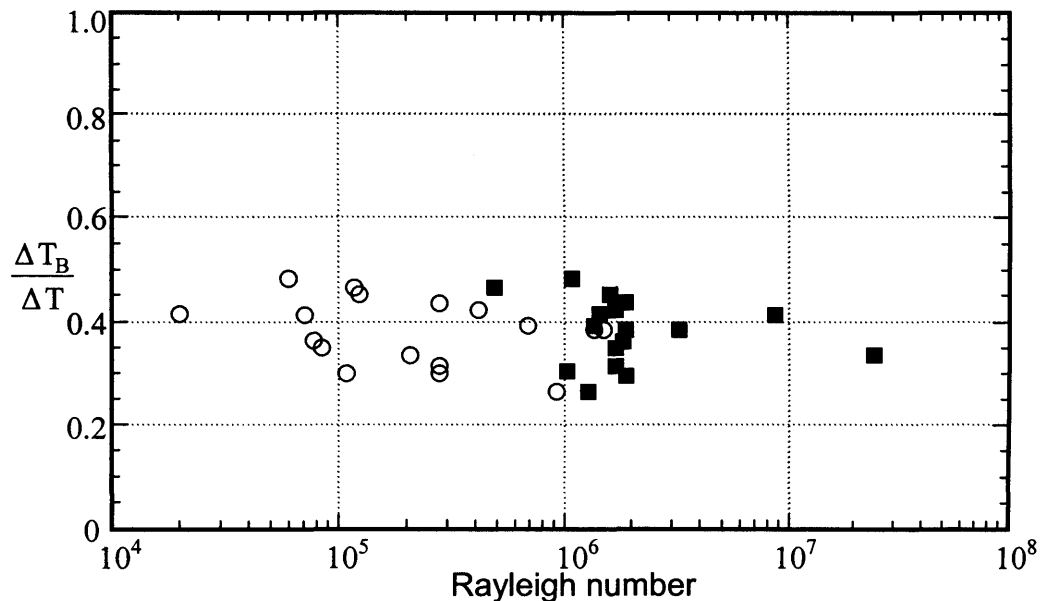


Figure 4.10

‘Thermochemical’ signal: amplitude of the interfacial temperature fluctuations as a function of the Rayleigh number. It is approximately constant and scales as $[0.38 \pm 0.06] \times \Delta T$. \circ lower layer \blacksquare upper layer.

Taken from Davaille [1999b]

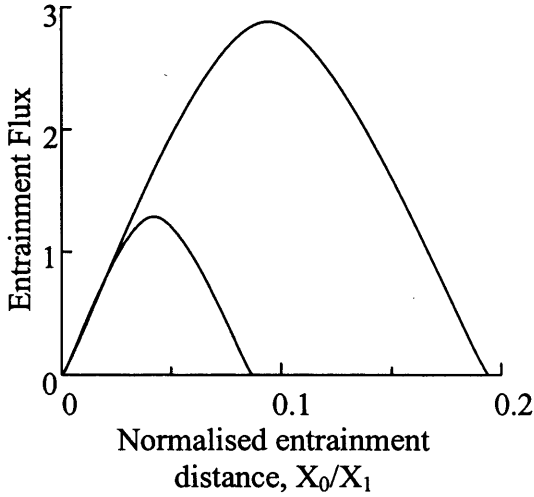


Figure 4.11

The flux of entrained material in arbitrary units is shown as a function of the entrainment distance for two normalized densities. The models were computed assuming two orders of magnitude viscosity variation with temperature. The curves are independent of the chemical density for small entrainment thickness. The broad maxima imply that small variations of the entrainment some distance away from the maximum do not greatly affect the estimated entrainment.

X_0 and X_1 are the entrainment and sheet thickness respectively. The lower curve shows a buoyancy ratio of 4 with the higher curve having a value of 2.

Taken from Sleep 1988

4.4.4 Comparing predicted entrainment with a numerical example

To test the scaling law derived by Davaille [1999b] and Gonnerman [2002] we ran a simulation and measured the change in volume of the layers. The case run used an icosahedron grid with 1,354,980 data points ($mt=64$; see section 3.3.3 Domain decomposition in TERRA). A denser layer is present with the interface between the two layers at 1000km depth[†] and a 4% density increase across the layer. We use the parameters in table 4.7 and equations 4.14 and 4.15 to predict the material flow over the boundary...

$$Q_{\uparrow} = C_1 \frac{\kappa h_0}{B^2} Ra_2^{1/2} ; Q_{\downarrow} = C_2 \frac{\kappa h_0}{B} Ra_1^{1/2}$$

$$B = \frac{\Delta\rho}{\rho\alpha\Delta T} ; Ra_{1,2} = \frac{\alpha g \rho \Delta T h_0^3}{\kappa \eta_{1,2}}$$

$$Q_{\uparrow} \text{ Plumes} = 0.0826 \text{ m}^3 \text{ s}^{-1} \text{ per cell}$$

$$Q_{\downarrow} \text{ Sheets} = 0.9173 \text{ m}^3 \text{ s}^{-1} \text{ per cell}$$

[†] This depth was chosen because it approximately agrees with the depth at which the two layers would have equal volume.

Dynamic viscosity of the upper layer	η_2	2.0×10^{22} Pa s
Dynamic viscosity of the lower layer	η_1	2.0×10^{22} Pa s
Gravitational acceleration	g	10 m s^{-1}
Volume coefficient of thermal expansion	α	$2.5 \times 10^{-5} \text{ K}^{-1}$
Thermal diffusivity	κ	$4.8 \times 10^{-7} \text{ m}^2 \text{ s}^{-1}$
Temperature difference across the mantle	ΔT	2000 K
Reference density	ρ	$5 \times 10^3 \text{ kg m}^{-3}$
Density contrast	$\Delta \rho$	$0.2 \times 10^3 \text{ kg m}^{-3}$ (4%)
Depth of the interface between the layers	$H-h_0$	1000 km
Depth of the mantle	H	2870 km
Buoyancy ratio B ($\Delta \rho \div \rho \alpha \Delta T$)	B	0.8
Rayleigh number of the upper layer	Ra_2	2.53×10^5
Rayleigh number of the lower layer	Ra_1	1.65×10^6

Table 4.7

Parameters used in the entrainment calculation

From this we would expect the lower layer to be gaining volume at a rate of $0.9173 - 0.0826 = 0.345 \text{ m}^3 \text{ s}^{-1}$ per cell. We have to decide how many cells will be present on the deformable boundary. Davaille uses the assumption that the Length scales of the cells are equal to the depth of the more viscous lower layer, in our case this is 1870km. The area of a cell would therefore be $1870 \text{ km} \times 1870 \text{ km} = 3.50 \text{ M km}^2$; the total area of the surface is $4\pi r^2 = 4\pi \times 4870000^2 = 362 \text{ M km}^2$; so we would expect $362 \div 3.50 = 104$ cells. We use this to find the total predicted rates of entrainment.

$$\begin{aligned}
 Q_{\uparrow} &= 0.0826 \text{ m}^3 \text{ s}^{-1} \text{ per cell} \\
 &= 0.0826 \times 104 \text{ m}^3 \text{ s}^{-1} = 8.5904 \text{ m}^3 \text{ s}^{-1} \\
 &= 8.5904 \times 60^2 \times 24 \times 365.25 \text{ m}^3 \text{ per year} = 2.70 \times 10^8 \text{ m}^3 \text{ per year} \\
 &= 2.70 \times 10^8 \times 10^{-9} \text{ km}^3 \text{ per year} = 0.270 \text{ km}^3 \text{ per year} \\
 Q_{\downarrow} &= 0.9173 \text{ m}^3 \text{ s}^{-1} \text{ per cell} \\
 &= 0.9173 \times 104 \text{ m}^3 \text{ s}^{-1} = 95.400 \text{ m}^3 \text{ s}^{-1} \\
 &= 95.40 \times 60^2 \times 24 \times 365.25 \text{ m}^3 \text{ per year} = 3.00 \times 10^9 \text{ m}^3 \text{ per year} \\
 &= 3.00 \times 10^9 \times 10^{-9} \text{ km}^3 \text{ per year} = 3.00 \text{ km}^3 \text{ per year}
 \end{aligned}$$

$$Q_{\uparrow} \text{ Plumes} = 0.2700 \text{ km}^3 \text{ per year}$$

$$Q_{\downarrow} \text{ Sheets} = 2.9997 \text{ km}^3 \text{ per year}$$

The total rate of change of volume of the lower layer predicted by Davaille's equations for our case we have run is therefore $2.9997 - 0.2700 = 2.73 \text{ km}^3$ per year

We cannot measure material flow over the deformable interface directly. We can however measure the change in volume of the lower layer during a run. The observed run and predicted rates are displayed in figure 4.12. Initially there is a rapid distortion

of the deformable boundary and a rapid change in its volume. After 100,000 years the system has settled into what appears to be a quasi steady state with the volume of the lower layer increasing at a reasonably constant rate. By fitting a least square line to the volume of the lower layer between 1 and 4 G years we arrive at a rate of change of volume of 9.018 km^3 per year. This compares with a predicted rate of entrainment of 2.730 km^3 per year from Davaille's equations. This agreement is good enough for us to concede that the equations 4.14 & 4.15 cannot be dismissed on the strength of these results.

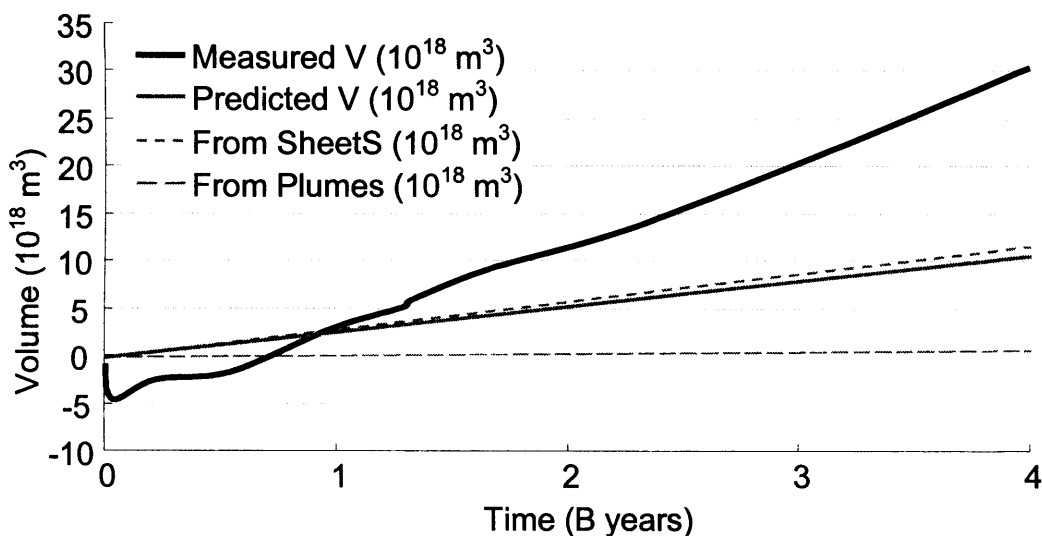


Figure 4.12

The change in volume of the lower layer of a layered system during a simulation. The observed change in volume is shown as a solid black line. The change in volume predicted using Davaille's entrainment calculations.

We have seen that entrainment in Earth's mantle is small and does not significantly affect convection [section 4.4.2, Davaille 1999b, Gonnerman et al. 2003, Zhong & Hager 2003, Sleep 1988]. However, over long time spans entrainment can cause the volume of a deep layer to change. In our simulations we are forced to model the mantle over hundreds of billions of years. This is due to the long time taken for a system to reach a quasi-steady state [see section 5.4]. Unfortunately over these time-spans we find that the entrainment would affect the system. Since this is not a process we are interested in studying we radially rescale the heights of the markers to remove the effects of entrainment, keeping the volumes of the layers constant. If this were not

performed the system would never reach a steady state and we would not be able to comment on the stable thermal structure of a layered mantle.

4.4.6 A simple constraint on entrainment from a deep layer

If we consider a deep layer present in the mantle today we must account for its continued existence since the Archaean. If material is being entrained from a deep layer in to the upper mantle the amount of material entrained in the last 4.2 G years cannot be sufficient to disperse the layer. We investigate this further by making a number of assumptions. Firstly, we assume the rate of entrainment has been constant. Secondly, that the initial depth of the layer was 670km[†]. Thirdly, that in last 4.2 G years the lower layer has retreated to the CMB.

Assuming a layer has retreated from 670km to the CMB over the last 4.2 G years. E = Volumetric entrainment rate.

$$E = \frac{\text{Total volume lost}}{\text{Time}}$$

$$E = \frac{\frac{4}{3}\pi(6.37 \times 10^6 - 6.60 \times 10^5)^3 - \frac{4}{3}\pi(6.37 \times 10^6 - 2.80 \times 10^6)^3}{4.2 \times 10^9}$$

$$E = 1.4 \times 10^{11} \text{ m}^3 \text{ year}^{-1} = 143 \text{ km}^3 \text{ year}^{-1}$$

Present day convection is expected to be less vigorous than convection in the Archaean so we would equally expect past entrainment to be more efficient than present entrainment. We can therefore probably consider the value of entrainment of 143km³ year⁻¹ as the top end estimate of present day entrainment from a deep layer.

[†] This is unrealistic since the upper layer in today's mantle would contain too much of the entrained material. However, we are looking at an end member case.

5 The effect of the heating mode on layered convection

There are a number of physical processes that will affect the nature of a layered convecting system: e.g. the density and viscosity contrast [Davaille et al. 2003], the depth of the interface [Le Bars & Davaille 2004], the vigour of convection [Davaille 1999a], and the value of the coefficient of thermal expansion of the lower layer. In this section we look at the effects of changing the depth and density contrast of the lower layer and the heating mode used to drive the system. We have chosen to investigate only these three effects for mainly practical reasons. Incorporating a viscosity increase across the interface between the two layers would mean activating the part of the TERRA code that is used for temperature dependent viscosity. This is not very stable and frequently causes TERRA to crash. A sharp viscosity increase (such as a chemical boundary) would add to these problems. Changing the coefficient of thermal expansion of the layers would mean making substantial alterations to the TERRA code. The case of increasing the vigour of convection is dealt with in the next chapter.

5.1 Producing initial cases for layered convection models

An initial temperature field is the field applied at the beginning of a simulation. We require an initial temperature field that is suitable for layered convection simulations. The main requirement is that the thermal field should not have anomalies that are so large that they produce an immediate overturn of the layered system and therefore destroy any layering. In this section we describe the method used to produce the initial temperature field that was used by the layered mantle convection models. We also discuss unsuccessful methods of producing initial temperature fields that were explored.

The TERRA program can produce a number of initial temperature fields using mathematical formulae; spherical harmonic functions of variable degree and order as well as random functions can be used. It would be possible to apply a spherical harmonic temperature field and start a simulation with a deformable boundary. However, if this is done the calculation is very unlikely to finish. As we discussed in section 4.2.2 the introduction of an active boundary causes the TERRA code to run slower than in an unlayered case. Consequently it takes much longer (in wall clock time) for a layered case to move away from the initial spherical harmonic field than an unlayered case. In many cases when a spherical harmonic temperature field is used

directly with an active layer in place the multi-grid method used by TERRA to find the velocity field is unable to find a solution and the TERRA program crashes. When this happens I will say that the calculation has ended with a multi-grid problem.

Spherical harmonic temperature fields used by TERRA have large amplitudes since they are designed to kick start convection. However, when layered mantle convection is present this has the effect of pulling the layer apart. To correct for this a smaller amplitude can be used but this can be so small that convection is not efficiently started and TERRA crashes with a multi-grid problem.

Alterations were made to the TERRA code to allow for a layered spherical harmonic field to be applied in both layers. In the temperature fields investigated the spherical harmonic temperature fields in the upper and lower layers had the same degree and were arranged so that thermal anomalies were anti-symmetrical across the interface between the two layers. However, this method did not work. The system would either immediately over turn or else TERRA would crash with the multi-grid problem. To produce an initial temperature field the marker surface is turned off and we allow the mantle to convect as a single layer. An initial temperature field with $l=8$ and $m=4$ was applied and system was allowed to convect for several hundred overturns until all trace of the initial temperature field was removed. The system had reached a steady-state with whole mantle convection. Initial temperature fields produced in this way only very occasionally crashed due to the multi-grid problem once layered convection was introduced. If this did happen it was nearly always when layering is introduced with a large density increase at the deformable boundary. In these cases a successful initial case can be produced by applying a layer with a smaller density increase and then allowing convection to take place for a short time (around half an over turn of the system). The thermal field produced will then work at the higher density increase.

All attempts to use a spherical harmonic temperature field as an initial condition for a layered mantle convection simulation were unsuccessful. Instead the initial temperature field used for layered convection was a steady-state whole mantle convection temperature field.

5.2 Changes in the interfacial area once the system has reached a quasi-steady state

When a TERRA simulation ends, several variables and parameters are outputted. If the system has reached a quasi steady state we can use these values to represent the system and compare cases. However in a quasi-steady state, variables are not fixed but oscillate around a mean value (a process to explain this behaviour is examined in section 5.4 the thermal evolution of the system). It is this mean value that we should use when comparing variables from different simulations. Not all variables are outputted during a simulation and so it is useful to know the amplitude and form of these oscillations.

To investigate the effect of oscillations of variables we measured the value of the non-dimensional area variable ϕ throughout a series of runs. These runs were started from an initial case that was produced in the normal way (see section 5.1). The simulations were allowed to convect until a quasi-steady state had been reached. The cases presented here had a Rayleigh number of 2×10^4 and had radially dependent viscosity. A full description can be seen in section 6.1 and table 5.1.

Parameter		Value
Outer shell radius	R_S	6.370×10^6 m
Inner shell radius	R_{CMB}	3.500×10^6 m
marker surface shell radius	R_K	4.370×10^6 m
Temperature of surface	T_S	1060 K
Temperature of CMB	T_{CMB}	3000 K
Density of the upper layer	ρ_u	5.00×10^3 kg
Density of the lower layer	ρ_l	$5.05 - 5.24 \times 10^3$ kg
Density contrast	$\rho_l - \rho_u / \rho_u$	1.0 - 4.8 %
Dynamic viscosity	η	8.25×10^{22} Pa s
Rate of internal heating	q_{rad}	0.450×10^{-12} W m ⁻³ kg ⁻¹ (with internal heating)
Thermal conductivity	k	2.4 W m ⁻¹ K ⁻¹
Gravitational acceleration	g	10 N kg ⁻¹
Volume coefficient of thermal expansion	α	2.0×10^{-5} K ⁻¹
Specific heat at constant volume	C_V	1×10^3 J kg ⁻¹ K ⁻¹

Table 5.1

The parameters used in the convection simulations presented in this section.

Consider in detail one example when the density increase across the interface was 3.0%. The size of ϕ throughout the run before and after a quasi-steady state had been reached can be seen in figure 5.1. Initially the deformable boundary is a spherical

surface and so its surface area increased as convection causes deformation. The system appears to reach a quasi-steady state somewhere between 50 and 100 G years into the simulation. Once this state has been reached there continues to be fluctuations in φ , however these are small and are centred on a mean value.

There are several features worthy of comment in figure 5.1a. The non-dimensional area variable increases in size consistently once the simulation has begun and then fluctuates around a stable value. There is no initial rapid distortion of the deformable boundary followed by a recovery phase. This is significant because it suggests that the initial case does not have a thermal structure that causes the layer to break apart. In cases in which this occurs the system may be able to find a quasi steady state but the initial condition contains thermal anomalies that are too severe. A more surprising feature is the sudden decrease in the value of φ that occurs several times (at $\sim 200, 325$ & 370 G years) once the system has reached a quasi steady state. This is the opposite to the expected behaviour where one would predict seeing a rapid increase in φ when up-welling (plumes) or down-welling (plates) material impact with the deformable boundary. The nature of a process that could cause this behaviour is unclear. We will speculate that it could be caused by the sudden migration of hot material from above a doming region. This would then rapidly be replaced by colder denser material that would cause the retreat of the dome.

To measure the size of variations of φ the mean and standard deviations of the run were calculated once it had reached the quasi-steady state. This was judged to have happened after 90.3 G years (5000 iterations).

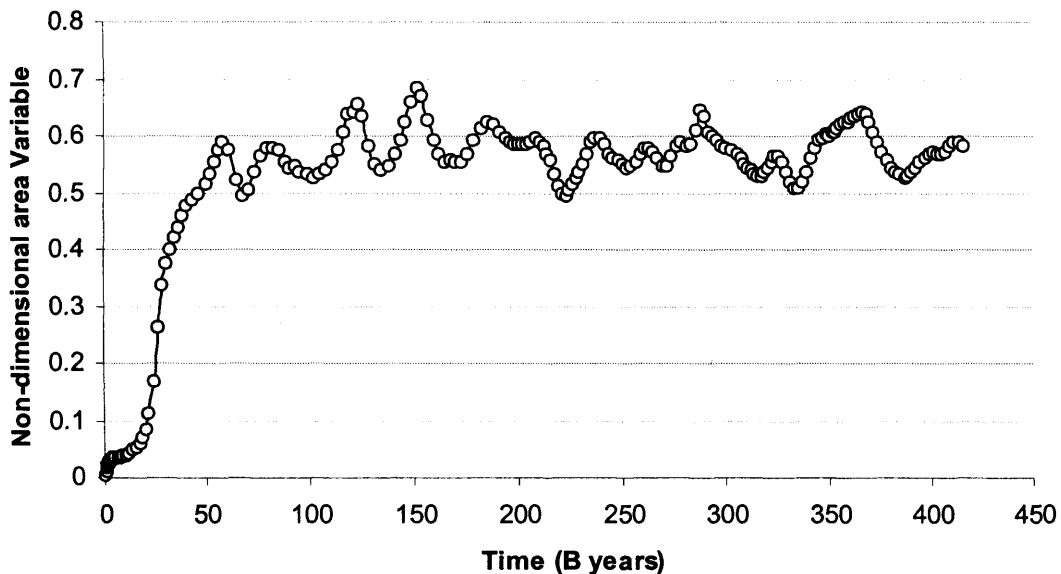
The mean value was found to be 0.591 with a standard deviation of 0.038. A histogram of the frequency of the values of φ was also found and is shown in figure 5.1b. This shows that the deviation of φ from the average value has an approximately Gaussian distribution.

$$G(x) = \frac{1}{\sigma\sqrt{2\pi}} e^{-(x-\mu)^2/(2\sigma^2)} \quad (5.1)$$

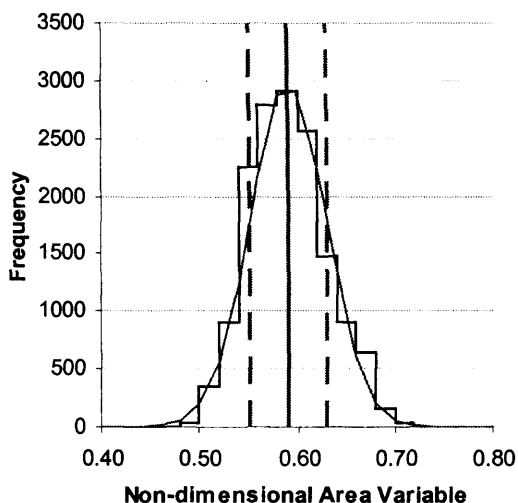
Where $G(x)$ is the Gaussian distribution, σ is the standard deviation and μ is the mean.

We now consider a series of simulations with only the chemical density contrast across the deformable interface changing. We find that as the density of the lower layer

increases the mean value of the non-dimensional area variable ϕ decrease showing that the layer is becoming flatter (see sections 5.5 & 6.4). As long as the layered system is stable the variation of ϕ from its mean value remains Gaussian. The standard deviation from the mean value however increases as the density contrast decreases. This suggests that as the density of the lower layer becomes lighter the interface between the two layers becomes more dynamic with larger amplitude distortions. When the system moves away from a stratified regime the distribution is not gaussian and large variations ($\sim 2.6\text{-}3.0\%$) are seen. See figure 5.2.



a,



b,

Figure 5.1

a, The variation of the non-dimensional area variable during a simulation with the deformable boundary at 2000km with a density increase of 3% across it. Initially the boundary is set as a spherical shell.

b, The frequencies of the values of the non-dimensional area variable ϕ once the system has reached a quasi-steady state. The black line shows the frequency of each value of ϕ . The thick grey line shows the mean values of ϕ while the dashed lines represent the mean \pm the standard deviation of ϕ . The thin grey line shows the Gaussian distribution that corresponds to the same values of the mean and standard deviation.

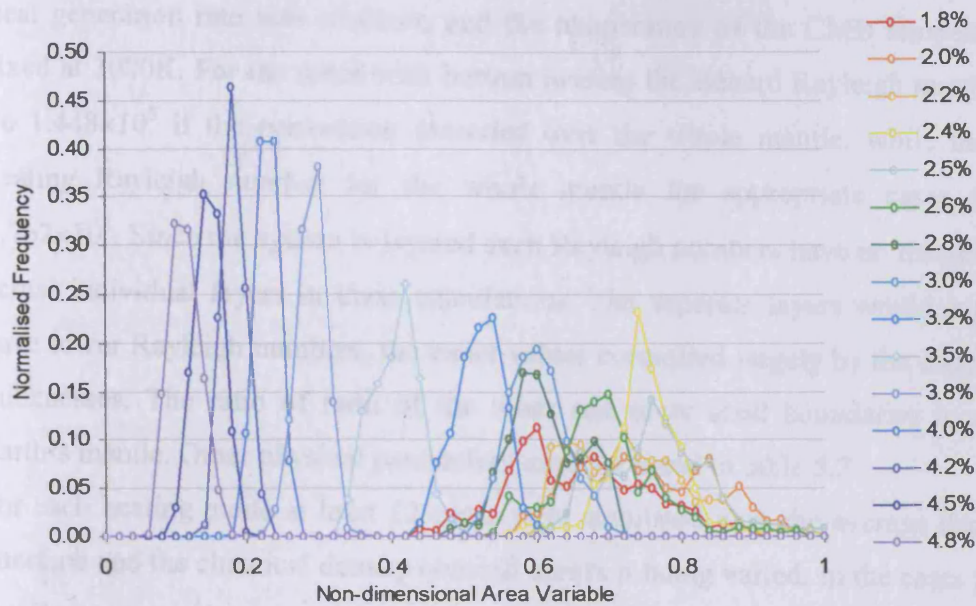


Figure 5.2

A series of histograms showing the change in the non-dimensional area variable as the density increase across the deformable interface varies. The y-axis represent the frequency (i.e. the number of time steps in a calculation) in which ϕ had a particular value. A rainbow colour scale is used to represent change in as the density increase across the deformable interface: red – light; violet – Heavy.

5.3 Cases studied

We simulated layered systems with a mantle-like geometry with three different heating modes. In the first mode only internal heating was present to drive convection (e.g. simulating radioactivity and /or secular cooling). In these cases the value of the local internal heating ($0.450 \times 10^{-12} \text{ W kg}^{-1}$) was kept the same in both the upper and lower layers. A boundary condition of zero heat flux was applied at the lower shell boundary. Consequently while the heat energy generated per unit volume within the lower layer was constant for each case simulated the total energy generated in the lower layer varied with its volume. In the second heating mode only bottom heating was active (simulating heating by the core across the core-mantle boundary (CMB)). In these cases the temperature of the CMB was kept fixed at 3000K. Since the internal temperature and the thickness of the thermal gradient at the CMB varied, so too did the heat energy entering the lower layer in this mode. The third mode was a combination of the previous two modes, i.e. it had both internal and bottom heating applied. Again in these

cases the total heat entering the system varied between cases. In this mode the local heat generation rate was constant, and the temperature of the CMB temperature was fixed at 3000K. For the cases with bottom heating the Bénard Rayleigh number would be 1.448×10^5 if the convection extended over the whole mantle; while the internal heating Rayleigh number for the whole mantle for appropriate cases would be 5.762×10^5 . Since the system is layered such Rayleigh numbers have no meaning for the actual individual layers in these calculations. The separate layers would individually have lower Rayleigh numbers, the exact values controlled largely by the different shell thicknesses. The ratio of radii of the inner and outer shell boundaries is similar to Earth's mantle. Other physical parameters used are listed in table 5.2.

For each heating mode at least 12 cases were simulated with the average depth of the interface and the chemical density contrast across it being varied. In the cases presented the Boussinesq approximation was used for an incompressible fluid. The viscosity, thermal conductivity and the volume coefficient of thermal expansion were kept constant with depth. The velocity boundary condition on both the upper and lower shells was free slip.

Parameter		Value
Outer shell radius	R_S	6.370×10^6 m
Inner shell radius	R_{CMB}	3.500×10^6 m
Depth of marker surface	D_K	500, 1000, 1500, 2000 & 2500 km
Temperature of surface	T_S	1060 K
Temperature of CMB	T_{CMB}	3000 K (In cases where bottom heating was active)
Density of the upper layer	ρ_u	5.00×10^3 kg
Density of the lower layer	ρ_l	$5.05, 5.10, 5.15, 5.20$ & 5.25×10^3 kg
$\Delta\rho/\rho$		1, 2, 3, 4 & 5 %
Dynamic viscosity	η	4.125×10^{23} Pa s
Rate of internal heating	q_{rad}	0.450×10^{-12} W kg ⁻¹ (with internal heating)
Thermal conductivity	k	2.4 W m ⁻¹ K ⁻¹
Gravitational acceleration	g	10 N kg ⁻¹
Volume coefficient of thermal expansion	α	2.0×10^{-5} K ⁻¹
Specific heat at constant volume	C_V	1×10^3 J kg ⁻¹ K ⁻¹

Table 5.2

The parameters used in the calculations presented in this chapter. The effects of varying the depth of the deformable boundary and the density of the lower layer were studied and several values are listed for these parameters. Different heating modes were also used, and in the cases when there was bottom heating the lower boundary was insulating.

Depth	Heating mode		
	Bottom	Both	Internal
500km	$\Delta\rho=2,3,4,5$	$\Delta\rho=2,3,4,5$	$\Delta\rho=1,2,3,4,5$
1000km	$\Delta\rho=2,3,4,5$	$\Delta\rho=2,3,4,5$	$\Delta\rho=1,2,3,4,5$
1500km	$\Delta\rho=2,3,4,5$	$\Delta\rho=2,3,4,5$	$\Delta\rho=1,2,3,4,5$
2000km	$\Delta\rho=2,3,4,5$	$\Delta\rho=2,3,4,5$	$\Delta\rho=1,2,3,4,5$
2500km	$\Delta\rho=2,3,4$	$\Delta\rho=2,3,4$	$\Delta\rho=1,2,3,4$

Table 5.3

An overview of the cases simulated that are presented in this chapter. A range of depths and density contrasts (%) across the deformable interface ($\Delta\rho$) were simulated for three different heating modes.

The lab experiments of Davaille [1999a] can be used to predict the behaviour of our simulations. The location of our experiments on the graph (labelled with heating mode) shows that we expect to be in the stratified regime for $B > 0.5$ (see section 2.7.1 and equation 2.10 for a definition of the buoyancy ratio B). In these cases the buoyancy ratio is defined entirely by input parameters and so can itself be considered an input parameter. The grey diagonally striped line show experiments in which only internally heating was present. The temperature of the CMB was able to vary during the experiment. As a result the temperature contrast across the mantle changed. The values of the buoyancy ratio presented here used the temperature contrast once the system has reached a steady state. For these internally heated cases the buoyancy ratio must be thought of as an output value of the experiment.

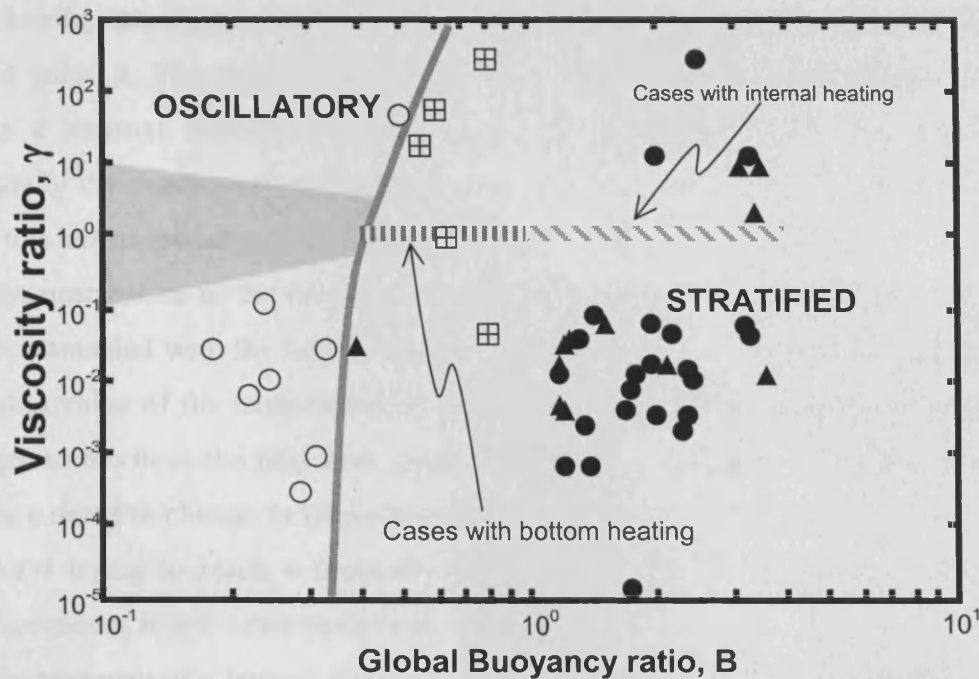


Figure 5.3

The behaviour of layered convecting systems as a function of the buoyancy ratio B and the viscosity ratio γ for 3D Cartesian geometry adapted from figure 2 of Davaille [1999a]. The grey vertically striped line shows the experiments in which bottom heating is present

5.4 The thermal evolution of layered convection

As we have discussed in sections 5.1 and 5.2 a layered convection simulation is started with a thermal temperature field that is a steady state solution for whole mantle convection with a similar Rayleigh number.

When layered convection is initiated there is no thermal boundary at the interface between the two layers. For the layered system to exist in a quasi-steady state, heat energy entering each layer must approximately equal the heat energy leaving it. In our cases heat energy enters the lower layer either through the thermal boundary at the CMB, from radioactive decay or from both of these heat sources. Heat energy can only leave the lower layer by means of conductive cooling across the deformable boundary. The initial lack of a thermal boundary at the interface means that the lower layer is gaining heat faster than it loses it. Consequently the mean temperature in the lower layer increases. Equally, the upper layer must also be thermally balanced. Heat energy will enter the layer across the thermal boundary at the deformable interface, from radioactive heating or from both these heat sources. Since there is initially very little

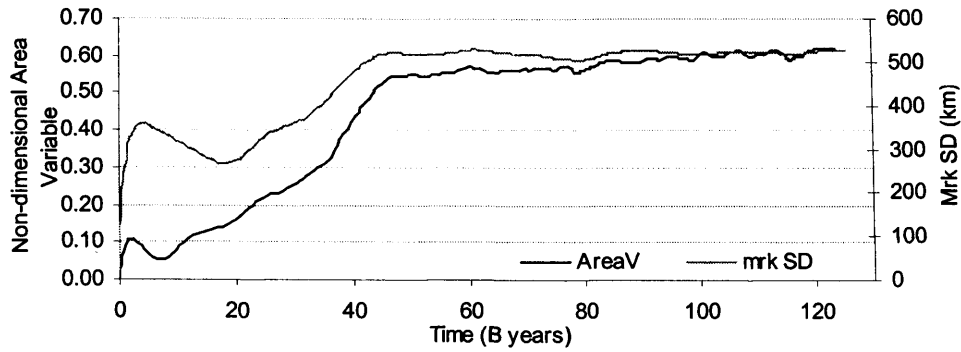
heat flowing across the deformable interface the upper layer loses heat energy faster than it gains it. The upper layer cools down while the lower layer warms up. This causes a thermal boundary to develop at the interface between the two layers. Eventually the system will reach a state in which both layers are thermally balanced. Once this has happened we say the layered system is in a quasi-steady state.

The dynamic nature of the interface between the two layers causes oscillations in most values associated with the layered system such as the surface area of the interface and the mean value of the temperature in both layers. As the surface area of the interface changes so too does the heat flow across it and so the temperature increase across the interface needs to change to keep the system thermally balanced. In this way the system is always trying to reach a thermally balanced state but the dynamic nature of the interface means it will never achieve it completely.

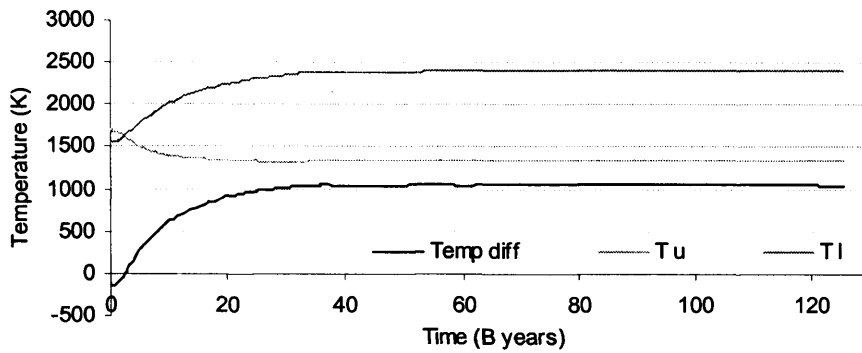
The development of a layered system to a quasi steady state is shown in figure 5.4. We see as the system leaves the initial case the upper layer cools; the lower layer warms and consequently the temperature increase across the deformable increases. The temperature difference tends towards a value of 1050K, which it reaches after around 30 G years. The heat flow over both the surface and core mantle boundary decrease when layering is introduced and have reached a constant values after around 30 G years. The layer is initially a flat spherical shell and its surface area increases until it reaches a stable value after 50 G years. It is interesting that the increasing surface area seems to lag behind the thermal structure of the system. We will offer two possible reasons as to why this could be the case. The thermal structure may dictate the deformation of the boundary between the two layers and the lag could be an adjustment time of the system. Equally we could argue that amplitude of the deformation of the deformable interface stops increasing after 40 G years. The surface area of the interface continues to increase since small-scale features might be still developing on the interface. If these features have amplitudes that are smaller than the thickness of the thermal boundary then they will have no effect on the heat flow over the interface. However we can rule out this second explanation since the standard deviation of the marker heights continues to increase after 30 G years (see figure 5.4a). If the surface area were only increasing in size because of small-scale features then the standard deviation of the marker heights would remain constant.

If we accept the first suggestion that the size of the thermal anomaly across the deformable interface dictates the deformation of the boundary then we can continue

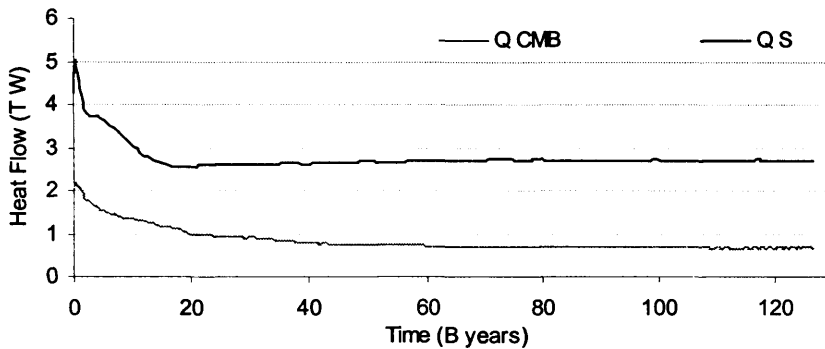
this train of thought to determine a means by which a layered system will organise itself towards a steady layered state. We consider a layered system in a steady state with a thermal structure that produces a balanced heat flow across the CMB, the chemical boundary and the surface. If we increase the surface area of the interface then since the thermal structure has not changed the total heat flow across the boundary will increase. The lower layer is now losing heat energy faster than it is gaining it and so it cools down, likewise the upper layer warms up. This produces a decrease in the temperature increase across the layer. A decreased thermal contrast will increase the density increase across the layer and so the negative buoyancy of the lower layer. This results in less deformation of the now less buoyant lower layer and so the surface area of the interface decreases. So an increase in the surface area of the interface will feed back into the system to decrease the surface area of the interface and the system will self organise itself to have a particular thermal structure and surface area. See figure 5.5.



a,



b,



c,

Figure 5.4

An example of the development of a quasi-steady state in a layered convection simulation.

a, The increasing surface area (areaV) of the deformable boundary with time and the standard deviation of the marker heights (mrk sd) which is plotted on the right y-axis.

b, The thermal development of the layered system. T_u & T_l are the temperatures in the upper and lower layers respectively. Temp diff is the difference between these two temperatures.

c, The total heat energy flowing over the Core Mantle Boundary and Surface.

The case shown is presented in detail in the next chapter. It had Rayleigh number of 3.4×10^4 , and a deformable boundary at 1500km depth with a 3.4% density increase across it, both internal and bottom heating were present in the system.

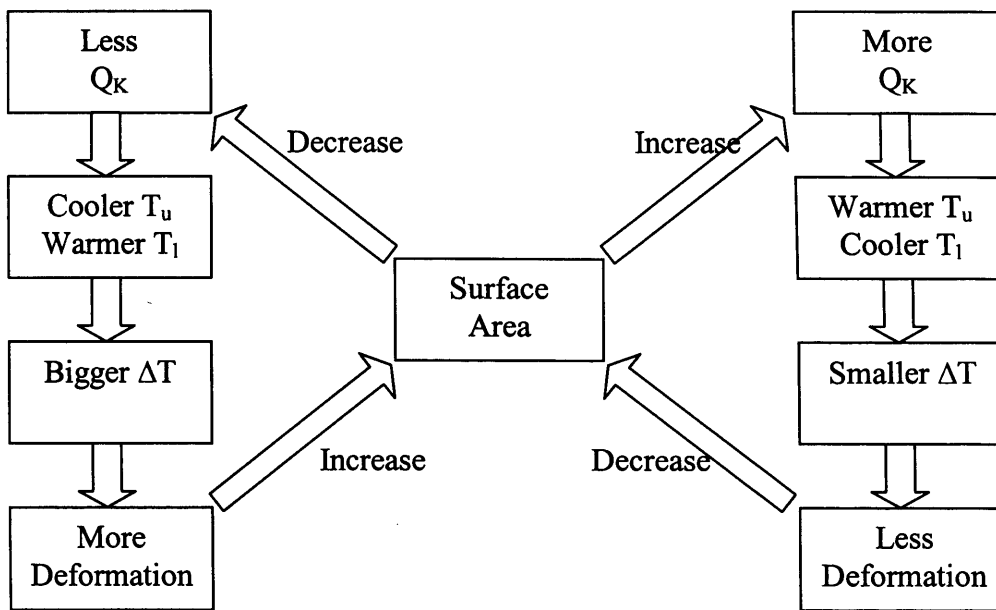


Figure 5.5

A suggested process by which a layered convecting system keeps itself thermally balanced. A change in the surface area of the interface between the two layers will feed back into the system to correct for the change and keep the surface area of the layer and the thermal structure of the system at certain stable values.

5.5 Results

Full results of the simulations presented in this chapter are displayed in table 5.4 & 5.5.

The amplitude of the interface's undulations reached a maximum in cases where the layer was in the upper mid-mantle. At this depth (around 1050km) the volume of the two layers was equal with each being 50% of the total volume of the mantle.

High peaks in the deformable boundary had two forms. The first was a large dome that had a hot region below it and was caused by the buoyant uprising of the hot material. The second were cusped ridge structures that were caused by the presence of cold subducted material above the boundary. Cold material that had descended in slab form from the surface built up in 'packets' over the deformable boundary and often caused depressions in it. Where two of these 'packets' pressed together the deformable boundary was squeezed into a cusped ridge.

5 The effect of the heating mode

Heating mode	Depth (km)	$\Delta\rho$ %	Stable ?	Non-dimensional Area Variable	T_u (K)	T_l (K)	ΔT (K)
Internal	500	1	n	0.14	1324.55	1618.28	293.73
Internal	500	2	y	0.04	1318.33	2017.33	699.00
Internal	500	3	y	0.02	1372.75	2188.75	816.00
Internal	500	4	y	0.01	1373.58	2199.58	826.00
Internal	500	5	y	0.01	1235.48	2072.48	837.00
Internal	1000	1	n	0.93	1378.30	1719.44	341.14
Internal	1000	2	y	0.16	1405.75	1919.75	514.00
Internal	1000	3	y	0.05	1422.58	1974.58	552.00
Internal	1000	4	y	0.03	1416.25	1998.25	582.00
Internal	1000	5	y	0.01	1412.23	1987.23	575.00
Internal	1500	1	n	1.30	1430.94	1714.08	283.14
Internal	1500	2	y	0.09	1444.35	1777.35	333.00
Internal	1500	3	y	0.02	1456.86	1796.86	340.00
Internal	1500	4	y	0.01	1456.55	1795.55	339.00
Internal	1500	5	y	0.01	1456.59	1792.59	336.00
Internal	2000	1	n	0.72	1479.81	1652.54	172.72
Internal	2000	2	y	0.08	1536.89	1731.89	195.00
Internal	2000	3	y	0.02	1547.99	1720.99	173.00
Internal	2000	4	y	0.01	1546.60	1718.60	172.00
Internal	2000	5	y	0.01	1547.32	1713.32	166.00
Internal	2500	1	n	0.59	1499.23	1505.56	6.33
Internal	2500	2	y	0.08	1513.08	1560.08	47.00
Internal	2500	3	y	0.03	1518.27	1560.27	42.00
Internal	2500	4	y	0.02	1514.72	1568.72	54.00
Bottom	500	2	n	0.21	1211.32	1612.19	400.87
Bottom	500	3	n	0.16	1282.43	1843.31	560.89
Bottom	500	4	y	0.07	1315.31	2028.31	713.00
Bottom	500	5	y	0.06	1334.67	2109.67	775.00
Bottom	1000	2	n	0.56	1266.14	1772.82	506.68
Bottom	1000	3	y	0.34	1364.11	2099.11	735.00
Bottom	1000	4	y	0.13	1361.59	2162.59	801.00
Bottom	1000	5	y	0.07	1369.34	2169.34	800.00
Bottom	1500	2	n	1.09	1359.67	1942.75	583.08
Bottom	1500	3	y	0.69	1380.96	2163.96	783.00
Bottom	1500	4	y	0.24	1342.98	2193.98	851.00
Bottom	1500	5	y	0.11	1338.50	2258.50	920.00
Bottom	2000	2	n	1.39	1416.31	2041.04	624.73
Bottom	2000	3	y	0.49	1325.51	2195.51	870.00
Bottom	2000	4	y	0.16	1308.30	2250.30	942.00
Bottom	2000	5	y	0.05	1288.97	2307.97	1019.00
Bottom	2500	2	n	1.29	1462.05	2220.93	758.88
Bottom	2500	3	n	1.01	1425.43	2290.43	865.00
Bottom	2500	4	y	0.22	1349.83	2345.83	996.00
Both	500	2	n	1.12	1657.65	2293.63	635.97
Both	500	3	y	0.38	1447.44	2231.44	784.00
Both	500	4	y	0.11	1480.99	2568.99	1088.00
Both	500	5	y	0.03	1502.41	2671.41	1169.00
Both	1000	2	n	1.46	1518.55	2098.69	580.14
Both	1000	3	y	0.56	1571.41	2466.41	895.00
Both	1000	4	y	0.19	1556.11	2552.11	996.00
Both	1000	5	y	0.06	1555.94	2590.94	1035.00
Both	1500	2	n	1.88	1438.43	1991.60	553.18
Both	1500	3	y	0.75	1614.67	2382.67	768.00
Both	1500	4	y	0.28	1586.02	2464.02	878.00
Both	1500	5	y	0.09	1585.24	2518.24	933.00
Both	2000	2	n	1.51	1593.07	2205.78	612.72
Both	2000	3	y	0.58	1614.05	2388.05	774.00
Both	2000	4	y	0.17	1599.02	2434.02	835.00
Both	2000	5	y	0.05	1605.53	2471.53	866.00
Both	2500	2	n	1.37	1772.16	2367.44	595.28
Both	2500	3	n	0.69	1751.84	2427.37	675.52
Both	2500	4	y	0.19	1706.11	2457.11	751.00
Hot	2000	5	y	0.02	1278.24	2282.61	1004.37

Table 5.4

Output from the cases simulated. The values shown are those outputted at the end of each simulation once the system has reached a quasi-steady state. Values in grey belong to cases where the marker method has (in our opinion) failed.

5 The effect of the heating mode

Heating mode	Depth (km)	$\Delta\rho$ %	Stable ?	Standard deviations of marker heights (km)	Q_{CMB} (T W)	Q_s (T W)	Nusselt N^{θ}
Internal	500	1	n	802	0.00	2.73	6.041
Internal	500	2	y	113	0.00	1.62	2.944
Internal	500	3	y	71	0.00	1.88	2.490
Internal	500	4	y	47	0.00	1.87	2.478
Internal	500	5	y	37	0.00	1.86	2.453
Internal	1000	1	n	670	0.00	1.87	4.620
Internal	1000	2	y	278	0.00	1.82	3.378
Internal	1000	3	y	93	0.00	2.02	3.109
Internal	1000	4	y	76	0.00	2.03	3.100
Internal	1000	5	y	56	0.00	2.03	3.700
Internal	1500	1	n	849	0.00	2.33	4.120
Internal	1500	2	y	137	0.00	1.99	3.847
Internal	1500	3	y	75	0.00	2.03	3.705
Internal	1500	4	y	47	0.00	2.03	3.718
Internal	1500	5	y	35	0.00	2.03	3.720
Internal	2000	1	n	706	0.00	2.14	4.439
Internal	2000	2	y	203	0.00	2.05	3.709
Internal	2000	3	y	97	0.00	2.03	3.823
Internal	2000	4	y	69	0.00	2.03	3.845
Internal	2000	5	y	52	0.00	2.03	3.887
Internal	2500	1	n	514	0.00	1.98	5.964
Internal	2500	2	y	202	0.00	2.04	5.193
Internal	2500	3	y	127	0.00	2.01	5.187
Internal	2500	4	y	102	0.00	2.02	5.106
Bottom	500	2	n	398	3.28	2.75	6.059
Bottom	500	3	n	282	2.79	2.79	6.139
Bottom	500	4	y	203	2.27	2.16	4.756
Bottom	500	5	y	170	2.00	2.07	4.544
Bottom	1000	2	n	667	2.75	2.42	5.321
Bottom	1000	3	y	456	2.05	2.01	4.414
Bottom	1000	4	y	308	1.88	1.88	4.146
Bottom	1000	5	y	200	1.88	1.88	4.146
Bottom	1500	2	n	778	2.38	2.17	4.763
Bottom	1500	3	y	525	1.87	1.86	4.096
Bottom	1500	4	y	328	1.82	1.82	3.997
Bottom	1500	5	y	187	1.86	1.87	4.112
Bottom	2000	2	n	734	2.63	2.45	5.396
Bottom	2000	3	y	419	1.66	1.66	3.655
Bottom	2000	4	y	198	1.61	1.61	3.537
Bottom	2000	5	y	104	1.62	1.59	3.507
Bottom	2500	2	n	623	3.52	3.17	6.967
Bottom	2500	3	n	496	3.31	3.12	6.862
Bottom	2500	4	y	294	2.14	2.08	4.580
Both	500	2	n	592	2.73	5.01	1.103
Both	500	3	y	347	2.10	4.10	9.030
Both	500	4	y	198	1.14	3.17	6.966
Both	500	5	y	116	1.23	3.25	7.149
Both	1000	2	n	711	2.22	3.77	8.284
Both	1000	3	y	485	1.27	3.26	7.165
Both	1000	4	y	323	1.17	3.21	7.056
Both	1000	5	y	162	1.23	3.25	7.149
Both	1500	2	n	848	1.70	3.84	8.446
Both	1500	3	y	553	1.27	3.30	7.263
Both	1500	4	y	322	1.27	3.30	7.261
Both	1500	5	y	183	1.29	3.31	7.282
Both	2000	2	n	771	1.93	4.11	9.045
Both	2000	3	y	460	1.19	3.22	7.078
Both	2000	4	y	211	1.15	3.16	6.958
Both	2000	5	y	119	1.14	3.16	6.951
Both	2500	2	n	387	2.60	4.78	10.810
Both	2500	3	n	238	2.19	4.17	9.180
Both	2500	4	y	238	1.60	3.63	7.977
Hot	2000	5	Y	70	0.00	1.51	

Table 5.5

Output from the cases simulated. The values shown are those outputted at the end of each simulation once the system has reached a quasi-steady state. Values in grey belong to cases where the marker method has (in our opinion) failed.

For **bottom heated** cases the total heat entering the lower layer ranged between 1.822×10^{12} W and 3.519×10^{12} W with the most heat being added in cases when the chemical boundary was deeper in the mantle and had a smaller density contrast across it. This variation in heat input was caused by different temperature gradients across the CMB. The size of the temperature gradient was determined by the temperature of the lower layer; the hotter the lower layer the less heat was conducted into it since the temperature of the CMB was fixed at 3000K. The largest temperature contrasts across the deformable boundary were seen when the boundary was deeper in the mantle and $\Delta\rho$ was larger. Explaining this variation in the temperature contrast is a two-stage process. The greater temperature contrast for deeper layers can be explained by considering the surface area of the layer. Since heat can only leave the layer by conduction then the larger its surface-area the less need for a larger temperature contrast. For a deeper layer the surface area is smaller and so a larger thermal boundary is needed. The increase in the temperature contrast with the chemical density contrast across the deformable boundary is explained by considering that less-dense layers had undulations with larger amplitudes and hence a greater surface area over which they could conduct heat. This is complicated further by the fact that the amount of heat entering the lower layer is not the same for all cases. Since the temperature of the CMB and the surface are fixed the system must thermally balance itself by arranging values of the average temperature in the upper and lower layers such that the heat flux across all three boundaries is equal.

For cases where the layer is placed deep in the mantle at a depth of 2500km the distortions of the interface are so large that sections of the boundary are pressed against the CMB. As a result some heat flux from the CMB is transferred directly to the upper layer. Consequently the temperature contrast across the two layers is not as large as one would expect from extrapolating results in the mid-mantle. Likewise in cases where the layer is placed in the upper-mantle (500km depth) undulations can press sections of the interface against the surface resulting in a colder lower layer and very high heat flow at these surface regions.

For the **internally heated** cases internal heating was active in both the upper and lower layer and so the total heat generated in the system was constant at 2.032×10^{12} W. However, heat generated in the lower layer ranged between 0.14×10^{12} W and

1.50×10^{12} W. Cases were found to be stable with the amplitude of undulations being relatively small. The lower layer had little to no lateral thermal heterogeneities. This is presumably caused by the lack of a thermal boundary at the CMB that could drive convection in the lower layer. The topography of the deformable boundary was dictated by the presence of cold material from above. Altering only the density contrast had little effect on the temperature contrast across the interface. There is little change in the amplitude of the undulations and so likewise there is little effect on the surface area to cause a change in the size of the thermal gradient.

When the interface was placed deep in the mantle it had a smaller volume and so less heat was generated in it relative to cases where the interface was higher in the mantle. This can be seen by the fact that deeper interfaces require a smaller thermal contrast across the deformable boundary.

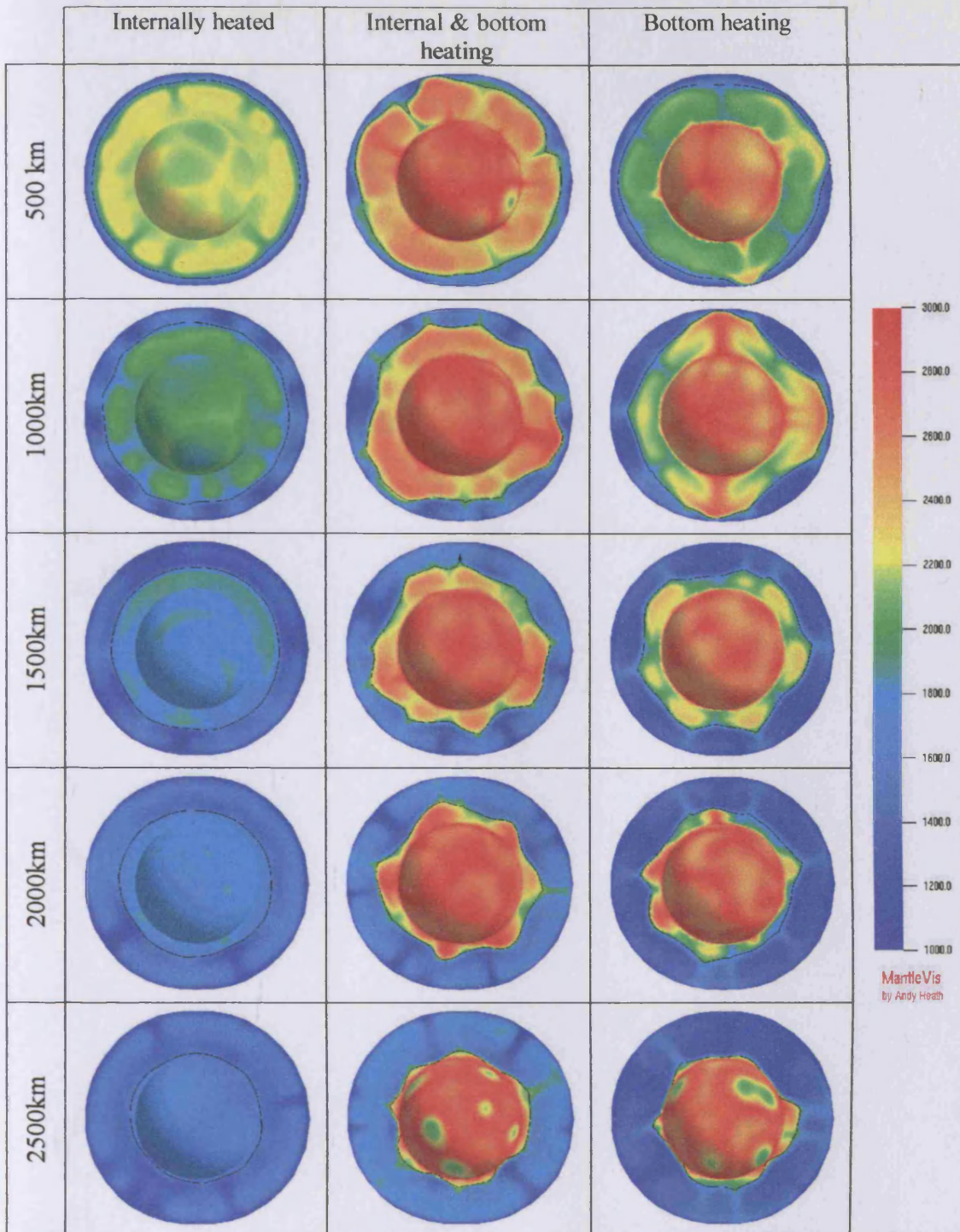


Figure 5.6

Temperature fields for cases with a 4% density increase across the deformable interface. All three heating modes are shown for the 5 different depths at which the layer's boundary was modelled.

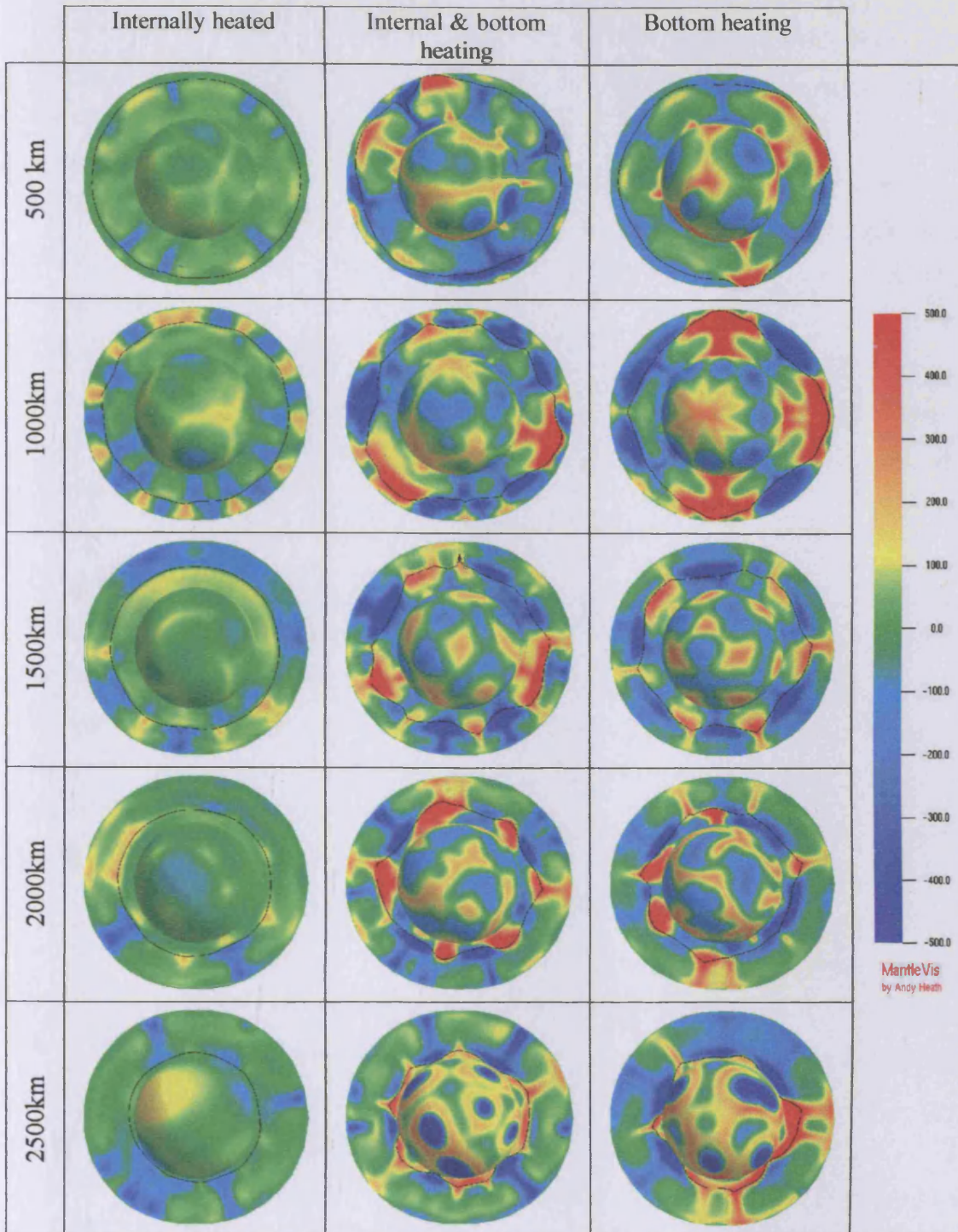


Figure 5.7

Temperature field with the radial average temperature removed for cases with a 4% density increase across the deformable interface. All three heating modes are shown for the 5 different depths at which the interface was modelled.

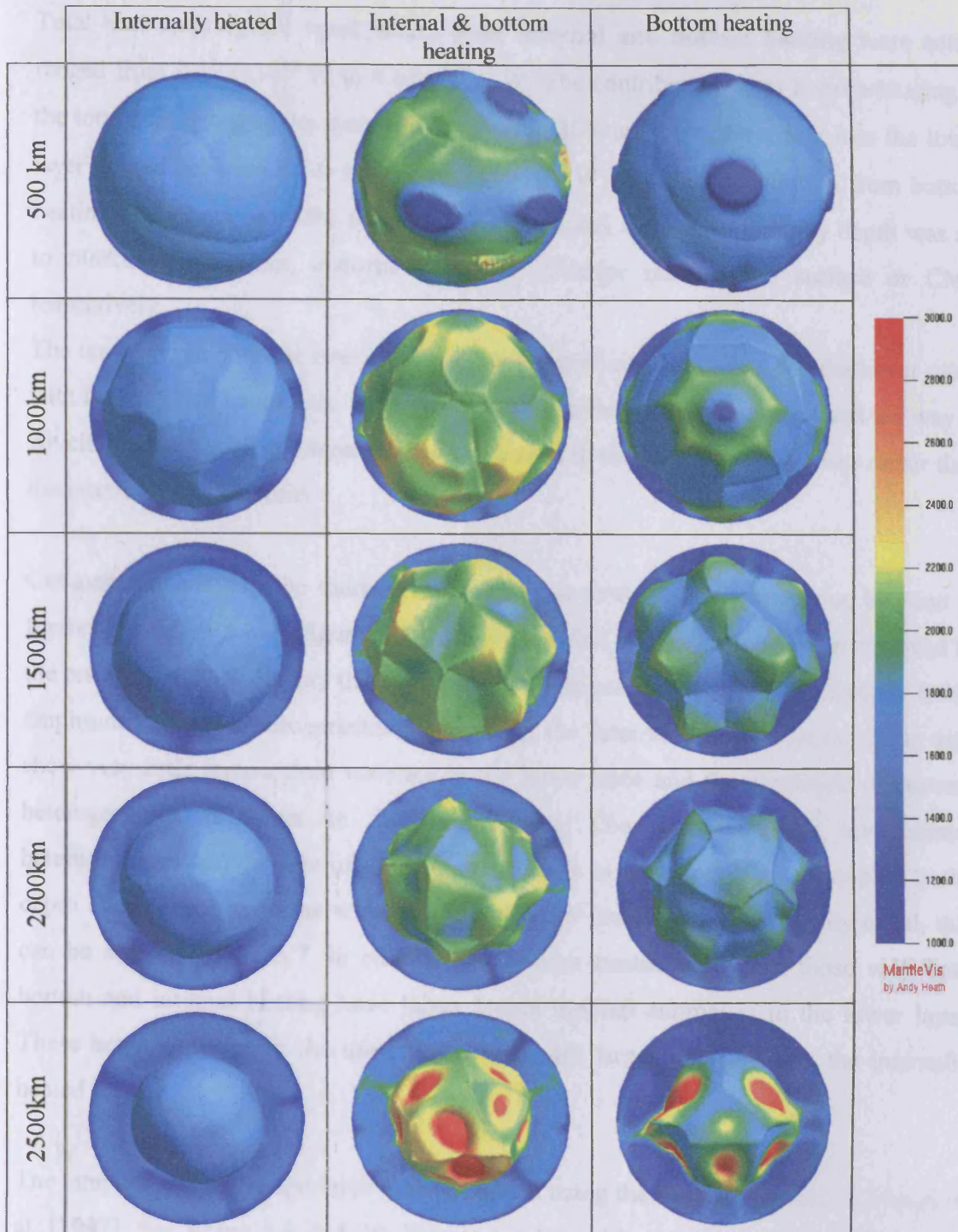


Figure 5.8

Temperature field for cases with a 4% density increase across the deformable interface with the deformable boundary shown. All three heating modes are shown for the 5 different depths at which the interface was modelled. The results shown here were outputted at the same time as those shown in figures 5.6 & 5.7. This figure is identical to figure 5.6 save that the surface of the interface is shown. This has the advantage that the plan form of the interface can be seen but the disadvantage that the temperature variation across the full depth of the mantle is not displayed.

Total heat entering the cases where **both internal and bottom heating** were active ranged from 3.172×10^{12} W to 4.630×10^{12} W. The contribution from bottom-heating to the total heat entering the system was between 36% and 56%. Heat flux into the lower layer ranged between 3.74×10^{12} W to 3.60×10^{12} W with the contribution from bottom heating being between 44% & 91%. For some cases when the boundary depth was set to 500km or 2500km, distortions of the interface reached the surface or CMB respectively.

The temperature contrast over the deformable interface was largest for shallower cases with larger density contrasts. Both the values of the temperature contrast and the way in which they vary with depth resembled those seen in the bottom heated cases rather than the internally heated cases.

Cut-aways displaying the thermal structure of several different cases can be seen in figures 5.6, 5.7 & 5.8. In figure 5.7 the average radial temperature has been removed so the resulting images display the lateral temperature heterogeneities. Significantly lower amplitude thermal heterogeneities are seen in the internally heated cases. These also show very little temperature variance in the lower layer and the amplitude of thermal heterogeneities is larger in the upper layer. The wavelength of the thermal heterogeneities and the size of the convection cells in the upper layer is coupled to the depth of the layer; with the width of the cells and the depth being roughly equal, this can be seen in figure 5.7. In contrast the bottom heated cases and those with both bottom and internal heating have larger lateral thermal anomalies in the lower layer. These heterogeneities in the upper layer were still larger than those in the internally heated cases.

The temperature power spectrum was calculated using the method outlined by Bunge et al. [1997]. See figure 5.9 & 5.10. This is a spherical harmonic analysis of the lateral variations in temperature for all depths in the mantle. In all cases the peak of the power spectrum is at the depth of the deformable interface rather than either the surface or CMB. Though in the deeper internally heated cases the contribution of the surface heterogeneities can be seen. Similarly in the shallower bottom heated cases the heterogeneities at the CMB are significant.

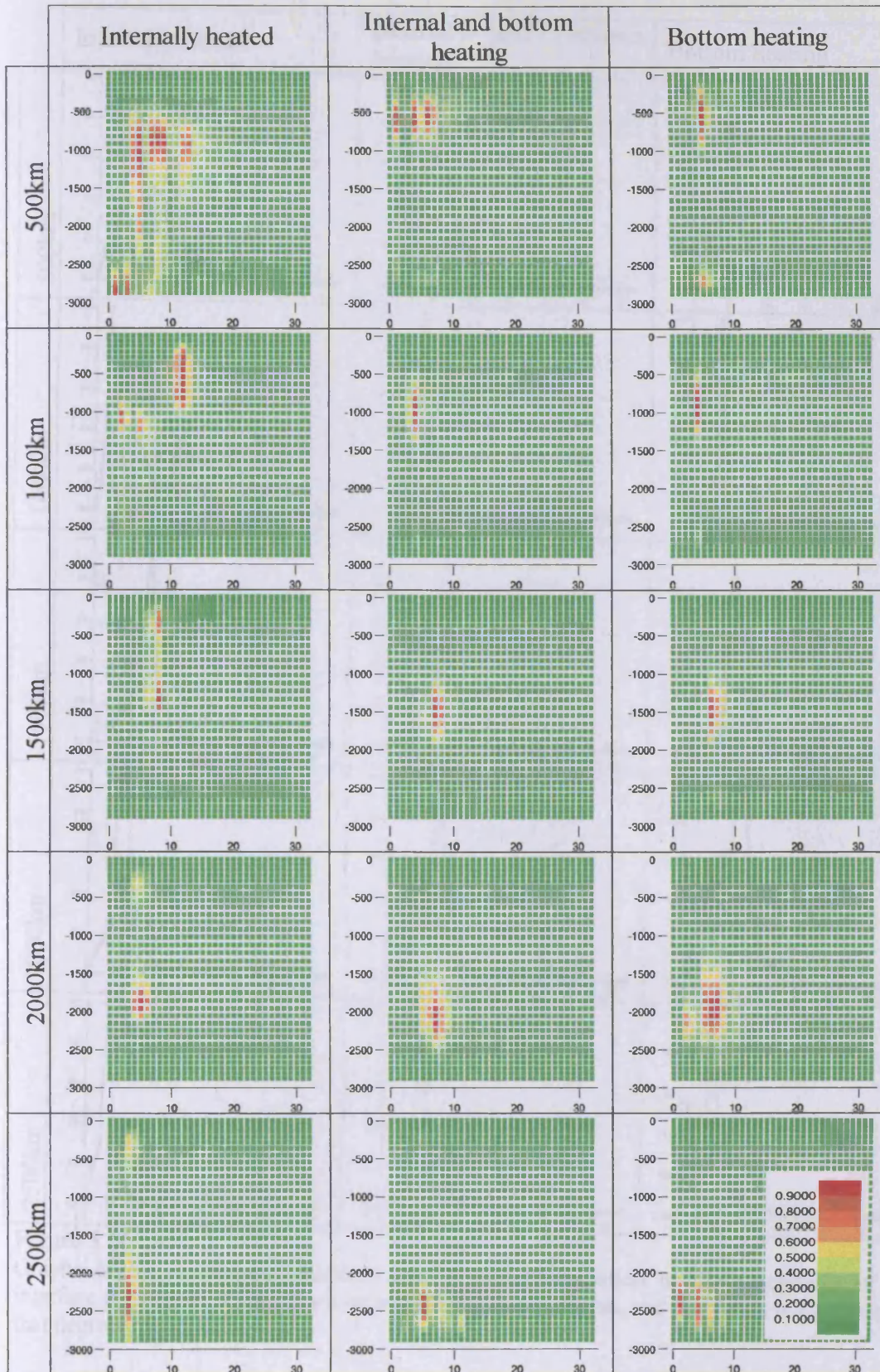


Figure 5.9 Spherical harmonic contour plots of the thermal field output of the 4% runs for all three heating modes. The x-axis is the harmonic degree, while the y-axis is the depth (km).

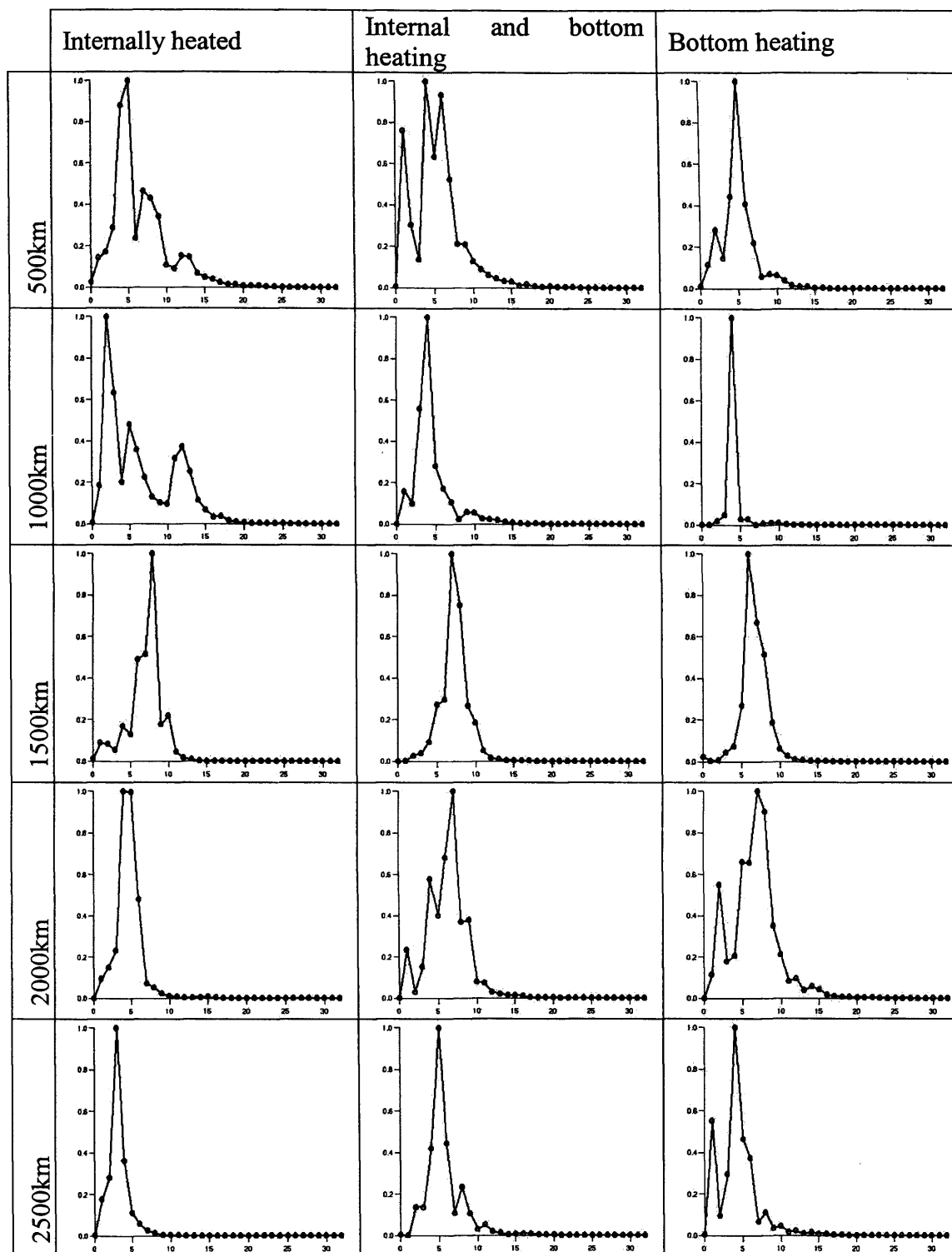


Figure 5.10

Graphs of the normalised spherical harmonic decomposition of the topography of the interface for various cases. The x-axis is the harmonic degree, and the y-axis is the power in that degree.

The effective density contrast over the boundary can be defined as the chemical density contrast minus that due to thermal expansion.

$$\Delta\rho_{\text{eff}} = \left((\rho_l - \rho_u) \div \rho_u \right) - \alpha\Delta T \quad (5.2)$$

Where $(\Delta\rho)_{\text{eff}}$ is the effective density contrast, ρ_u and ρ_l are the chemical reference densities in the upper and lower layers respectively, α is the volume coefficient of thermal expansion, ΔT is the temperature contrast associated with the thermal boundary as illustrated in figure 5.11.

The effective density contrast for all the stable steady states are illustrated in figure 5.11. The small temperature contrast needed in the internally heated cases suggests that the contribution of thermal expansion does not significantly change the density contrast over the layer. This is due to the relatively low heat energy that is being inputted into the lower layer in the internally heated cases, rather than the heat mode itself. For internally heated cases and cases with both internal and bottom heating the shallower and less dense interfaces had the smallest effective density. However, for bottom heated cases thermal expansion removes chemical density contrast in the lower layer most effectively for deep layers with a small density increase across the deformable interface.

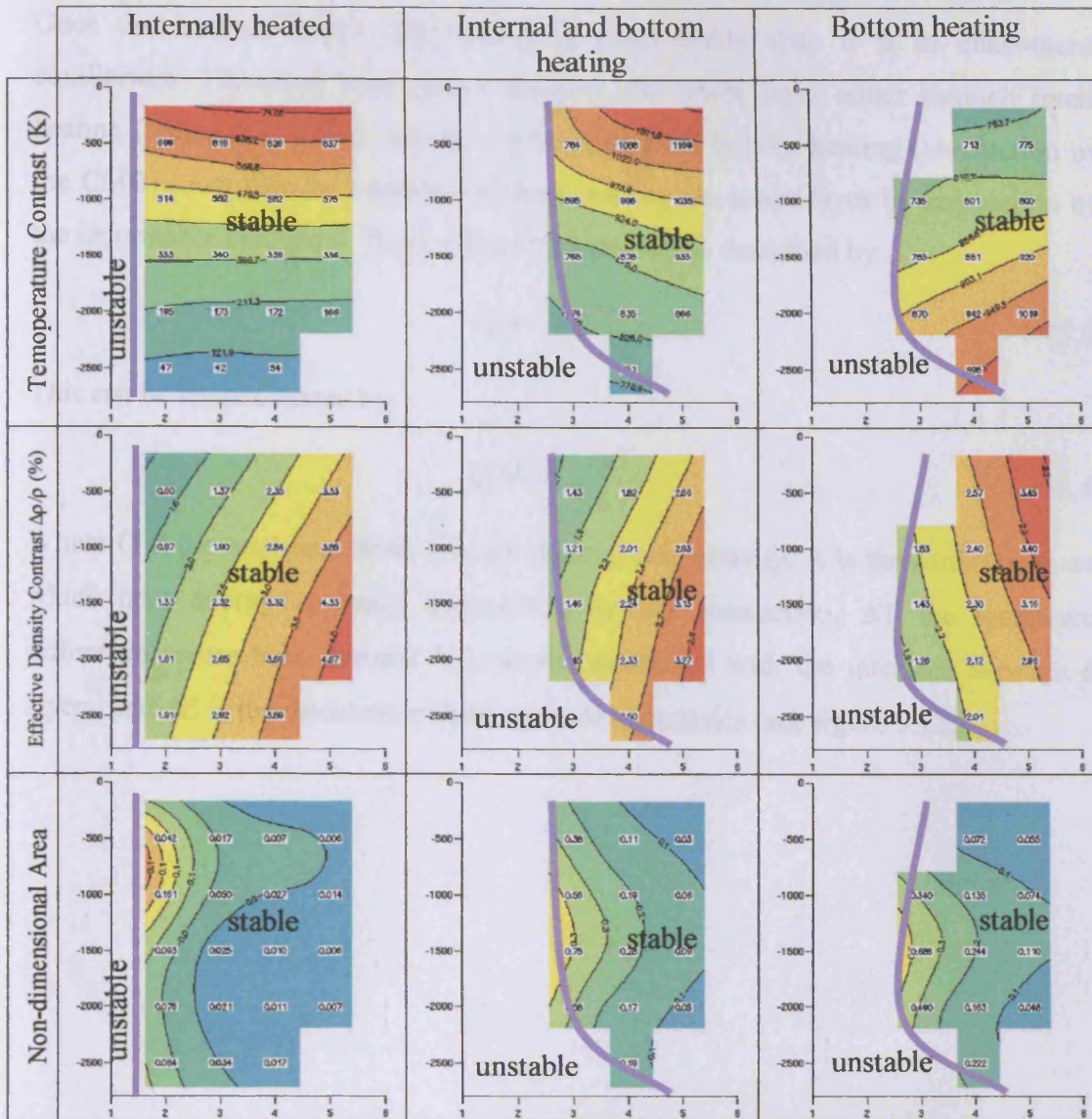


Figure 5.11

Contour plots showing how several physical characteristics of the layered systems alter with the depth of the boundary and the density contrast across it. The density contrast is shown on the x-axis, and the depth of the boundary on the y-axis.

The temperature in the upper and lower layer is defined as the average temperature half way between the deformable interface and either the surface or the CMB. The temperature contrast used here is the difference between these two values.

The effective density contrast is the chemical density contrast minus that due to thermal expansion and is defined in equation 5.2. The non-dimensional Area Variable ϕ is the fractional increase in the surface area of the interface relative to the area of a shell at the same depth as the interface. So $\phi = 0$ implies a flat layer and increasing values of ϕ represent a more deformed boundary. The purple line shows where the regime changes from stable to unstable.

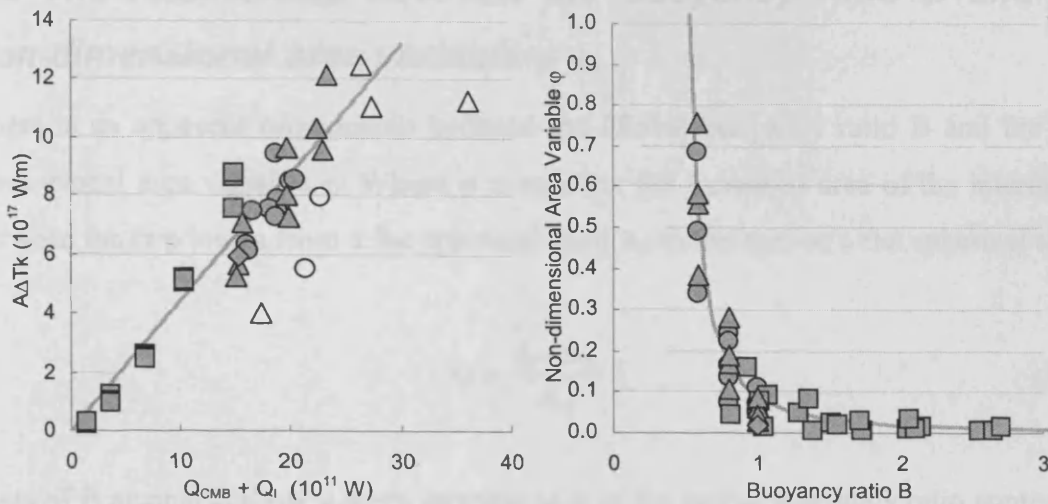
Once the layered system has reached a quasi-steady state it is in quasi-thermal equilibrium. Therefore heat energy entering the lower layer either through internal heating (radioactive decay, secular cooling) or from bottom heating (conduction over the CMB) must then be balanced by heat leaving the lower layer by conduction over the deformable boundary. This conductive heat flow is described by.

$$Q = -kA \frac{dT}{dz} \quad (5.3)$$

This can be approximated by.

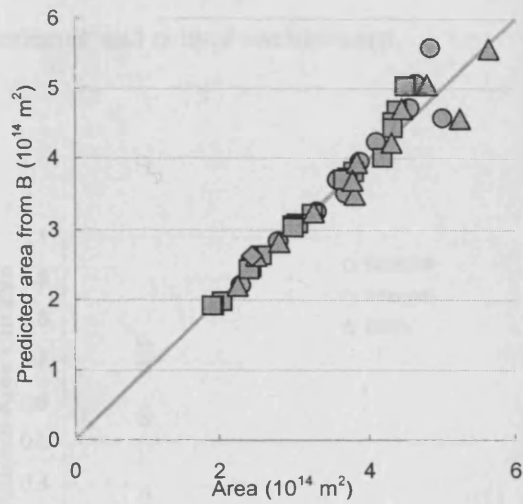
$$Q = -kA \frac{\Delta T}{\Delta Z} \quad (5.4)$$

Where Q is the total heat flow, k is the thermal conductivity, A is the surface area over which heat energy is being transported by the conduction, ΔT the temperature difference across both thermal boundaries associated with the interface between the layers, and ΔZ is the thickness of both thermal boundaries (see figure 5.12).



a,

b,



c,

Figure 5.12

Each symbol represents the result of one simulation. Unfilled symbols represent cases where the deformable boundary pushes against either the CMB or the surface.

a, Heat balance in the lower layer. The grey line displays the best fit that corresponds to a ΔZ of 437km.

b, The relationship between the non-dimensional area variable and the buoyancy ratio. The grey line represents $B = 0.07 \div (B^2 - 0.48^2)$

c, The predicted surface area of the deformable boundary using the Buoyancy values against the observed areas.

○ Bottom Heated □ Internally heated △ Both Heated ◇ Internally heat Hot

5.6 The relationship between the Buoyancy ratio B and the non-dimensional area variable ϕ

There is an apparent relationship between the Global buoyancy ratio B and the non-dimensional area variable ϕ . Where ϕ is equal to the increased area of the interface A between the two layers from a flat spherical shell A_0 to the area of a flat spherical shell.

$$\phi = \frac{A - A_0}{A_0} \quad (5.5)$$

Plots of B against ϕ show a steep increase in ϕ as the global buoyancy ratio approaches around 0.5. As the value of B increases towards infinity the deformation of the surface decreases and ϕ approaches zero.

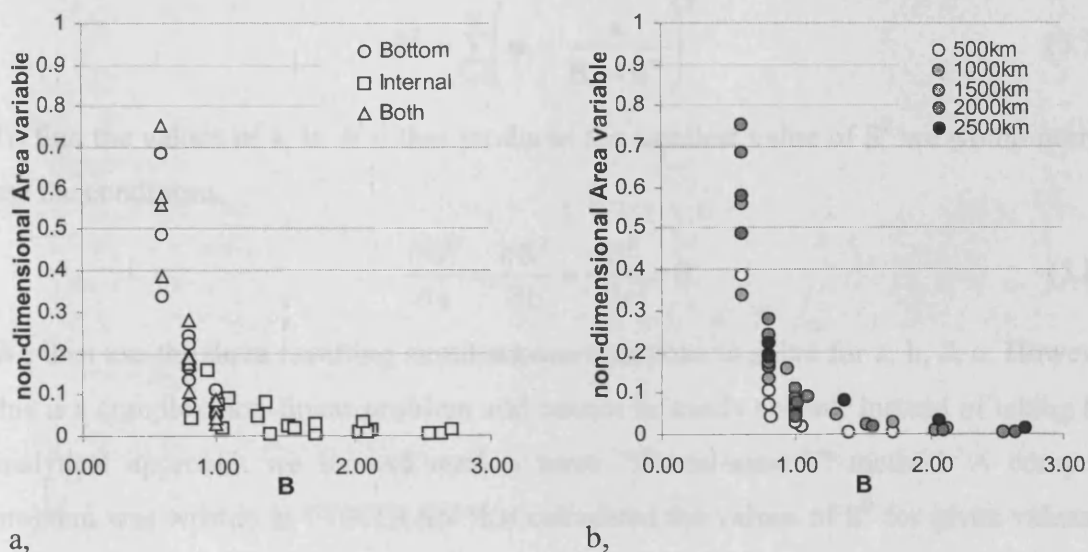


Figure 5.13

The relationship between the global buoyancy ratio B and the non-dimensional area variable ϕ .

- Different heating modes are represented with different symbols.
- Symbols represent the depth of the deformable interface.

5.6.1 Characterising the B - φ relationship

The relationship between φ and B is clearly some sort of inverse power law, suggesting that $\varphi \propto 1 \div B^\alpha$, where α is a constant. However the surface area tends towards infinity for some arbitrary value of B. We can account for this lag by adding an extra term to our equation: $\varphi \propto 1 \div (B^\alpha - b^\alpha)$. Adding a constant of proportionality to this relationship we arrive at.

$$\varphi = \frac{a}{B^\alpha - b^\alpha} \quad (5.6)$$

Where 'a' is a constant, α is some power and b is the value of B for which φ tends to infinity.

The best values of a, b, & α could be found using a least squares method to find the best solution. We represent our values of the non-dimensional area variable and the global buoyancy ratio as (φ_i, B_i) where $i=1,2,3\dots N$. If we consider the deviation of $a \div (B_i^\alpha - b^\alpha)$ from φ_i then we can describe the least squared error as.

$$S^2 = \sum_{i=1}^N \left(\varphi_i - \frac{a}{B_i^\alpha - b^\alpha} \right)^2 \quad (5.7)$$

To find the values of a, b, & α that produces the smallest value of S^2 we would normally use the conditions.

$$\frac{\partial S^2}{\partial a} = \frac{\partial S^2}{\partial b} = \frac{\partial S^2}{\partial \alpha} = 0 \quad (5.8)$$

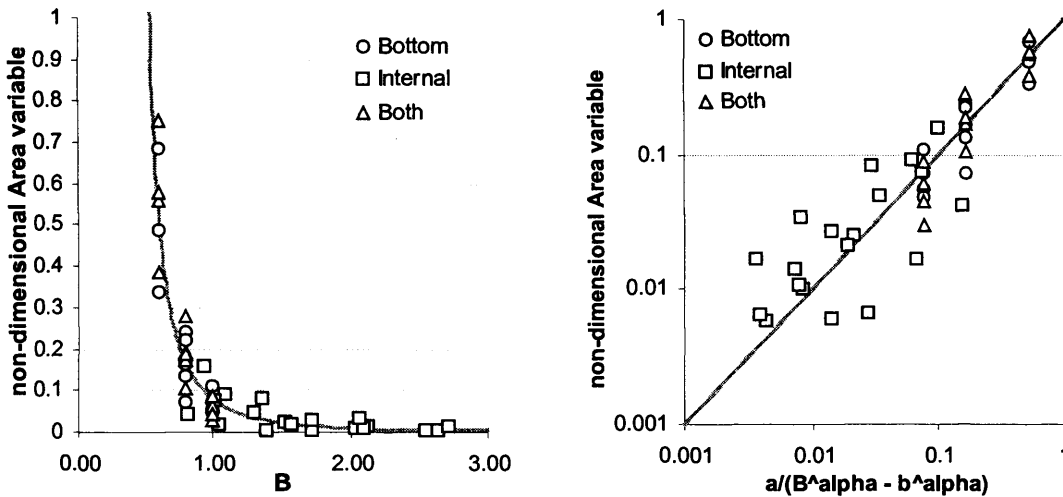
We then use the three resulting simultaneous equations to solve for a, b, & α . However, this is a complex non-linear problem and cannot be easily solved. Instead of taking this analytical approach we instead used a more "frontal-assault" method. A computer program was written in FORTRAN that calculated the values of S^2 for given values of a, b & α . This program can be seen in appendix G - Solving $\varphi = a \div (B^\alpha - b^\alpha)$. This parameter space was then investigated in detail with all the possible permutations of a, b & c shown below being calculated.

$$\begin{aligned} a &= 0.000, 0.001, 0.002\dots 1.000; \\ b &= 0.000, 0.010, 0.020\dots 1.00; \\ c &= 0.000, 0.010, 0.020\dots 5.00. \end{aligned}$$

The smallest values of $S^2/44$ was found to be $S^2/44=0.0102$ when $a=0.071$; $b=0.44$, $\alpha = 3.00$

The best fit between the observed non-dimensional area variable and the global buoyancy ratio is.

$$\phi = \frac{0.071}{B^3 - 0.44^3} \quad (5.9)$$



a,
Figure 5.14

b,

The least square best fit of the $\phi = a \div (B^\alpha - b^\alpha)$ relationship.

a, The Global buoyancy ratio against the non-dimensional area variable ϕ . The grey line shows the best least square fit, when $a=0.071$; $b=0.44$, $\alpha = 3.00$.

b, The values of ϕ predicted by equation 5.9 using the values of a , b & α that produced the smallest least squared error. A perfect fit should plot along the grey line.

The values of b & α that produce the smallest RMS error have some significance. The value of b corresponds the point at which the area of the deformable boundary tends towards infinity. Systems with a global buoyancy ratio below this value are unlikely to be stable in a steady state. In the cases studied here, $b=0.44$ corresponds to a density contrast of 2.64% in the cases with bottom heating.

To confirm the $\phi \propto B^3$ relationship the least squared fit values of S^2 were calculated for values of $\alpha=0.2, 0.4, 0.6 \dots 5.0$ and only a & b allowed to vary. The smallest RMS errors found for each case are plotted in figure 5.15; the value of S^2 tending towards a minimum value when $\alpha=3$. The absence of any local minimum suggests that the $\phi \propto B^3$

is the dominant power relationship. I.e. if $\phi = aB^{-1} + bB^{-2} + cB^{-3} + dB^{-4} + \dots$ then the B^{-3} term will be dominant.

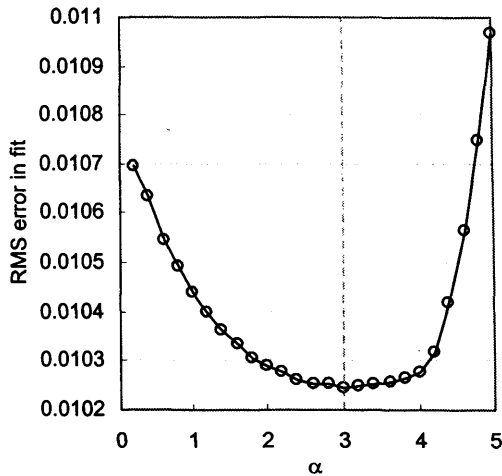


Figure 5.15
The best RMS error achieved when a & b where varied but α was varied in the $\phi = a \div (B^\alpha - b^\alpha)$ relationship. The grey dashed line shows the best result when $\alpha = 3.0$

5.6.2 Is depth a factor in the $\phi = a \div (B^\alpha - b^\alpha)$ relationship?

Figure 5.13 shows plots of B against ϕ in which the symbols represent both the heating mode used to generate convection and the depth of the interface. The heating mode are scattered randomly and do not seem to affect the nature of the relationship between ϕ and B . However there does appear to be some pattern in the distribution of the depths. We investigated this further by finding the least square solutions for each depth. The qualities of the solutions are shown in table 5.6 and figure 5.16. These results show some anomalies. The least squares fit for cases at 2500km depth results in a value of b of 0.04. However we have run cases at this depth with values of $B=0.4$ which have proven to be unstable. The problem lies in the relatively small number of data points for each depth and the small range over which the data is distributed. Consequently there may be a number of combinations of values of a , b & α that fit the data. This is illustrated in Figure 5.17 that shows four possible solutions for the case of an interface at 2500km. The four solutions displayed all appear to give a reasonable fit of the data points however their values of a , b & α suggest different behaviour. In particular the different values of b all suggest different values of B for which the layered system becomes unstable.

Depth	a	b	A	$\sqrt{(S^2)/N}$
500	0.0290	0.52	3.0	0.005352
1000	0.0760	0.43	2.2	0.017102
1500	0.1140	0.14	3.6	0.006191
2000	0.0650	0.21	4.1	0.006616
2500	0.1370	0.04	1.8	0.004944

Table 5.6

The results of the least squared to the $\varphi = a \div (B^a - b^a)$ relationship is the depth of the deformable layer is varied.

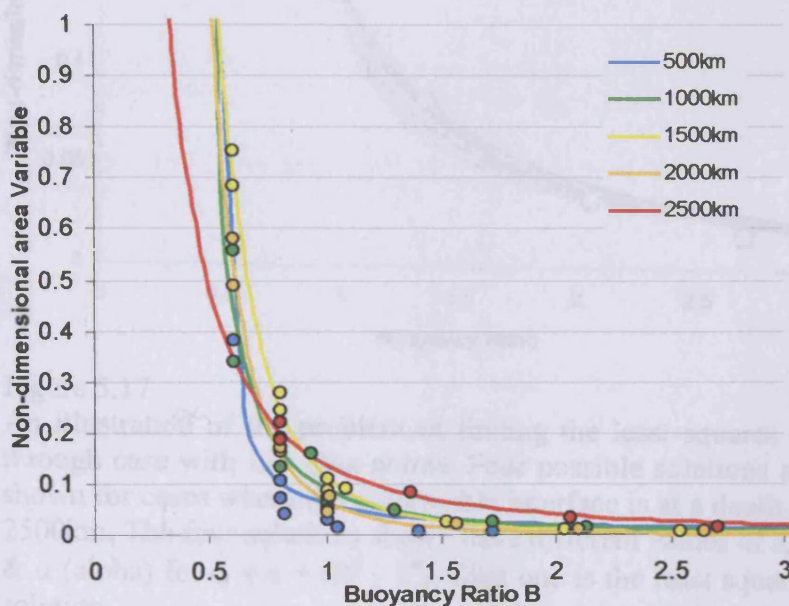


Figure 5.16

The Global Buoyancy Ratio plotted against the Non-dimensional Area variable. The colour of the data points represents the depth of the deformable interface and the coloured lines are the least squares best fit of $\varphi = a \div (B^a - b^a)$.

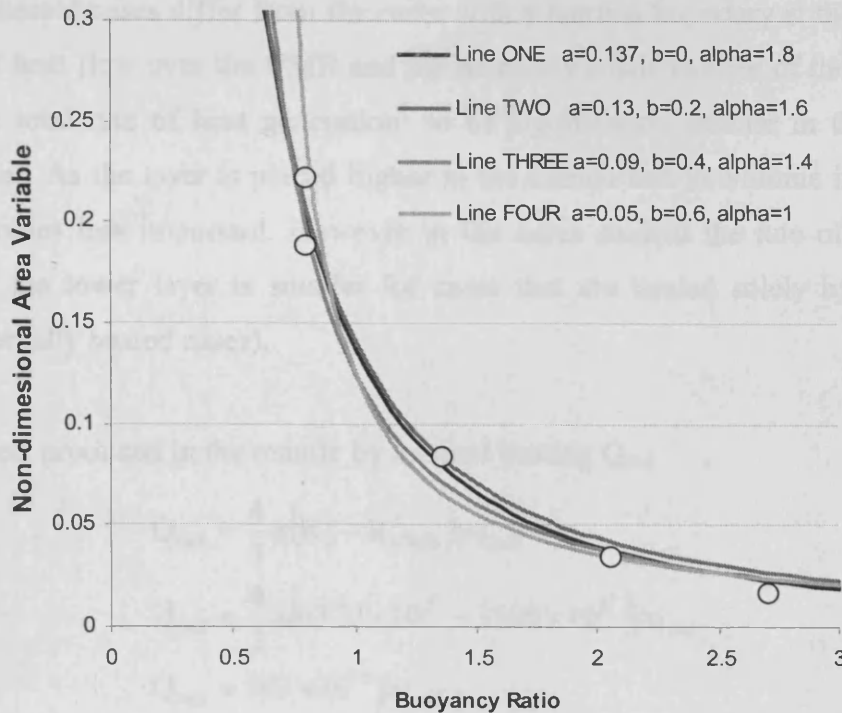


Figure 5.17

An illustration of the problem of finding the least squares fit through case with few data points. Four possible solutions are shown for cases where the deformable interface is at a depth of 2500km. The four solutions shown have different values of a , b & α (alpha) for $\varphi = a \div (B^{\alpha} - b^{\alpha})$. Line one is the least squares solution.

5.7 Internally heated case with accelerated heating rates

The internally heated cases presented so far in this chapter had a rate of heat produced per unit mass of $0.450 \times 10^{-12} \text{ W kg}^{-1}$. This value was chosen because it is consistent with the rate of heat production in the upper mantle (see Davies [1999, p193]). However this contributes a small fraction of the total heat produced in the mantle ($2.032 \times 10^{12} \text{ W}^{\dagger}$). We can compare this to the total amount of heat energy entering or being produced in the mantle for cases with bottom heating or both internal and bottom heating. These range from $1.62 \times 10^{12} \text{ W}$ to $3.63 \times 10^{12} \text{ W}$, this suggests that the internally heated cases did not differ significantly from the other heating modes in terms of the total amount of heat energy present in the system. However if we look at figure 5.6 we see that the internally heated cases are consistently colder than the other heating modes. If we consider the total rate of heat energy present in the lower layer we see how the

[†] We have ignored the effects of increasing the reference density over the deformable boundary since this would complicate the calculation and would (at most) increase the total heat energy produced by 5% which would not affect our argument.

internally heated cases differ from the cases with a thermal boundary at the CMB. The absence of heat flow over the CMB and the relatively small volume of the lower layer causes the total rate of heat generation[†] to be significantly smaller in the internally heated cases. As the layer is placed higher in the mantle and its volume increases this effect becomes less important. However in the cases studied the rate of heat energy present in the lower layer is smaller for cases that are heated solely by radioactive decay (internally heated cases).

Total heat produced in the mantle by internal heating Q_{rad}

$$Q_{\text{rad}} = \frac{4}{3} \pi (R_S^3 - R_{\text{CMB}}^3) \rho q_{\text{rad}}$$

$$Q_{\text{rad}} = \frac{4}{3} \pi (6370 \times 10^3 - 3500 \times 10^3) \rho q_{\text{rad}}$$

$$Q_{\text{rad}} = 903 \times 10^{18} \rho q_{\text{rad}}$$

$$Q_{\text{rad}} = 903 \times 10^{18} \times 5 \times 10^3 \times 450 \times 10^{-9}$$

$$Q_{\text{rad}} = 2.032 \times 10^{12} \text{ W}$$

As we saw in section 5.5 internally heated cases were much more stable than cases with a thermal boundary at the CMB and had a thermal structure that was cooler with smaller thermal heterogeneities. It was not clear if this was because of the heating mode or because of the relatively low rate of heat energy production in the lower layer. To see which was the case an internally heated case was run with an increased rate of heat produced per unit mass.

The case run had a deformable boundary at 2000km depth with a 5% density increase across it. The parameters used were identical to those in table 5.2 save those values in table 5.7. The rate of heat production in the upper layer was set to zero and was $1.8 \times 10^{-12} \text{ W kg}^{-1}$ in the lower layer. The total rate of heat energy present in the whole mantle was $1.53 \times 10^{12} \text{ W}$ with all of this heat energy being produced in the lower layer. This compares to the case in which only bottom heating was active with a layer at 2000km and a 5% density increase across the deformable interface in which there was $1.62 \times 10^{12} \text{ W}$ of heat energy flowing across the CMB. These two cases are very similar; the heat energy flowing in to the system that is driving convection has similar values

[†] The total rate of heat generation in the mantle is not simply an input parameter since it has contributions from both internal heating (controlled by input parameters) and bottom heating that is dependent on the thickness and size of the thermal boundary and is not defined by input parameters.

(they agree to within 6%). In both cases the heat flow is only entering the lower layer and must cross the deformable interface via conduction. The only way in which the two systems vary is the heating mode used to drive convection in the lower layer.

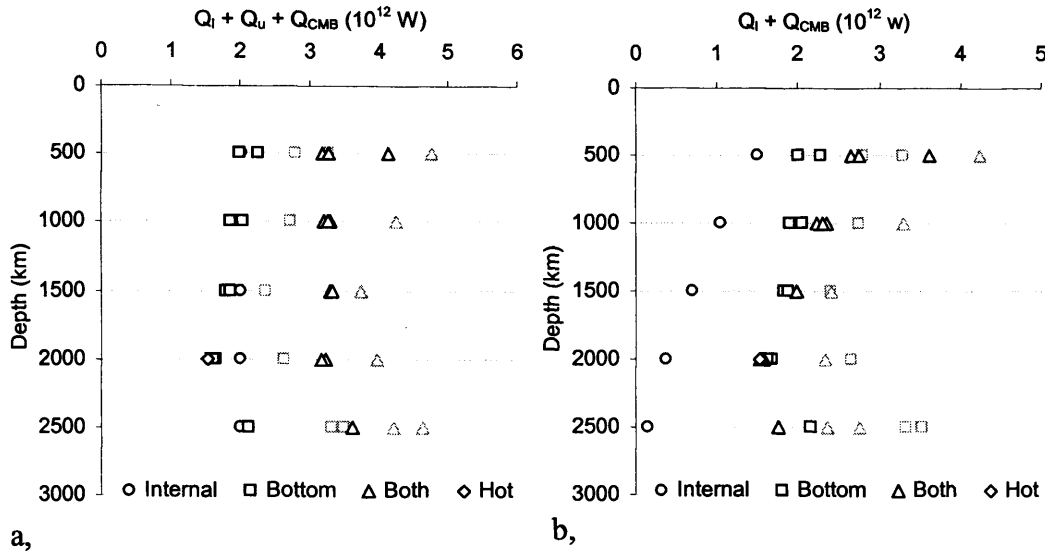


Figure 5.18

The rate of heat energy present in the system as the heating mode and depth of the deformable boundary vary.

- a, The x-axis displays the rate of heat energy present in the whole mantle: the energy produced from radioactive decay in the whole mantle Q_{rad} plus the total rate of heat energy flowing over the core mantle boundary Q_{CMB} .
- b, The x-axis displays the rate of heat energy present in the lower layer: the energy produced from radioactive decay in the lower layer Q_i plus the total rate of heat energy flowing over the core mantle boundary Q_{CMB} .

Parameter	Value
Depth of marker surface	D_K 2000 km
Temperature of surface	T_S 1060 K
Density of the upper layer	ρ_u 5.00×10^3 kg
Density of the lower layer	ρ_l 5.25×10^3 kg
$\Delta\rho/\rho$	5 %
Rate of internal heating in the upper layer	q_u 0 W kg^{-1}
Rate of internal heating in the lower layer	q_l $1.800 \times 10^{-12} \text{ W kg}^{-1}$

Table 5.7

The parameters used in the internally heat case with an accelerated rate of heat production in the lower layer.

The results of this “hot” internally heated case are shown in tables 5.4 & 5.5 and are repeated in table 5.8 along with the bottom heated case to allow an easy comparison. A

comparison of the thermal structure including its power spectrum is shown in figure 5.18. Both cases reach a quasi steady state and have a very similar thermal structure. However the amplitude of the deformations of the deformable layer are larger in the bottom heated case with both the standard deviations of the markers' heights and the surface area of the interface being around double that in the internally heated case.

The thermal structure is not affected by the increased surface area since in both cases the size of the deformations is relatively small with the surface area increasing in size from a flat spherical shell by only 2 & 5%. The power spectrum of the thermal structure shown in figure 5.19 shows a wider range of wavelengths in the bottom heated case compared to the internally heated case. This pattern also extends to the power spectrum of the height of the interface between the two layers. This is consistent with the observation we can make from figures 5.9 & 5.10 that the power spectrum of the thermal field and of the interface tends to contain a wider range of wavelengths as the interface between the layers is placed deeper in the mantle, in bottom heat case; in all internally heated cases and especially when the interface is high in the mantle; and as the depth of the layer is made deeper in bottom heated cases. There is no simple relationship between the heating mode and the power spectrum of a layered system and so we must also consider the depth of the layer.

Parameter		Internally heated – Hot	Bottom Heated
Stable		yes	yes
Area Variable	γ	0.02	0.05
Standard deviations of the markers' heights	Mrk sd	70 km	104 km
Temperature of the upper layer	T_u	1278.24 K	1288.97 K
Temperature of the lower layer	T_l	2282.61	2307.97
Temperature difference between the layers	ΔT	1004.37	1019.00
Rate of heat energy flowing across the CMB	Q_{CMB}	1.62 T W	0 W
Rate of heat energy generated in the lower layer by radioactive decay.	Q_l	0 W	1.53 T W
Total rate of heat energy present in the lower layer	$Q_{\text{CMB}}+Q_l$	1.62 T W	1.53 T W
Rate of heat energy flowing across the upper surface	Q_s	1.59 T W	1.51 T W
RMS surface velocity	RMS v_s	0.0492 cm/year	0.0524 cm/year
Total time simulated		67.91 G years	129.00 G years
No of over-turns		6.0	12.1

Table 5.8

Results of two simulations with an interface at 2000km depth with a 5% density increase across the layer. In one case the lower layer is heated by internal heating and in the other a thermal gradient across the CMB powers the convection.

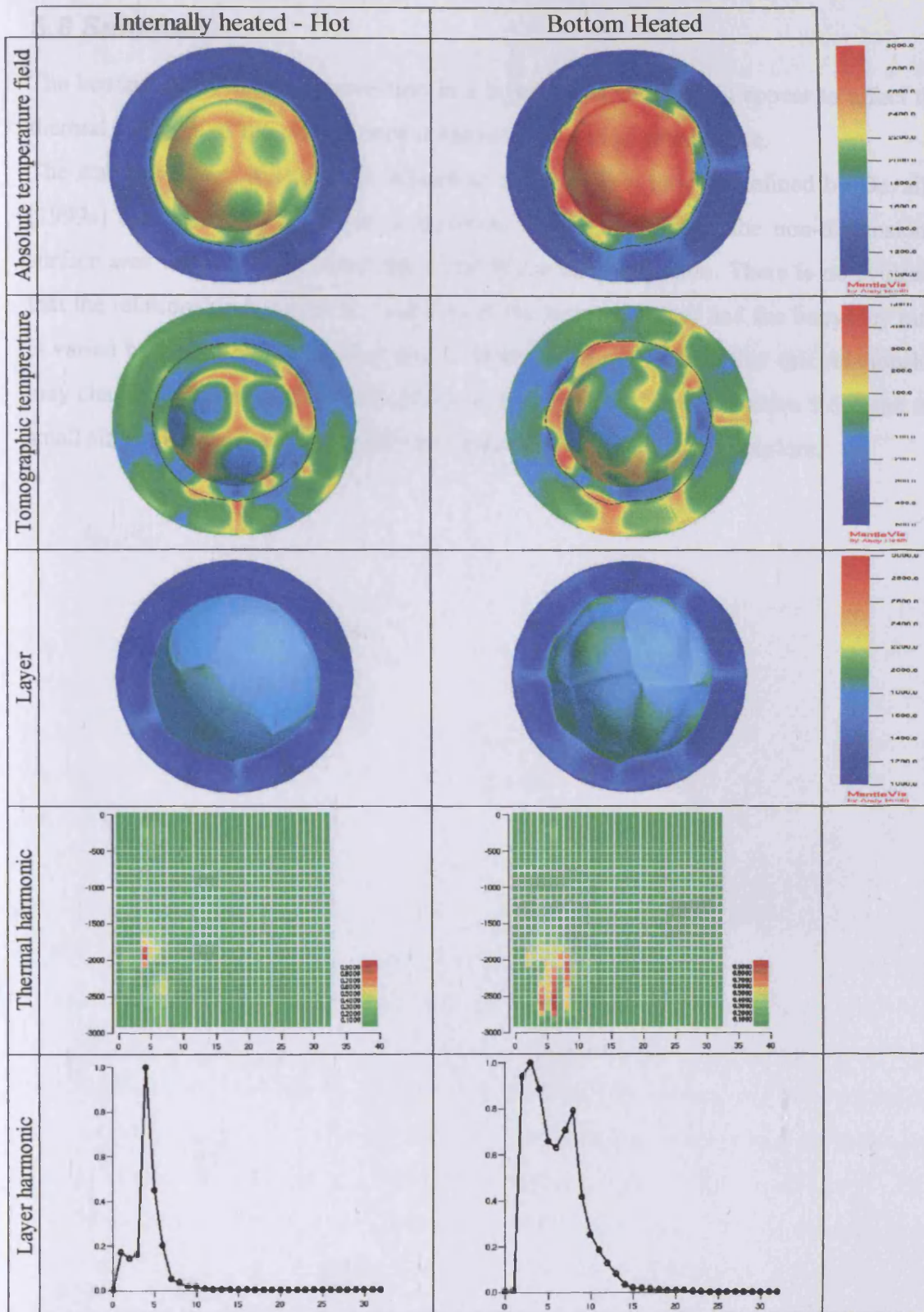


Figure 5.19

A comparison of the internally heated and bottom heated case. The cases are identical save for the heat mode. Absolute temperature field, a section of the temperature field; tomographic temperature, the temperature field with the radial average temperature removed; layer, shows the temperature field of the interface; thermal harmonic, presents the spherical harmonic power spectrum of each radial layer and layer harmonic give the power spectrum of the height of the deformable boundary.

5.8 Summary

The heating mode driving convection in a layered system does not appear to affect the thermal structure of the system once it has reached a quasi steady state.

The stability of the layer can be related to the buoyancy ratio as defined by Davaille [1999a] see figure 5.11b. There is however a large variance in the non-dimensional surface area variable for a particular value of the buoyancy ratio. There is no evidence that the relationship between the stability of the layered system and the buoyancy ratio is varied by changing the heating mode. There is some evidence that this relationship may change with the depth of the interface. Problems outlined in section 5.6.2 and the small size of the data set have made this impossible to conclusively explore.

6 The effects of Rayleigh number on the stability of a layered mantle

In the previous chapter we looked at the effect the heating mode, as well as the depth and density of the lower layer had on the convecting system. The cases studied were not Earth-like in several ways. One the largest limitations of these cases were that convection was not as vigorous as that in Earth's mantle. Because of this it is difficult to apply the results directly to Earth's mantle. We decided to investigate how the layered system is affected by changes in viscosity (and hence Rayleigh number Ra) so that we could project our earlier results to an Earth-like Rayleigh number and comment on the possibility of actual mantle layering.

6.1 Cases investigated

We investigated cases in which the boundary of the deformable interface was at a depth of 1500km. This depth was chosen since it is at that lower end of the proposed depth range of a Kellogg layer [Tackley 2000]. Results from the earlier section suggest that mid mantle depths produce the more stable layering. So layering at 1500km depth is the most likely to be stable and within the estimated depth range of the Kellogg layer. Hence, we studied the most stable end-member case of a Kellogg-type layer. Since a range of Rayleigh numbers Ra were studied the resolutions of the TERRA grid were different between the runs. Two resolutions were used, with $m_t=64$ and $m_t=128$ [see section 3.2.5]. To make the cases more Earth-like a radially dependent viscosity structure was used. For the different resolutions studied a first order extrapolation was used to map the radial viscosity field from the higher order field to the lower. The radial viscosity profile is shown in figure 6.1. Both internal heating and bottom heating were present in the systems with the contributions of bottom heating varying from case to case (since the size of the thermal boundary at the CMB could vary). The contribution from internal heating varied from between 45 and 75% of the total heat energy entering the system. Parameters used were kept as Earth-like as possible with only the viscosity having non Earth-like values. Viscosity was changed to alter the value of the Rayleigh number of the calculations. Cases were simulated with five different Rayleigh numbers varying from 3.4×10^4 to 4.0×10^5 (the Rayleigh number used here is the Rayleigh number calculated within TERRA, Ra_T in appendix F). For

each Rayleigh number a series of cases were run with the density increase from the upper to lower layer varying. The density contrasts ranged from 2.4% to 5.0% and in most cases were incremented in steps of 0.2%. Parameters used in the calculations are shown in table 6.1.

The same initial cases were used for all cases that ran at the same grid resolution. These were produced in the same manner described in section 5.1; with a spherical harmonic thermal field allowed to convect until a single layered system had developed.

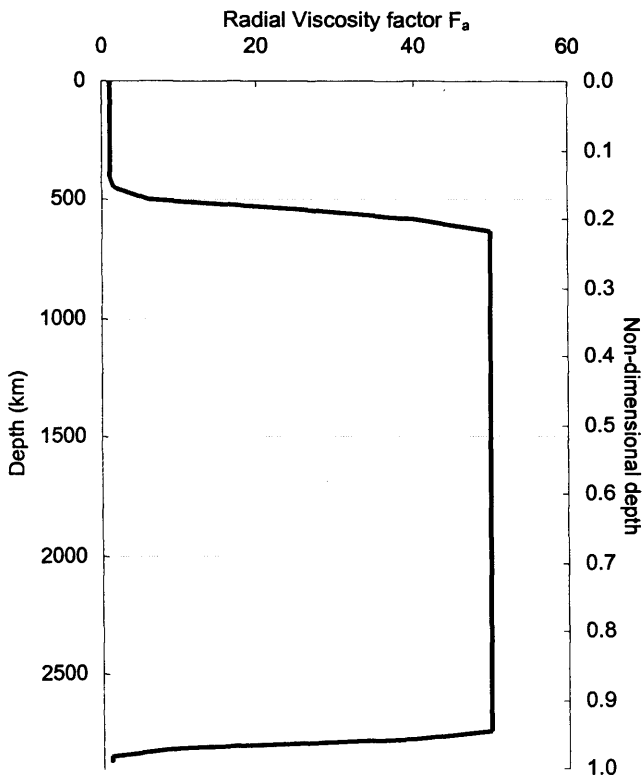


Figure 6.1

The viscosity structure used in these runs. The structure does not vary with mt .

The radial viscosity factor (f_a) describes the applied viscosity (η) at a given depth relative to the reference viscosity (η_0) quoted in table 6.1.

$$\eta = f_a \eta_0$$

Parameter		Value
Outer shell radius	R_S	6.370×10^6 m
Initial radius of the deformable interface	R_k	4.870×10^6 m
Inner shell radius	R_{CMB}	3.500×10^6 m
Depth of marker surface	D_k	1500 km
Temperature of surface	T_S	1060 K
Temperature of CMB	T_{CMB}	3000 K
Reference density in the upper layer	ρ_u	5.00×10^3 kg m ⁻³
Reference density in the lower layer	ρ_l	5.10 to 5.25×10^3 kg m ⁻³
Chemical density increase	$\Delta\rho/\rho$	1.0 to 5.0 %
Dynamic reference viscosity	η_0	8.250×10^{21} to 1.000×10^{23} Pa s
Rate of internal heating (with internal heating)	q_{rad}	0.450×10^{-12} W kg ⁻¹
Thermal conductivity	k	2.4 W m ⁻¹ K ⁻¹
Gravitational acceleration	g	10 N kg ⁻¹
Volume coefficient of thermal expansion	α	2.0×10^{-5} K ⁻¹
Specific heat at constant volume	C_V	1×10^3 J kg ⁻¹ K ⁻¹
Thermal diffusivity	κ	4.8×10^{-7} m ² s ⁻¹

Table 6.1

The Parameters used in the calculations presented in this chapter.

6.2 The thermal evolution of the layered system

All the cases presented in this section started with an initial temperature field that had a single-layer structure. Once a deeper layer was introduced a thermal boundary developed at the deformable interface and the system worked towards a quasi-steady thermal state. This was achieved once the system was thermally balanced; with the heat flow over each of the surfaces balancing heat energy entering the layer below it. To do this, the bottom layer heated up and the temperature of the upper layer decreased to accommodate a thermal boundary at the deformable interface. The evolution of the thermal structure of a range of Rayleigh numbers is shown in figure 6.2. The use of the average radial temperature in figure 6.2 has the complication that for radial shells near to the depth of the interface the mean radial value will sample temperatures in both the upper and lower layers. Consequently the physical size of the thermal boundary associated with the deformable boundary will appear artificially large for interfaces with large undulations.

In all cases the physical size of the thermal boundary (ΔZ) at the surface was smaller than ΔZ at the CMB. This is expected since there is higher viscosity in the deeper mantle in our simulations. However, ΔZ at both the surface and CMB decrease once layered convection takes place. The thinning of the thermal boundaries when layered

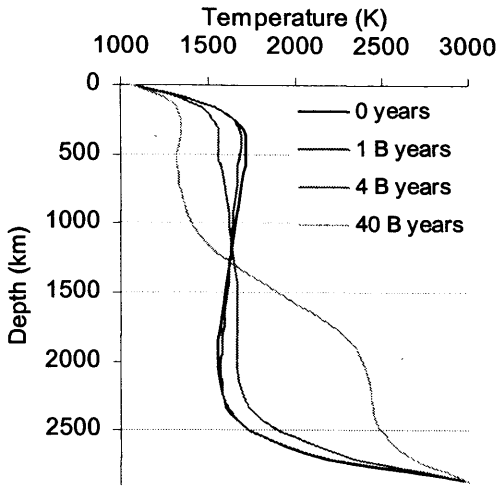
convection is applied can be predicted from the equation relating the size of the thermal boundary to the length scale of convection and the Rayleigh number (equation 2.8; section 2.5; repeated below)

$$\Delta Z = D \left(\frac{Ra_c}{Ra} \right)^\beta \quad (2.8)$$

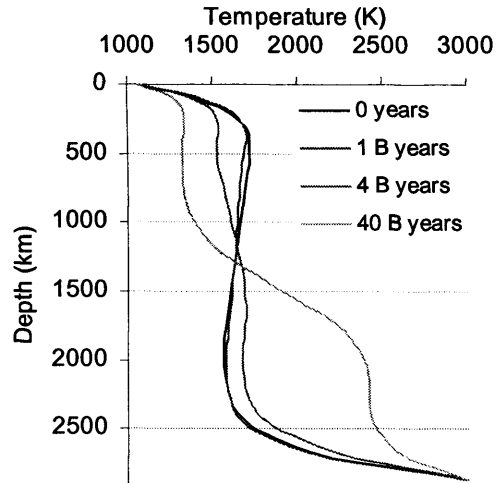
Where: $87 < Ra_c < 1100$; $0 < \beta < 0.3$ for Earth's mantle [McNamara et al 2000]

When layering is introduced, the system is divided in two, decreasing the length scale of convection (D) in each layer. Equation 2.8 predicts that $\Delta Z \propto D^{1-3\beta}$. The power β is expected to have a value of less than 0.3; so as D decreases so too will the width of the thermal boundary. It is not possible to directly test this relationship since the initial temperature field used for cases in which Ra was less than 10^5 were produced from an unlayered case in which $Ra = 1.8 \times 10^4$. The decrease in the size of ΔZ can be seen in case in figure 6.2a & 6.2e, in these cases the initial case and the layered case had the same Rayleigh number.

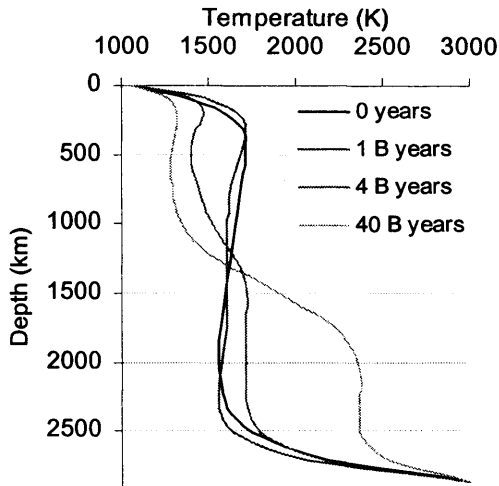
Figure 6.2 shows that the thermal boundary has equal magnitude on either side of the deformable boundary. This can be compared to the two cases considered by McNamara & van Keken [2000]. In the first the entire thermal boundary is contained in the lower layer and in the second it is distributed evenly over both the layers. Our results are in agreement with the latter.



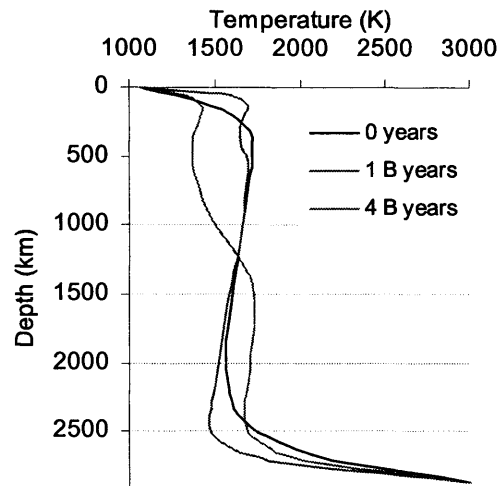
a, $Ra_T = 3.4 \times 10^4$



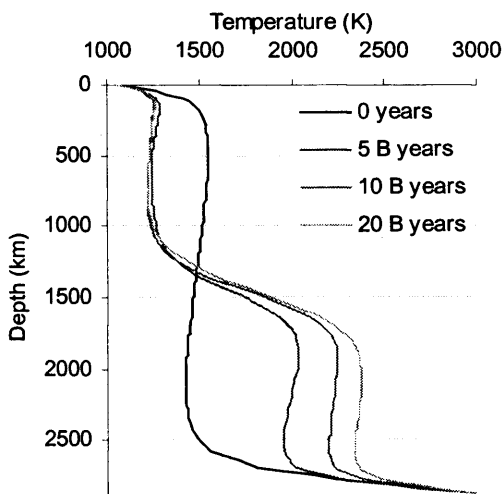
b, $Ra_T = 4.1 \times 10^4$



c, $Ra_T = 8.7 \times 10^4$



d, $Ra_T = 1.7 \times 10^5$



e, $Ra_T = 4.0 \times 10^5$

Figure 6.2

Temperature cross-sections through the depth of the mantle showing the thermal evolution of the system from an initially single layered thermal structure to a two-layer system. Cases shown had the interface at a depth of 1500km and a 4% density increase across it.

The x-axis represents the average radial temperature of the mantle (K) and the y-axis represents the depth (km).

Figure 6.3 shows the quasi-steady state thermal structure of layered convection for each of the cases presented in this chapter. One striking feature is that the average radial temperature at the depth of the deformable interface is very consistent for most cases with the same Rayleigh number. We consider the average radial temperature at the average depth of the interface between the two layers to represent the temperature at the deformable interface T_k . For cases with a Rayleigh number of 1.8×10^4 the average value of T_k was 1995K, and this value varied with a standard deviation of only 15K. For cases with larger Rayleigh numbers the T_k increases. For each Ra there are some cases where the average temperature at the mean depth of the deformable interface does not agree with the values of most of the simulations. These cases are always those with the lowest density increase across the boundary and suggest that in these cases the system is not in a stratified layered case. This deviation of the mean radial temperature from the consistent values might indicate the failure of the marker method and suggest the layered system is moving into a regime that is not stratified.

As the chemical density contrast across the deformable interface increases the temperature gradient increases. This increase continues until a negative temperature gradient is present. We can explain this change in thermal gradient within the layers by making the following assumptions: firstly, all four thermal boundaries widths $\Delta Z_{1,2,3,4}$ remains constant (for cases with the same Rayleigh number) as the density increase over the interface changes, see figure 6.3d. Secondly, the temperature change across the thermal boundaries $\Delta T_{1,2,3,4}$ changes so that the thermal gradient over the boundary produces a heat flow that balances the heat energy entering the layer below it. Thirdly, the temperature structure within each layer is approximately a linear trend connecting the values at the edge of the thermal boundaries at the top and bottom of the layer. A consequence of these assumptions is that the thermal gradients at the CMB and the surface remain constant: effectively fixing the size of $\Delta T_{1\&4}$. The thermal gradients at the deformable interface will change with the density contrast across it. As the lower layer is made denser the deformation of the interface will become smaller and its surface area will decrease (see section 5.5). To carry the same heat energy over a surface with a smaller area a larger thermal gradient is needed. Since we have assumed that $\Delta Z_{2\&3}$ remains constant $\Delta T_{2\&3}$ must be made larger to increase the thermal gradient. Using assumption three the temperature gradient (dT/dZ) within the layers will become larger as the density ratio across the layers increases. This will eventually

reach infinity and then have negative values for cases with a large density increase and hence flat interface. Examples of the thermal structure predicted by these assumptions is shown in figure 6.4, these are in agreement with the results shown in figure 6.3 where the size of the thermal boundary at the deformable interface increases with density contrast and thermal gradient within the layers increases eventually becoming negative.

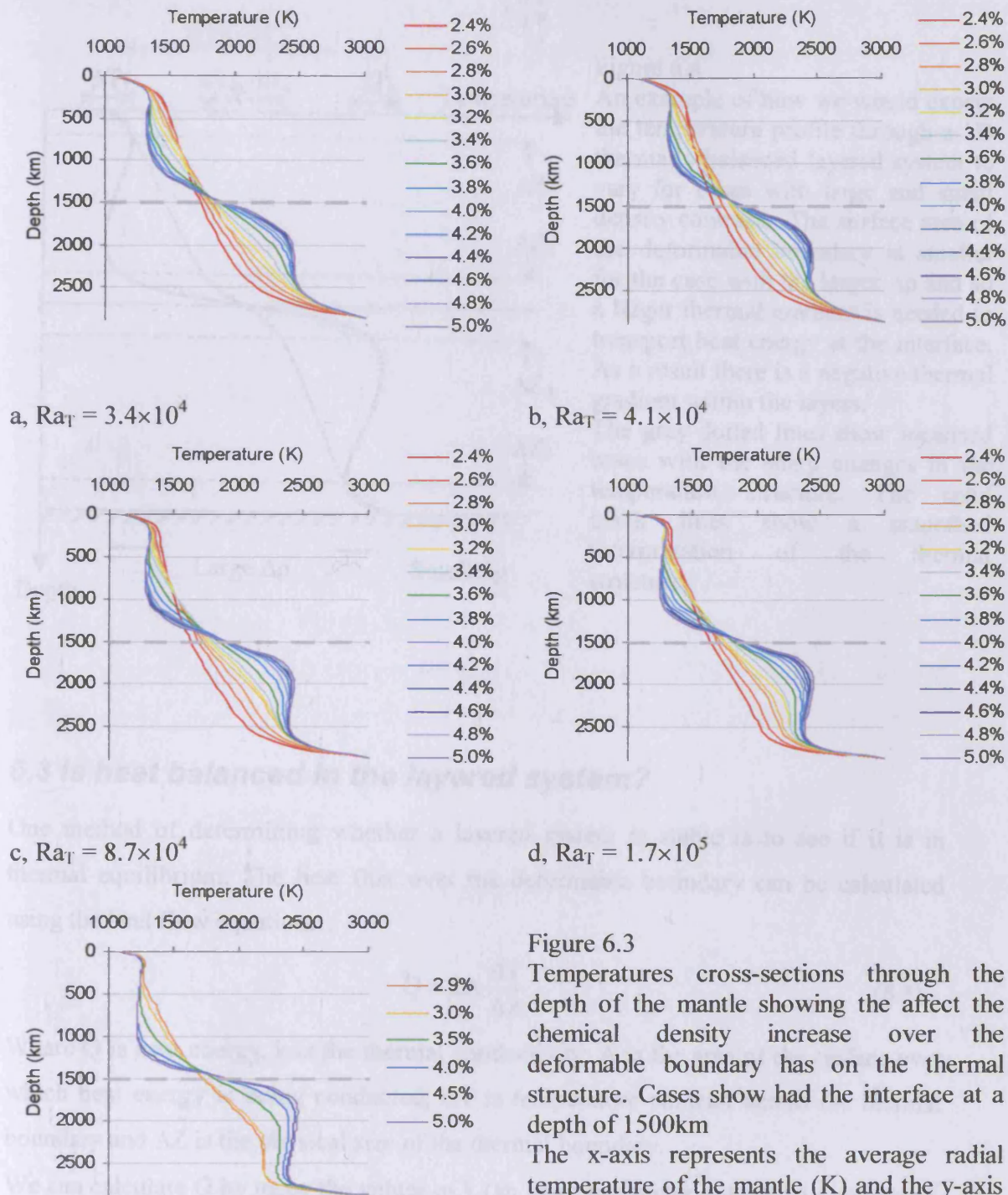


Figure 6.3

Temperatures cross-sections through the depth of the mantle showing the affect the chemical density increase over the deformable boundary has on the thermal structure. Cases show had the interface at a depth of 1500km

The x-axis represents the average radial temperature of the mantle (K) and the y-axis represents the depth (km).

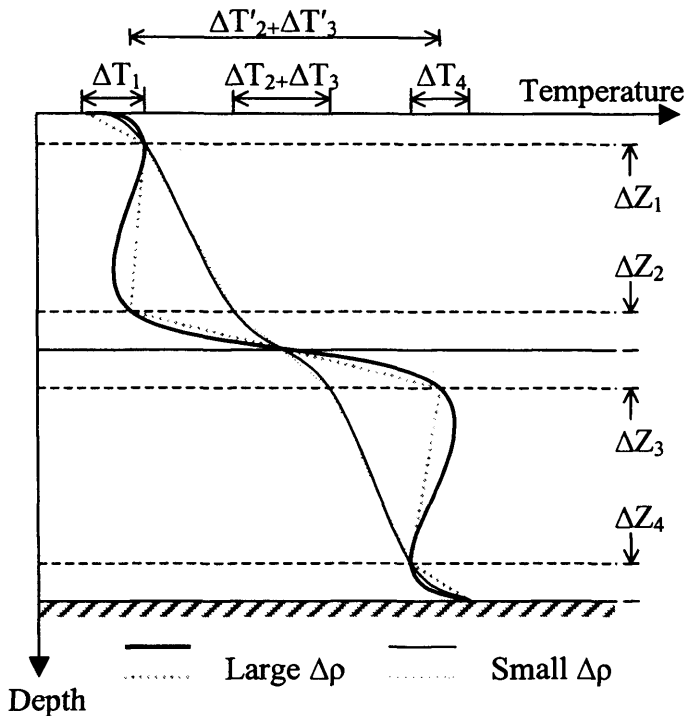


Figure 6.4

An example of how we would expect the temperature profile through a 1D thermally balanced layered system to vary for cases with large and small density contrasts. The surface area of the deformable boundary is smaller for the case with the larger $\Delta\rho$ and so a larger thermal gradient is needed to transport heat energy at the interface. As a result there is a negative thermal gradient within the layers.

The grey dotted lines show idealised cases with the sharp changes in the temperature structure. The solid black lines show a smoothed interpretation of the thermal structure.

6.3 Is heat balanced in the layered system?

One method of determining whether a layered system is stable is to see if it is in thermal equilibrium. The heat flux over the deformable boundary can be calculated using the heat flow equation...

$$Q = kA \frac{\Delta T}{\Delta Z} \quad (6.1)$$

Where Q is heat energy, k is the thermal conductivity, A is the area of the surface over which heat energy is being conducted, ΔT is temperature contrast across the thermal boundary and ΔZ is the physical size of the thermal boundary.

We can calculate Q by using the values of k (an input parameter defined in *interra*), A (see section 3.6.2), and ΔT (see section 3.6.1). To find ΔZ we used equation 2.8 $\Delta Z = L(Ra_c \mp Ra)^\beta$. Where L is the length scale of convection, Ra_c is the critical Rayleigh number thought to have a value between 87 and 1100, and β is an experimentally derived constant thought to have a value between 0 and 0.3 [M^cNamara et al 2000].

We use the value of k shown in table 6.1, for A we use the mean value of the area of the Kellogg boundary once it has reached a quasi steady state. To find ΔZ we used

values of $L=2500\text{km}$, $Ra_c=500$ and $\beta=0.3$. We use the calculated heat energy flowing over the Kellogg interface to calculate the total heat entering the lower layer. Figure 6.5 shows a simple 1D model of the thermal structure of a layered mantle. If the system is thermally balanced then...

$$Q_s = Q_u + Q_k \quad (6.2)$$

$$Q_k = Q_u + Q_{CMB} \quad (6.3)$$

$$Q_s = Q_u + Q_i + Q_{CMB} \quad (6.4)$$

We can test to see if the system is thermally balanced by plotting each of these three equations as a graph. See figure 6.6. Each of the three graphs in figure 6.6 represents one of these equations (6.2, 6.3 & 6.4). If the system is thermally balanced with the heat energy flowing over each of the surfaces (CMB, Kellogg and the surface) equalling the heat energy entering the layer below it then the results should plot on the grey lines. Figure 6.6b does not use the calculation of the heat flow over the Kellogg interface and so can be thought of as a test of the amount of scatter we would expect. Figures 6.6a & 6.6b show that the system does appear to be thermally balanced in most cases. Cases in which $\Delta\rho < 3.0\%$ are thought to be unresolved by the marker methods and appear in grey. These cases correspond to those where the interface temperature starts to decrease.

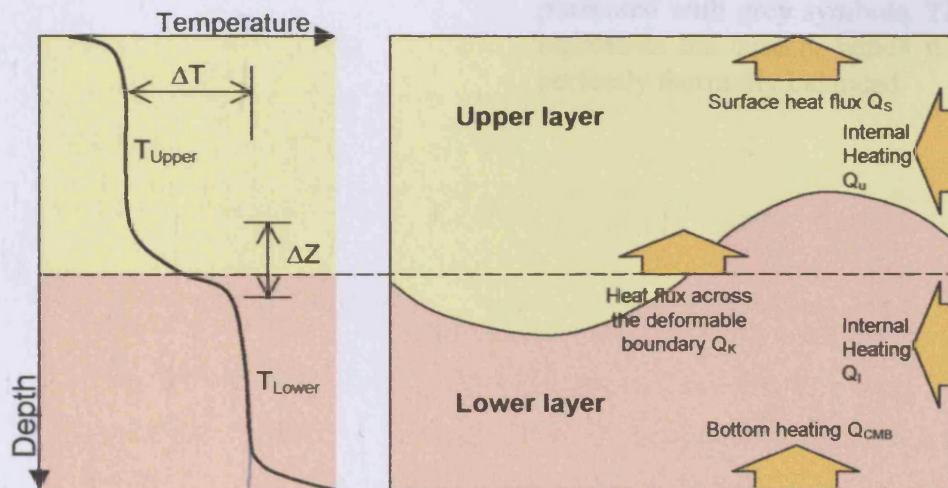
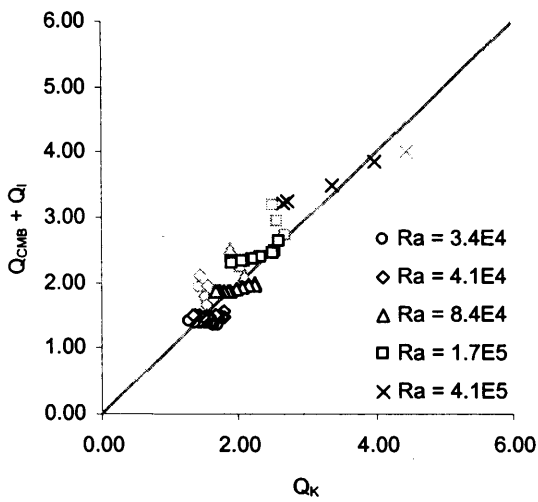
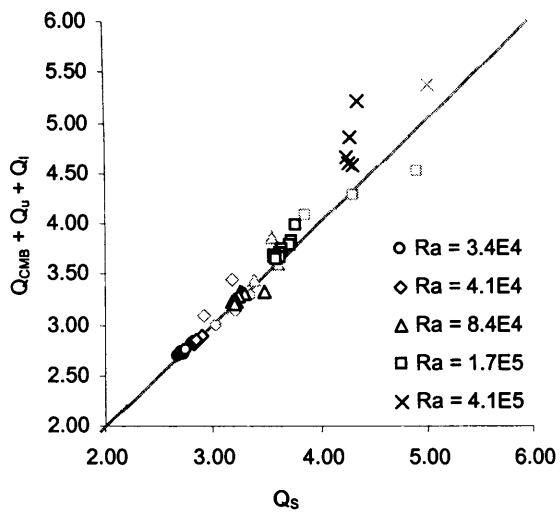


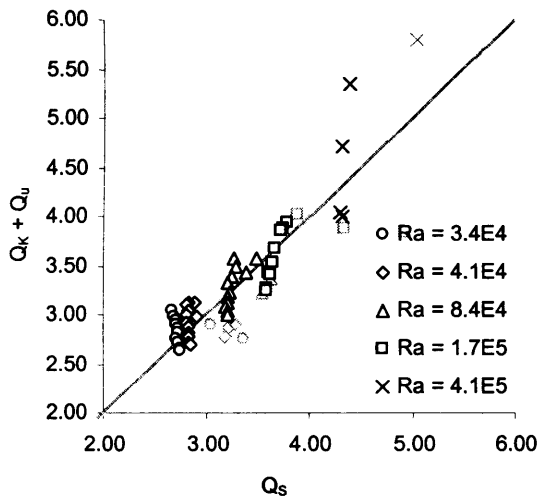
Figure 6.5
A simple 1D thermal model of a layered mantle.



a,



b,



c,

Figure 6.6

Testing the thermal balance assumption. Q_u and Q_l is heating energy being generated in the upper and lower layers respectively. Q_s and Q_{CMB} is the heat energy flowing over the surface and CMB respectively. Q_k is the heat energy flowing over the Kellogg interface calculated using equations 2.8 & 6.1.

Results for all the simulations presented in this section are shown. Cases with a density contrast of less than 3% are presented with grey symbols. The grey line represents the case in which the system is perfectly thermally balanced.

6.4 Stability of the layering

A near complete set of output data from the simulations presented in this chapter are shown in the tables 6.2 & 6.3. Many of the results from chapter 5 are repeated. We see an increase in the surface area of the deformable boundary as the density contrast across the interface decreases. The temperature increase across the interface becomes larger as the density increases.

In figure 6.7a we can see the relationship between the surface area variable γ and the Rayleigh number. The value of γ for higher resolution runs has been scaled down to account for the effects of measuring the surface area with a higher resolutions grid (see section 4.3 resolution test). For all Rayleigh numbers the behaviour of the system is similar. As the density of the lower layer becomes smaller the non-dimensional area parameter become larger; at some point the density increase across the lower layer is not sufficient to counter the thermal buoyancy of the lower layer and the system becomes unstable. In figure 6.3 we see that the mean radial temperature at the deformable interface starts to fall when the density increase across the layer approaches 3%. In Figure 6.6 there is evidence that as the density contrast falls below 3% the layered system is no longer in thermal equilibrium suggesting entrainment at the interface becomes much larger. In the next section we shall see that at the 3% density contrast there is a break in the relationship between non-dimensional area parameter and the density increase (see figure 6.10a). This suggests that the layer becomes unstable when the density contrast falls below around 3%.

The layered system becomes unstable when the density contrast falls below around 3%.

Over the range of Rayleigh number investigated there is little if any evidence that the density contrast below which the system becomes unstable changes significantly with the Rayleigh number. However, the surface area of the interface between the two layers at a given density contrast does become smaller (i.e. the layer is flatter) as the Rayleigh number increases. This suggests that as a convecting system becomes more vigorous layering becomes more sustainable; these results are in agreement with Davaille et al. [2003]

These results suggest that a layered system becomes more stable as the Rayleigh number increases.

The thermal structure of the layered system is shown in figures 6.7b & 6.7d. The conclusions of the previous chapter are repeated with an increasing density contrast across the boundary causing the temperature in the lower layer T_l to increase; the temperature in the upper layer T_u to decrease and the temperature contrast across the deformable interface to increase. Increasing the Rayleigh number makes the temperature of the lower layer T_l cooler, the temperature of the upper layer T_u also cooler and the temperature difference across the interface shows little variation.

Ra	Density (%)	Stable?	Mean Area variable $\hat{\gamma}$	\hat{T}_u (K)	\hat{T}_l (K)	\hat{T}_{diff} (K)	Mrk SD (km)
3.40E+04	2.4	N	0.9148 ± 0.1073	1366.20 ± 5.90	2130.55 ± 13.66	764.39 ± 12.05	819.12 ± 28.90
3.40E+04	2.6	N	0.8529 ± 0.0683	1363.50 ± 6.65	2203.85 ± 16.10	840.35 ± 14.58	772.68 ± 27.17
3.40E+04	2.8	N	0.7342 ± 0.0353	1358.19 ± 2.57	2283.83 ± 13.22	925.65 ± 13.30	694.86 ± 31.31
3.40E+04	3.0	Y	0.6612 ± 0.0562	1355.37 ± 3.70	2343.79 ± 13.51	988.40 ± 14.18	632.40 ± 13.23
3.40E+04	3.2	Y	0.6982 ± 0.0363	1354.55 ± 2.06	2389.08 ± 4.61	1034.52 ± 6.34	561.87 ± 7.55
3.40E+04	3.4	Y	0.6062 ± 0.0193	1349.28 ± 1.90	2403.71 ± 5.01	1054.46 ± 6.37	520.42 ± 6.21
3.40E+04	3.6	Y	0.5253 ± 0.0125	1342.42 ± 1.51	2423.59 ± 1.97	1081.29 ± 2.68	473.26 ± 8.57
3.40E+04	3.8	Y	0.4471 ± 0.0132	1334.23 ± 1.29	2445.80 ± 3.45	1111.58 ± 3.91	410.24 ± 7.91
3.40E+04	4.0	Y	0.3676 ± 0.0133	1329.10 ± 0.93	2466.19 ± 2.30	1137.13 ± 2.67	353.77 ± 6.66
3.40E+04	4.2	Y	0.3107 ± 0.0243	1325.70 ± 1.37	2483.44 ± 2.28	1157.68 ± 3.51	297.76 ± 11.49
3.40E+04	4.4	Y	0.2490 ± 0.0247	1323.71 ± 1.40	2495.18 ± 2.28	1171.43 ± 3.48	260.08 ± 8.47
3.40E+04	4.6	Y	0.1865 ± 0.0213	1321.20 ± 1.83	2505.73 ± 3.33	1184.58 ± 4.60	224.05 ± 10.84
3.40E+04	4.8	Y	0.1380 ± 0.0157	1320.59 ± 1.70	2511.20 ± 4.47	1190.58 ± 5.72	189.99 ± 7.98
3.40E+04	5.0	Y	0.1042 ± 0.0106	1318.60 ± 0.71	2516.56 ± 2.53	1197.95 ± 2.75	162.69 ± 6.57
4.10E+04	2.4	N	0.8371 ± 0.0615	1341.00 ± 2.54	2096.44 ± 12.88	755.42 ± 14.23	788.02 ± 22.91
4.10E+04	2.6	N	0.8145 ± 0.0460	1342.39 ± 3.73	2174.46 ± 18.68	832.06 ± 19.32	757.48 ± 28.02
4.10E+04	2.8	N	0.7598 ± 0.0378	1343.20 ± 3.19	2244.84 ± 21.75	901.63 ± 20.98	692.35 ± 20.80
4.10E+04	3.0	Y	0.7354 ± 0.0644	1344.29 ± 3.86	2338.45 ± 9.15	994.14 ± 9.71	628.72 ± 17.55
4.10E+04	3.2	Y	0.6590 ± 0.0399	1340.20 ± 2.61	2386.11 ± 7.15	1045.91 ± 7.10	561.88 ± 11.12
4.10E+04	3.4	Y	0.6230 ± 0.0298	1334.75 ± 1.82	2388.63 ± 1.84	1053.91 ± 3.23	537.73 ± 13.20
4.10E+04	3.6	Y	0.5495 ± 0.0315	1327.89 ± 2.06	2401.34 ± 6.74	1073.25 ± 8.25	473.73 ± 13.93
4.10E+04	3.8	Y	0.4574 ± 0.0176	1319.44 ± 0.88	2427.71 ± 3.23	1108.21 ± 3.62	407.11 ± 11.31
4.10E+04	4.0	Y	0.3557 ± 0.0262	1314.00 ± 0.37	2451.82 ± 4.38	1137.74 ± 4.13	350.16 ± 15.51
4.10E+04	4.2	Y	0.2933 ± 0.0256	1310.31 ± 0.30	2468.42 ± 3.25	1158.02 ± 3.14	307.00 ± 12.08
4.10E+04	4.4	Y	0.2247 ± 0.0283	1307.82 ± 0.79	2487.62 ± 2.04	1179.77 ± 2.61	258.21 ± 12.29
4.10E+04	4.6	Y	0.1662 ± 0.0188	1306.60 ± 0.38	2497.70 ± 2.57	1191.10 ± 2.80	220.51 ± 10.20
4.10E+04	4.8	Y	0.1200 ± 0.0120	1305.89 ± 0.50	2504.18 ± 2.57	1198.34 ± 2.87	187.70 ± 8.08
4.10E+04	5.0	Y	0.0899 ± 0.0110	1305.51 ± 0.48	2511.64 ± 2.30	1206.17 ± 2.42	156.39 ± 7.06
8.40E+04	2.4	N	0.9071 ± 0.0483	1295.90 ± 3.72	2073.88 ± 15.22	778.00 ± 12.73	763.07 ± 12.69
8.40E+04	2.6	N	0.8640 ± 0.0690	1293.56 ± 4.08	2143.41 ± 14.25	849.85 ± 17.33	709.87 ± 11.15
8.40E+04	2.8	N	0.7986 ± 0.0571	1295.71 ± 4.18	2209.96 ± 8.89	914.28 ± 9.95	665.42 ± 26.56
8.40E+04	3.0	Y	0.7536 ± 0.0323	1292.13 ± 3.22	2289.18 ± 17.32	997.05 ± 18.54	595.21 ± 18.65
8.40E+04	3.2	Y	0.7141 ± 0.0308	1290.30 ± 2.54	2312.11 ± 17.54	1021.77 ± 16.80	551.90 ± 18.53
8.40E+04	3.4	Y	0.6416 ± 0.0499	1286.11 ± 1.21	2315.25 ± 3.17	1029.08 ± 3.96	501.08 ± 27.66
8.40E+04	3.6	Y	0.5244 ± 0.0447	1282.26 ± 1.74	2341.47 ± 2.12	1059.29 ± 2.09	436.51 ± 28.72
8.40E+04	3.8	Y	0.4042 ± 0.0464	1277.38 ± 1.93	2381.76 ± 5.33	1104.39 ± 5.65	384.69 ± 29.67
8.40E+04	4.0	Y	0.3154 ± 0.0404	1276.84 ± 1.43	2402.62 ± 5.75	1125.79 ± 6.44	306.77 ± 29.68
8.40E+04	4.2	Y	0.2573 ± 0.0421	1274.36 ± 1.61	2420.63 ± 5.12	1146.24 ± 6.58	269.01 ± 24.78
8.40E+04	4.4	Y	0.1964 ± 0.0363	1274.39 ± 1.36	2439.38 ± 7.68	1165.04 ± 8.88	231.24 ± 19.57
8.40E+04	4.6	Y	0.1561 ± 0.0307	1275.15 ± 1.67	2451.83 ± 9.54	1176.71 ± 11.02	206.61 ± 21.90
8.40E+04	4.8	Y	0.1224 ± 0.0199	1272.71 ± 2.48	2463.56 ± 11.27	1190.83 ± 13.70	181.49 ± 12.34
8.40E+04	5.0	Y	0.0823 ± 0.0101	1273.50 ± 2.57	2473.31 ± 12.72	1199.84 ± 15.24	153.89 ± 8.28
1.70E+05	2.4	N	1.0010 ± 0.0536	1287.50 ± 7.31	2049.69 ± 8.00	792.18 ± 5.57	709.77 ± 19.99
1.70E+05	2.6	N	0.8747 ± 0.0950	1250.44 ± 4.94	2114.08 ± 20.13	863.60 ± 18.97	656.29 ± 57.71
1.70E+05	2.8	N	0.8694 ± 0.1282	1250.09 ± 3.86	2161.80 ± 21.51	911.71 ± 18.25	583.33 ± 50.67
1.70E+05	3.0	Y	0.7222 ± 0.1349	1248.81 ± 4.53	2205.06 ± 29.60	956.23 ± 26.68	528.02 ± 85.93
1.70E+05	3.2	Y	0.6068 ± 0.1115	1245.52 ± 2.41	2251.44 ± 27.08	1005.90 ± 24.94	485.79 ± 75.42
1.70E+05	3.4	Y	0.5496 ± 0.1191	1247.38 ± 3.32	2276.05 ± 19.78	1028.80 ± 17.12	414.47 ± 71.70
1.70E+05	3.6	Y	0.4024 ± 0.0905	1244.92 ± 1.70	2303.92 ± 32.02	1058.95 ± 30.44	335.14 ± 52.99
1.70E+05	3.8	Y	0.2846 ± 0.0788	1245.06 ± 0.94	2333.20 ± 37.19	1088.16 ± 36.98	282.99 ± 46.90
1.70E+05	4.0	Y	0.2164 ± 0.0649	1244.30 ± 1.04	2334.42 ± 61.49	1090.12 ± 61.61	232.35 ± 37.42
1.70E+05	4.2	Y	0.1653 ± 0.0367	1246.47 ± 1.31	2368.91 ± 38.55	1122.44 ± 39.60	203.13 ± 25.45
1.70E+05	4.4	Y	0.0983 ± 0.0128	1244.89 ± 0.72	2354.85 ± 62.08	1109.93 ± 61.97	165.06 ± 19.99
1.70E+05	4.6	Y	0.0714 ± 0.0087	1246.81 ± 0.79	2375.87 ± 66.42	1129.04 ± 66.04	148.93 ± 17.36
1.70E+05	4.8	Y	0.0582 ± 0.0058	1246.99 ± 1.30	2400.12 ± 61.36	1153.13 ± 61.52	130.44 ± 15.50
1.70E+05	5.0	Y	0.0460 ± 0.0028	1245.56 ± 0.89	2398.31 ± 58.62	1152.73 ± 58.02	107.67 ± 6.40
4.00E+05	2.9	N	1.2260	978.93	2217.04	978.93	592.87
4.00E+05	3.0	Y	0.9641	996.94	2222.42	996.94	517.28
4.00E+05	3.5	Y	0.4840	1112.56	2330.68	1112.56	352.36
4.00E+05	4.0	Y	0.2010	1163.63	2380.19	1163.63	202.90
4.00E+05	4.5	Y	0.1000	1200.60	2416.89	1200.60	124.61
4.00E+05	5.0	Y	0.0700	1215.38	2433.30	1215.38	87.84

Table 6.2

Output from the cases simulated. For values with \pm figures quoted the values refers to the mean value of the variable once the system has reached a quasi steady state in these cases the \pm figure refers to the standard deviation of the variable from its mean position. In cases where \pm values are not quoted then the necessary data to calculate the mean and standard deviation were not output during the simulation and the values at the end of the simulation are used. Values printed in grey belong to cases that are thought to be unstable and where the marker method employed has failed.

Ra	Density (%)	Stable?	\hat{Q}_{CMB} (G W)	\hat{Q}_s (G W)	Nusselt Number	RMS Surface Velocity (cm / year)	Total Time Simulated (B years)	N ^o Of Over Turns
3.40E+04	2.4	N	1330 ± 36.7	3400 ± 208.0	7.40	0.093	23.92	1.2
3.40E+04	2.6	N	1120 ± 34.6	3190 ± 172.0	7.11	0.093	75.75	0.8
3.40E+04	2.8	N	907 ± 30.2	2990 ± 141.0	6.69	0.080	155.90	1.6
3.40E+04	3.0	Y	793 ± 17.0	2850 ± 61.0	6.17	0.067	155.90	1.4
3.40E+04	3.2	Y	695 ± 16.1	2730 ± 36.7	5.88	0.061	155.10	1.3
3.40E+04	3.4	Y	692 ± 12.4	2730 ± 28.3	5.95	0.064	29.46	1.3
3.40E+04	3.6	Y	691 ± 12.2	2730 ± 27.8	5.95	0.067	70.64	2.4
3.40E+04	3.8	Y	700 ± 9.1	2740 ± 27.6	5.96	0.070	229.60	9.4
3.40E+04	4.0	Y	698 ± 9.9	2750 ± 28.7	6.02	0.072	588.50	23.9
3.40E+04	4.2	Y	703 ± 8.5	2750 ± 27.6	6.00	0.072	862.00	36.0
3.40E+04	4.4	Y	706 ± 9.2	2750 ± 26.5	5.98	0.071	45.54	2.9
3.40E+04	4.6	Y	708 ± 13.5	2760 ± 26.6	6.02	0.072	79.11	4.4
3.40E+04	4.8	Y	718 ± 15.5	2770 ± 27.1	6.05	0.074	242.30	14.8
3.40E+04	5.0	Y	726 ± 13.4	2770 ± 26.2	6.06	0.075	309.70	19.4
4.10E+04	2.4	N	1380 ± 33.6	3440 ± 228.0	7.02	0.111	309.60	19.6
4.10E+04	2.6	N	1210 ± 50.1	3340 ± 186.0	7.22	0.103	118.51	6.4
4.10E+04	2.8	N	1030 ± 35.2	3120 ± 138.0	6.42	0.090	256.20	18.7
4.10E+04	3.0	Y	881 ± 24.3	2930 ± 57.7	6.37	0.076	258.00	18.2
4.10E+04	3.2	Y	801 ± 18.9	2840 ± 37.3	6.22	0.074	258.20	18.4
4.10E+04	3.4	Y	802 ± 19.7	2830 ± 32.9	6.20	0.075	67.92	4.8
4.10E+04	3.6	Y	816 ± 11.7	2850 ± 30.2	6.23	0.079	41.62	2.6
4.10E+04	3.8	Y	813 ± 11.2	2850 ± 30.5	6.21	0.080	258.80	17.6
4.10E+04	4.0	Y	801 ± 14.8	2840 ± 28.8	6.18	0.080	259.00	17.6
4.10E+04	4.2	Y	799 ± 13.6	2840 ± 27.7	6.23	0.082	266.90	19.1
4.10E+04	4.4	Y	804 ± 12.0	2850 ± 28.0	6.25	0.082	23.94	2.1
4.10E+04	4.6	Y	810 ± 12.0	2860 ± 28.1	6.25	0.083	290.20	16.0
4.10E+04	4.8	Y	813 ± 13.4	2860 ± 27.5	6.23	0.083	322.70	9.7
4.10E+04	5.0	Y	824 ± 14.7	2870 ± 27.1	6.28	0.087	314.20	7.9
8.40E+04	2.4	N	1780 ± 71.4	3880 ± 188.0	7.81	0.148	22.55	1.4
8.40E+04	2.6	N	1610 ± 49.0	3670 ± 188.0	7.97	0.142	334.10	14.0
8.40E+04	2.8	N	1470 ± 40.7	3500 ± 128.0	7.47	0.120	260.70	12.1
8.40E+04	3.0	Y	1340 ± 53.6	3310 ± 103.0	7.67	0.114	303.10	14.1
8.40E+04	3.2	Y	1310 ± 48.8	3260 ± 63.8	7.18	0.120	30.11	1.7
8.40E+04	3.4	Y	1310 ± 42.9	3270 ± 65.3	7.25	0.125	175.40	10.3
8.40E+04	3.6	Y	1290 ± 51.8	3260 ± 52.3	7.13	0.123	153.70	10.0
8.40E+04	3.8	Y	1250 ± 45.3	3230 ± 41.1	7.05	0.122	181.90	12.9
8.40E+04	4.0	Y	1250 ± 50.1	3230 ± 35.1	7.10	0.125	36.80	3.0
8.40E+04	4.2	Y	1240 ± 44.6	3240 ± 35.2	7.06	0.124	67.00	5.1
8.40E+04	4.4	Y	1240 ± 40.7	3240 ± 32.0	7.07	0.127	89.90	7.8
8.40E+04	4.6	Y	1230 ± 50.3	3230 ± 31.0	7.02	0.127	129.00	12.1
8.40E+04	4.8	Y	1230 ± 43.9	3240 ± 30.8	7.05	0.130	29.30	4.1
8.40E+04	5.0	Y	1230 ± 33.7	3240 ± 30.9	7.05	0.134	29.50	3.9
1.70E+05	2.4	N	2510 ± 87.7	4410 ± 287.0	10.85	0.196	29.60	3.9
1.70E+05	2.6	N	2280 ± 79.0	3940 ± 320.0	9.53	0.195	19.78	1.9
1.70E+05	2.8	N	2130 ± 103.0	3770 ± 207.0	8.53	0.174	256.39	18.5
1.70E+05	3.0	Y	2050 ± 124.0	3650 ± 208.0	8.35	0.174	303.29	13.4
1.70E+05	3.2	Y	1950 ± 151.0	3560 ± 156.0	8.22	0.173	211.29	12.6
1.70E+05	3.4	Y	1940 ± 154.0	3590 ± 133.0	8.19	0.180	23.88	1.8
1.70E+05	3.6	Y	1920 ± 159.0	3570 ± 111.0	8.05	0.184	211.29	11.0
1.70E+05	3.8	Y	1860 ± 173.0	3570 ± 100.0	8.01	0.187	209.09	11.7
1.70E+05	4.0	Y	1880 ± 203.0	3540 ± 95.9	7.92	0.190	296.59	17.7
1.70E+05	4.2	Y	1800 ± 136.0	3580 ± 82.6	7.97	0.195	29.65	2.2
1.70E+05	4.4	Y	1870 ± 193.0	3540 ± 88.6	7.89	0.206	107.99	7.1
1.70E+05	4.6	Y	1840 ± 180.0	3560 ± 87.1	7.87	0.210	119.09	9.4
1.70E+05	4.8	Y	1800 ± 187.0	3560 ± 83.5	7.87	0.212	165.79	14.0
1.70E+05	5.0	Y	1810 ± 165.0	3560 ± 80.5	7.91	0.215	55.49	4.6
4.00E+05	2.9	N	3380 ± 82.4	4600 ± 336.0	11.10	0.275	86.99	7.8
4.00E+05	3.0	Y	3410 ± 128.0	4170 ± 105.0	9.66	0.279	125.79	12.5
4.00E+05	3.5	Y	3000 ± 152.0	4220 ± 84.8	9.49	0.287	209.19	22.4
4.00E+05	4.0	Y	2940 ± 248.0	4210 ± 98.3	9.41	0.306	45.99	6.0
4.00E+05	4.5	Y	2900 ± 281.0	4240 ± 115.0	9.47	0.326	45.09	4.9
4.00E+05	5.0	Y	2890 ± 268.0	4250 ± 111.0	9.51	0.333	66.19	7.2

Table 6.3

Output from the cases simulated. For values with \pm figures quoted the values refers to the mean value of the variable once the system has reached a quasi steady state in these cases the \pm figure refers to the standard deviation of the variable from its mean position. In cases where \pm values are not quoted then the necessary data to calculate the mean and standard deviation were not output during the simulation and the values at the end of the simulation are used. Values printed in grey belong to cases that are thought to be unstable and where the marker method employed has failed.

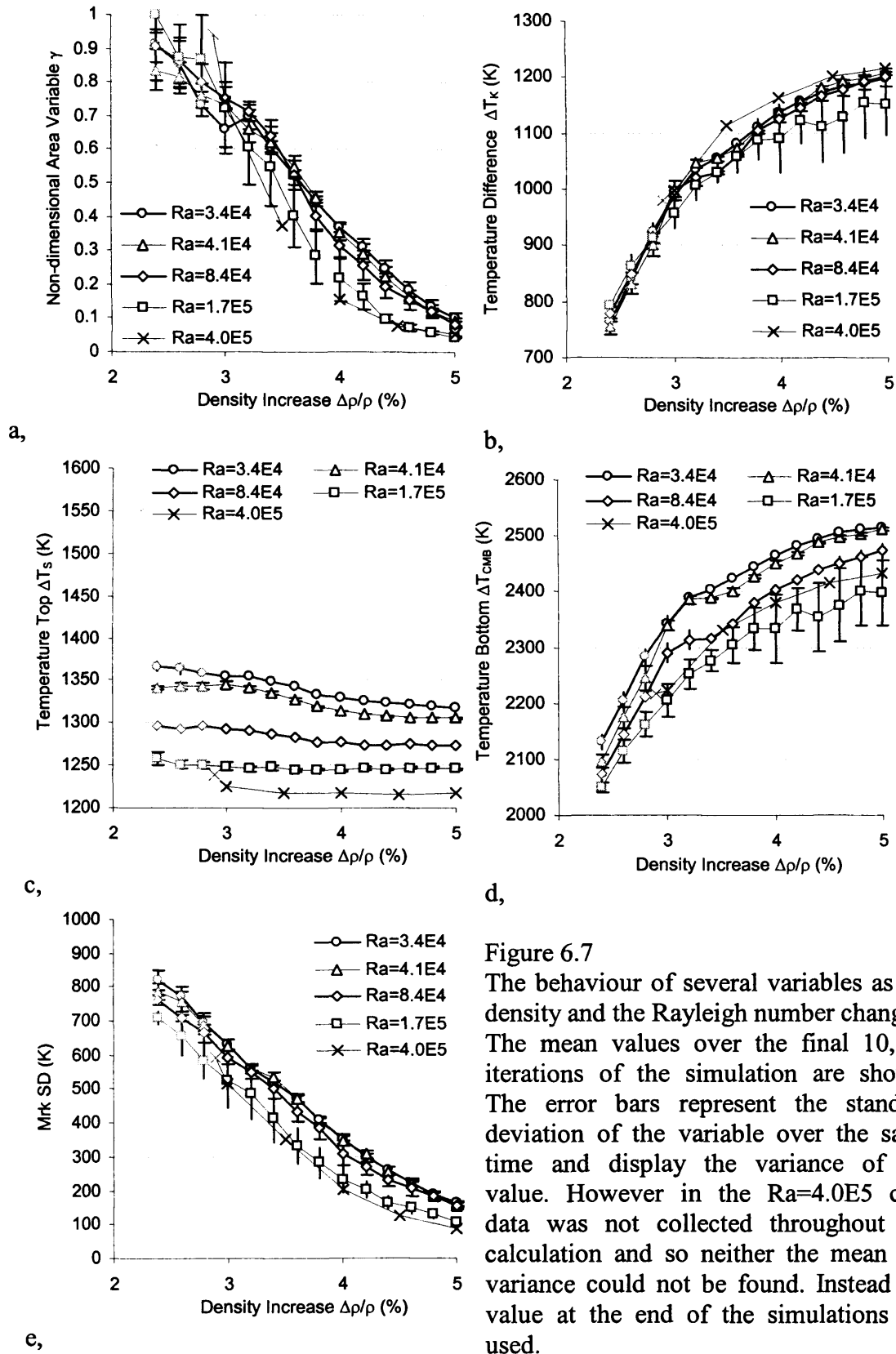


Figure 6.7

The behaviour of several variables as the density and the Rayleigh number change. The mean values over the final 10,000 iterations of the simulation are shown. The error bars represent the standard deviation of the variable over the same time and display the variance of the value. However in the $Ra=4.0E5$ case data was not collected throughout the calculation and so neither the mean nor variance could not be found. Instead the value at the end of the simulations are used.

6.5 Coupling between the layers

To investigate the type of coupling between the two layers we looked at the up-welling and down-welling structures in the simulations. We calculated the component of the flow velocity that was in the radial direction ($v_{\text{rad}}\%$) for each of the data points in the TERRA grid. This was achieved by taking the dot product of the velocity vector (\underline{v}) at a given data point with the normalised unit vector to the data point from the origin ($\hat{\underline{r}}$).

$$v_{\text{rad}} \% = \frac{\underline{v} \cdot \hat{\underline{r}}}{|\underline{v}|} \times 100\% \quad (6.5)$$

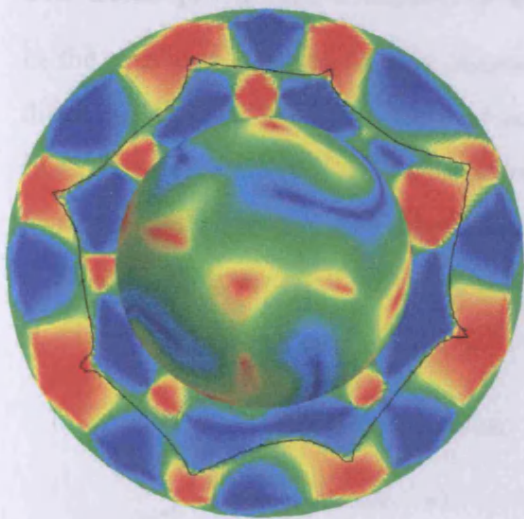
The values of $v_{\text{rad}}\%$ can then be outputted in a format that can be interpreted in the same manner as the thermal field by the Mantlevis visualisation program. This method reduces the vector velocity field to a scalar field; an alternative would be to look directly at the vector field. We have chosen not to look at the vector field for a number of reasons. It is difficult to display a vector as part of a larger 3D image. This may be possible in a 3D stereo visualisation suite but the images produced would not translate well to figures that could be used in publication. It is possible to reduce the vector data to 2D and this can be displayed easily in a 2D image. However the images produced can be misleading as a 2D slice is taken through a more complex 3D structure. A second advantage to reducing the velocity field to a scalar field is that scalar fields can be represented in Mantlevis that is the most powerful visualisation tool available for data from TERRA calculations.

The component of the velocity in the radial direction is shown in figure 6.8. Up-wellings are shown as red and down-welling in blue. In section 2.7.3 we discuss that there are two modes in which the boundary between the two layers could be coupled. In the first, viscosity forces dominate the flow field at the interface between the two layers. In this case the flow field is symmetrical across the interface between the two layers. The second case is when thermal buoyancy forces dominate, causing up-welling and down-wellings to continue through across the interface.

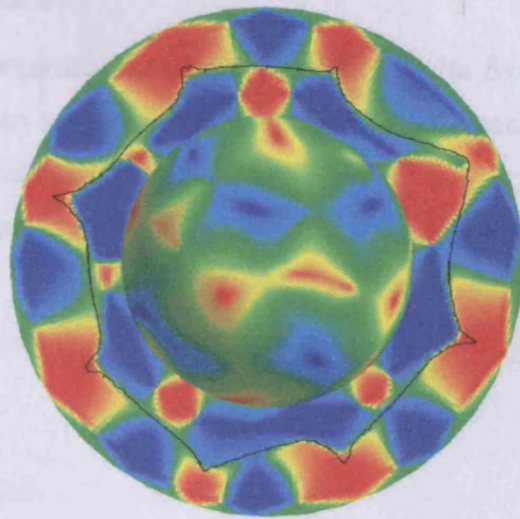
In figure 6.8a 6.8b we see that the up-welling and down-welling structures are symmetrical across the interface suggesting that the layers are viscously coupled. As the Rayleigh number increases the system seems to move away from a viscously coupled state and we see increasing signs of thermal coupling. The highest Rayleigh

number case presented is shown in 6.8 and displays signs of both viscous and thermal coupling with neither coupling systems obviously being dominant.

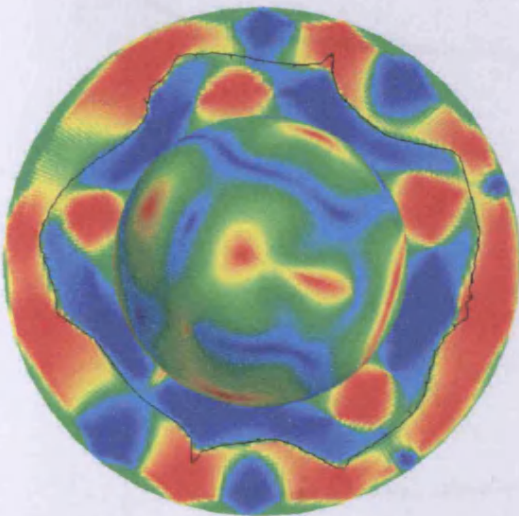
There is evidence that as the Rayleigh number increases the system moves from viscous coupling to thermal coupling.



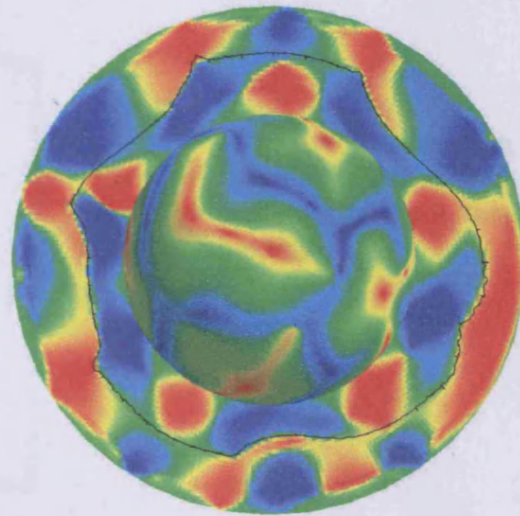
a, $Ra_T = 3.4 \times 10^4$



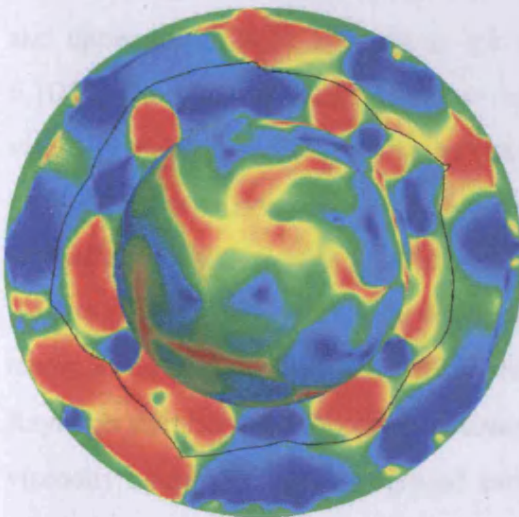
b, $Ra_T = 4.1 \times 10^4$



c, $Ra_T = 8.1 \times 10^4$



d, $Ra_T = 1.7 \times 10^5$



e, $Ra_T = 4.0 \times 10^5$

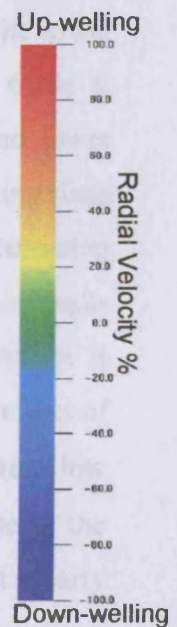


Figure 6.8
The velocity structure of a series of layered cases with different Rayleigh numbers. A cross section of the mantle is shown with colour representing the proportion of the velocity of flow that is radially outward i.e. red sections are up-wellings while blue are down-wellings. The cases shown have reached their quasi steady state and have a layer at 1500km depth and a density increase of 4.0%.

6.6 Changing the viscosity structure

In the previous sections of this chapter we presented data from simulations with five different Rayleigh numbers. Four of these cases were repeated with the only difference from the earlier runs being that a different radial viscosity profile was applied.

The cases run had the same parameters as those presented in table 6.1 with reference viscosities of 1.00×10^{23} , 8.25×10^{22} , 4.00×10^{22} & 2.00×10^{22} . These result in Rayleigh numbers Ra_T of 1.751×10^4 , 2.122×10^4 , 4.377×10^4 & 8.755×10^4 respectively.

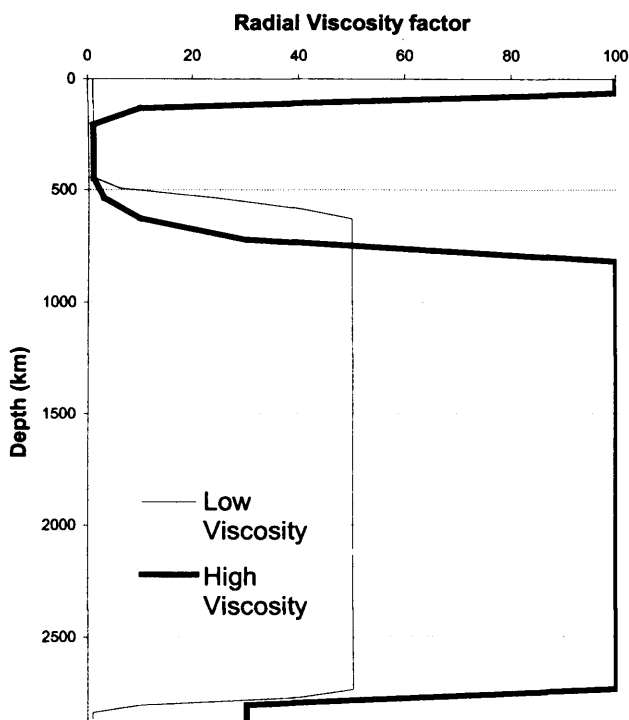


Figure 6.9
The viscosity structure used in the runs presented in this section (bold line) and the earlier in this chapter (thin line).

Results do agree with the earlier cases in many respects: the temperature in the lower and upper layers both increase as the Rayleigh number is decreased (Figure 6.10c & 6.10d). Though the temperature in both layers is significantly hotter in the lower viscosity cases presented in this section. The temperature contrasts across the interface between the two layers are however largely unchanged (Figure 6.10b). The decreasing temperature contrast with increasing Rayleigh number is not apparent in these results (Figure 6.10b). Analysis of the thermal balance of the system suggests that system is not in a stratified layered state when the density contrast falls below 3%. The effect of Rayleigh number on the non-dimensional area variable γ is not as clear in these low viscosity results as those presented earlier in the chapter. This is probably due to the smaller range of Rayleigh numbers studied. However, figure 6.10a while not clearly showing a trend does suggest that an increase in the Rayleigh number could produce an

increase in γ ; suggesting that increasing Ra makes a layered system less stable. This is contrary the conclusion we reached in section 6.4 (Stability of the layering) where we concluded that an increase in Ra would make the system more stable. Figure 6.10e does not show a clear effect on the standard deviation of the marker heights when the Rayleigh number is increased. The range of Rayleigh numbers studied for this viscosity structure is not sufficient to determine the effect of Ra on the stability of layered system.

When the viscosity jump in the lower mantle is increased the temperature of both the upper and lower layers is increased. The temperature increase across the deformable boundary remains the same.

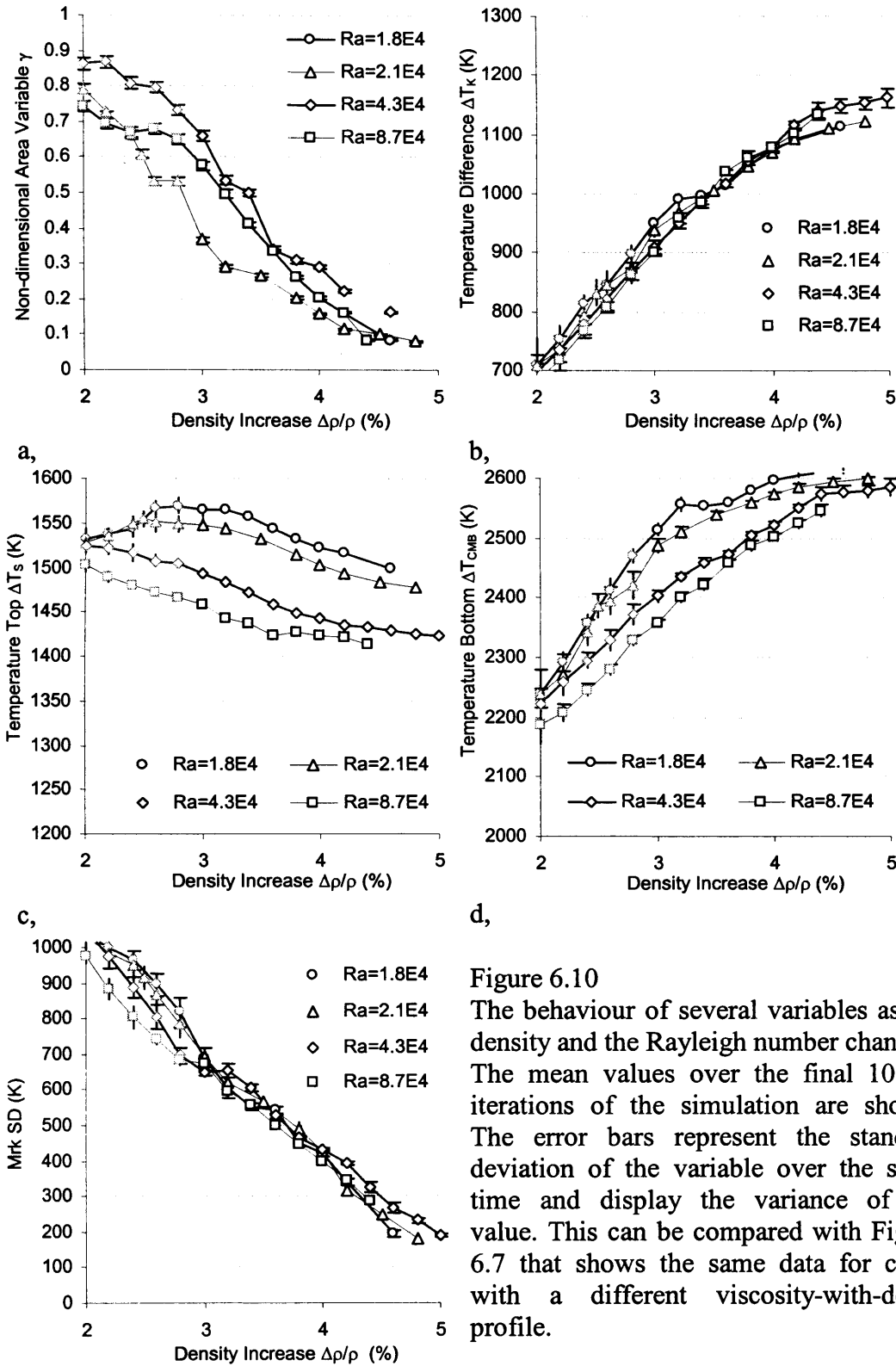


Figure 6.10

The behaviour of several variables as the density and the Rayleigh number change. The mean values over the final 10,000 iterations of the simulation are shown. The error bars represent the standard deviation of the variable over the same time and display the variance of the value. This can be compared with Figure 6.7 that shows the same data for cases with a different viscosity-with-depth profile.

7 Implications for Earth

Recall from chapter 2 that using previous work we can place the following limitations on a layered mantle.

1. A deep layer is not expected to have an effective density contrast $(\Delta\rho/\rho)_{\text{eff}}$ greater than 0.4 across it [Masters & Gubbins 2003].
2. To remain invisible to seismic scattering imaging techniques the interface between the two layers must have regions in which the inclination is greater than 30° [Castle & van der Hilst 2003a].
3. The maximum rate of entrainment from the deep layer over the last 4.2 G years must be less than 150km^3 per year (else the layer would have mixed).
4. The rate of internal heat production in an enriched layer is likely to be around $5 \times 10^{-12} \text{ W kg}^{-1}$ [Becker et al. 1999]

It is the aim of this chapter (and indeed this thesis) to add some limitations to this list and if possible confirm some of these existing constraints.

7.1 Using entrainment to constrain the density contrast across the deformable boundary

Davaille [1999b] derives two equations (4.14 & 4.15) to describe the rates of entrainment across a layered system, see section 4.4. These two equations describe upwards (plume-like) entrainment Q_\uparrow and down-wards (sheet-like) entrainment Q_\downarrow per cell. A cell is defined as a square region on the interface between the two layers containing one plume and surrounded by sheet-like entrainment (see figure 4.7).

$$Q_\uparrow = C_1 \frac{\kappa h_0}{B^2} \text{Ra}_u^{1/3} \quad (4.14)$$

$$Q_\downarrow = C_2 \frac{\kappa h_0}{B} \text{Ra}_l^{1/5} \quad (4.15)$$

In section 4.4 we saw that Davaille makes an assumption that viscosity forces are negligible to entrainment and re-derived her equations with these forces to produce the following equations.

$$Q_\uparrow = C_1 \frac{\kappa}{h_0} \left\{ \frac{h_0}{B} \text{Ra}_u^{1/6} - \frac{\eta_u \kappa}{\Delta\rho g h_0^2} \text{Ra}_u^{7/6} \right\}^2 - \text{Plumes} \quad (4.44)$$

$$Q_{\downarrow} = C_2 \left\{ \frac{\kappa h_0}{B} Ra_1^{1/5} - \frac{\eta_1 \kappa^2}{\Delta \rho g h_0^2} Ra_1^{1/5} \right\} - \text{Sheets} \quad (4.38)$$

Where Ra_u & Ra_l are the Rayleigh numbers of the upper and lower layers respectively...

$$Ra_l = \frac{\alpha_l \rho g \Delta T h_0^3}{\kappa \eta_l} \quad (4.45)$$

$$Ra_u = \frac{\alpha_u \rho g \Delta T (H - h_0)^3}{\kappa \eta_u} \quad (4.46)$$

We can use equations 4.14, 4.15 and the maximum rate of entrainment derived in section 4.4.5 to find the minimum density contrast at a given depth required for a layer to survive entrainment over Earth history.

E_{\max} is the maximum rate of entrainment possible in a layered system.

$$E_{\max} = 150 \text{ km}^3 \text{ year}^{-1}.$$

$$(Q_{\uparrow} + Q_{\downarrow}) \times \{N^{\circ} \text{ of cells}\} = E_{\max} \quad (7.1)$$

The number of cells in a layer can be calculated by using Davaille's assumption that the width of a cell is equal to the depth of the lower layer. We can then calculate how many cells will fit onto the deformable boundary.

$$\{N^{\circ} \text{ of cells}\} = \frac{4 \pi R_K^2}{h_0^2} \quad (7.2)$$

Combining equations 7.1, 7.2, 4.14, 4.15 and 2.10 $B = \Delta \rho \div \rho (\alpha_l T_{\text{CMB}} - \alpha_u T_s)$

$$4 \pi R_K^2 C_1 \left(\frac{\rho}{\Delta \rho} \right)^2 (\alpha_l T_{\text{CMB}} - \alpha_u T_s)^2 \frac{\kappa}{h_0} Ra_u^{1/5} +$$

$$4 \pi R_K^2 C_2 \left(\frac{\rho}{\Delta \rho} \right) (\alpha_l T_{\text{CMB}} - \alpha_u T_s) \frac{\kappa}{h_0} Ra_l^{1/5} = E_{\max}$$

Which is rewritten as...

$$E_{\max} \left(\frac{\Delta \rho}{\rho} \right)^2 - K_1 \left(\frac{\Delta \rho}{\rho} \right) - K_2 = 0$$

Where...

$$K_1 = 4 \pi R_K^2 C_2 (\alpha_l T_{\text{CMB}} - \alpha_u T_s) \frac{\kappa}{h_0} Ra_l^{1/5} \quad (7.3)$$

$$K_2 = 4 \pi R_K^2 C_1 (\alpha_1 T_{\text{CMB}} - \alpha_u T_S)^2 \frac{\kappa}{h_0} \text{Ra}_u^{1/3} \quad (7.4)$$

Which solves...

$$\left(\frac{\Delta \rho}{\rho} \right) = \frac{K_1 \pm \sqrt{K_1^2 + 4 E_{\text{max}} K_2}}{2 E_{\text{max}}} \quad (7.5)$$

We use equation 7.5 to find the density contrast that will produce the maximum rate of entrainment at a given depth. This density contrast can be thought of as the minimum possible value since if the density contrast were any smaller than this any layer would have completely entrained in the lifetime of Earth. Figure 7.1 shows the solutions of equation 7.5 for an Earth-like case with the parameters shown in table 4.5. There is a strong increase in the density contrast at the CMB due to the assumption used that the cell size is equal to the depth of the lower layer h_0 and the $1/h_0$ relationship that this causes. The values of the density contrast required to sustain a layered mantle throughout the history of Earth are very small and do not place any real constraint on the lower end of the likely density contrast of a deep layer.

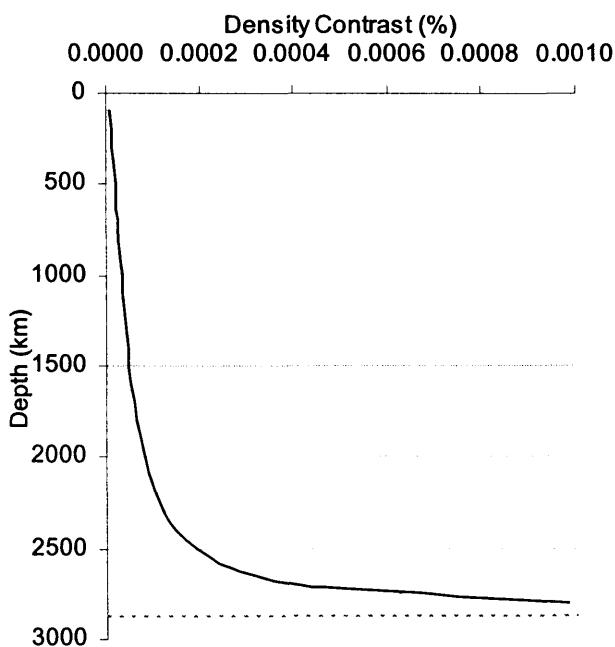


Figure 7.1

The minimum density contrast needed to keep entrainment sufficiently small to stop a layer from mixing in the lifetime of Earth based on Davaille's [1999b] equations.

In section 4.4.4 we saw that Davaille drops the viscosity terms in her calculations since they are negligible in the cases she studied. We saw that in Earth-like cases the viscosity term did have a significant effect. We repeat the above calculations but include the viscosity terms...

Combining equations 7.1, 7.2, 4.44, 4.38 and 2.10 $B = \Delta\rho \div \rho (\alpha_1 T_{\text{CMB}} - \alpha_u T_S)$

$$C_1 \frac{\kappa}{h_0} \frac{4\pi R_K^2}{h_0^2} \left\{ \left(\frac{\rho}{\Delta\rho} \right) (\alpha_1 T_{\text{CMB}} - \alpha_u T_S) h_0 \text{Ra}_u^{1/6} - \frac{\eta_u \kappa}{\Delta\rho g h_0^2} \text{Ra}_u^{1/6} \right\}^2 +$$

$$C_2 \frac{4\pi R_K^2}{h_0^2} \left\{ \left(\frac{\rho}{\Delta\rho} \right) (\alpha_1 T_{\text{CMB}} - \alpha_u T_S) \kappa h_0 \text{Ra}_1^{1/5} - \frac{\eta_1 \kappa^2}{\Delta\rho g h_0^2} \text{Ra}_1^{1/5} \right\} = E_{\text{max}}$$

Which can be rewritten as

$$B_1 \left\{ \left(\frac{\rho}{\Delta\rho} \right) B_2 - B_3 \right\}^2 + \left\{ \left(\frac{\rho}{\Delta\rho} \right) B_4 - B_5 \right\} - B_6 E_{\text{max}} = 0 \quad (7.6)$$

Where constants $B_{1,2,3,4,5}$ are...

$$B_1 = C_1 \frac{\kappa}{h_0} ; B_2 = (\alpha_1 T_{\text{CMB}} - \alpha_u T_S) h_0 \text{Ra}_u^{1/6} ; B_3 = \frac{\eta_u \kappa}{\Delta\rho g h_0^2} \text{Ra}_u^{1/6}$$

$$B_4 = C_2 (\alpha_1 T_{\text{CMB}} - \alpha_u T_S) \kappa h_0 \text{Ra}_1^{1/5} ; B_5 = C_2 \frac{\eta_1 \kappa^2}{\Delta\rho g h_0^2} \text{Ra}_1^{1/5} ; B_6 = \frac{h_0^2}{4\pi R_K^2}$$

Rearranging equation 7.4 gives...

$$B_1 B_2^2 \left(\frac{\rho}{\Delta\rho} \right)^2 - 2 B_1 B_2 B_3 \left(\frac{\rho}{\Delta\rho} \right) + B_1 B_3^2 + \left(\frac{\rho}{\Delta\rho} \right) B_4 - B_5 - B_6 E_{\text{max}} = 0$$

$$\left(B_6 E_{\text{max}} + B_5 - B_1 B_3^2 \right) \left(\frac{\Delta\rho}{\rho} \right)^2 - (B_4 - 2 B_1 B_2 B_3) \left(\frac{\Delta\rho}{\rho} \right) - B_1 B_2^2 = 0$$

$$A_1 \left(\frac{\Delta\rho}{\rho} \right)^2 - A_2 \left(\frac{\Delta\rho}{\rho} \right) - A_3 = 0$$

Where $A_1 = B_6 E_{\text{max}} + B_5 - B_1 B_3^2$; $A_2 = B_4 + 2 B_1 B_2 B_3$; $A_3 = B_1 B_2^2$

So the density contrast can be expressed as...

$$\left(\frac{\Delta\rho}{\rho} \right) = \frac{A_2 \pm \sqrt{A_2^2 + 4 A_1 A_3}}{2 A_1} \quad (7.7)$$

Where...

$$A_1 = \frac{h_0^2}{4\pi R_K^2} E_{\text{max}} + C_2 \frac{\eta_1 \kappa^2}{\Delta\rho g h_0^2} \text{Ra}_1^{1/5} - \frac{\eta_u^2 \kappa^2}{\Delta\rho^2 g^2 h_0^4} \text{Ra}_u^{1/3} \quad (7.8)$$

$$A_2 = C_2 (\alpha_1 T_{\text{CMB}} - \alpha_u T_S) \kappa h_0 \text{Ra}_1^{1/5} - 2 C_1 (\alpha_1 T_{\text{CMB}} - \alpha_u T_S) \frac{\eta_u \kappa^2}{\Delta\rho g h_0^2} \text{Ra}_u^{1/2} \quad (7.9)$$

$$A_3 = C_1 (\alpha_1 T_{\text{CMB}} - \alpha_u T_S)^2 \kappa h_0 \text{Ra}_u^{1/3} \quad (7.10)$$

Equation 7.7 cannot be solved directly but an iterative method can be used. A program was written to do this and is shown in appendix H. The results for an Earth like case are shown in figure 7.2. These are significantly different from the results shown in figure 7.1. The inclusion of the viscosity term generally increases the density contrast needed to reduce entrainment below the possible maximum values. The density increase needed becomes very large between 1500km and 2000km depth. If these results are accurate they rule out the possibility of a deep layer within the mantle.

However, the results of our calculations have shown numerous cases of deep layers that are indeed stable and that when these results are extrapolated to an Earth-like case remain stable. Davaille uses the assumption that the planform of entrainment is always upward plumes and downward sheets. In section 4.4.1 we challenged this assumption and demonstrated that in our runs the plan form of entrainment features changes with depth. For an interface high in the mantle, upwards entrainment takes the form of plumes and downwards entrainment takes the form of sheets. As the layer is placed deeper and deeper in the mantle however the plan-form changes with deep layers having upward sheet-like entrainment and down-ward plume like entrainment. If this is the case then Davaille's results shown in figures 7.1 & 7.2 are only valid in the upper half of the mantle. As the plan form changes the graph should look symmetrical round the mid-mantle and a layered system would require a smaller density contrast as the depth of the layer approached the CMB [Davaille et al. 2003].

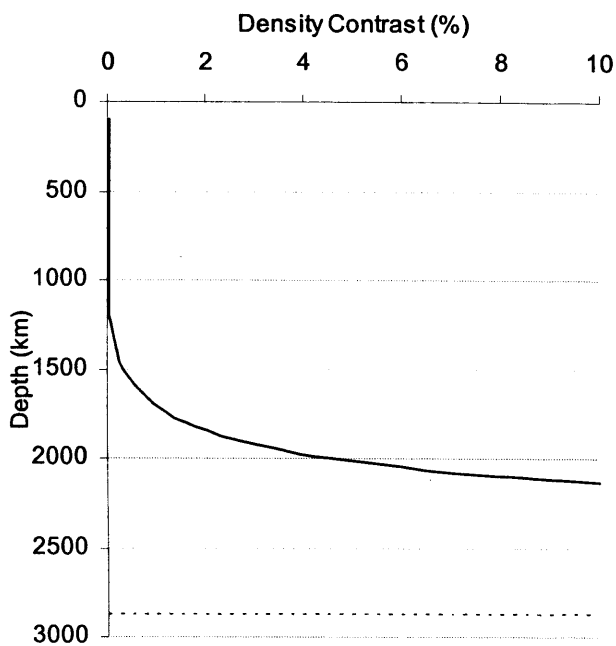


Figure 7.2

The minimum density contrast needed to keep entrainment sufficiently small to stop a layer from mixing in the lifetime of Earth based on Davaille's [1999b] equations with the viscosity forces term included.

This procedure can be repeated with time integration of the system to allow for the changing values of entrainment as the two layers mix (changing their densities) and thickness of the lower layer changes [Gonnermann et al. 2002]. In these calculations the time dependence of the maximum entrainment condition[†] may explain why their results are so different from those presented in this section. However, Gonnermann et al. [2002] follow on from the work of Sleep [1988]. It has been shown that this represents the upper limit of the possible entrainment [Zhong & Hager 2003]. This is unfortunate since we are trying to find a lower limit on the possible density contrast but it is possible that a dense layer with a smaller density contrast than that quoted by Gonnermann et al. [2002] could have survived throughout the history of Earth's mantle.

Calculations based on the rates of entrainment presented by Davaille [1999b] do not place any significant constraints on the lower-end estimates of the possible density increase of a lower layer.

However work by Gonnermann et al. [2002] suggest that a minimum buoyancy ratio of 1.8 is needed to maintain a layer at 2100km depth in a system with $Ra=10^8$ this

[†] Unfortunately Gonnerman et al. do not quote the maximum entrainment condition or the method they use to calculate the temperature in the lower layer and so it is not possible to repeat their calculations.

[†] Unfortunately Gonnerman et al. do not quote the parameters used in their calculations and this value is based on $\rho=5 \times 10^3$, $\alpha=1 \times 10^{-5}$, $\Delta T=2000 \div 3$.

corresponds to a density contrast of 1.2%. However, it is possible for a layer to remain within the mantle with a smaller density contrast than this [Zhong & Hager 2003] and so it cannot be considered as a true minimum value.

7.2 Coupling between the two layers

In section 4.4 we discuss how Davaille [1999b] uses the assumption that a layered system would have viscous coupling in the derivation of her rate of entrainment formula. We can use similar arguments to Davaille by considering the balance of viscous and thermal forces at the interface between two layers. We consider a small volume of the upper layer directly above the interface. The volume is travelling with a velocity v_1 compared to a plane of lower mantle material that has a velocity v_2 . This plane is driving the volume via a viscous stress field. The volume has a temperature T_k compared to T_u the temperature of the surrounding material, see figure 7.3.

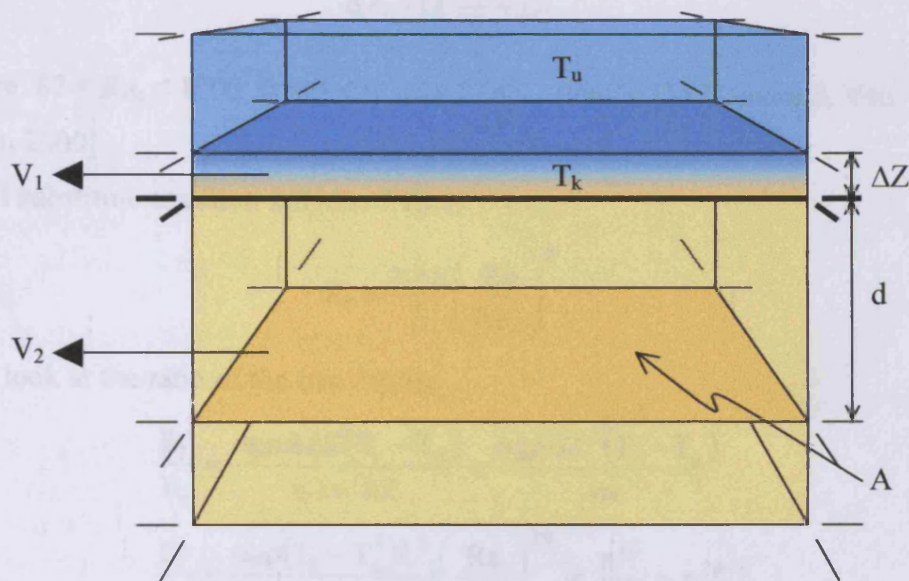


Figure 7.3

A schematic of the situation used to derive the equations for the viscous and thermal forces. A thin layer of thickness ΔZ is above the boundary between two layers and has two forces acting on it. The first is caused by the viscous drag of a plate a depth d below it. This plate represents the flow in the lower layer and has velocity v_2 . There is a shear stress zone between the plate and boundary that is moving with velocity v_1 . Thermal buoyancy causes a second force acting on the plate. The plate has a temperature T_k compared to the surrounding temperature of T_u . The boundary between the two layers is shown as a thick black line.

The thermal buoyancy force F_T is given by...

$$F_T = \alpha g \rho A \Delta Z (T_k - T_u) \quad (7.11)$$

The viscous drag force F_η is given by...

$$F_\eta = \frac{\eta A (v_2 - v_1)}{d} \quad (7.12)$$

If we assume that v_2 is zero and the vertical length scale of the stress field is the same as the thermal field then F_η can be rewritten as...

$$F_\eta = \frac{\eta A v}{\Delta Z} \quad (7.13)$$

As the viscosity approaches zero the Rayleigh number Ra approaches infinity.

Since F_T is independent of the viscosity it will remain constant, F_η will vary. We use the relationship between the thermal boundary thickness and Ra ...

$$\Delta Z = L \left(\frac{Ra_c}{Ra} \right)^\beta \quad (2.8)$$

Where: $87 < Ra_c < 1100$; $0 < \beta < 0.3$ for Earth's mantle [M^cNamara & Van Keken 2000]

...and substitute equation 2.8 into 7.13...

$$F_\eta = \frac{\eta A v}{L} \left(\frac{Ra}{Ra_c} \right)^\beta \quad (7.14)$$

If we look at the ratio of the two forces...

$$\begin{aligned} \frac{F_T}{F_\eta} &= \frac{\alpha g \rho A \Delta Z (T_k - T_u)}{\eta A v / \Delta Z} = \frac{\alpha g \rho \Delta Z^2 (T_k - T_u)}{\eta v} \\ \frac{F_T}{F_\eta} &= \frac{\alpha g \rho (T_k - T_u) L^2 \left(\frac{Ra}{Ra_c} \right)^{2\beta}}{\eta v} \propto \frac{\eta^{2\beta}}{\eta} = \eta^{2\beta-1} \end{aligned}$$

$$\frac{F_T}{F_\eta} \propto \frac{\eta^{2\beta}}{\eta} = \eta^{2\beta-1} \quad (7.15)$$

The values of β for Earth is thought to be less than 0.3 [M^cNamara & Van Keken 2000], so $2\beta-1$ will be negative. As viscosity decreases the thermal forces become much larger than the viscous forces. This explains the change from viscous to thermal coupling as the Ra number increases seen in section 6.5. It also agrees with the

predictions of Richter & Johnson [1974] that at very low Rayleigh number a system will exhibit viscous coupling and the observations of Davaille [2003] and Davaille et al. [1999b] that a layered system moves to thermal coupling when it has high Ra.

We calculate the magnitude of the force per unit area produced by both viscous drag and thermal buoyancy for an Earth-like system using parameters quoted in table 7.1. This results in a viscous stress $F_\eta/A = 3.2 \times 10^8 \text{ Nm}^{-2}$ and the buoyancy stress of $F_T/A = 4.1 \times 10^7 \text{ Nm}^{-2}$; $F_T/F_\eta = 0.13$. Given that the thermal buoyancy stress is an order of magnitude smaller than the viscous force we would expect the viscous coupling to dominate the system. However, the characteristic velocity used of 10cm per year could easily be an order of magnitude too big and in this case the ratio between the two forces would then be very close to one. These results predict that an Earth-like layered system would be viscously coupled though it is possible that neither type of coupling would dominate.

Parameter		Value
Depth of marker surface	D_k	2000 km
Temperature of interface	T_k	1800 K
Temperature of the upper layer	T_u	1200 K
Reference density	ρ	$5.00 \times 10^3 \text{ kg}$
Volume coefficient of thermal expansion	α	$2.0 \times 10^{-5} \text{ K}^{-1}$
Viscosity	η	$7 \times 10^{21} \text{ Pa s}$
Characteristic velocity of mantle flow	v	10 cm year^{-1} $3.2 \times 10^{-9} \text{ m s}^{-1}$
	Ra	1×10^8
Critical Rayleigh number	Ra_C	400
Length scale of convection	L	2870 km
Power used in equations 2.8 & 7.15	β	0.3
Thickness of the thermal boundary, calculated using L, β , Ra, Ra_C	ΔZ	69 km

Table 7.1

The parameters used to calculate the viscous and buoyancy forces at the interface between layers in an Earth-like system. T_k & T_u are extrapolated to Earth-like values from the results presented in chapter 06. The value of η used is that quoted for the lower mantle by Davies [1999, p163].

7.3 Plan form of convection

Previous investigations of mantle convection have shown a series of ridges connecting the plumes at the CMB [Dubuffet et al. 1999, Ratcliff et al. 1997]. These features are often accompanied by sheet-like down-welling. If we consider single-layer convection in which both up-welling and down-welling features are sheet-like then these sheets will collide in the mid-mantle and force a change in the planform of convection from sheet to plume for both the up-welling and down-welling features. Where these cold plumes impact on the CMB they push aside hot material into ridges that then form into the hot sheet-like up-wellings. Likewise at the surface the hot plumes will push cold material into ridges that will form the cold down-welling sheets. See figure 7.4. This change from sheet to plumes causes a planform that is self-sustaining as the plumes and sheets arrange themselves into regular cell patterns at either surface. In an Earth-like system the planform of these coupled sheet-to-plume structures would be determined by plate tectonics since it is the position of plate boundaries that determines the location of subduction material.

This self-sustaining model uses several unrealistic assumptions. We have considered a Cartesian system, in our models and Earth; spherical geometry will have an effect. The smaller surface area of the CMB compared to the Surface[†] means that as cold sheets move downward they would take up an increasingly large proportion of the volume of the mantle at their depth. We would therefore expect the contact between the upward and downward sheets to take place in the deeper mantle. This would also cause the impact of the down-welling features at the CMB to more rigorously dictate the position of the hot ridge structures than the impact of hot plumes will have on the position of cold sheets. For Earth, coupling between hot plumes and cold sheets at the surface can be neglected since the planform of subduction is dictated by plate tectonics not hot anomalies. However our line of reasoning suggests that plumes would exist away from subduction boundaries. This is a feature of hotspot locations [Weinstein & Olson 1989] though some hotspots do exist close to subduction zones. This can in part be explained by the arguments above concerning the less effective coupling at the surface compared to the CMB and by the suggestion that not all hotspots are fed by plumes with a deep origin [Courtillot et al. 2003]. The most significant failing of this model when applied

[†] Earth's surface has an area around 3.3 times bigger than the CMB.

to Earth is that it predicts that plumes should migrate at the same rate as subduction zones and so totally fails to predict the fixity of hotspots and the hot spot reference frame. This may be explained by the absence of a radial viscosity structure from the model or any chemical layering.

In a mantle with a deep deformable layer this coupled system will take place twice, first in the upper layer and again in the lower layer. The cold plumes impacting on the upper surface of the interface will cause downwards depressions; likewise hot plumes impacting on the bottom of the boundary will cause upward bulges. We saw in section 5.5 that the wavelength of undulations of the interface between the layers is longer than the wavelength of the thermal features that feed them. Where hot plumes reach the interface they spread out causing long wavelength features that can be fed by one or more plumes. These long wavelength features are caused by cold/hot reservoirs of material below/above the interface. A consequence of this is that coupling between planform of up-ward and down-ward convection is not as tightly coupled as it is in a whole mantle system. The position of cold plumes will not change the position of up-going sheets as long as they land on the deformable interface in such a way that they add material to a cold reservoir. In this way a layered mantle is able to keep the position of plumes anchored to the same spot [Davaille et al. 2002].

The same arguments used above to explain the fixity of hotspots in a layered mantle are not applicable in a 'pile' type arrangement [Tackely 2000]. Here chemically heterogeneous regions at the CMB are pushed into piles by cold subducted material that is building up there. This is very similar to the coupled model of whole mantle convection we have presented in this section with only the inclusion of these heterogeneous regions within the hot ridges at the CMB. In this arrangement it is unclear why the subducting material would not push these piles around at the same velocity as the plate boundaries wander and hence cause hot spots to also move.

7.4 Lateral coupling

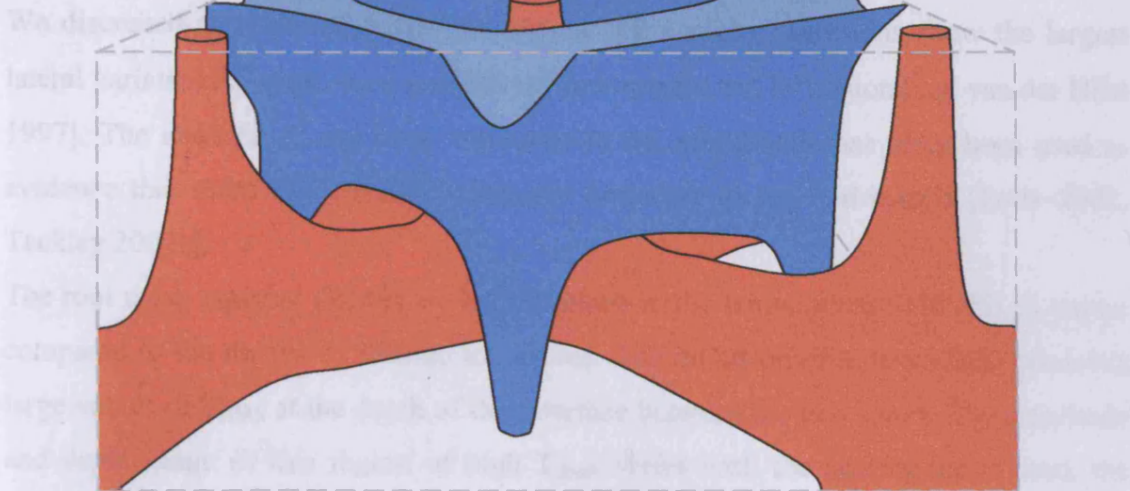


Figure 7.4

A schematic of the coupling between hot and cold anomalies. The blue surface represents cold down-going features, while the red surface represents hot up-going features. Both surfaces switch from sheet to plume like structure in the mid-mantle when they encounter each other. Consequently the hot/cold plumes that arrive the the surface/CMB are in the centre of shells bounded by cold/hot sheets. In this way the system is self sustaining.

7.4 Lateral temperature variations

We discussed in section 2.3.3.4 that seismic tomography inversions show the largest lateral variations in wave speeds in the shallow mantle and D'' region [e.g. van der Hilst 1997]. The absence of any large variations in the mid-mantle has often been used as evidence that there is no thermo chemical boundary in the mid-mantle [Forte 2002; Tackley 2002a].

The root mean squared (RMS) lateral variations in the temperature field (T_{RMS}) can be compared to the results of seismic inversions. The inclusion of a dense layer produces large values of T_{RMS} at the depth of the interface between the two layers. The amplitude and depth range of this region of high T_{RMS} varies with the heating mode used, the depth of the interface, and the density increase across it. In our simulations the boundary conditions causes T_{RMS} to be zero at the surface and also zero at the CMB in cases with bottom heating. However, in all cases with bottom heating the T_{RMS} anomaly associated with the interface is much larger than those at either the upper or lower boundary.

The heating mode used does significantly alter the form of the T_{RMS} anomaly. When only internal heating is present the amplitude of the anomaly at the interface is around 100-150K and is comparable in size to the anomaly produced at the upper boundary, see figure 7.5b and 7.5c. In simulations with bottom heating (or with both internal and bottom heating) the amplitude is much larger, 300-600K. There is very little variation in T_{RMS} between simulations with only bottom heating and those with both bottom and internal heating. This suggests that plumes generated by bottom heating at the CMB is the source of the large T_{RMS} anomaly. In cases with only internal heating there is a region of low T_{RMS} directly below the interface. The absence of plumes that would bring large volumes of hot material to the interface partly explains this. Though, it is uncertain why T_{RMS} would be smaller directly below this interface than in the rest of the lower layer. The size of T_{RMS} in the lower layer is smaller than it is in the upper layer in internally heated cases. In simulations with bottom heating T_{RMS} has similar values in both the upper and lower layer and the T_{RMS} anomaly associated with the interface has the same form on either side of the interface.

Denser lower layers produce T_{RMS} anomalies with smaller amplitudes and are spread across a smaller depth range, see figure 7.5b. The depth of the interface also affects the form of the T_{RMS} anomaly, with the amplitude of the anomaly being largest when the

interface is at a depth of around 1000km[†] and being smaller as the depth of the interfaces approached either the surface or CMB, see figure 7.5a. There is weak evidence over a limited range of Rayleigh numbers Ra that for larger Ra the amplitude of the T_{RMS} anomaly is larger and the depth range over which it is observed decreases, see figure 7.5d. Though changing Ra has the same effect on the T_{RMS} anomalies at the upper and lower boundaries as it does for the anomaly at the interface, i.e. the anomaly at the interface is always larger than those at the surface and CMB.

	Amplitude of T_{RMS} anomaly	The form of T_{RMS}
Heating mode	Internal heating – small values $T_{RMS} = 100-150K$ Bottom heating - big values $T_{RMS} = 300-600K$	Internal heating produces a low T_{RMS} region below the interface and T_{RMS} is smaller in lower layer than the upper layer. Bottom heating produces symmetrical T_{RMS} anomaly and T_{RMS} has similar values in the upper and lower layers.
Density contrast	Larger density contrasts $\Delta\rho/\rho$ produce T_{RMS} anomalies with smaller amplitudes.	Larger density contrasts $\Delta\rho/\rho$ produce T_{RMS} anomalies over a smaller depth range.
Depth	The amplitude has a maximum value when the interface between the layers is at a depth of around 1000km.	Unaffected
Ra	Increasing the Rayleigh number Ra increases the amplitude of the T_{RMS} anomaly.	Increasing the Rayleigh number Ra decreases the depth range of the T_{RMS} anomaly.

If we compare the lateral variations of the temperature in our layered convection simulations to the lateral variations of seismic wave speeds suggested by tomography inversion (figure 2.6) then we find few similarities. Our results are dominated by the large variations in temperature at the depth of the interface between the two layers. In contrast seismic results suggest maximum lateral variations at the surface and D'' regions. We can argue that seismic results sample chemical anomalies in the shallow mantle such as the continental tectosphere [Forte & Perry 2000] and D'' in the lower mantle; these features are not present in our simulations. The thermal boundary conditions in our calculations may also limit the thermal anomalies at the boundaries.

[†] This is around the depth at which the two layers would have the same volume and at which the deformation of the interface is greatest.

The internally heated cases do have a thermal structure that is more likely to produce a seismic structure like that. However, these cases are not realistic.

Our results show that a thermo-chemical boundary in the mantle would produce large lateral temperature variations at the depth of the interface. This is a feature that if present might be expected to be noticed by seismic tomography.

7.4.1 Lateral variations in density structure including chemical buoyancy

An obvious criticism of the root mean squared thermal anomalies presented in the pervious section is that they fail to take into account the seismic effect of the large chemical variations that dominate the convecting system. A temperature variation can be represented as a density change using equation 7.16...

$$\frac{\Delta\rho}{\rho_0} = \alpha\Delta T \quad (7.16)$$

...where $\Delta\rho$ is the temperature difference, ρ_0 is the reference density, α the thermal expansivity, & ΔT the temperature variation. However, in the previous section we presented results in terms of the RMS lateral variations in the temperature field. To compare the results of the combined thermal and chemical variations, instead of converting the temperature difference to an intrinsic density variation, we convert the intrinsic chemical variation to a temperature difference, $\Delta T_{\Delta\rho}$, by rearranging equation 7.17...

$$\Delta T_{\Delta\rho} = \frac{\Delta\rho}{\alpha\rho_0} \quad (7.17)$$

We calculate this value at all points in the TERRA grid: $\Delta T_{\Delta\rho}=0$ for any point in the upper layer; for a point in the lower layer $\Delta T_{\Delta\rho}$ has a fixed value based on the intrinsic density increase in the simulation, and a values somewhere between these upper and lower layer values for points that sample both the upper and lower layers. At these points the value of, $\Delta T_{\Delta\rho}$ is found based on the relative volumes of each layer in the volume 'owned' by the point; see section 3.4.

The RMS lateral temperature can then be calculated for only thermal effects, T_{RMS} ; for the chemical effects, Chem_{RMS} ; and for the thermal effects minus the chemical $T - \text{Chem}_{\text{RMS}}$. It is this final value that best represents the lateral density structure.

We might expect that $T\text{-Chem}_{\text{RMS}}$ of the thermo-chemical boundary would be less than T_{RMS} , however this is not always the case. For very dense layers the RMS anomaly caused by chemical variations is much larger than that produced by temperature variations. So while the chemical and thermal RMS anomalies always act such that they cancel each other out, chemical anomalies are more sensitive to the magnitude of the density contrast. For example, for high-density contrast the combinations of chemical and temperature anomalies can be greater in magnitude (and opposite in sign) than the temperature anomaly alone. E.g. compare figure 7.5b and 7.6b, including the effects of chemical variations increases the size of the effective RMS temperature anomaly. It is only when the density contrast has fallen to $\Delta\rho/\rho=2\%$ that the thermal and chemical effects cancel out.

In the earlier section we saw the amplitude of the T_{RMS} anomaly get smaller as the interface is placed in the shallow and very deep mantle, see figure 7.5a. In figure 7.6a we see the $T\text{-chem}_{\text{RMS}}$ anomaly has increasing amplitude for an interface in the shallow and very deep mantle. The effect of including the chemical component reduces the anomaly when layering is in the mid-mantle but increases it for an interface close to either the upper or lower boundary. The smaller anomaly, T_{RMS} , produced by internally heated cases is no longer the case, since the inclusion of the chemical density greatly increases the amplitude of the RMS anomaly.

The inclusion of the chemical density also changes the effect of the Rayleigh number Ra , see figure 7.6d. We now see a decrease in the amplitude of RMS anomaly as Ra increases.

In summary, the introduction of the chemical contributions to the RMS lateral variations depends greatly on the intrinsic density increase across the layer, $\Delta\rho/\rho$. Although the thermal and chemical contributions always oppose each other, at high $\Delta\rho/\rho$ the density increase causes a large amplitude RMS anomaly. As $\Delta\rho/\rho$ decreases this anomaly becomes smaller see figure 7.6b. This effect is only observed in internally heated cases, in simulations with bottom heating the system becomes unstable before $\Delta\rho/\rho$ reaches small enough values to oppose the temperature field.

These RMS temperature variations can be related directly to variations in lateral density, but unfortunately global seismic tomography cannot yet robustly constrain such variations. To rigorously compare the $T\text{-chem}_{\text{RMS}}$ to seismic tomography variations would require an understanding of the effect of the chemistry variations on

seismic velocity. We have not made any assumption as to the cause of the layering, e.g. whether it's enrichment in iron, silicon, or perovskite etc. These would have different effects, and some of the conversion factors are poorly constrained. Clearly more work (including mineral physics) is required to rigorously compare these results with tomography; though we do note that there is a good general correlation in most materials between seismic velocity and density.

7.4.2 Lateral variations in the seismic velocity structure inferred from a linear combination of the thermal and chemical effects

Another method for comparing the thermal and chemical fields produced by our simulations with the RMS seismic velocities is convert these fields to seismic velocities using a linear combinations method [Tackley 2002].

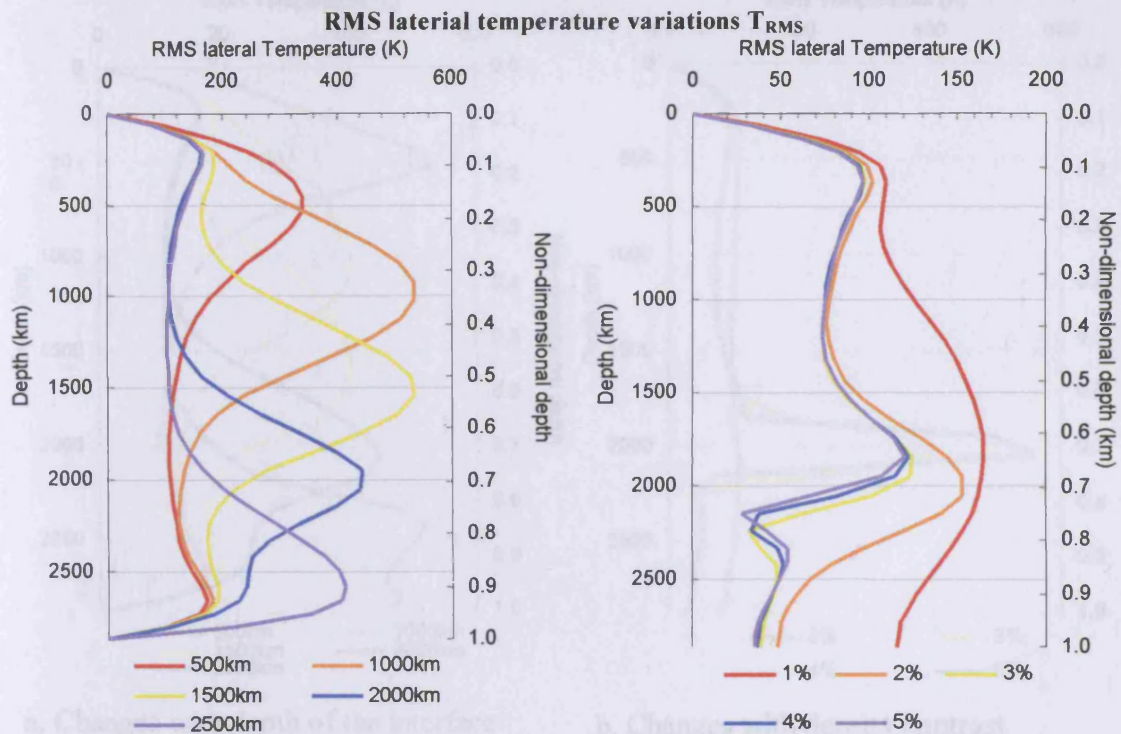
$$\Delta v \propto \Delta T + a \Delta C \quad (7.18)$$

Where v is seismic velocity, T is temperature and C is the compositional field having a value of 0 in the upper layer and 1 in the lower layer.

This allows us to express the RMS velocity anomaly, v_{RMS} , in terms of our thermal and compositional fields. The amplitude of the RMS anomaly is determined by the constant 'a' and we adjust this to produce the minimum value of v_{RMS} at the depth of the deformable interface. The results for a number of cases is shown in figure 7.7.

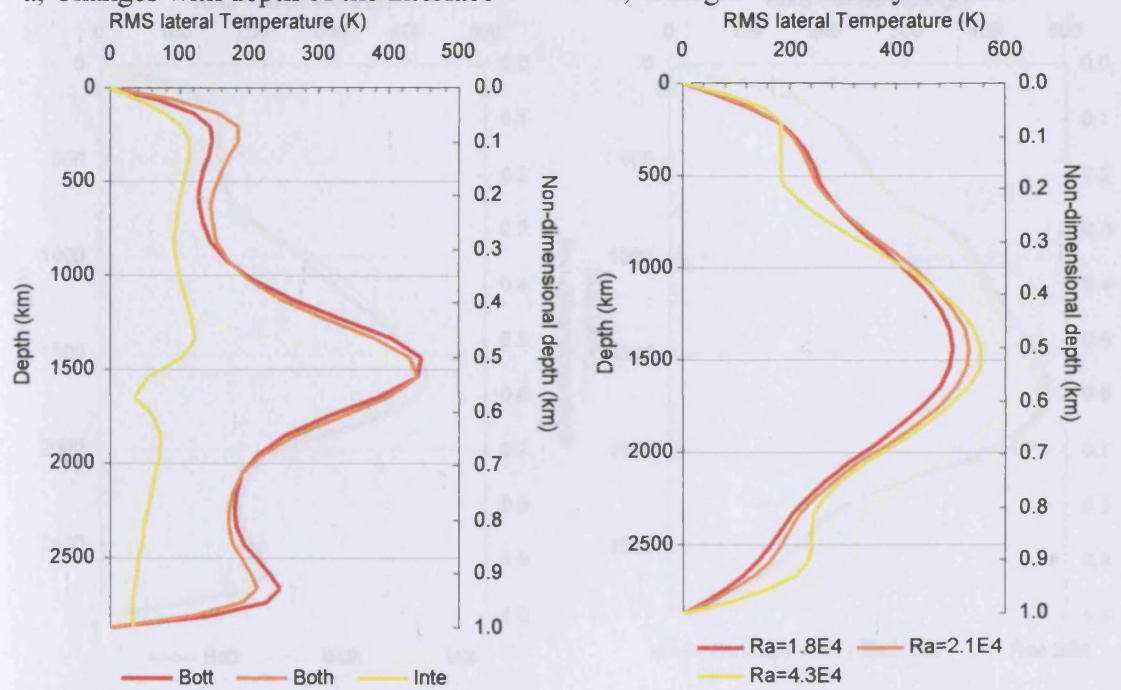
The v_{RMS} anomaly produced by the thermal and chemical boundaries has a different form to the results of the previous sections in which the RMS lateral temperature and density variations were displayed. The anomaly no longer has a smooth Gaussian shape that is centered at the depth of the interface. The anomaly tends to have a more truncated shape with the amplitude reaching a plateau around the depth of the interface. The amplitude of the anomaly is largest for interfaces in the deep mantle, see figure 7.7a. Reducing the density increase across the layer decreases the amplitude of the v_{RMS} anomaly at the interface. In the internally heated cases it is only possible to reduce the v_{RMS} to similar values to those at the surface and CMB by reducing the density contrast to low values (around 3%). In simulations with bottom heating this is not the case and a value of 'a' can be found that results in v_{RMS} anomaly at the interface that has a similar amplitude to those produced at the surface and CMB. However there is always a region of high v_{RMS} associated with the boundary and varying Ra has no clear effect on the

size of the v_{RMS} anomaly at the depth of the interface, see figure 7.7d. It seems likely that a large lateral variation in seismic waves speeds would be a characteristic of a deformable interface.



a, Changes with depth of the interface

b, Changes with density contrast



c, Changes with the heating mode

d, Changes with Rayleigh number

Figure 7.5

The RMS lateral variations in the temperature field

a, The cases shown had both internal and bottom heating and had a $\Delta\rho/\rho=4\%$. b, The cases show had only internal heating and the interface was 2000km deep. c, The cases shown had an interface at 1500km and $\Delta\rho/\rho=5\%$. d, The cases shown had an interface at 2000km and $\Delta\rho/\rho=4\%$.

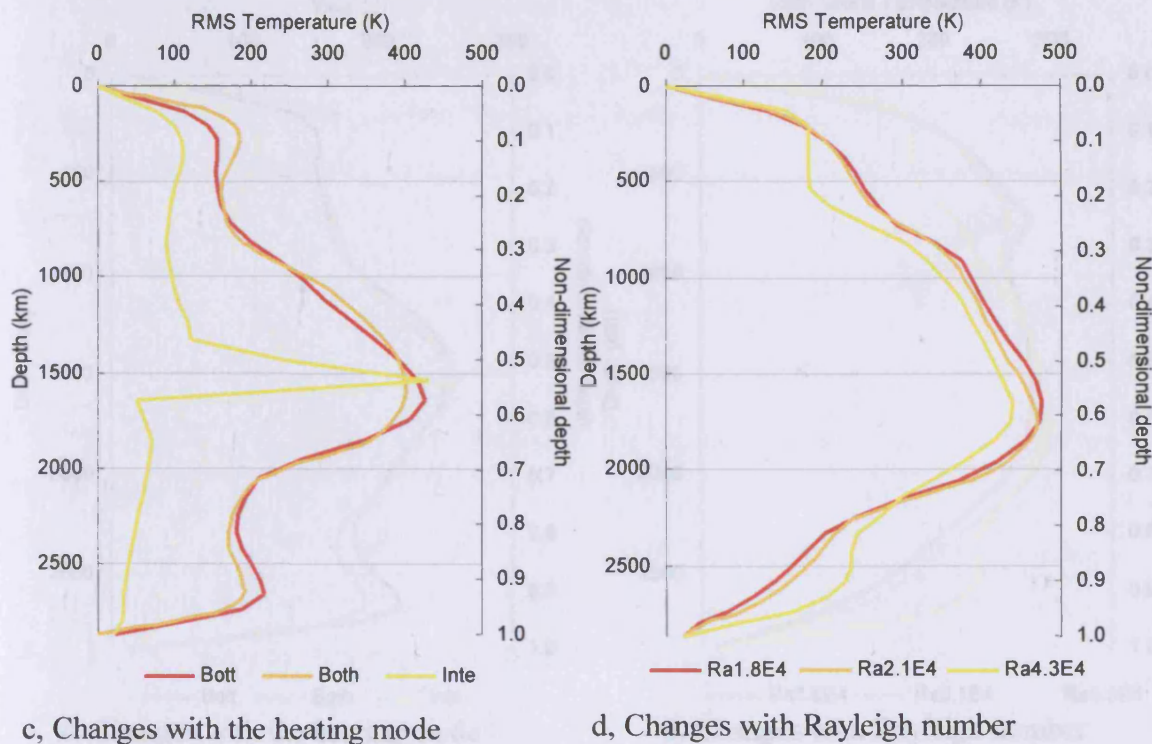
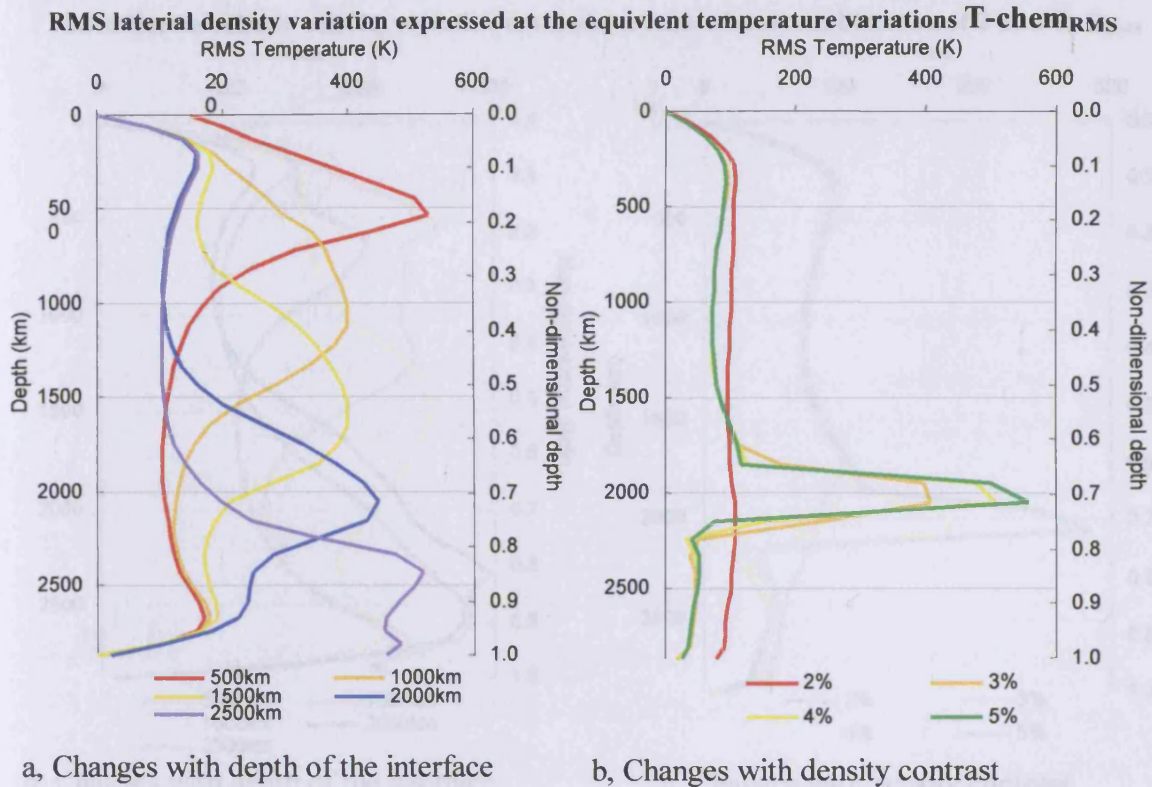


Figure 7.6

The RMS lateral variations in the temperature field with the effective temperature contrast caused intrinsic density change removed. a, The cases shown had both internal and bottom heating and $\Delta\rho/\rho=4\%$. b, The cases show had only internal heating and the interface was 2000km deep. c, The cases shown had an interface at 1500km and $\Delta\rho/\rho=4\%$. d, The cases shown had an interface at 2000km and $\Delta\rho/\rho=4\%$.

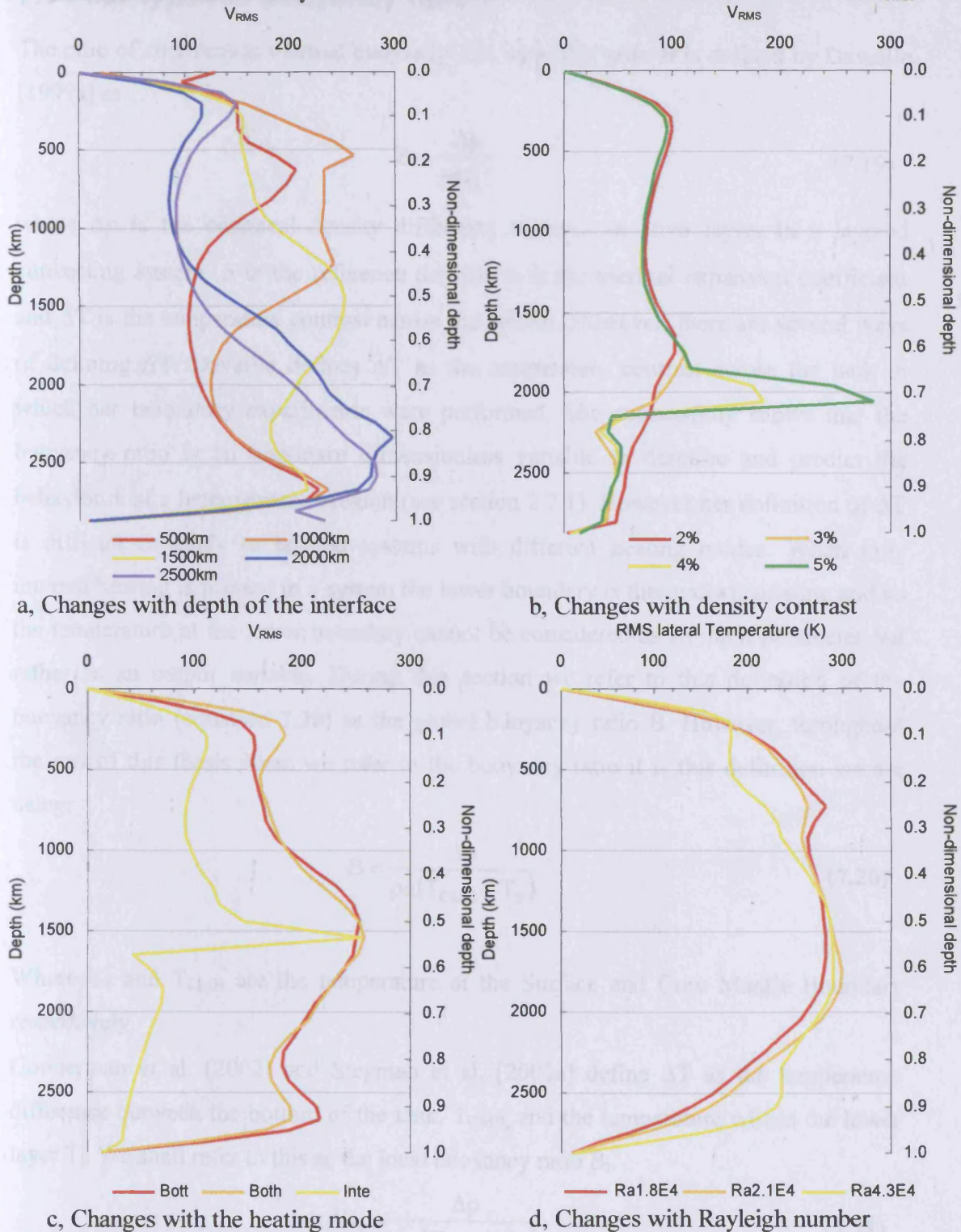
RMS lateral seismic velocity variation determined from a linear combination of T and C, R_{RMS} 

Figure 7.7

The RMS lateral variations in the velocity, V_{RMS} , field calculated with equation 7.18 and with a values of 'a' that produced the minimum value in V_{RMS} at the interface. a, The cases shown had both internal and bottom heating and $\Delta\rho/\rho=4\%$. b, The cases show had only internal heating and the interface was 2000km deep. c, The cases shown had an interface at 1500km and $\Delta\rho/\rho=4\%$. d, The cases shown had an interface at 2000km and $\Delta\rho/\rho=4\%$.

7.5 Four types of buoyancy ratio

The ratio of chemical to thermal buoyancy: the buoyancy ratio B is defined by Davaille [1999a] as...

$$B = \frac{\Delta\rho}{\rho\alpha\Delta T} \quad (7.19)$$

where $\Delta\rho$ is the chemical density difference between the two layers in a layered convecting system, ρ is the reference density, α is the thermal expansion coefficient and ΔT is the temperature contrast across the system. However, there are several ways of defining ΔT . Davaille defines ΔT as the temperature contrast across the tank in which her laboratory experiments were performed. She successfully shows that the buoyancy ratio is an important dimensionless variable to describe and predict the behaviours of a heterogeneous region (see section 2.7.1). However her definition of ΔT is difficult to apply to layered systems with different heating modes. When only internal heating is present in a system the lower boundary is thermally insulating and so the temperature at the lower boundary cannot be considered as an input parameter but rather as an output variable. During this section we refer to this definition of the buoyancy ratio (equation 7.20) as the global buoyancy ratio B . However, throughout the rest of this thesis when we refer to the buoyancy ratio it is this definition we are using.

$$B = \frac{\Delta\rho}{\rho\alpha(T_{\text{CMB}} - T_{\text{S}})} \quad (7.20)$$

Where T_{S} and T_{CMB} are the temperature at the Surface and Core Mantle Boundary respectively.

Gonnerman et al. [2002] and Stegman et al. [2003a] define ΔT as the temperature difference between the bottom of the tank, T_{CMB} , and the temperature within the lower layer T_{l} . We shall refer to this as the local buoyancy ratio B_{l} .

$$B_{\text{l}} = \frac{\Delta\rho}{\rho\alpha(T_{\text{CMB}} - T_{\text{l}})} \quad (7.21)$$

We shall now define two alternative versions of the buoyancy ratio. If we consider a heterogeneous 'blob' of material with a density ρ_{u} and a temperature T_{u} in a convecting system with a density ρ_{l} and a temperature T_{l} , see figure 7.8a, we can then define the buoyancy ratio as...

$$\text{Buoyancy Ratio} = B = \frac{\text{Chemical Buoyancy}}{\text{Thermal Buoyancy}} = \frac{(\rho_u - \rho_l)/\rho_l}{\alpha\Delta T} \quad (7.22)$$

Using Davaille et al.'s definition of $\Delta T = T_{\text{bot}} - T_{\text{top}}$ we see that the buoyancy ratio is unaffected by the temperature in the blob which when describing the motion of the blob, is clearly unrealistic. A definition of ΔT that describes the thermal contrast between the blob and the surrounding mantle would be $\Delta T = T_u - T_l$. In the case of a layered convecting system (figure 7.8b) this temperature contrast is the difference between the temperatures within the upper T_u and lower T_l layers. We shall refer to this buoyancy ratio as the regional buoyancy ratio B_r .

$$B_r = \frac{\Delta\rho}{\rho\alpha(T_l - T_u)} \quad (7.23)$$

We now define a version of the buoyancy ratio that is suitable for describing a system in which only internal heating is present. If we consider a box with top surface area A and a height ΔZ ; see figure 7.9a. If there is a temperature contrast across ΔZ of ΔT then the heat energy per unit time Q (W) across the top surface is given by...

$$Q = A k \frac{\Delta T}{\Delta Z} \quad (7.24)$$

Where k is the thermal conductivity.

We will now consider an equivalent system in which the heat flux across the upper surface of the box is being generated by internal heating, see figure 7.9b. We define the rate of heat generation q_{rad} (Wkg^{-1}) to be the rate at which heat energy is being generated per unit time per unit mass. The total heat generated in the box Q_{int} is therefore given by...

$$Q_{\text{int}} = q_{\text{rad}} M \quad (7.25)$$

Where M is the total mass of the box, so that...

$$Q_{\text{int}} = q_{\text{rad}} \rho A \Delta Z \quad (7.26)$$

Where ρ is the density. If we compare Q and Q_{int} by combining equation 7.24 & 2.26...

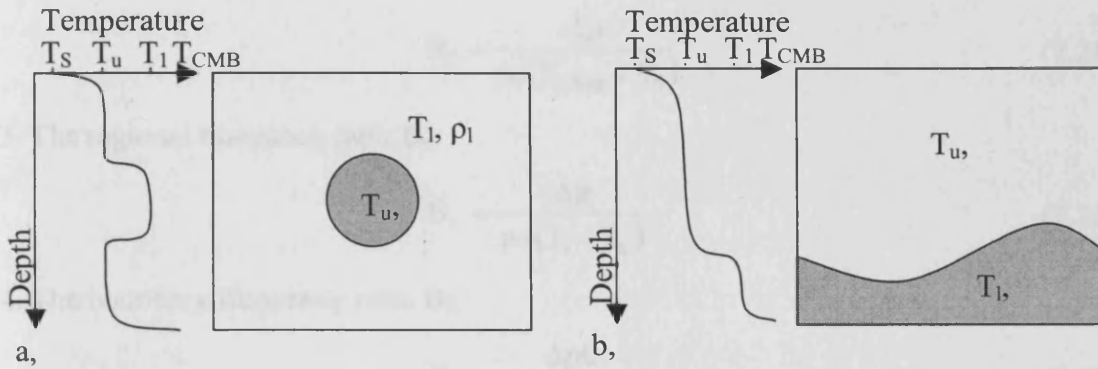
$$A k \frac{\Delta T}{\Delta Z} = q_{\text{rad}} \rho A \Delta Z \quad (7.27)$$

$$\Delta T = \frac{q_{\text{rad}} \rho \Delta Z^2}{k} \quad (7.28)$$

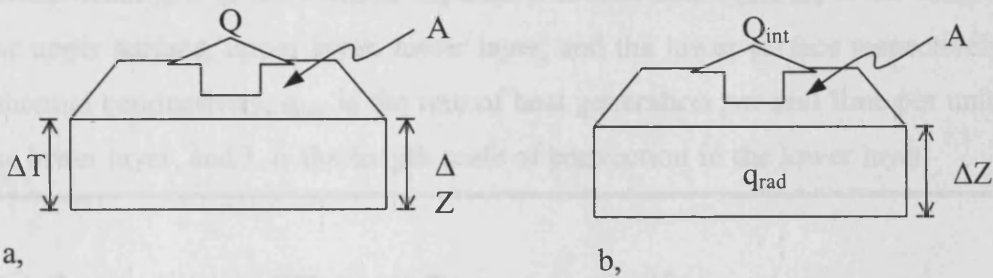
We replace ΔZ with the length scale L and substitute into equation 7.19...

$$B_b = \frac{\Delta\rho k}{\rho^2 \alpha q_{\text{rad}} L^2} \tag{7.29}$$

Which we refer to as the boundary buoyancy ratio B_b .



a,
Figure 7.8
A hot blob and dense layer



a,
Figure 7.9

- a, A box with a thermal boundary ΔT across it that causes a heat flux Q across its upper surface.
- b, A box with an internal rate of internal heating q_{rad} (heat energy generated per unit time per unit mass) that causes heat to be lost at a rate Q_{int} .

We have four different definitions of the buoyancy ratio that we shall summarise here...

1. The global buoyancy ratio B [Davaille 1999a].

$$B = \frac{\Delta\rho}{\rho\alpha(T_{\text{CMB}} - T_s)} \quad (7.20)$$

2. The local buoyancy ratio B_l [Gonnerman et al. 2002, Stegman et al. 2003a].

$$B_l = \frac{\Delta\rho}{\rho\alpha(T_{\text{CMB}} - T_l)} \quad (7.21)$$

3. The regional buoyancy ratio B_r .

$$B_r = \frac{\Delta\rho}{\rho\alpha(T_l - T_u)} \quad (7.23)$$

4. The boundary Buoyancy ratio B_b .

$$B_b = \frac{\Delta\rho k}{\rho^2 \alpha q_{\text{rad}} L^2} \quad (7.29)$$

Where $\Delta\rho$ is the chemical density difference between the two layers, ρ is the reference density, α is the thermal expansion coefficient, $T_{s,u,l,\text{CMB}}$ is the temperature of the upper surface, upper layer, lower layer, and the lower surface respectively. k is the thermal conductivity, q_{rad} is the rate of heat generation per unit time per unit mass in the lower layer, and L is the length scale of convection in the lower layer.

7.5.1 Comparing different Buoyancy ratios

We test the different definitions of the buoyancy ratio to see which is better at characterizing a layered system. We test the relationship of the buoyancy ratio to the non-dimensional surface area variable. This variable is chosen because (as we showed in section 5.6) it depends strongly on the global buoyancy ratio, is only weakly dependent on the depth of the interface and appears to be independent of the other dimensionless parameters that characterize layered convection [Davaille et al. 2003]. The results are shown in figure 7.10.

The non-dimensional area variable ϕ is defined as the ratio of the increase in the surface area of the interface between the two layers from a spherical shell to the area of the spherical shell, it can be used to characterise the stability of a layered system. For a small value of ϕ the system is in a stratified/stable state; for increasing values it becomes unstable. Both B & B_r show a reasonable dependence with ϕ , while the stability of the layered system displays little or no dependence on both B_l & B_b . The

local buoyancy ratio is particularly unsuitable for describing an internally heated system. In these systems there is often a negative temperature gradient in the lower layer due to the thermally insulating boundary condition at the CMB. This causes B_l to have negative values (see equation 7.21) that makes it unsuitable for predicting the behaviour of the system. B_r is of limited use since it is not comprised solely of input parameters but uses some output variables, because of this it not suitable for predicting the behaviour of systems. It also results in some anomalous points and so within the limits of this study cannot be trusted entirely. The global buoyancy ratio B [Davaille 1999a] is the most successful definition of the buoyancy ratio for a number of reasons. The non-dimensional area parameter and hence the stability of a system seem to depend reasonably strongly on it and so it can be used to predict the point at which a layered system will become unstable. B is defined entirely of input parameters (unless the system has only internal heating) and so can be used to predict the stability of a layered system. It is for these reasons that we use this definition of the buoyancy ratio throughout this thesis.

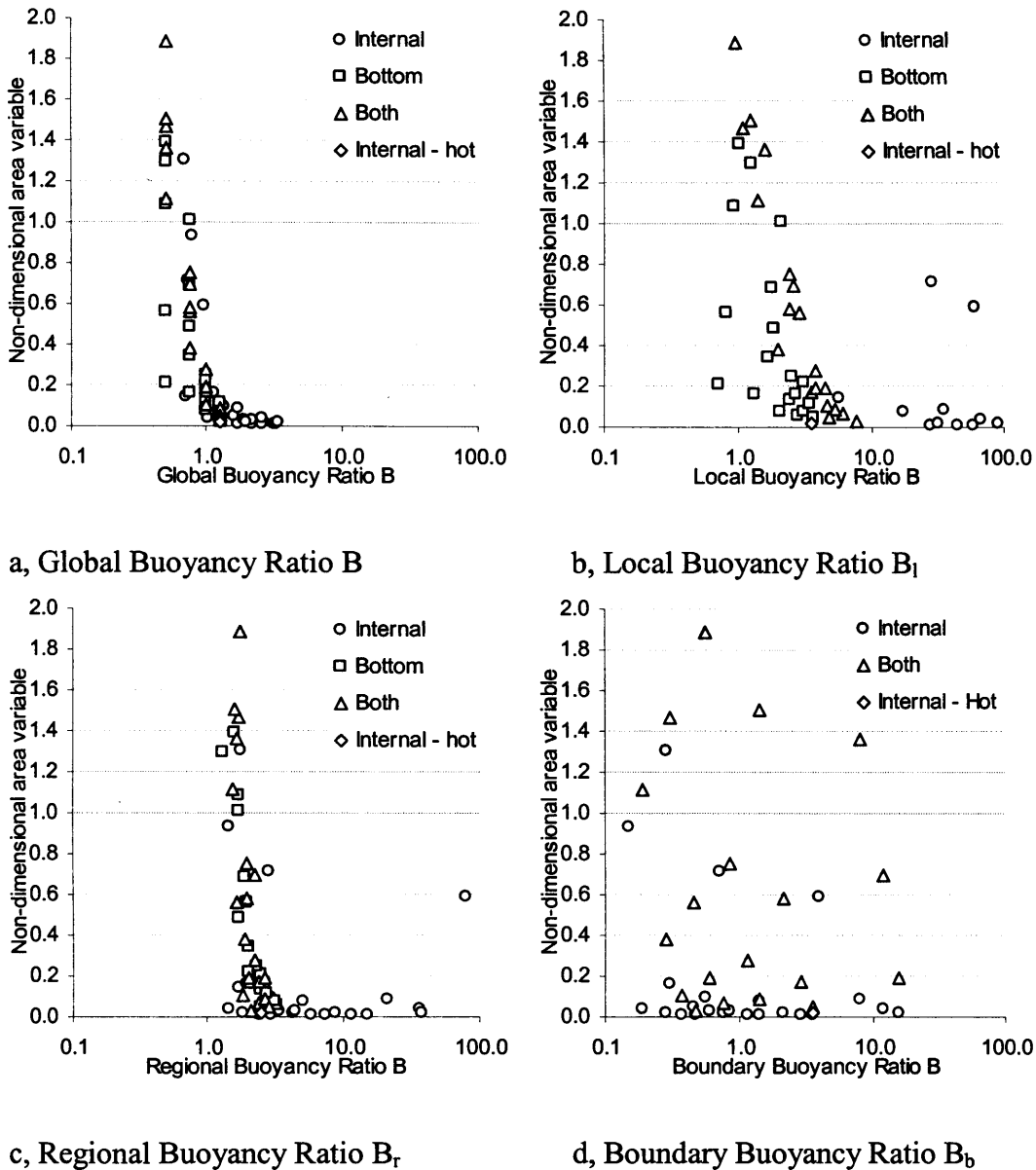


Figure 7.10

The relationship between the four definitions of the buoyancy ratio and the non-dimensional surface variable.

- For the cases with only internal heating, the ΔT used is the thermal contrast over whole mantle once a quasi-steady state has been reached.
- The temperature in the lower layer is found using the method outlined in section 3.4.1 once a quasi-steady state has been reached; in cases with only internal heating the temperature of the CMB used is the value once a quasi-steady state has been reached. This definition of the buoyancy ratio results in many large negative values of B_l in internally heated cases due to the negative temperature gradient in the lower layer.
- The temperature of the upper and lower layers is found using the method outlined in section 3.4.1) and the mean values are used once a quasi-steady state has been reached.
- Only input parameters are used, however B_b can only be calculated for cases with internal heating.

7.6 Seismic reflection constraints on the density contrast of layered convection

The maximum possible density contrast of layered convection can be constrained by considering at what density contrast it is invisible to seismic reflection investigations. Castle & van der Hilst [2003a&b] quote a number of circumstances under which their seismic reflection surveys would fail to detect an interface. In their first survey between 800 and 2000km [Castle & van der Hilst 2003a] this would happen when the S-wave speed contrast is less than 2%. In their second survey between 1800 and 2800km [Castle & van der Hilst 2003b] this would happen when the impedance contrast $\Delta I/I$ is less than 4%.

We use the parameterisation for the density ρ , S-wave and P-wave speeds given in the PREM model [Dziewonski & Anderson, 1981] to find the change in depth that causes a change in the S-wave velocity of 2%. The corresponding density contrast can then also be calculated. Since Castle & van der Hilst [2003a&b] quote values of 2% and 4% (to only one significant figure) we assume there is an uncertainty of $\pm 0.5\%$ in both cases. The resulting maximum values of the buoyancy ration can be seen in figure. The central value (corresponding to $\Delta V_s/V_s$ and $\Delta I/I$ values of 2.0% and 4.0% respectively) of the effective density contrast $\Delta\rho/\rho_{\text{eff}}^\dagger$ have values between $\Delta\rho/\rho_{\text{eff}} = 2.5\text{-}3\%$. For a deep layer between 800 and 2800km depth having $\Delta\rho/\rho_{\text{eff}} < 2\%$ we can say with reasonable certainty that it would be undetected by their seismic reflection method. However a layer with $(\Delta\rho/\rho)_{\text{eff}} > 2.5\text{-}4\%$ (depending on the depth of the layer see figure 7.11) would be seen by these methods. We will see in section 7.9 $(\Delta\rho/\rho)_{\text{eff}} > 2.5\text{-}4\%$ corresponds to a $\Delta\rho/\rho \sim 5\%$.

[†] Here we make the distinction between the chemical density contrast $\Delta\rho/\rho$ due of a deep layer (normally referred to in this thesis as simply the density contrast) which is the increase in the chemical density in the lower layer and the effective density contrast $(\Delta\rho/\rho)_{\text{eff}}$ that removes from this the effect of thermal expansion in the deeper/hotter layer.

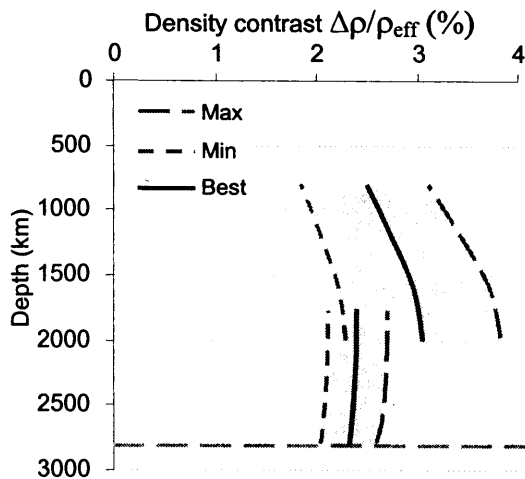


Figure 7.11

The minimum effective density contrast required for a deep layer detectable in the investigations of Castle & van der Hilst [2003a&b]. The grey regions show the uncertainty in this value. There are two values shown. The first between 800 and 2000km corresponds to Castle & van der Hilst 2003a, the second between 1800 and 2800km to Castle & van der Hilst 2003b.

7.6.1 The inclination of the boundary and its effect on seismic imaging

Seismic methods have been unable to find a seismic reflection from a deep layer [Vidale et al. 2001, Castle & van der Hilst 2003a, Castle & van der Hilst 2003b] with a few exceptions [Niu et al. 2003, Castle & van der Hilst 2003a, LeStunff et al. 2003]. Castle & van der Hilst [2003a] quote a number of circumstances under which their methodology would fail to detect an interface...

1. If it is deeper than 2000km (though they do investigate this possibility in a separate paper [Castle & van der Hilst 2003b]).
2. If the boundary is wider than 20km.
3. If the boundary is sloping at an angle steeper than 30° [Castle & Creager 1998].
4. If the wave speed contrast is less than 2%.

In this section we investigate the possibility that the slope of the interface is sufficiently large to make the boundary invisible to seismic reflection methods over most of its surface.

Figure 7.13 shows the changing planform of the inclination of the interface as the density contrast across the layer increases. The cases shown are those discussed in section 6.1, that have a Rayleigh number of 1.7×10^5 . In cases with a smaller density contrast the surface has steeper slopes. The planform is similar to that suggested by Davaille [1999b] (see figure 4.7) with steep sided troughs forming linear features that form cells containing plume/point-like up-wellings. In this case the direction of

entrainment is reversed with sheet-like up-wellings and plume-like down-wellings (see figure 7.13f).

The change in planform with the Rayleigh number Ra is shown in figure 7.12 for cases with a 3.2% density increase across the boundary between the two layers. The cellular planform is less obvious in these low-density contrast cases. There appears to be no change in planform as the Rayleigh number changes.

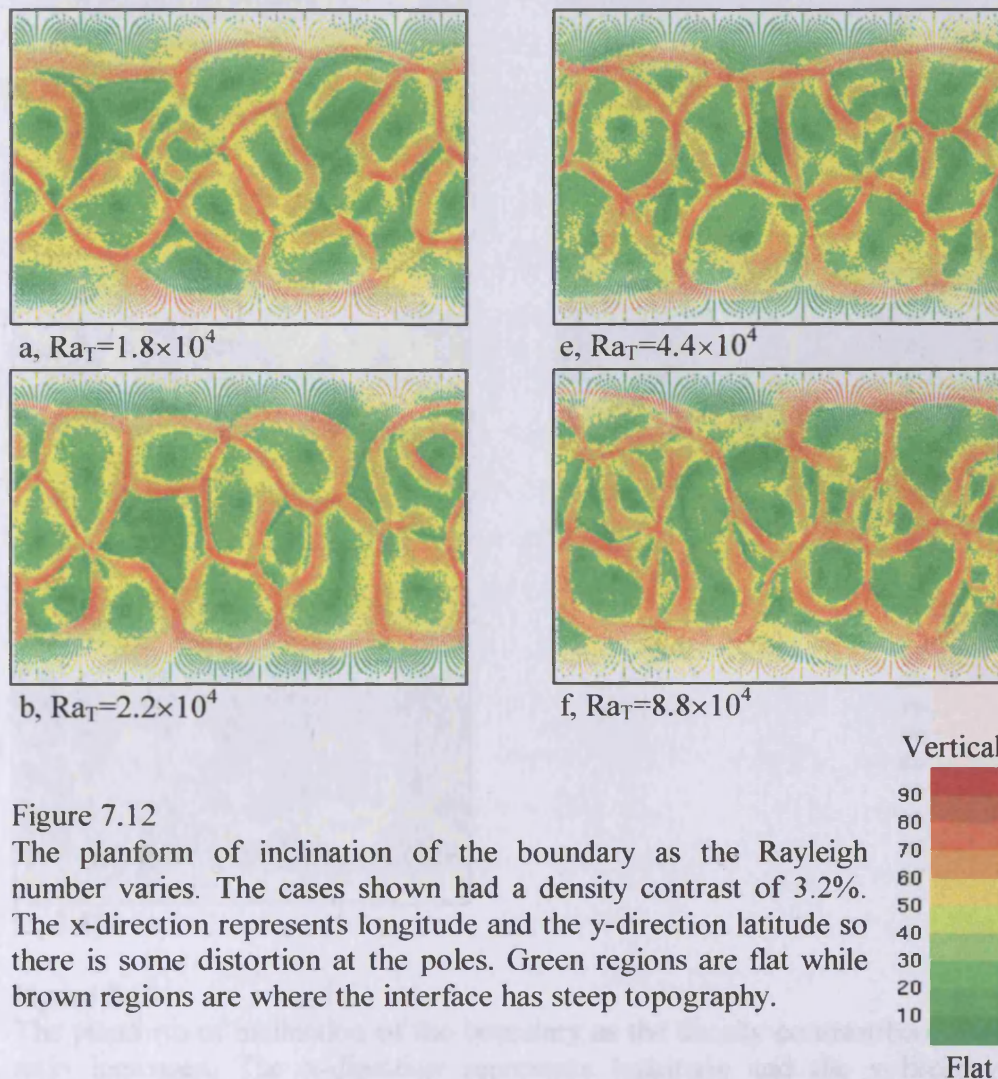


Figure 7.12

The planform of inclination of the boundary as the Rayleigh number varies. The cases shown had a density contrast of 3.2%. The x-direction represents longitude and the y-direction latitude so there is some distortion at the poles. Green regions are flat while brown regions are where the interface has steep topography.

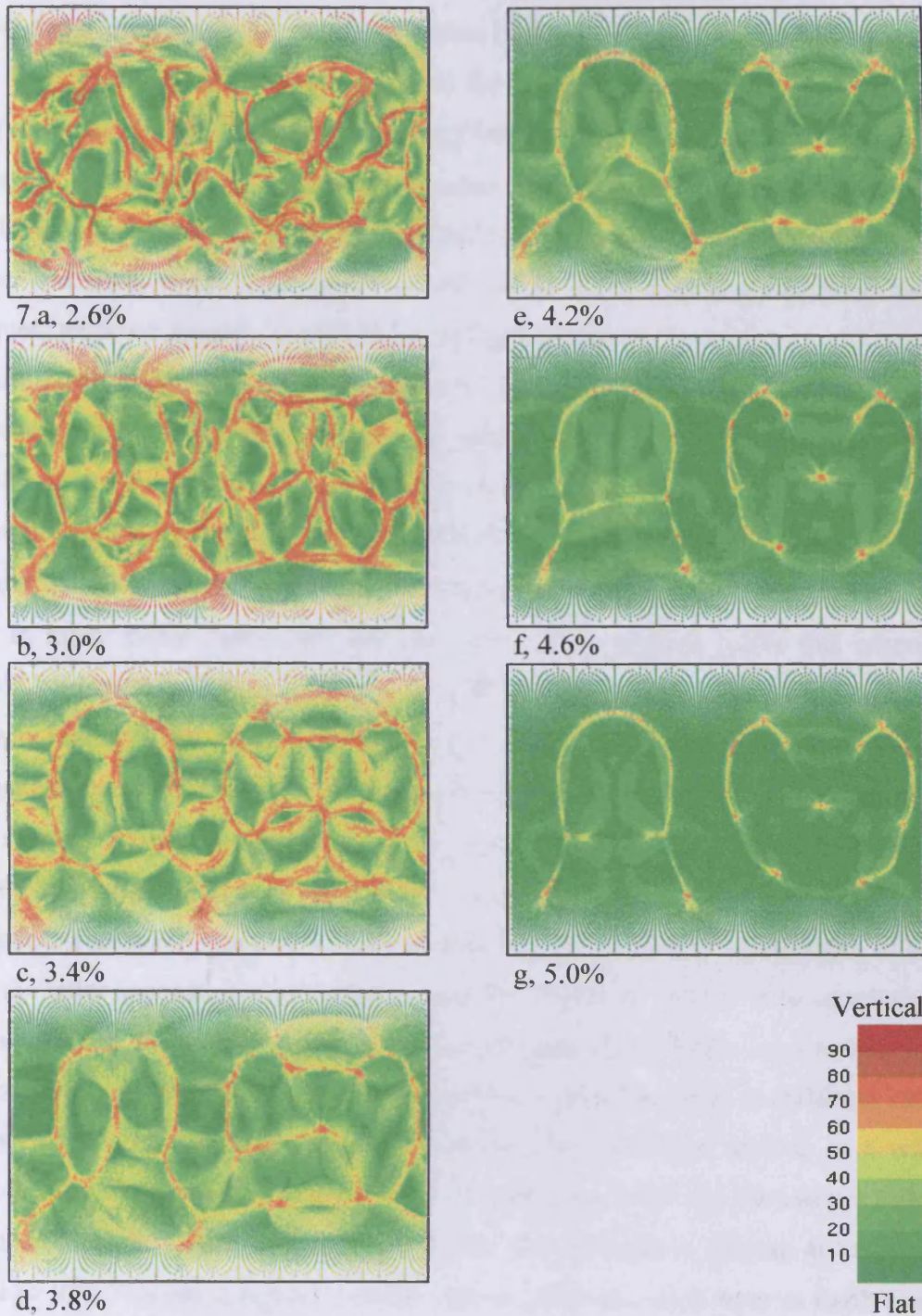


Figure 7.13

The planform of inclination of the boundary as the density contrast/buoyancy ratio increases. The x-direction represents longitude and the y-direction latitude so there is some distortion at the poles. Green regions are flat while brown regions are where the interface has steep topography. The steep regions form linear features. In cases with lower density contrasts there are more complex topographic features on the boundary.

Histograms showing the angle of inclination of the surface in figure 7.14a show that as the density increases (from red to violet) the layer becomes flatter with an increasing proportion of its surface having a slope of less than 30° . The distribution of the slopes does not appear to be Gaussian and in none of the cases shown is the most frequent angle of inclination zero. Thus even in a well stratified regime the interface between the upper and lower layers is sloping. Although as the lower layer is made denser the most frequent angle of inclination tends towards flatter values.

Figure 7.14b shows limited evidence that as the Rayleigh number of a layered system increases the layer becomes flatter. The range of Rayleigh numbers is probably too small to determine if the topography of the interface does vary with Ra .

If we now consider the limitation of Castle & van der Hilst [2003a]: a layer sloping at greater than 30° will be undetected by seismic refraction methods. Figure 7.14a shows that in many stable cases less than only 40% of the surface fulfils this criteria and would be detected. Though this figure would increase in cases where the lower layer is denser. Figure 7.14b shows that as the Rayleigh number increases towards Earth-like values the fraction of the surface with a slope below 30° does not change significantly and so suggests that possibly the results in figure 7.14a can be applied to Earth-like Ra .

Castle & van der Hilst [2003a] surveyed four locations: the northwest Pacific, South America, Tonga/Fiji and Marianas, with the former three showing no signs of a layer and the latter suggesting a boundary at 1660km. Castle & van der Hilst concluded that the absence of the layer in the other locations suggested this was a local feature such as a blob [Becker et al. 1999] or subducted oceanic crust [Kaneshima & Helffrich 1999].

Each of the areas surveyed was approximately the same size and so as a working hypothesis we assume that around 25% of the surface is visible to the seismic reflection method. The remaining 75% of the interface (we assume) is sloping at too steep an angle ($>30^\circ$). Assuming figure 7.14a is representative of a deep layer in Earth's mantle we see that even in cases which are becoming unstable around 35% of the surface is visible to seismic reflection. In these cases the possibility of sampling four points in unrelated regions of the interface and detecting it in only one or less of the regions is 0.56 (see the bracketed section below for the calculation). In the case of a very stratified layer up to 90% of the surface is flatter than 30° and so the possibility of the layer being detected in only one or less of the survey regions is 0.004.

If the A is the possibility of an event happening (i.e. a boundary being detected) and $B=1-A$ is the possibility of the event not happening (i.e. a boundary not being detected). In four events the possibility of A not occurring four times: $4B$'s...

$$4B's = B^4 = (1-A)^4$$

...and A not occurring 3 times and occurring once: $3B's1A$...

$$3B's1A = 4B^3A = 4A(1-A)^3$$

Where the '4' is needed since the A could fail to happen in the first, second, third or fourth event.

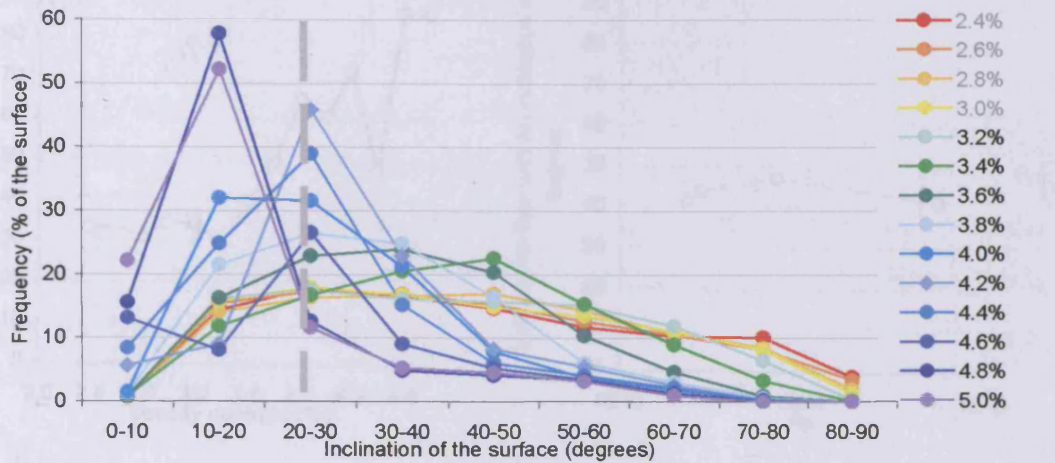
So the possibility of the layer being detected in only one or less of the regions when four regions are surveyed is given by...

$$\left\{ \begin{array}{l} \text{Prob of detecting layer} \\ \text{in one or less region} \end{array} \right\} = (1 - P_{<30^\circ})^4 + 4P_{<30^\circ}(1 - P_{<30^\circ})^3$$

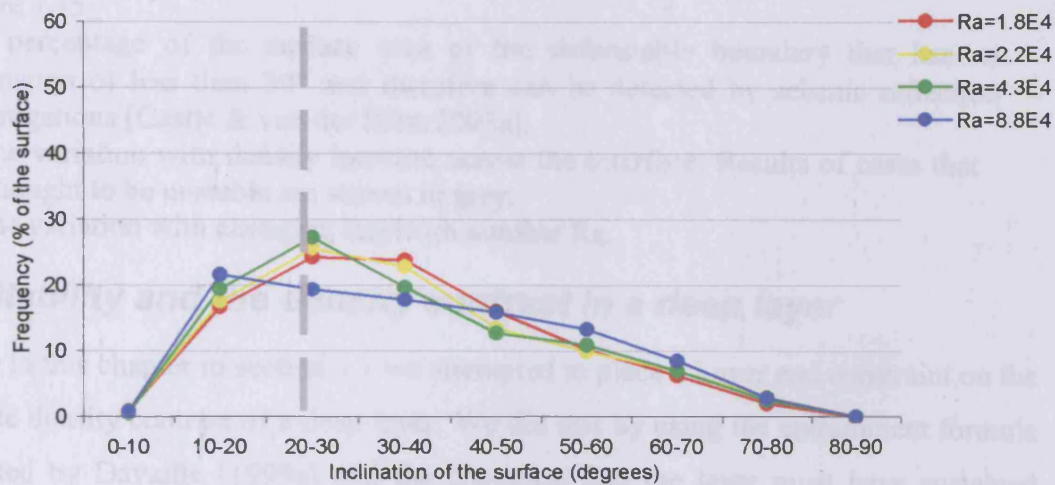
Where $P_{<30^\circ}$ is the fraction of the interface that has a slope less than 30° . So for $P_{<30^\circ}=0.35$ {prob}=0.56; for $P_{<30^\circ}=0.90$ {prob}=0.0037; for $P_{<30^\circ}=0.08$ {prob}=0.97.

The undulations of the interface between two layers in a convecting system causes the interface to have a steeply sloping surface with as much as 65% of the layer having a slope steeper than the 30° needed to make the interface observable by seismic reflection methods [Castle & Creager 1998]. The failure to detect a deep layer in three out of the four regions surveyed by Castle & van der Hilst [2003a] can be explained by an interface with around only 40% of its surface having a slope below 30° . This requires a density contrast of less than 3.5-4.0% (figure 7.14a). This is equivalent to a buoyancy ratio of less than 0.7-0.8.

We can explain the failure of seismic reflection methods to detect a deep layer by having a deep layer with a buoyancy ratio of less than 0.7-0.8 ($\Delta\rho/\rho=3.5-4.0\%$)



a,



b,

Figure 7.14

Histograms showing the inclination of the surface separating the upper and lower layers in a convecting system.

a, The variance of the inclination caused by changes in the density of lower layer.

Those cases that are thought to be unstable are displayed in grey in the legend.

b, The variance of the inclination caused by changes in the Rayleigh number.

The grey dashed line represents the point at which the inclination of the boundary is 30° . Surfaces with inclinations greater than this angle cannot be detected using current seismic reflection methods [Castle & van der Hilst 2003a].

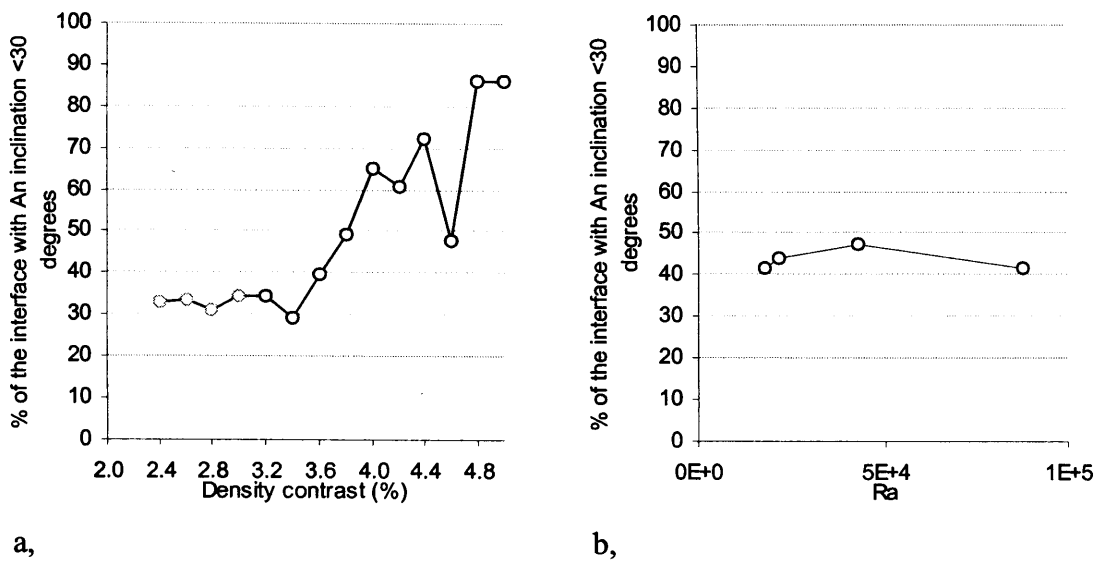


Figure 7.15

The percentage of the surface area of the deformable boundary that has an inclination of less than 30° and therefore can be detected by seismic reflection investigations [Castle & van der Hilst 2003a].

a, The variation with density increase across the interface. Results of cases that are thought to be unstable are shown in grey.

b, The variation with changing Rayleigh number Ra .

7.7 Stability and the density contrast in a deep layer

Earlier in this chapter in section 7.1 we attempted to place a lower end constraint on the possible density contrast of a deep layer. We did this by using the entrainment formula presented by Davaille [1999a] and the condition that the layer must have sustained itself throughout Earth's history (4.2 G years). The resulting density contrasts were so small that they did not place any meaningful lower limit on the possible density of a lower layer. In this section we shall again attempt to place a minimum constraint on the possible density of a lower layer based on the dynamic stability of a layered system.

In section 5.5 we saw how the behaviour of a layered system varied with the heating mode, the depth of the layer and the density increase across the layer. In some cases we decided that the layered system was 'unstable'. In these cases the marker method used to simulate the layered system failed due to the large amplitude of undulations on the interface between the two layers and the development of folding structures in the surface. When the system is in this state we do not assume that a chemical reservoir is unsustainable, we merely concede that it is not a mode of convection that can be modelled by our approach. A number of criteria is used to determine if a simulation has reached an unstable state these include the non-dimensional area variable, the standard

deviation of the marker heights, heat balance considerations and the average radial temperature at the mean depth of the boundary.

We found that the stability is strongly dependent on the buoyancy ratio B of a layered system, weakly dependent on the depth of the interface (or the non-dimensional depth [Davaille 2003]), and is (as far as we could ascertain) independent of the heating mode. In section 6.4 we see that over the range of Rayleigh numbers we investigated the stability of the layered system is only weakly dependent on the Rayleigh number, this is consistent with the observation of layered systems in laboratory tank experiments [e.g. Davaille 2003, section 2.7.1].

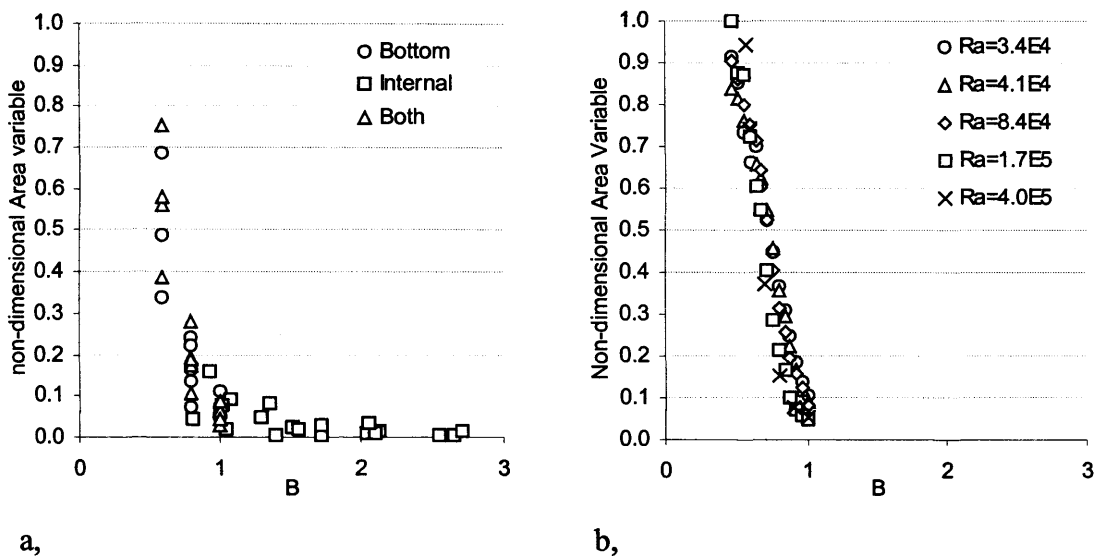


Figure 7.16

The variation of the non-dimensional area variable ϕ with the buoyancy ratio (when ϕ is zero the layer is a flat spherical shell, when ϕ is 1 its surface area has doubled).

- The relationship between ϕ and B as the heating mode is changed. There is little or no dependence with the heating mode and we see ϕ increasing sharply as B tends towards 0.5.
- The relationship between ϕ and B as the Rayleigh number varies. As B tends towards 0.5, ϕ increases to unrealistically large values.

In figure 7.16 we see how the non-dimensional area variable ϕ tends toward very large values as B tends towards 0.5. Figure 7.16 displays results with varying Ra , depth of the interface, and heating mode, none of which seems to affect this relationship. Davaille [1999a] quotes a critical values of $B_c \approx 0.3$ at which the system moves from a stratified regime to whole layer convection. We could be suggesting a larger value than Davaille, because we are unable to model cases in which the system is layered but there

is extreme deformation of the boundary between the layers or the change to a spherical geometry may have changed the value of B_c .

The trend of ϕ towards infinity in figures 7.16a & 7.16b is reasonably different. There is only one way in which these cases vary that we have not already shown does not affect the ϕ - B relationship. The most likely reason for the variance is the radial viscosity structure used in 7.16b (see section 6.1). The systems had a 100-fold viscosity increase across the depth of the mantle; and so a viscosity ratio of $\gamma=10^2$. Previous work has shown that as the viscosity ratio increases the behaviour of a layered system becomes increasingly sensitive to changes in B [Le Bars & Davaille 2002]. This suggests that the viscosity structure is an important parameter controlling the nature of convection [Bunge et al. 1997].

It is tempting to take the value of B_c and calculate the values of $\Delta\rho/\rho$ for a range of temperature differences ΔT that apply to a range of layered cases [Davaille 1999a]. However, the ΔT we have used to find B_c is defined as temperature contrast across the whole convecting system and hence the buoyancy ratio is the global buoyancy ratio (see section 7.5: the different types of B section). If we were using a different definition of ΔT , as Davaille [1999a], in our equations for B we would also need to use a different buoyancy ratio (either B_l or B_r). As we saw in section 7.5 the behaviour of the system in reference to these different definitions of the buoyancy ratio is not the same. Any behaviour interpreted using this method would therefore be difficult to justify.

Instead we calculate the critical values of the density contrast using Earth-like values.

$$\left(\frac{\Delta\rho}{\rho}\right)_{\text{crit}} = B_c \alpha \Delta T \quad (7.30)$$

If we use values of $B_c=0.5$, $\alpha=2\times 10^{-5}$ and $\Delta T=2000\text{K}$ then $(\Delta\rho/\rho)_{\text{crit}}=2\%$, suggesting that a density contrast of at least 2% is needed to maintain a deep layer in Earth's mantle.

The assumptions used to achieve this result need some investigation. Firstly, we have used a value of B_c of 0.5. As we found from our experiments the value of B_c is weakly dependent on the non-dimensional depth of the interface between the layers [section 5.6.2] and the Rayleigh number [section 6.4, Davaille 2003]. Consequently the value of B_c will be smaller for deeper boundaries (varying from as much as 0.52 at 500km to 0.21 at 2000km) and will increase as Ra is scaled up to Earth-like values (though this increase will be small, see figure 2.13). The uncertainty in radial structure of the

thermal expansivity in Earth's mantle and its possible value in a primitive reservoir is perhaps the biggest limitation to our estimate of $(\Delta\rho/\rho)_{\text{crit}}$. Since there are no estimates of the value of α in a deep layer we shall ignore the effect of different chemistry and assume a decrease in α with depth suggested by Zhao & Yuen [1987], α will decrease by a factor 5 to 10 across the mantle [Hansen et al. 1993] which in turn will decrease $(\Delta\rho/\rho)_{\text{crit}}$ by the same amount and so is the greatest uncertainty in our calculations. The thermal contrast over the mantle is also an estimated parameter and the uncertainty in the critical Buoyancy ratio is also included. The range of values of these parameters is shown in table 7.2.

If we first consider the size of the thermal contrast across the mantle, we take a minimum value of 1700K a maximum of 3500K and a best guess of 2000K (for references see table 7.2). We allow the critical buoyancy ratio to vary linearly with depth [section 5.6.2] as governed by equation 7.31.

$$B_c(D) = \left(\frac{B_c(\text{CMB}) - B_c(S)}{H} \right) D + B_c(S) \quad (7.31)$$

Where $B_c(D)$ is the critical buoyancy ratio at a depth D , $B_c(\text{CMB})$ & $B_c(S)$ are the critical buoyancy ratio at the core mantle boundary and at the surface respectively and H is the depth of the mantle taken to be 2870km. We take the maximum, minimum and best guess values of $B_c(\text{CMB})$ to be 0.32, 0.21, 0.24 respectively and for $B_c(S)$ to be 0.54, 0.34 & 0.43. The results can be seen in figure 7.17a. There is little change in the value of B_c with depth, but at each particular depth there are a range of possible values of B_c within a window of ± 0.1 .

To calculate the thermal expansivity at a given depth we use the following equation [Zhao & Yuen 1987, Hansen et al. 1993, section 2.8]...

$$\alpha(z_d) = \left(\frac{m+1}{(1+m(z_d+1))} \right)^3 \alpha(0) \quad (2.18)$$

Where z_d is the non-dimensional depth, $\alpha(0)$ is the value of α at the surface and 'm' is a non-dimensional parameter that controls the increase of α with depth.

We take the maximum, minimum and best guess values of the thermal expansivity at the surface to be 3.0×10^{-5} , 2.0×10^{-5} , 2.5×10^{-5} respectively. The decrease $\alpha(0)/\alpha(1)$ across the mantle can be expressed in terms of m (see section 2.8)...

$$\frac{\alpha(0)}{\alpha(1)} = \left(\frac{2m+1}{m+1} \right)^3 \quad (7.32)$$

This suggests that the maximum possible decrease across the mantle of α is eightfold. We choose a maximum possible decrease of 8, a minimum of 2 and best guess of 3.3. These correspond to values of m of infinity, 1.0 and 0.45 respectively. The resulting variation in the thermal expansivity α with depth is shown in figure 7.17b.

The critical density increase is calculated using the maximum, minimum and best guess values of ΔT , $\alpha(D)$ & $Bc(D)$ and is shown in figure 7.18. There is a large range of values of $(\Delta\rho/\rho)_{\text{crit}}$ due mostly to the uncertainty in the value of the thermal expansivity with depth. However, we are able to make some useful observations. A layer in the shallow mantle requires a density increase greater than 1%, if such a layer existed it is unlikely that it would be unnoticed by seismic imaging. However the presence of a phase boundary (e.g. the 670km phase boundary) may help sustain layering with a lower density contrast. An interface in the deeper mantle is possible with a lighter lower layer compared to cases higher in the mantle. This is largely due to the decreasing coefficient of thermal expansion with depth. We can say that a layer 1500km deep in the mantle will almost certainly be stable with a density increase greater than 3% and possibly with a density contrast as low as 1%.

Parameter		Range of values
Temperature contrast over the mantle	ΔT	1700 ^b , 2600 ^g , 3300 ^h , 3500 ^c K
Thermal expansivity at the surface	α_s	3.0×10^{-5a} , 3.0×10^{-5b} , 2.0×10^{-5f} K ⁻¹
Thermal expansivity at the CMB	α_{CMB}	0.9×10^{-5a} , $1.0 \times 10^{-5b,i}$, $2.0 \times 10^{-6f,i}$ K ⁻¹
Critical buoyancy ratio at the surface	Bc_s	0.6 ^d , 0.32 ^e
Critical buoyancy ratio at the CMB	Bc_{CMB}	0.10 ^d , 0.32 ^e

Table 7.2

The variance in the parameters used to calculate the critical density increase in an Earth-like layered system.

a, Davies 1999, p203; b, Ranalli 1995, p181; c, Fowler 1990, p248; d, section 5.6.2; e, Davaille 2003; f, Hansen 1993; g, Lay 1989; h, Montague & Kellogg 2000; i, Chopelas & Boehler 1992.

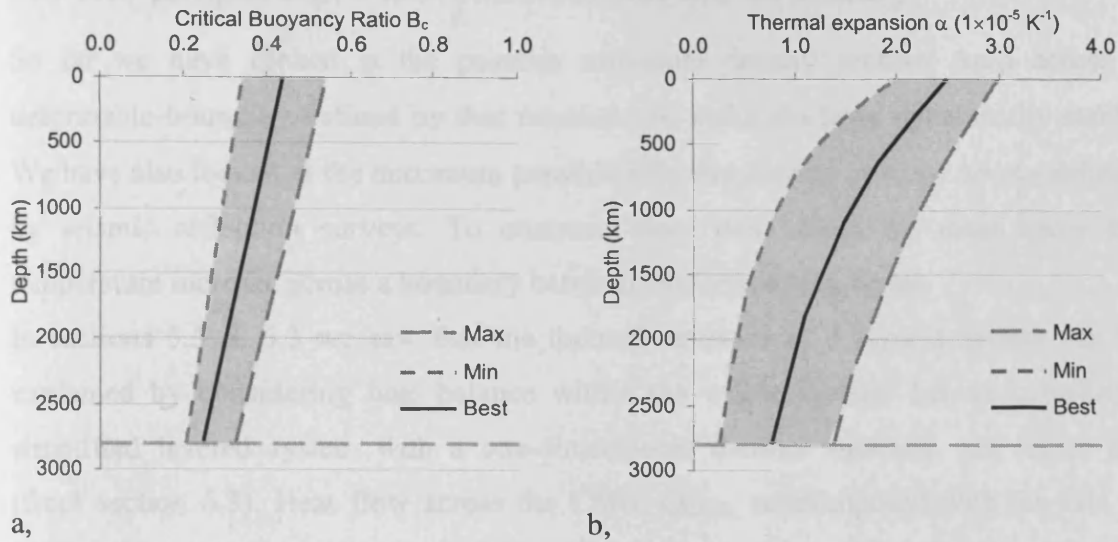


Figure 7.17

The variance of the parameters used to calculate the critical density contrast across a deformable interface in Earth's mantle. The maximum (max), minimum (min) and best guess (best) values are shown.

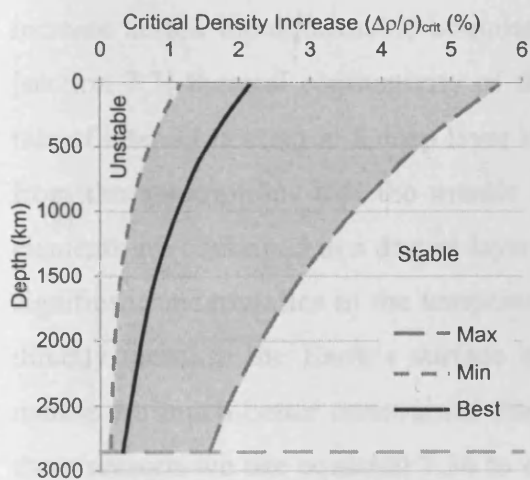


Figure 7.18

The critical density increase across a deformable interface with depth. Shown are three possible relationships due to our uncertainty in parameters controlling the value of $(\Delta\rho/\rho)_{crit}$: The maximum (max), minimum (min), and the best guess (Best) values. In the region marked 'unstable' a layered system will convect as a single layer, in the 'stable' region a stable layered system is possible. The grey region represents the uncertainty in the density contrast that borders these two regimes.

7.8 The temperature increase across the boundary

So far we have looked at the possible minimum density contrast $\Delta\rho/\rho$ across a deformable boundary defined by that necessary to make the layer dynamically stable. We have also looked at the maximum possible effective density contrast $\Delta\rho/\rho_{\text{eff}}$ defined by seismic reflection surveys. To compare these two values we must know the temperature increase across a boundary between two convecting layers.

In sections 5.5 & 6.3 we saw that the thermal structure of a layered system can be explained by considering heat balance within the whole system. Let us consider a simplified layered system with a one-dimensional thermal structure, see figure 6.5 (from section 6.3). Heat flow across the CMB, Q_{CMB} , superimposed with the rate of heat generated in the lower layer from radioactive decay, Q_l , is balanced by the heat flow across the Kellogg boundary, Q_K . Equally the heat flow over the surface, Q_s , must be balanced by the rate of heat generated in the upper layer from radioactive decay, Q_u , and Q_K .

$$Q_K = Q_{\text{CMB}} + Q_l \quad (7.33)$$

$$Q_K = Q_s - Q_u \quad (7.34)$$

We could use either of these formulas to calculate Q_K , and then the temperature increase across the deformable boundary ΔT_K . However as we have already discussed [section 7.7] thermal conductivity of the deep mantle is poorly constrained. Also the rate of internal heating in a deep layer is poorly constrained, our only estimates coming from the assumptions that the mantle has a bulk earth composition and all enriched elements are contained in a deeper layer [section 2.5, Becket et al. 1999]. There are also significant uncertainties in the temperature increase across the CMB. However we can directly measure the Earth's surface heat flow, Q_s , and the properties of the upper mantle are much better constrained than those in the deep mantle or a deep layer. For these reasons we use equation 7.34 to estimate the temperature increase from an upper layer in Earth's mantle to a lower layer.

The rate of heat energy flowing over the deformable interface, Q_K , is given by...

$$Q_K = A_K k \frac{\Delta T_K}{\Delta Z_K} \quad (7.35)$$

...where A_K is the surface area of Kellogg layer, k is the thermal conductivity at the depth of the interface and ΔZ_K is the thickness of the thermal boundary at the Kellogg layer.

So we can express the temperature contrast over the Kellogg interface by...

$$\Delta T_K = \frac{(Q_S - Q_u(D))\Delta Z_K(D)}{A_K(D)k(D)} \quad (7.36)$$

Where (D) denotes that the term is a function of depth of the interface.

Present estimates suggest that the flow of heat over the Earth's surface is currently 44TW [Kellogg et al. 1999] with 6TW coming from the radioactive decay in the crust and an unknown amount coming from secular cooling (cooling of the whole Earth).

The rate of internal heating in the upper layer q_u is estimated to be 1 pWkg⁻¹ [Davies 1999, p193]. The rate of heat generated in the upper layer Q_u is given by...

$$Q_u = M_u q_u = \frac{4}{3} \pi \rho_u (R_S^3 - R_K^3) q_u \quad (7.37)$$

...where M_u is the mass of the upper layer, ρ_u is the density of the upper layer, R_S and R_K are the radius of the Earth and the Kellogg layer respectively.

The value of A_K is difficult to estimate since the size of the undulations of a Kellogg layer in Earth-like conditions have not been studied in detail outside of this thesis. However, the author is reasonably confident that equation 5.9 describing the non-dimensional area parameter ϕ in terms of the buoyancy ratio B (see section 5.6.1) is applicable in Earth-like systems and in the absence of any alternatives we are forced to use it although we concede that there may be large errors associated with the calculation of A_K ...

$$\phi = \frac{0.071}{B^3 - 0.44^3} \quad (5.9)$$

Therefore...

$$A_K(D) = 4\pi R_K^2 \left(\frac{0.071}{B^3 - 0.44^3} + 1 \right) \quad (7.38)$$

There are two thermal boundaries associated with the Kellogg interface. The thickness of both of these thermal boundaries, ΔZ , can be found using the following scaling law (see section 2.5)...

$$\Delta Z = L \left(\frac{Ra_c}{Ra} \right)^{\beta} \quad (2.8)$$

Where Ra is the Rayleigh number, Ra_c is the critical Rayleigh number having a value between 87 & 1100, L is the length scale of convection, $0 < \beta < 0.3$ for Earth's mantle [M^cNamara & Van Keken 2000]. The thickness of the thermal boundary above the layer is used since this is the less viscous layer and will therefore be more effective at removing heat.

$$\Delta Z_K(D) = (R_S - R_K) \left(\frac{Ra_c}{Ra_u(D)} \right)^\beta \quad (7.39)$$

The formula used to calculate the Rayleigh numbers...

$$Ra_u = \frac{\alpha(D_u)gC_v\rho_0^2\Delta T(R_S - R_K)^3}{k(D_u)\eta_u} \quad (7.40)$$

Where Ra_u is the Rayleigh numbers of the upper layer; D_u is the non-dimensional depth at the middle of the upper layer; g is the gravitational constant, ΔT is the temperature contrast cross the mantle and η_u is the dynamic viscosity upper layer.

For α equation 2.8 is used.

To describe the variation of the thermal conductivity with depth we use the work of Hofmeister [1999] and determine a form...

$$k(z_d) = (1.2983z_d^3 - 3.438z_d^2 + 5.367z_d + 2.9728) \pm 3\% \quad (7.41)$$

...where $k(z_d)$ is the thermal conductivity at a non-dimensional depth z_d . This form works well describing the range of values of k between 800km and 2600km ($0.28 < z_d < 0.9$). Below this depth (2600km) there is expected to be a sharp decrease in k near to the CMB. The $\pm 3\%$ range is used to incorporate the range of values between an adiabatic mantle and one with the maximum possible temperature, see figure.

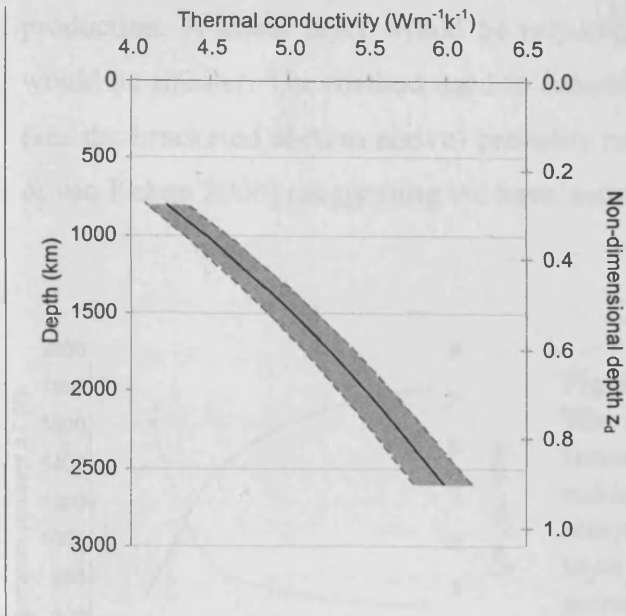


Figure 7.19

The form used to represent the change in thermal conductivity in Earth's mantle with depth based on equation 7.36, which is in turn based on the work of Hofmeister [1999]. Thermal conductivity is only represented over a range of depths between 800km and 2600km ($0.28 < z_d < 0.9$), above this does we are not considering a deep layer and below it any deep layer would probably press against the CMB and the thermal balance considerations used in this section are not valid.

The method used to calculate the values of the terms in equation 7.36 with depth are shown in the bracketed section above and the parameters in table 7.3. The temperature increase across the deformable boundary depends not only on the depth of the interface (the amount of heat from the upper mantle, thermal conductivity and the thickness of the thermal boundary) but also on the buoyancy ratio B that controls the surface area of the boundary. As the lower layer is made heavier (increasing B) the interface between the two layers becomes flatter and the surface area of the interface smaller. A smaller interface requires a larger temperature contrast to produce the same total heat flow across it. An example of the change of the temperature increase and its dependence with B is shown in figure 7.20.

The variation in ΔT_K with the depth of the interface between the two layers is shown for a range of values of ΔT is shown in figure 7.21. A larger temperature contrast is needed when a layer is placed deeper in the mantle. This is despite the increasing value of k & Q_U , and is due to the falling area of the spherical surface as its radius decreases. The effect that undulations have on increasing the surface area of the interface between two layers is an important factor when considering the thermal structure of a layered system. As is the r^2 dependence of the surface area on the radius of the boundary between the layers.

There are however many uncertainties in the calculations used here. Bercovici & Karato [2003] suggested that a melt layer at 410km depth could act as a filter removing incompatible elements and so producing the depleted signatures of MORB. In this model the mantle below 410km would have an increased rate of radiogenic heat

production. A lower layer would be required to conduct less heat energy and so ΔT_K would be smaller. The method used to determine the thickness of the thermal boundary (see the bracketed section above) probably represents the minimum likely [McNamara & van Keken 2000] (suggesting we have under estimated ΔT_K).

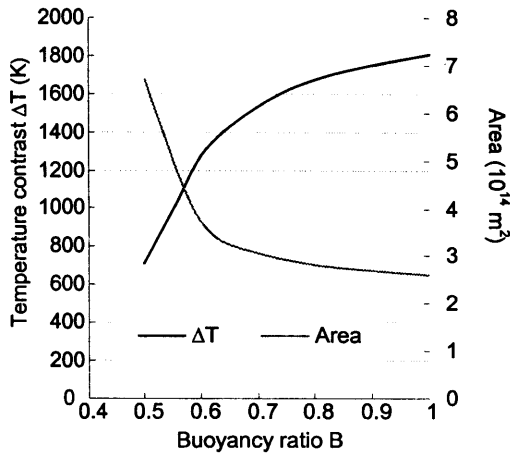


Figure 7.20

The dependence of the temperature predicted across the deformable interface (using equation 7.36) and interface a, on the buoyancy ratio. The results are shown for a layer with an interface 2000km deep. As B increases the interface becomes flatter and so a larger temperature contrast is needed to produce the heat flow observed at Earth's surface.

Parameter		Value
Heat flow across Earth's surface (after removing that generated in continental crust); i.e. mantle surface heat flux.	Q_S	38 T W
Density	ρ_o	5000 kg m ⁻³
Buoyancy ratio	B	0.55, 0.6, 0.7, 0.8 & 0.9
Non-dimensional area parameter (found using equation 3.36)	ϕ	0.87, 0.54, 0.28, 0.17 & 0.11
Radius of Earth	R_S	6370 km
Radius of the CMB	R_{CMB}	3500 km
The rate of internal heating in the upper layer	q_u	1 p W kg ⁻¹
The Critical Rayleigh number	Ra_c	1000
Parameter in equation 2.8	β	0.33
The gravitational acceleration	g	10 ms ⁻²
Specific heat capacity	C	1000 J kg ⁻¹ K ⁻¹
Temperature contrast across the mantle	ΔT	2000 K
Thickness of the thermal boundary	ΔZ	100 km
Dynamic viscosity of the upper layer	η_u	10 ²¹ Pa s
Dynamic viscosity of the lower layer	η_l	10 ²³ Pa s

Table 7.3

Earth-like parameters used to calculate the temperature increase across a layer in the mantle using equation 7.36.

This method uses the assumption that the mantle is currently thermally balanced. The contribution to the current surface heat flow from secular cooling is unknown though it is unlikely to be larger than 20TW with a most likely value of 10TW. It is not known how much of this heat would have to flow over a Kellogg interface. We have also not considered the contribution of entrainment to the heat flow across an interface. In the calculations presented in chapters 5 & 6 we saw how our layered models start from an initially steady single layered state. When a layer was introduced the lower layer heated up and it could take billions of years before the lower layer was hot enough for the layer to be in thermal balance [section 5.5]. This suggests that a layered mantle stores more heat than a mantle that is convecting as a single layer. The Earth will not have started in a cold state and heated up but will have begun hot and cooled down. It is debatable whether the high temperatures in the past will have made chemical layering more stable [Montague & Kellogg 2000] or more unstable. In the numerical experiments presented in this thesis and the lab work of Davaille and co-workers [e.g. Davaille 1999] an initially stratified layer becomes increasingly unstable as the temperature of the lower layer in a system increases. Le Bars & Davaille [2002] also find that the critical buoyancy ratio B_c increases with Ra , suggesting that in a hotter (higher Ra) mantle layering would be less stable [see section 2.7.1 for a more detail discussion]. In the case of Earth the lower layer will not have heated up (as is the case in our numerical models) but will have cooled down starting from an initially very hot state. For this reason it is likely that the temperature of the lower layer would be very large, and may even be larger than those suggested by the method used here.

In summary the methods used to calculate the temperature increase across a deformable interface can be criticised. Some assumptions are expected to cause an underestimate of ΔT_K : the method used to find ΔZ ; and other assumptions to overestimate ΔT_K : increased heating in the upper mantle, the contribution of secular cooling and the heat transported out of the lower layer by entrainment. For these reasons we must be cautious of these results. The shape of the graph in figure 7.21 is most likely correct, however the exact values could be very different from those shown, for a true Earth-like system.

The thermal contrast across a deformable boundary must have some maximum value. At high temperatures mantle material will melt and it is very unlikely that large pockets

of molten magma in the mantle would be undetected by seismic methods. The temperature at which lower mantle rocks would melt is uncertain but is thought to be around 7000K [Zerr & Boehler, 1993]. Since this melting temperature is quite high it is not a strong constraint. The mantle temperature at the core mantle boundary is thought to be around 2650K [Boehler, 1992]. This estimate might be slightly low, but even so, we would not expect a temperature jump across the interface to exceed 2000K in an Earth-like system.

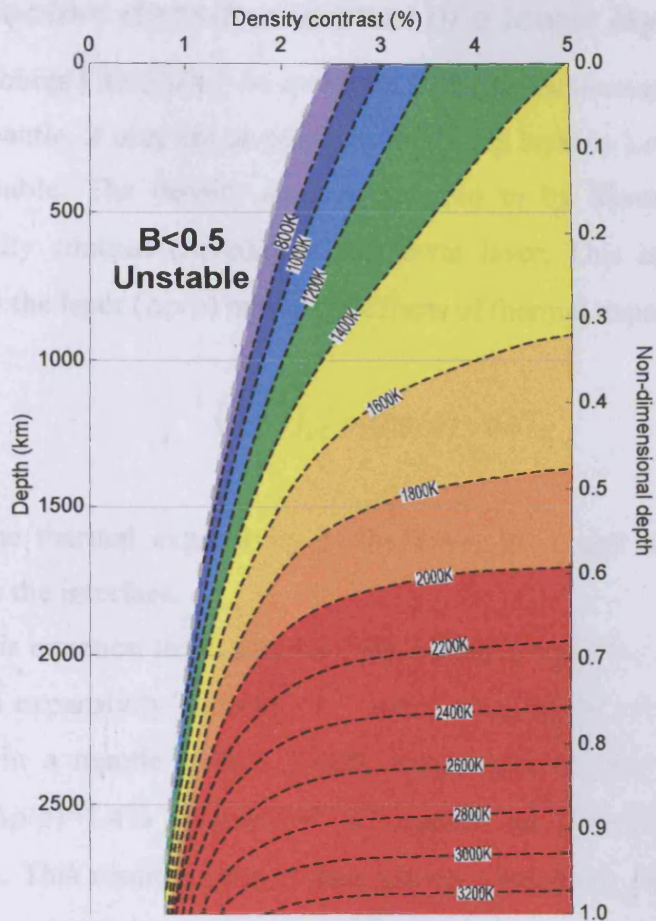


Figure 7.21

The temperature contrast across the interface required to supply Earth-like surface heat flow predicted by equation 7.36. Very hot temperatures are required in the lower layer for deep layers. The decrease of the temperature contrast as the density contrast decreases to unstable values is caused by the increasing surface area of the layer. Black dashed lines represent contour lines, the grey dashed line represents the point at which the buoyancy ratio falls below 0.5 and layering becomes unstable.

7.9 The effective density contrast of a lower layer

Masters & Gubbins [2003] find no evidence for a density increase of greater than 0.4% in the lower mantle. It may not be possible for a deep layer to have such a small density and remain stable. The density contrast referred to by Masters & Gubbins is the effective density contrast $(\Delta\rho/\rho)_{\text{eff}}$ of the lower layer. This is the chemical density contrast across the layer $(\Delta\rho/\rho)$ minus the effects of thermal expansion of the layer.

$$(\Delta\rho/\rho)_{\text{eff}} = (\Delta\rho/\rho) - \alpha\Delta T_K \quad (7.42)$$

Where α is the thermal expansivity of the lower layer and ΔT_K is the temperature increase across the interface.

We can use this equation to do some simple calculations: if we consider a lower layer with a thermal expansivity of $1 \times 10^{-5} \text{ K}^{-1}$ and a temperature increase of 1000K across the boundary in a mantle with a 2000K temperature increase across it. A density increase of $(\Delta\rho/\rho)=1.4\%$ is required to produce an effective density contrast of $(\Delta\rho/\rho)_{\text{eff}}=0.4\%$. This results in the system having a buoyancy ratio of $B=0.7$, which is sufficient for layering to be stable.

From equation 7.42...

$$\begin{aligned} (\Delta\rho/\rho) &= (\Delta\rho/\rho)_{\text{eff}} + \alpha\Delta T_K \\ (\Delta\rho/\rho) &= 0.004 + 1 \times 10^{-5} \times 1000 \\ (\Delta\rho/\rho) &= 0.014 \\ (\Delta\rho/\rho) &= 1.4\% \end{aligned}$$

We use equation 2.10 to find the buoyancy ratio...

$$\begin{aligned} B &= (\Delta\rho/\rho) \div \alpha\Delta T_K \\ B &= 0.014 \div 1 \times 10^{-5} \times 2000 \\ B &= 0.014 \div 0.02 \\ B &= 0.7 \end{aligned}$$

A more detailed investigation of the $(\Delta\rho/\rho)_{\text{eff}}$ using the values of ΔT_K suggested by equation 7.42 is shown in figure 7.22. It shows a range of depths and chemical density contrasts at which a deep layer can be both stable and undetected by free oscillation

measurements. These results (though far from conclusive) do suggest that there may be some regimes in which a deep layer could have an effective density contrast of less than 0.4% and still be dynamically stable.

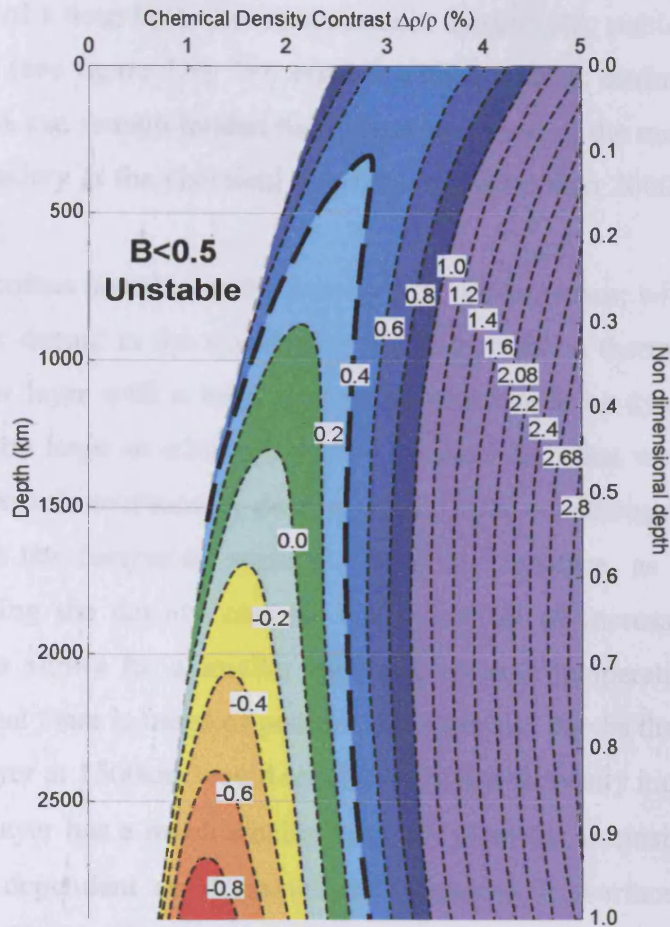


Figure 7.22

Contour plot of the effective density contrast $(\Delta\rho/\rho)_{\text{eff}}$ (the chemical density contrast minus the effects of thermal expansion) of a lower layer in Earth's mantle from equation 7.42. A deep layer with a density contrast of less than 0.4 is thought to be invisible to free oscillation methods. The $(\Delta\rho/\rho)_{\text{eff}}=0.4$ contour line is shown as a bold dashed line, below this a layer would be undetected. The point at which layering is likely to become unstratified is shown as a grey dashed line.

7.10 Summary

We can combine figures 7.21 & 7.22 to produce an estimate of the possible depth and density contrast of a deep layer that could remain dynamically stable and undetected by free oscillations (see figure 7.9). We assume a layer with an intrinsic density increase of less than 0.4% can remain hidden throughout the depth of the mantle, and that when the thermal boundary at the chemical interface is greater than 2000K the bottom layer becomes too hot.

A deep layer becomes unstable as the density contrast decreases; with a smaller density increase possible deeper in the mantle due to the decrease in thermal expansivity with depth. A shallow layer with a large density contrast would be dynamically stable but would produce too large an effective density increase such that we would expect it to be detected by seismic methods. A deeper, denser layer would require a larger thermal boundary due to the decreasing surface area of the interface, as it is deeper in the mantle. Decreasing the density contrast has the effect of increasing the interface's undulations. This allows for a smaller and more realistic temperature increase. These results suggest that there is range of possible densities and depths that fulfil our criteria. A mid-mantle layer at 1500km would require an intrinsic density increase between 1.5-3%. A D'' type layer has a much smaller range of plausible intrinsic density increases and is strongly dependent on deformations increasing its surface area to maintain thermal balance. Thermal balance can also be achieved by having sections of the layer pushed against the CMB allowing heat to flow from the core directly into the upper layer.

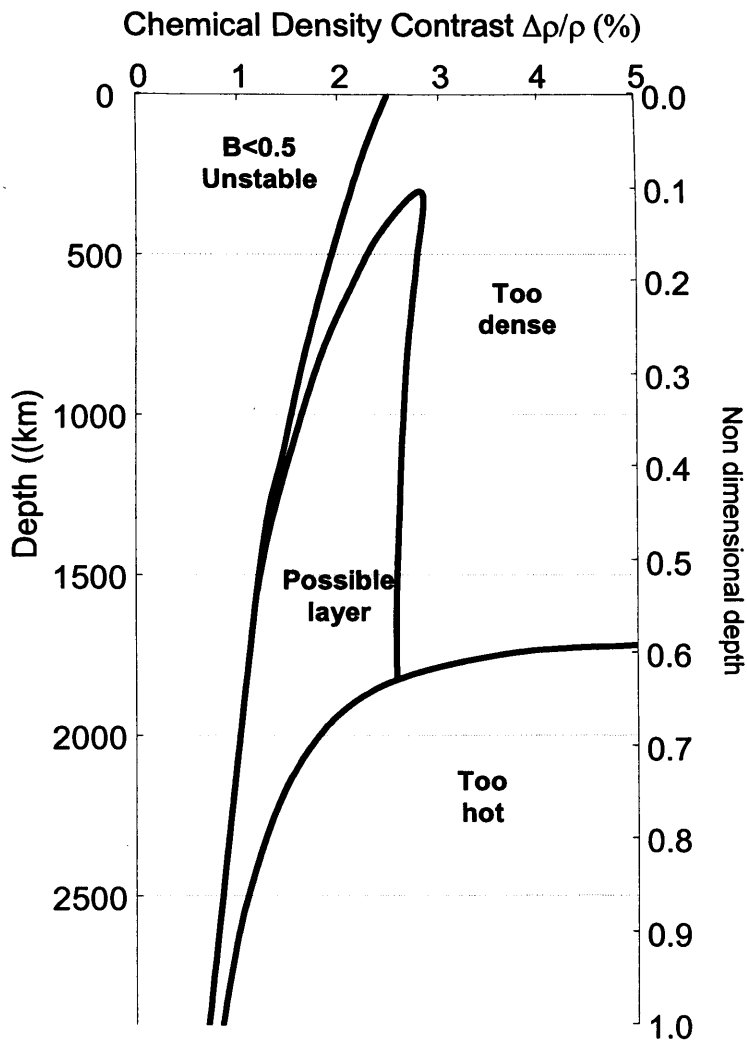


Figure 7.23
The possible intrinsic chemical density contrast and depth of a layered mantle that is dynamically stable and unobserved by free oscillations.

8 Conclusions and summary

We have shown that the marker method reliably models a layered spherical system, however it is limited to stratified cases. Our implementation is unable to model a system in which the side of the markers' boundary approaches the near vertical. In cases where the surface distorts into plume head structures the method undoubtedly fails. To model more complex chemically stratified systems such as blobs or a marble cake mantle a more flexible method such as particles could be used [Stegman 2002a]. This comes with its own drawbacks and the increased RAM needed by the particle method would limit the resolution of any calculation dramatically. However, as computer power continues to increase this becomes less important for mantle simulations and the particle method will almost certainly be used more and more in the future.

The radial thermal structure was found to be relatively unaffected by the heating mode used to power convection. The stability of a deeper layer and the thermal boundary across the chemical interface is controlled by the total heat energy being added to the lower layer, rather than the heating mode. We find no evidence that the values of the critical buoyancy ratio B_c is dependent on the heating mode which conflicts with the results of Tackley [1998] though we use a different definition of the buoyancy ratio.

We are able to characterize the stability of convection with a non-dimensional variable: the surface area variable ϕ ...

$$\phi = \frac{A - A_0}{A_0} \quad (5.5)$$

Where A is the area of the interface and A_0 is the area of a spherical shell at the same depth as the interface. The value of ϕ is found to be strongly dependent on the buoyancy ratio B , independent of the heating mode and only weakly dependent on the depth of the interface. In a system with a uniform viscosity, ϕ , can be represented by the form...

$$\phi = \frac{0.071}{B^3 - 0.44^3} \quad (5.9)$$

Entrainment of material from a lower layer is necessary to produce the enriched signatures of OIB, in the classic geochemical model. The rate of entrainment must be such that a deep layer could have survived throughout Earth's history without mixing completely into the upper layer. For current estimates of the rate of entrainment of a deep layer [Sleep 1988, Davaille 1999b, Zhong & Hager 2003] this requirement does not significantly challenge the proposal of a deep layer within Earth's mantle [Gonnerman et al. 2002]. We investigate the current entrainment equations used in the literature, and extend them to include viscous forces. We conclude that entrainment is unlikely to be significant for a layered Earth-like system, since it would require density contrasts of less than 0.5%, which are not dynamically stable.

The coupling mode is an important characteristic of a layered systems. The rate of entrainment and the formation of plume structures at the thermal chemical boundary between the two layers is dependent on the coupling mode. We have observed that as the system moves from low to high Ra there is a change from viscous to thermal coupling [section 6.5, figure 6.8, Davaille 2003]. This can be predicted by considering the ratio between the viscous and thermal buoyancy forces acting on the boundary [section 7.2, Richter & Johnson 1974]. Our calculations suggest that in an Earth-like system neither thermal nor viscous forces would dominate and so coupling at a boundary would likely be a hybrid of the two modes. There is some evidence [section 7.2] though that thermal coupling may be the more dominant.

One of the less successful elements of the classical geodynamical mantle model is its failure to explain the apparent fixity of hotspot locations. The inclusion of a more viscous layer in the deep mantle would aid the fixture of plumes forming at the boundary. Davaille et al. [2002] argue that layered convection can reduce hotspot mobility. The two mega-plume structures observed in the lower mantle [section 2.3.2.3] make very attractive locations for a chemically distinct primitive region [e.g. Ni & Helmberger 2003] and so suggest a long wavelength structure for a deep layer. However this model does not explain the fixity of hotspots such Hawaii and Reunion that are not associated with superswells. The wavelength of the deformation of a deformable boundary is dependent on the non-dimensional depth of the boundary (figure 5.9). The peak harmonic degree of the undulations tends towards smaller values when the interface is placed near to the lower shell boundary. This suggests that if the

interface were placed in the mid-mantle then it would have more peaks and troughs than a layer deeper in the mantle. Given the presence of the two megaplumes and the apparent two-cell convection taking place in the mantle then in the layered scenario a deeper layer seems more likely.

We can place constraints on the possible density increase across a stable chemical interface in the lower mantle, $\Delta\rho/\rho$, using two methods. Firstly, a minimum possible value of $\Delta\rho/\rho$ can be found that is required to keep a lower layer dynamically stable. Secondly, a maximum value of $\Delta\rho/\rho$ can be found by considering observations from seismic methods. If a deep layer does exist in the Earth's mantle then it must have a density increase between these two values. In section 7.6 we showed that a layer at a depth of 2000km would need a density increase between 0.2-2.2% to have a stratified structure, with the most likely values being $\Delta\rho/\rho > 0.5\%$.

The most demanding constraints placed on the maximum value of $\Delta\rho/\rho$ are by free oscillation data. The observation of Masters & Gubbins [2003] required an effective density contrast of $(\Delta\rho/\rho)_{\text{eff}} < 0.4\%$. In section 7.9 we showed that this related to a chemical density contrasts of $\Delta\rho/\rho < 2.8\%$. Larger values of $\Delta\rho/\rho$ though required very high temperatures increases across the deformable interface in the lower mantle and beneath 1800km depth a value of $\Delta\rho/\rho < 2.0\%$ is more likely. Minimum values of $\Delta\rho/\rho$ found using the constraints of seismic reflection techniques are much larger (3.5-4% and 5%). We find a range of intrinsic density contrasts and depths for which a layer is able to meet the criteria of being dynamically stable, unnoticed by seismic reflection and free oscillation observations, and have a realistic thermal structure (see figure 7.23).

Lateral variations in the mantle seismic velocity structure are predicted by tomography inversions to be largest in the uppermost mantle and the CMB (figure 2.6). However, the lateral temperature variations produced by our simulations have a large amplitude (300-600K) at the depth of the interface between the two layers, unlike the tomography. We then advance the comparison, by removing the effects of the chemical density contrast. We find that the lateral density variations (converted to temperature) as a

function of depth do reduce the anomaly although it remains present. We continue to try and remove this anomaly by using a linear combination of temperature and intrinsic density to represent the seismic velocity. Even after allowing the scaling coefficient to have a value that minimizes the amplitude of the anomaly it still persists. It seems likely that a layered mantle would have a large lateral seismic anomaly at the depth of the interface. The absence of any such anomaly in present seismic tomography models suggests that Earth's mantle is unlikely have an interface far away from the surface or CMB.

9 References

- Albarède, F. Time dependent models of U-Th_He and K-Ar evolution and the layering of mantle convection, *Chem. Geol.*, 145, 413-429, 1998
- Albers, M., & U. R. Christensen, The excess temperature of plumes rising from the core-mantle boundary, *Geophys. Res. Lett.*, 23, 3567-3570, 1996
- Anders, E., Chemical composition of the Moon, Earth and eucrite parent body, *Philos. Trans. R. Soc. London*, A285, 23-40, 1977
- Anderson, D. L., Mantle Plume Debate, *Astronomy and Geophysics, Royal Astronomical Society*, 44, 10-11, 2003
- Anderson, D. L., A statistical test of the two reservoir model for helium isotopes, *Earth Planet. Sci. Lett.*, 193, 77-82, 2001
- Anderson, D. L., The statistics of helium isotopes along the global spreading ridge system and central limit theorem, *Geophys. Res. Lett.*, 27, 2401-2404, 2000a
- Anderson, D. L., The statistics and distribution of helium in the mantle, *Int. Geol. Rev.*, 42, 289-311, 2000b
- Anderson, D. L., Equation for thermal expansivity in planetary interiors, *J. Geophys. Res.*, 72, 3661-3668, 1967
- Anderson, O. L., Chopelas, A., & R. Boehler, Thermal expansivity versus pressure at constant temperature: a re-examination, *Geophys. Res. Lett.*, 17(6), 685-688, 1990
- Baumgardner, J. R., & P. O. Frederickson, Icosahedral discretization of the two-sphere, *SIAM J. Numerical Anal.*, 22, 1107-1155, 1985
- Baumgardner, J. R., A three-dimensional finite element model for mantle convection, *P.h.D. Thesis*, Uni. Of California, 1983
- Becker, T. W., J. B. Kellogg, & R. J. O'Connell, Thermal constraints on the survival of primitive blobs in the lower mantle, *Earth Planet. Sci. Lett.*, 171, 351-365, 1999
- Bercovici, D., & S. Karato, Whole mantle convection and the water transition-zone water filter, *Nature*, 425, 39-44, 2003
- Bijwaard, H., & W. Spakman, Nonlinear global P-wave tomography by iterated linearized inversion, *Geophys. J. Int.*, 141, 71-82, 2000
- Bijwaard, H., & W. Spakman, Tomographic evidence for a narrow whole mantle plume below Iceland, *Earth Planet. Sci. Lett.*, 166, 121-126, 1999

- Boehler, R., Melting of Fe-FeO and the Fe-FeS systems at high pressure: constraints on core temperatures, *Earth Sci. Planet. Lett.*, 111, 217-227, 1992
- Boussinesq, J. Theorie analytique de le Chaleur mise en harmonie avec la thermodynamic et avec la theorie mechanique de la lumiere, vol 2, 157-176, Gauthiers-Villars, Paris, 1903
- Brandt, A., Multi-level adaptive solutions to boundary value problems, *Mathematics of computation*, 31, 333-390, 1977
- Bréger, L., B. Romanowicz, & C. Ng, The Pacific plume as seen by S, ScS, and SKS, *Geophys. Res. Lett.*, 28, 859-1862, 2001
- Bunge, H. P., & J. H. Davies, Tomographic models of a mantle circulation model, *Geophys. Res. Lett.*, 28(1), 77-80, 2001
- Bunge, H. P., & P. Grand, Mesozoic plate-motion history below the northeast Pacific ocean from seismic images of the subducted Farallon slab, *Nature*, 405, 337-340, 2000
- Bunge, H. P., M. A. Richards, C. Lithgow-Bertelloni, J. R. Baumgardner, S. P. Grand, & B. A. Romanowicz, Time scales and heterogeneous structure in the geodynamic Earth models, *Science*, 280, 91-95, 1998
- Bunge, H. P., M. A. Richards, & J. R. Baumgardner, A sensitivity study of three-dimensional spherical mantle convection at 10^8 Rayleigh number: effects of depth-dependent viscosity, heating mode, and an endothermic phase boundary, *J. Geophys. Res.*, 102(B6), 11991-12007, 1997
- Bunge, H. P., Global mantle convection models, *P.h.D. Thesis*, Uni. Of California, 1996
- Bunge, H. P., & J. R. Baumgardner, Mantle convection modelling on parallel virtual machines, *Computers in Physics*, 9 No 2, 207, 1995
- Castle, J., R. D. van der Hilst, Searching for seismic scattering off mantle interfaces between 800km and 2000km depth, *J. Geophys. Res.*, 108 (B2), 2095-2108, 2003a
- Castle, J., R. D. van der Hilst, Using ScP precursors to search for mantle structures beneath 1800km depth, *Geophys. Res. Lett.*, 30(8), art. No. 1422, 2003b
- Castle, J., & K. C. Creager, Topography of the 660km seismic discontinuity beneath Izu-Bonin: Implications for tectonic history and slab deformation, *J. Geophys. Res.*, 103(B6), 12511-12527, 1998
- Chopelas, A., & R. Boehler, Thermal expansivity in the lower mantle, *Geophys. Res. Lett.*, 19(19), 1983-1986, 1992

- Chopelas, A., & R. Boehler, Thermal expansion measurements at very high pressure, systematics, and a case for a chemically homogenous mantle, *Geophys. Res. Lett.*, 16(16), 1347-1350, 1989
- Christensen, U. R., & D. A. Yuen, The interaction of a subducting lithospheric slab with a chemical or phase boundary, *J. Geophys. Res.*, 89(B6), 4389-4402, 1984
- Coltice, N., & Y. Ricard, Geochemical reservoirs and the one layer mantle, *Earth Planet. Sci. Lett.*, 174, 125-137, 1999
- Courtillot, V., A. Davaille, J. Besse, & J. Stock, Three distinct types of hotspots in the Earth's mantle, *Earth Planet. Sci. Lett.*, 205, 295-308, 2003
- Craig, H., & J. E. Lupton, Primordial neon, helium, and hydrogen in oceanic basalts, *Earth Planet. Sci. Lett.*, 31, 369-385, 1976
- Daly, S. F., The vagaries of variable viscosity convection, *Geophys. Res. Lett.*, 7, 841-844, 1980
- Davaille, A., M. Le Bars, & C. Carbonne, Thermal convection in a heterogeneous mantle, *C. R. Geoscience*, 335, 141-156, 2003
- Davaille, A., F. Girard, & M. Le Bars, How to anchor hotspots in a convecting mantle?, *Earth Planet. Sci. Lett.*, 203, 621-634, 2002
- Davaille, A., Simultaneous generation of hotspots and superswells by convection in a heterogeneous planetary mantle, *Nature* 402, 756-689, 1999a
- Davaille, A., Two-layer thermal convection in miscible viscous fluids, *J. Fluid Mech.*, 379, 223-253, 1999b
- Davies, G. F., Dynamic Earth: plates, plumes and mantle convections, *Cambridge University Press*, ISBN: 0521599334, 1999
- Davies, G. F., Mantle convection model with a dynamic plate: topography heat flow and gravity anomalies, *Geophys. J.*, 98, 461-464, 1989a
- Davies, G. F., Effect of a low viscosity layer on long-wavelength topography upper mantle case, *Geophys. Res. Lett.*, 17(7), 625-628, 1989b
- Davies, G. F., Ocean bathymetry and mantle convection large-scale flow and hotspots, *J. Geophys. Res.*, 93(B9), 10467-10480, 1988
- Davies, G. F., Geophysical and isotopic constraints on mantle convection: an interim synthesis, *J. Geophys. Res.*, 89, 6017-6040, 1984
- DePaolo, D. J., & M. Manga, Deep origin of hotspots – the mantle plume model, *Science*, 300, 920-921, 2003

- Dietz, R. S., Continent and ocean evolution by spreading of the sea floor, *Nature*, 190, 854-847, 1961
- Drake, M. J., K. Righter, Determining the composition of the Earth, *Nature*, 416, 39-44, 2002
- Dubuffet, F., D. A. Yuen, & M. Rabinowicz, Effects of a realistic thermal conductivity on the patterns of 3D convection, *Earth and planet. Sci Lett.*, 171, 401-409, 1999
- Dziewonski, A. M., & D. L. Anderson, Preliminary reference Earth model, *Phys. Earth Planet. Int.*, 25, 297-356, 1981
- Ferrachat, Y., & Y. Ricard, Regular vs. chaotic mantle mixing, *Earth Planet. Sci Lett.*, 155, 75-86, 1998
- Forte, A. M., J. X. Mitrovica, & A. Espeset, Geodynamic and seismic constraints on the thermochemical structure and dynamics of convection in the deep mantle, *Philos. T. Roy. Soc.*, 260(1800), 2521-2543, 2002
- Forte, A. M., & J. X. Mitrovica, Deep-mantle high-viscosity flow and thermochemical structure inferred from seismic and geodynamic data, *Nature*, 410, 1049-1056, 2001
- Forte, A.M. & Perry, H.K.C., Geodynamic evidence for a chemically depleted continental tectosphere, *Science*, 290: 1940-1944, 2000
- Foulger, G. R., & J. H. Natland, Is "hotspot" volcanism a consequence of plate tectonics, *Science*, 300, 921-922, 2003
- Foulger, G. R., M. J. Pritchard, B. R. Julian, J. R. Evans, R. M. Allen, G. Nolet, W. J. Morgan, B. H. Bergsson, P. Erlendsson, S. Jakobsdottir, S. Ragnarsson, R. Stefansson, K. Vogfjörð, Seismic tomography shows that upwelling beneath Iceland is confined to the upper mantle, *Geophys. J. Int.*, 146, 504-530, 2001
- Fowler, C. M. R., The solid Earth, An introduction to global geophysics, *Cambridge University Press*, ISBN 0-521-38590-3, 1990
- Fukao, Y., S. Widiyantoro, & M. Obayashi, Stagnant slabs in the upper and lower mantle transition region, *Rev. Geophys.*, 39, 291-323, 2001
- Garboczi, E.J., Three-dimensional mathematical analysis of particle shape using X-ray tomography and spherical harmonics: application to aggregates used in concrete, *Cement and Concrete Research*, 32 (10), 1621-1638, 2002
- Glatzmaier, G. A., & G. Schubert, Three-dimensional models of layered and whole mantle convection, *J. Geophys. Res.*, 98(B12), 21969-21976, 1993
- Gonnermann, H. M., M. Manga, & M. Jellinek, Dynamics and longevity of an initially stratified mantle, *Geophys. Res. Lett.*, 29(10), 1399, 2002

- Gonzalez, R. C., & R. E. Woods, Digital image processing, Reading, Mass: Addison-Wesley, 1992
- Grand, S., R. van der Hilst, & S. Widiyantoro, Global seismic tomography: a snapshot of convection in the Earth, *G.S.A. Today*, 7, 1-7, 1997
- Grand, S. P., Mantle shear structure beneath the Americas and surrounding oceans, *J. Geophys. Res.*, 99, 11591-11621, 1994
- Gurnis, M., J. X. Mitrovica, J. Ritsema, & H. J. van Heijst, Constraining mantle density structure using geological evidence of surface uplift rates: the case of the African superplume, *Geochem. Geophys. Geosyst.*, 1, 35 (Article), 1999GC000035, 1999
- Gurnis, M., & G. F. Davies, The effect of depth-dependent viscosity on convective mixing in the mantle and the possible survival of primitive mantle, *Geophys. Res. Lett.*, 13, 541-544, 1986
- Hall, R., & W. Spakman, Subducted slabs beneath the eastern Indonesia-Tonga region: insights from tomography, *Earth Planet. Sci. Lett.*, 201, 321-366, 2002
- Hansen, U. & D. A. Yuen, Extended-Boussinesq thermal-chemical convection with moving heat sources and variable viscosity, *Earth Planet. Sci. Lett.*, 176, 401-411, 2000
- Hansen, U., D. A. Yuen, S. E. Kroening, & T. B. Larsen, Dynamical consequences of depth-dependent thermal expansivity and viscosity on mantle circulations and thermal structure, *Phys. Earth Planet. Int.*, 77, 205-223, 1993
- Hedlin, A. H., P. M. Shearer, & P. S. Earle, Seismic evidence for small-scale heterogeneity throughout the Earth's mantle, *Nature*, 387, 145-150, 1997
- Helffrich, G. R., & B. J. Wood, The Earth's mantle, *Nature*, 412, 501-507, 2001
- Hoffman, A. W., Mantle geochemistry: the message from oceanic volcanism, *Nature*, 285, 219-229, 1997
- Hoffman, N. R. A., & McKenzie, D. P., The destruction of geochemical heterogeneities by differential fluid motions during mantle convections, *Geophys. J. R. astr. Soc.*, 82, 163-206, 1985
- Hofmeister, A. M., Mantle values of thermal conductivity and the geotherm from phonon lifetimes, *Science*, 283, 1699-1706, 1999
- Housemann, G., The dependence of convection planform on mode of heating, *Nature*, 332, 346-349, 1988

- Hunt, D. L., & L. H. Kellogg, Quantifying mixing and age variations of heterogeneities in models of mantle convection: Role of depth-dependent viscosity, *J. Geophys. Res.*, 106 (B4), 6747-6759, 2001
- Jellinek, A. M., & M. Manga, The influence of a chemical boundary layer on the fixity, spacing and lifetime of mantle plumes, *Nature*, 418, 760-763, 2002
- Jellinek, A. M., A. Lenardic, & M. Manga, The influence of interior mantle temperature on the structure of plumes: heads for Venus, tails for the Earth, *Geophys. Res. Lett.*, 29(11), 10.1029/2001GL014624, 2002
- Janney, P. E., J. D. Macdougall, J. H. Natland, & M. A. Lynch, Geochemical evidence from the Pukapuka volcanic ridge system for a shallow enriched mantle domain beneath the south Pacific superswell, *Earth Planet. Sci. Lett.*, 181, 47-60, 2000
- Kaneshima, S., & G. Helffrich, Dipping Low-Velocity Layer in the Mid-Lower Mantle: Evidence for Geochemical Heterogeneity, *Science*, 283, 1888-1891, 1999
- Kárason, H., & R. D. van der Hilst, Tomographic imaging of the lowermost mantle with times of refracted and diffracted core phases, *J. Geophys. Res.*, 106(B4), 6569-6587, 2001
- Karato, S., & B. Karki, Origin of lateral variation of seismic wave velocities and density in the deep mantle, *J. Geophys. Res.*, 106(B10), 21771-21783, 2001
- Kellogg, L. H., B. H. Hager, R. D. van der Hilst, Composition stratification in the deep mantle, *Science*, 283, 1881-1884, 1999
- Kennett, B. L. N., S. Widiyantoro, & R. D. van der Hilst, Joint seismic tomography for bulk sound and shear wave speed in the Earth's mantle, *J. Geophys. Res.*, 103(B6), 12469-12495, 1998
- Knittle, E., & R. Jeanloz, Simulating the Core-Mantle boundary – an experimental study of high pressure reaction between silicates and liquid iron, *Geophys. Res. Lett.*, 609-612, 1989
- Lay, T., Structure of the core-mantle transition zone: A chemical and thermal boundary layer, *Eos Trans. AGU*, 70, 49, 54-55, 58-59, 1989
- Le Bars, M., & A. Davaille, Large deformations of the interface in two-layer thermal convection of miscible viscous fluids, *J. Fluid Mech.*, 499, 75-110, 2004
- Le Bars, M., & A. Davaille, Stability of thermal convection in two superimposed miscible viscous fluids, *J. Fluid Mech.*, 471, 339-363, 2002
- LeStunff, Y., C. Wicks, B. Romanowicz, P'P' Precursors Under Africa: Evidence for Mid-Mantle Reflectors, *Science*, 270, 74-77, 1995

- Lithgow-Bertelloni, C., & P. G. Silver, Dynamic topography plate driving forces and the African superswell, *Nature*, 395, 269-272, 1998
- Maclennan, J., D. M^cKenzie, & K. Gronvöld, Plume-driven upwelling under central Iceland, *Earth Planet. Sci. Lett.*, 194, 67-82, 2001
- Masters, G. & D. Gubbins, On the resolution of density in the Earth, *Phys. Earth Planet. Int.*, 140, 159-167, 2003
- Masters G., G. Laske, H. Bolton, & A. Dziewonski, The Relative Behavior of Shear Velocity, Bulk Sound Speed, and Compressional Velocity in the Mantle: Implications for Chemical and Thermal Structure in: S. Karato, A.M. Forte, R.C. Liebermann, G. Masters and L. Stixrude (eds.) "Earth's Deep Interior", AGU Monograph 117, AGU, Washington D.C., 2000
- Matyska, C., & D. A. Yuen, Profiles of the Bullen parameter from mantle convection modelling, *Earth Planet. Sci. Lett.*, 178, 39-46, 2000
- Matyska, C., J. Moser, & D. A. Yuen, The potential influence of radiative heat transfer on the formation of megaplumes in the lower mantle, *Earth Planet. Sci. Lett.*, 125, 255-266, 1994
- McDonough, W. F., & S. Sun, The composition of the Earth, *Chem. Geo.*, 120, 223-253, 1995
- McNamara, A. K., P. E. Van Keken, & S. Karato, Development of anisotropic structure in the Earth's lower mantle by solid state convection, *Nature*, 416, 310-314, 2002
- McNamara, A. K., S. I. Karato, & P. E. Van Keken, Localization of dislocation creep in the lower mantle: implications for the origin of seismic anisotropy, *Earth Planet. Sci. Lett.*, 191, 85-99, 2001
- McNamara, A. K., & P. E. van Keken, Cooling of the Earth: a parameterised convection study of whole versus layered models, *Geochem. Geophys. Geosyst.*, 1(Article), 2000GC000045, 2000
- Megnin, C., & B. Romanowicz, The three-dimensional shear velocity structure of the mantle from the inversion of body surface and higher-mode waveforms, *Geophys. J. Int.*, 143, 709-728, 2000
- Meibom, A., & D. L. Anderson, The statistical upper mantle assemblage, *Earth Planet. Sci. Lett.*, 217, 123-139, 2003
- Montague, N. L. & L. H. Kellogg, Numerical models of a dense layer at the base of the mantle and implications for the geodynamics of D", *J. Geophys. Res.*, 105 (B5), 11101-11114, 2000

- Morgan, W. J., Plate motions and deep mantle convection, *Nature*, 230, 42-43, 1971
- Nataf, H. C., Seismic imaging of mantle plumes, *Ann. Rev. Earth Planet. Sci.*, 28, 391-417, 2000
- Ni, S., and D. V. Helmberger, Seismological constraints on the South African superplume; could be the oldest distinct structure on earth, *Earth Planet. Sci. Lett.*, 206, 119-131, 2003
- Niu, F., H. Kawakatsu & Y. Fukao, Seismic evidence for a chemical heterogeneity in the midmantle: A strong and slightly dipping seismic reflector beneath the Mariana subduction zone, *J. Geophys. Res.*, 108 (B9), 2419-2430, 2003
- Niu, Y., & M. J. O'Hara, Origin of ocean island basalts: A new perspective from petrology, geochemistry, and mineral physics considerations, *J. Geophys. Res.*, 108 (B4), 2209-2228, 2003
- Oldham, D. N., & J. H. Davies, Numerical investigation of layered convection in a 3D shell with application to planetary mantles, *Geochem. Geophys. Geosyst.*, under revision, 2004
- Olson, P., & C. Kincaid, Experiments on the interaction of thermal convection and compositional layering at the base of the mantle, *J. Geophys. Res.*, 96, 4347-4354, 1991
- Olson, P., G. Schubert, C. Anderson, Structure of axisymmetric mantle plumes, *J. Geophys. Res.*, 98, 6829-6844, 1993
- Ono, S., E. Ito, & T. Katsura, Mineralogy of subducted basaltic crust (MORB) from 25 to 37 GPa and chemical heterogeneity of the lower mantle, *Earth Planet. Sci. Lett.*, 190, 57-63, 2001
- Ranalli, G. R., Rheology of the Earth (second edition), *Chapman & Hall*, ISBN 0-412-54670-1, 1995
- Rasenet, S., F. H. Busse, & I. Rehberg, A theoretical and experimental study of double-layer convection, *J. Fluid Mech.*, 199, 519-540, 1989
- Ratcliff, J. T., P. J. Tackley, G. Schubert, & A. Zebib, *Phys. Earth Planet Int.*, Transitions in thermal convection with strong variable viscosity, *Phys. Earth Planet Int.*, 102, 201-212, 1997
- Rhodes, M., & J. H. Davies, Tomographic imaging of multiple mantle plumes in the uppermost lower mantle, *Geophys. J. Int.*, 147, 88-92, 2001
- Richards, M. A., & D. C. Engebretson, Large-scale mantle convection and the history of subduction, *Nature*, 355, 437-440, 1992

- Richards M.A., & R.W. Griffiths, Deflection of plumes by mantle shear flow: experimental results and a simple theory. *Nature*, 342, 900-902, 1988
- Richards, M. A., B. Hager & N. Sleep, Dynamically supported geoid highs over hotspots: Observations and theory, *J. Geophys Res.*, 93, 7690-7708, 1988
- Richter, F. M., & D. P. McKenzie, On some consequences and possible causes of layered mantle convection, *J. Geophys. Res.*, 86(B7), 6133-6142, 1981
- Richter, F. M., & C. E. Johnson, Stability of a chemically layered mantle, *J. Geophys. Res.*, 79(11), 1635-1639, 1974
- Ride, N. M., U. R. Christensen, The dynamic origin of Hawaiian volcanism, *Earth Planet. Sci. Lett.*, 171, 517-531, 1999
- Ringwood, A. E., Origin of the Earth and Moon, *Springer. New York*, 1979
- Ringwood, A. E., The Chemical composition of the core and implications for the origin of the Earth, *Geochem. J.*, 11, 111-135, 1977
- Ritsema, J., & H. J. van Heijst, Seismic imaging of structural heterogeneity in Earth's mantle: Evidence for large-scale mantle flow, *Science Progress*, 83, 243-259, 2000
- Ritsema, J., H. J. van Heijst, & J. Woodhouse, Complex shear wave velocity structure related to mantle upwellings beneath Africa and Iceland, *Science*, 286, 1925-1928, 1999
- Robertson, G. S., & J. H. Woodhouse, Ratio of relative S to P velocity heterogeneity in the lower mantle, *J. Geophys. Res.*, 101(B9), 20041-20052, 1996
- Romanowicz, B., 3D structure of the Earth's lower mantle, *C. R. Geoscience*, 335, 141-156, 2003
- Rossby, H. T., On thermal convection driven by non-uniform heating from below: an experimental study, *Deep-Sea Res.*, 12, 9-16, 1965
- Samuel, H., & C. G. Farnetani, A denser and relatively undegassed lower mantle reservoir: geochemical and seismological model predictions, *Eos Trans. AGU (Fall meeting suppl.)*, 82, abstract T21A-0874, 2001
- Schmalzl, J., G. A. Houseman, U. Hansen, Mixing in vigorous time-dependent three-dimensional convection and application to Earth's mantle, *J. Geophys. Res.*, 101 (B10), 21847-21858, 1996
- Schmeling, H., G. Marquart, & T. Ruedas, Pressure and temperature-dependent thermal expansivity and the effect on mantle convection and surface observables, *Geophys. J. Int.*, 154, 224-229, 2003

- Schmeling, H., Numerical models of Rayleigh-Taylor instabilities superimposed upon convection, *Bull. Geol. Inst. Univ. Uppsala*, 14, 95-109, 1988
- Schott, B., D. A. Yuen, & A. Braun, The influences of composition and temperature-dependent rheology in thermal-chemical convection on entrainment of the D''-layer, *Phys. Earth Planet Inter.*, 129, 43-65, 2002
- Schubert, G., P. Cassen, & R. E. Young, Sudsolidus convective cooling histories of terrestrial planets, *Icarus*, 38, 192-211, 1979
- Sharma, M. N., & S. Gupta, Temperature and pressure dependence of the Anderson-Grüneisen parameter δ for NaCl crystal, *Phys. Rev. B*, 12(8), 3458-3463, 1975
- Shen, Y., S. C. Solomon, I. T. Bjarnason, & C. J. Wolf, Seismic evidence for a lower-mantle origin of the Iceland plume, *Nature*, 395, 62-65, 1998
- Singer, H. A., Heat transport by steady state plumes with strongly temperature-dependent viscosity, *PhD Thesis*, The John Hopkins University, Baltimore, MD, 196pp, 1986
- Sleep, N. H., Simple features of mantle-wide convection and the interpretation of lower-mantle tomograms, *C. R. Geoscience*, 335, 9-22, 2003
- Sleep, N. H., Gradual entrainment of a chemical layer at the base of the mantle by overlying convection, *Geophysics J.*, 95, 2345-2348, 1998
- Spohn, T., and G. Schubert, Modes of mantle convection and the removal of heat from the earth's interior, *J. Geophys. Res.*, 87, 4682-4696, 1982
- Stacey, F. D., Physics of the earth (3rd), *Brookfield Press*, Kenmore, Australia, ASIN: 0471819565, 1992
- Stegman, D. R., A. M. Jellinek, S. A. Zatman, J. R. Baumgardner, and M. A. Richards, An early lunar core dynamo driven by thermochemical mantle convection, *Nature*, 421, 143-146, 2002a
- Stegman, D. R., M. A. Richards, & J. R. Baumgardner, Effects of a depth-dependent viscosity and plate motions on maintaining a relatively uniform mid-ocean ridge basalt reservoir in whole mantle flow, *J. Geophys. Res.*, 107 (B2), 10.1029/2001JB000192, 2002b
- Steinberger, B., & R. J. O'Connell, Advection of plumes in mantle flow: implications for hotspot motion, mantle viscosity and plume distribution, *Geophys. J. Int.* 132, 412-434, 1998

- Su, W. J. & A. M. Dziewonski, Simultaneous inversion for 3-D variations in shear and bulk velocity in the mantle, *Phys. Earth Planet. Inter.*, 100, 135-156, 1997
- Su, W. J., & A. M. Dziewonski, Predominance of long-wavelength heterogeneity in the mantle, *Nature*, 352, 121-126, 1991
- Tackley. P. J., Strong heterogeneity caused by deep mantle layering, *Geochem. Geophys. Geosyst.*, 4(Article), 2001GC000167, 2002a
- Tackley. P. J., and S. Xie, The thermo-chemical structure and evolution of earth's mantle: constraints and numerical models, *Phil. Trans. R. Soc London A.*, 2002b
- Tackley, P. J., Mantle convection and plate tectonics: toward an integrated plate model, *Science*, 288, 2002-2006, 2000
- Tackley. P. J., Three-dimensional simulations of mantle convection with a thermo-chemical basal boundary layer: D"?, in *The Core-Mantle Boundary Region*, vol. 28, *Geodyn. Ser.*, edited by M. Gurnis et al. pp. 231-254, AGU, Washington D. C., 1998
- van der Hilst, R. D., & H. Kárason, Compositional Heterogeneity in the Bottom 1000 Kilometers of Earth's Mantle: Toward a Hybrid Convection Model, *Science*, 283, 1885-1888, 1999
- van der Hilst, R. D., & S. Widiyantoro, and E. R. Engdahl, Evidence for deep mantle circulation from global tomography, *Nature*, 386, 578-584, 1997
- van Keken, P. E., C. J. Ballentine, & E. Hauri, Geochemistry of the mantle and core, Chapter contributed to Volume 2 of the Treatise of Geochemistry (Turekian and Holland, editors), *Elsevier*, 2003
- van Keken, P. E., E. H. Hauri, & C. J. Ballentine, Mantle Mixing: the generation, preservation and destruction of chemical heterogeneity, *Ann. Rev. Earth. Planet. Sci.*, 30, 493-525, 2002
- van Keken, P. E., Cylindrical scaling for dynamic cooling models of the Earth, *Phys. Earth. Planet. Int.*, 124, 119-130, 2001
- van Keken, P. E., C. J. Ballentine, & D. Porcelli, A dynamical investigation of the heat and helium imbalance, *Earth Planet. Sci. Lett.*, 188, 421-434, 2001
- van Keken, P. E., & C. J. Ballentine, Dynamic models of mantle volatile evolution and the role of phase transitions and temperature-dependent rheology, *J. Geophys. Res.*, 104, 7137-7168, 1999
- van Keken, P. E., & S. Zhong, Mixing in a 3D spherical model of present-day mantle convection, *Earth Planet. Sci. Lett.*, 171, 533-547, 1999

- van Keken, P. E., & C. J. Ballentine, Whole-mantle versus layered mantle convection and the role of a high-viscosity lower mantle in terrestrial volatile evolution, *Earth Planet. Sci. Lett.*, 156, 19-32, 1998
- van Keken, P. E., H. Schmeling, U. R. Christensen, D. Neumeister, & M. Doin, A comparison of methods for the modelling of thermochemical convection, *J. Geophys. Res.*, 102, 22477-22496, 1997
- Vidale, J.E., G. Schubert, & P.S. Earle, Unsuccessful initial search for a midmantle chemical boundary with seismic arrays, *Geophys. Res. Lett.*, 28, 859-862, 2001
- Vidale, J.E., & A. H. Hedlin, Evidence for partial melt at the core–mantle boundary north of Tonga from the strong scattering of seismic waves, *Nature*, 391, 682-685, 1998
- Wänke, H, Constitution of terrestrial planets, *Philos. Trans. R. Soc. London*, A303, 287-302, 1981
- Weinstein, Q., & P. Olson, The proximity of hotspots to convergent and divergent plate boundaries, *Geophys. Res. Lett.*, 16, 433-436, 1989
- Williams, Q., J. Revenaugh, E. Garnero, A correlation between ultra-low basal velocities in the mantle and hot spots, *Science*, 281, 546-549, 1998
- Williamson, D. L., Integration of the barotropic vorticity equation on a spherical geodesic grid, *Tellus*, 20, 642-653, 1968
- Wolfe, C. J., I. T. Bjarnason, J. C. VanDecar, & S. C. Solomon, Seismic structure of the Iceland mantle plume, *Nature*, 385, 245-247, 1997
- Yang, W. S., & Baumgardner, J. R. A matrix-dependent transfer multigrid method for strongly variable viscosity infinite Prandtl number thermal convection. *Geophys. Astrophys. Fluid* 92, 151-195, 2000
- Yang, W. S., Variable viscosity thermal convection at infinite Prandtl number in a thick spherical shell, *P.h.D. Thesis*, Uni. Of Illinois at Urbana-Champaign, 1997
- Zerra, A. Boehler, R., Melting of (mg,fe)sio₃-perovskite to 625 kilobars - indication of a high-melting temperature in the lower mantle, *Science*, 262, 553-555, 1993
- Zhao, D., Seismic structure and origin of hotspots and mantle plumes, *Earth Planet. Sci. Lett.*, 192, 251-265, 2001
- Zhao, W., & D. A. Yuen, The effects of abiabatic and viscous heating on plumes, *Geophys. Res. Lett.*, 14, 1223-1227, 1987
- Zhong, S., & B. H. Hager, Entrainment of a dense layer by thermal plumes, *Geophysics. J. Int.*, 154, 666-676, 2003

Zienkiewicz, O.C., & R.L. Taylor, *The Finite Element Method* (fifth edition),
Butterworth-Heinemann, ISBN: 0750650494, 2000

Appendix A - Glossary of terms and important equations

Symbol	Description	Units
a	The non-dimensional depth ratio ($a=h_0\div H$)	
A	Area	m^2
A_0	Area of a spherical shell $A_0 = 4\pi R^2 \div 3$	m^2
B	The Buoyancy ratio. The ratio of the chemical buoyancy to thermal buoyancy. Defined by Davaille [1999a] using the temperature contrast over the whole system. When we calculate this value of our layered convection cases we use the difference between the average temperature at the surface and the CMB. In cases where there is bottom heating both these values are fixed and so we can consider B as an input parameter. However in cases where only internal heating is present the average temperature of the CMB can vary. So for internally heated cases B must be considered as a variable that can change during the simulation.	
B_l	The local Buoyancy ratio; defined by Gonnerman et al. [2002]. They define the temperature contrast as the difference between the temperature in the lower layer and at the Core Mantle Boundary	
B_r	The regional Buoyancy ratio. The temperature contrast is defined as the difference between the temperatures in the two layers.	
B_b	The boundary Buoyancy ratio. This can be used when the bottom shell is insulating. It uses the heat energy entering the system. See section 7.4.	
B_c	The critical buoyancy ratio. The value of B at which a layered system moves from stratified layered convection ($B>B_c$) to convecting as a whole layer ($B<B_c$). Davaille [1999b] finds $B_c=0.4$, we find $B=0.4-0.5$. However B_c is a (weak) function of the Rayleigh number, and the non-dimensional depth of the interface.	
\bar{B}_c	The value of B_c at the critical Rayleigh number. Davaille [1999b] finds $\bar{B}_c = 0.3$	
C_v	Specific heat at constant volume	$J\ kg^{-1}\ K^{-1}$
C_p	Specific heat at constant pressure	$J\ kg^{-1}\ K^{-1}$
D	Depth	m
D_K	Depth of the Kellogg interface (R_S-R_K)	m
E	The entrainment rate (upward + downward volume flux)	m^3/m^2
Ek	The Ekman number. The ratio of viscous forces to the Coriolis force (the inertial force produced by the Earth's rotation). $Ek>10^7$ for Earth.	
g	Gravitational acceleration	
G	The gravitational constant, 6.672×10^{-11}	$N\ kg^{-1}$

h_0	Thickness of the lower layer ($R_K - R_{CMB}$)	m
H	Thickness of the mantle ($R_S - R_{CMB}$)	m
J	The rate of radioactive heating per unit volume	$W m^{-3}$
k	Thermal conductivity $k = \kappa \rho C_p$	$W m^{-1} K^{-1}$
L	The length scale of convection	m
M	Mass	kg
M_u	Mass of the upper layer in a layered system	kg
M_l	Mass of the lower layer in a layered system	kg
M_r	The mass below a radius r	kg
Nu	The Nusselt number A dimensionless number that can be thought of as the rate of heat transfer by convection to which would occur only via conduction	
Pr	The Prandtl number, $Pr = \nu \div \kappa$. The ratio of momentum diffusivity and thermal diffusivity. $Pr \approx 10^{24}$ for Earth.	
P	Pressure	$N m^{-2}$ or Pa
q_{rad}	The rate of radioactive heating per unit mass	$W kg^{-1}$
q_u	The rate of radioactive heating per unit mass in the upper layer	$W kg^{-1}$
q_l	The rate of radioactive heating per unit mass in the upper layer	$W kg^{-1}$
Q	The rate of heat energy	W
Q_S	The rate of heat energy following over Earth's surface	W
Q_K	The rate of heat energy following over the Kellogg layer	W
Q_{CMB}	The rate of heat energy following over the Core Mantle Boundary	W
Q_{rad}	The rate of heat energy being added to the mantle by radioactive decay/ internal heating	W
Q_u	The rate of heat energy being added to the upper layer by radioactive decay/ internal heating	W
Q_l	The rate of heat energy being added to the lower layer by radioactive decay/ internal heating	W
\hat{r}	The radial unit vector This is unit vector from the origin to a point p.	
R	Radius	m
R_S	Radius of the earth normally taken as 6,370,000m	m
R_K	Radius of the Kellogg layer	m
R_{CMB}	Radius of the Core Mantle Boundary usual taken as 3,500,000m	m
Ra	The Bénard Rayleigh number or the thermal Rayleigh number The ratio of buoyancy to viscous forces.	
Ra_c	The critical Rayleigh number. The Rayleigh number at which a system starts to convect. This is thought to have a value between 87 and 1100 in Earth's mantle [M ^c Namara et al. 2000].	
Ra_u	The Bénard Rayleigh number of the upper layer	
Ra_l	The Bénard Rayleigh number of the lower layer	

Ra_b	Boundary Rayleigh number. The Rayleigh number using the effective temperature contrast caused by internal heating.	
Ra_G	The Rayleigh number used by Gonnerman et al. [2002] to describe their layered system. It uses the thermal contrast between the lower layer and the CMB, the length scale of the whole system (both layers) and the viscosity of the upper layer.	
Ra_T	Rayleigh number calculated by TERRA that takes into accounts for the adiabatic gradient as well as radial viscosity. A full description of the formula can be seen in appendix F.	
$Ra_{\Delta\rho}$	Rayleigh number using the buoyancy forces	
$RMS v_s$	The Root Mean Squared surface velocity at the surface shell.	ms^{-1} or cm/year
t	Time	s
T	Temperature	K
T_s	Temperature at the upper surface of the mantle	K
T_k	Temperature at the interface between two layers in the mantle.	K
T_{CMB}	Temperature at the Core Mantle Boundary	K
\hat{T}	Average radial temperature Note the ^ notion is often added to the other temperature terms to note the average temperature. Most often the average of a value once the layered system has reached a quasi-steady state.	K
\hat{T}_K	Average temperature at the interface between two layers	K
T_{RMS}	The root mean squared temperature of a radial layer. This is a measure of the lateral variation in the temperature structure.	K
ΔT	A temperature contrast The normally refers to the temperature contrast across the whole mantle	K
ΔT_K	The temperature contrast across the deformable interface between the two convecting layers	K
\underline{v}	The velocity vector.	ms^{-1}
v_p	Velocity of P seismic waves	ms^{-1}
v_s	Velocity of S seismic waves	ms^{-1}
V	Volume.	m^3
v_{rad}	The radial velocity	ms^{-1}
$v_{rad}\%$	The percentage of the velocity at a given point that is in the radial direction. ie $v_{rad}\%=100\%$ in an up-welling, $v_{rad}\%=-100\%$ in an down-welling and $v_{rad}\%=0$ for tangential flow.	%
Z	Depth	m
ΔZ	A change in depth. This normally means the width of a thermal boundary	m
α	Volume coefficient of thermal expansion. The fractional increase in volume per unit temperature at constant pressure.	K^{-1}
α_l	Volume coefficient of thermal expansion in the lower layer.	K^{-1}
α_u	Volume coefficient of thermal expansion in the upper layer.	K^{-1}

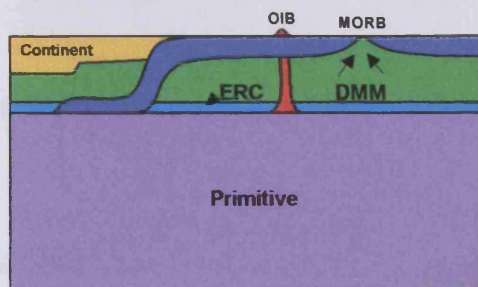
γ	The viscosity ratio: $\gamma = \nu_l \div \nu_u$ The ratio of the kinematic viscosities of the lower and upper layers.	
δ_T	Anderson-Grüneisen constant A parameter controlling the relationship between thermal expansivity and density in Earth's mantle, thought to have a value of 0.55 [Schmeling et al. 2003]	
η	Dynamic viscosity $\eta = \nu\rho$ Note: 1 Pa = 1 N m ⁻²	Pa s
κ	Thermal diffusivity $\kappa = k \div \rho C_p$	m ² s ⁻¹
κ_m	Bulk modulus A measure of a material's resistance to a change in volume.	N m ⁻² or Pa
μ_m	Rigidity modulus A measure of a material's resistance to a change in shape.	N m ⁻² or Pa
ν	Kinematic viscosity $\nu = \eta \div \rho$	m ² s ⁻¹
ν_u	Kinematic viscosity of the upper layer	m ² s ⁻¹
ν_l	Kinematic viscosity of the lower layer	m ² s ⁻¹
ρ	Density	kg m ⁻³
ρ_u	Chemical density of the upper layer	kg m ⁻³
ρ_l	Chemical density of the lower layer	kg m ⁻³
$\Delta\rho/\rho$	A fraction density increase. The normally refers to the chemical density increase from the upper to lower layer.	% or as a fraction
$\Delta\rho/\rho_{\text{eff}}$	The effective density increase/decrease from the upper to lower layer in a convecting system. This is the chemical density increase minus the effects of the thermal expansion of the lower layer. This is density increase that will be measured by seismic reflection and free oscillation	% or as a fraction
τ	Radial shear stress	Pa
φ	The non-dimensional area parameter. The ratio of the area increase from a spherical shell of the deformable interface to the area of the spherical shell.	
Φ	Heat flux. The rate of heat flow per unit time per unit area.	W m ⁻³
Φ_S	Heat flux across Earth's surface	W m ⁻³
Φ_{CMB}	Heat flux across the core-mantle boundary	W m ⁻³
Ω	Angular velocity.	rad s ⁻¹

TERRA	The parallel program written by J. R. Baumgardner [1983] and P. Bunge [1996] used in this thesis to simulate convection in Earth's mantle.
Initial case/field	The temperature field used at the beginning of a simulation. This is important in layered convection cases since the initial field must not have high amplitude thermal anomalies that tear the layer apart as soon as a simulation is started.
Multi-grid	The mathematical method used by TERRA to solve the velocity field. The calculation is performed in parallel.
Multi-grid problem	A problem within the TERRA code that stops a simulation from running and causes TERRA to crash. The multi-grid method has the problem that it is unable to solve some fields with discontinuities, such as those imposed by layering. When this happens the TERRA code stops running with what we refer to as a multi-grid problem.
Domain decomposition	The task of subdividing a finite element grid in a serial computer program so that the program can be run in parallel.
Marker surface	A surface within the TERRA code defined by an array of markers. The marker surface defines the deformable boundary between two layers within the mantle.
Marker	A point inside the TERRA code that defines a single point on the interface between two convecting layers. The markers position is stored in meters, in Cartesian co-ordinates.
Quasi-steady state	The final state of a layered system. The system never reaches a true steady state because of the dynamic nature of the boundary between the two layers. See section 5.4. The constantly changing surface area of the interface causes the heat flow to vary across the interface and so the thermal structure must change to accommodate for this. Consequently the thermal structure oscillates around mean structure but never reaches it. See section 5.2
Mantlevis	A parallel visualisation program written by Andy Heath specifically to be used with TERRA.
mt	The number of grid points along the edge of a primary triangle that make up the icosahedron grid. Its value must be a power of 2.
nt	The number of subdomains along the edge of a diamond in the icosahedron grid. Its value must be a power of 2.
nd	The number of diamonds mapped onto each processor. Must have a value of 5 or 10.
nr	The number of layers in the icosahedron grid.
i1, i2	Coordinates defining the position of a point in one of the diamond shaped subdomains on which the icosahedron grid employed by TERRA.
ir	The coordinate of the radial layer in the icosahedron grid. 1 is the surface nt+1 the bottom.
id	The coordinate of the subdomain in the icosahedron grid
nm	The number of markers per allan key
mv	Number of extra or missing marker per allan key
mp	The number of prisms along a spoke within an allan key. Must have a value such that $6mp^2 > nm-mv$
im	The coordinate marker number

Size.h	An input files used by TERRA to define the resolutions of the icosahedron grid and the domain decomposition.
Interra	An input files used by TERRA to define the parameters used in a simulation.
Mega plumes	Large hot upwelling regions in the mantle. There are thought to be two present in Earth's mantle below Tonga and Western Africa. They have a strong seismic signal that is probably produced by thermal and chemical sources.
Superswell	An anomalously hot and uplifted region of Earth's surface with a high concentration of hot spots. There are two superswells present on Earth today, one in western Africa and the other in the Southwest Pacific.
Hotspot	A region of volcanism that is not associated with a plate margin. A good example being Hawaii.
Craton	A region of the crust that is amorously cold.
Tectosphere	Regions of the mantle lying below cratons.
CMB	The Core Mantle Boundary
RMS	Root mean square
Internal heating	Heat generated by radioactive decay.
Bottom heating	Heat inputted in to a convecting system by conduction across a thermal boundary at the bottom of the layered system. In Earth's mantle this would take place at the CMB.
Thermal mode convection	Convection is driven by small-scale plumes that form at the thermal boundary at the bottom of the system
Thermo-chemical convection	Large scale convection and deformation of the interface between the two layers is driven by the interaction between the instable thermal gradient and the stable chemical density gradient
Trace element	An element found in less than ~1000 parts per billions in the Bulk Earth.
Incompatible element	Trace elements that prefer to be in the melt phase in upper mantle conditions.
Depleted	A region that has low abundances of incompatible elements.
Enriched	A region that has high abundances of incompatible elements.
MORB	Mid Ocean Ridge Basalts These are thought to represent the composition of the upper mantle and are depleted in trace elements
OIB	Ocean Island Basalts These are thought to originate deeper in the mantle than MORB and are either less depleted MORB or are enriched. This leads to the suggestion that they are sampling a deep reservoir.
ERC	Enriched Recycled Crust.
DMM	Depleted MORB Mantle

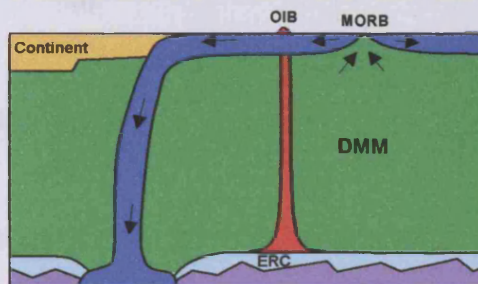
The Classic Geochemical Model

Two-layers with the boundary between the layers placed at a depth of 660km. The lower primitive layer is sampled by plumes and the source of OIB, the depleted upper layer is the source of MORB.



The Classic Geodynamical Model

A deep reservoir at the base of the mantle and single layer convection with the source of plumes at the Core Mantle Boundary (CMB).



Secular cooling

Cooling of the mantle (and the planet as a whole) from stored heat energy.

Viscous coupling

Viscous forces dominate at the boundary between convecting layers. As a results the thermal strucutres in the layers are anti-symmetric.

Thermal coupling

Thermal forces dominate at the boundary between convecting layers. As a results the thermal strucutres in the layers are symmetric.

Quasi-steady state

The final state of a stable layered system when the thermal profile of the system has reached reasonably stable values. Most properties of the system such as the interfacial surface area reach a constants value but oscillate around a central value with the amplitude of these oscillations varying from case to case [see section 5.2].

Seismic wave speeds

$$V_p = \sqrt{\frac{\kappa_m + \frac{4}{3}\mu_m}{\rho}} \quad V_s = \sqrt{\frac{\mu_m}{\rho}} \quad (2.2)$$

Rayleigh number Ra – general form

$$Ra = \frac{\text{buoyant forces}}{\text{viscous forces}} = \frac{\alpha g \rho \Delta T L^3}{\kappa \eta} \quad (2.3)$$

Boundary Rayleigh number

$$Ra_b = \frac{\alpha g \rho Q_{\text{rad}} L^4}{\kappa \kappa \eta} = \frac{\alpha g \rho^2 q_{\text{rad}} L^5}{\kappa \kappa \eta} \quad (A1)$$

Rayleigh number – used by Gonnerman et al. [2002]

$$Ra_G = \frac{\alpha g \rho (T_{\text{CMB}} - T_1) H^3}{\kappa \eta_u} \quad (A2)$$

Chemical buoyancy Rayleigh number

$$Ra_{\Delta\rho} = \frac{\Delta\rho g L^3}{\kappa \eta} \quad (A3)$$

Nusselt number Nu

$$Nu = \frac{\Phi L}{k \Delta T} = \left(\frac{Ra}{Ra_c} \right)^\beta \quad (2.4 \& 2.5)$$

Thermal boundary thickness

$$\Delta Z = L \left(\frac{Ra_c}{Ra} \right)^\beta \quad (2.8)$$

Where: $87 < Ra_c < 1100$; $0 < \beta < 0.3$ for Earth's mantle [M^cNamara & van Keken 2000]

Buoyancy ratio B – general form

$$\text{Buoyancy Ratio} = B = \frac{\text{Chemical Buoyancy}}{\text{Thermal Buoyancy}} = \frac{\Delta\rho/\rho_o}{\alpha\Delta T} \quad (2.10)$$

Viscosity ratio

$$\gamma = \frac{v_l}{v_u} \quad (2.12)$$

Entrainment rate [Gonnerman et al. 2002]

$$E = \frac{\rho C_p}{k} \frac{CH^{-1}B^{-2}Ra^{1/3}}{1 + \gamma B^{-1}} \quad (2.13)$$

Non-dimensional depth variable

$$a = \frac{h_0}{H} \quad (2.14)$$

The volume coefficient of thermal expansion (thermal expansivity)

$$\alpha = \frac{1}{V_0} \left(\frac{dV}{dT} \right)_p \quad (2.15)$$

Prandtl number Pr

$$\text{Pr} = \frac{\text{viscous forces}}{\text{inertial forces}} = \frac{\nu}{\kappa} = \frac{\eta C_p}{k} \quad (3.1)$$

Ekman number Ek

$$\text{Ek} = \frac{\text{viscous forces}}{\text{coriolis force}} = \frac{\nu}{2\Omega L^2 \sin\theta} \quad (3.2)$$

The governing equations

$$\text{Mass} \quad \nabla \cdot \underline{v} = 0 \quad (3.3)$$

$$\text{Momentum} \quad \frac{1}{\rho} \nabla P = \nu \nabla^2 \underline{v} - \alpha g \Delta T \quad (3.4)$$

$$\text{Energy} \quad \frac{\partial T}{\partial t} + \underline{v} \cdot \nabla T = \kappa \nabla^2 T + \frac{J}{\rho C_p} \quad (3.5)$$

$$\left\{ \begin{array}{l} \text{Total number} \\ \text{of data points} \end{array} \right\} = (10mt^2 + 2) \left(\frac{1}{2}mt + 1 \right) \quad (3.11)$$

$$\left\{ \begin{array}{l} \text{Number of} \\ \text{processors} \end{array} \right\} = \left(\frac{mt}{nt} \right)^2 \left(\frac{nd}{10} \right) \quad (3.12)$$

Entrainment – Davaille's equations

$$Q_{\uparrow} = C_1 \frac{\kappa h_0}{B^2} \text{Ra}_2^{3/5} \quad (4.14)$$

$$Q_{\downarrow} = C_2 \frac{\kappa h_0}{B} \text{Ra}_1^{3/5} \quad (4.15)$$

Entrainment – Davaille's equations with viscous forces

$$Q_{\uparrow} = C_1 \frac{\kappa}{h_0} \left\{ \frac{h_0}{B} \text{Ra}_2^{3/5} - \frac{\eta_2 \kappa}{\Delta \rho g h_0^2} \text{Ra}_2^{3/5} \right\}^2 - \text{Plumes} \quad (4.44)$$

$$Q_{\downarrow} = C_2 \left\{ \frac{\kappa h_0}{B} \text{Ra}_1^{3/5} - \frac{\eta_1 \kappa^2}{\Delta \rho g h_0^2} \text{Ra}_1^{3/5} \right\} - \text{Sheets} \quad (4.38)$$

Where...

$$Ra_1 = \frac{\alpha_1 \rho g \Delta T h_0^3}{\kappa \eta_1} \quad (4.45)$$

$$Ra_2 = \frac{\alpha_2 \rho g \Delta T (H - h_0)^3}{\kappa \eta_2} \quad (4.46)$$

Non-dimensional surface area variable

$$\phi = \frac{\text{Increase in area from a flat shell}}{\text{area of a flat shell}} = \frac{A - A_0}{A_0} \quad (5.5)$$

The global buoyancy ratio (normally referred to as just the buoyancy ratio B)

$$B = \frac{(\rho_1 - \rho_u) / \rho_u}{\alpha (T_{CMB} - T_s)} \quad (7.20)$$

The local buoyancy ratio B_l

$$B_l = \frac{(\rho_1 - \rho_u) / \rho_u}{\alpha (T_{CMB} - T_l)} \quad (7.21)$$

The regional buoyancy ratio B_r

$$B_r = \frac{(\rho_1 - \rho_u) / \rho_u}{\alpha (T_1 - T_u)} \quad (7.23)$$

The boundary buoyancy ratio B_b

$$B_b = \frac{(\rho_1 - \rho_u) / \rho_u}{\rho_u \alpha q_{rad} L^2 / k} \quad (7.29)$$

N ^o of Processors	mt				
	16	32	64	128	256
1	nt=16 nd=10	nt=32 nd=10	nt=64 nd=10	nt=128 nd=10	nt=256 nd=10
4	nt=8 nd=10	nt=16 nd=10	nt=32 nd=10	nt=64 nd=10	nt=128 nd=10
8	nt=8 nd=5	nt=16 nd=5	nt=32 nd=5	nt=64 nd=5	nt=128 nd=5
16	nt=4 nd=10	nt=8 nd=10	nt=16 nd=10	nt=32 nd=10	nt=64 nd=10
32	nt=4 nd=5	nt=8 nd=5	nt=16 nd=5	nt=32 nd=5	nt=64 nd=5
64	nt=2 nd=10	nt=4 nd=10	nt=8 nd=10	nt=16 nd=10	nt=32 nd=10
128	nt=2 nd=5	nt=4 nd=5	nt=8 nd=5	nt=16 nd=5	nt=32 nd=5
256	nt=1 nd=10	nt=2 nd=10	nt=4 nd=10	nt=8 nd=10	nt=16 nd=10

Appendix B - The halo swap process

As discussed in section 3.3.4 the procedure of a halo swap in an icosahedron grid is complex and will not be of interest to everyone reading this thesis. However it is a critical part of the alterations made to the TERRA code and so a discussion is necessary for the benefit of anyone who is unlucky enough to have to edit my code. It is strongly recommended that section 3.3.4 should be read as a preliminary to this appendix. Throughout this section we shall use the example of an $nt=16$, $mt=4$, $nd=5$ case as an example. This is chosen because it is the smallest possible grid size and parallel size that can be used to explain all the features of the parallel communication.

Halo region swaps are performed by first swapping data on the right side of the halo region and then from the left side. This is to keep the size of the buffers used to a minimum. Each of these can be broken down into three smaller tasks. Firstly, storing the correct data in the buffer; secondly, communicating this data with the correct processors; and thirdly, storing the received data in the correct location of the halo region in the relevant arrays. Each of these tasks must be performed twice once when passing data to the left and again when it is sent to the right. These six tasks are performed in separate subroutines, see the boxed section of code below for the details.

```

subroutine mrkcom (irkstep)
c   Copy mrks left boundaries into the arrays edgl and crnr.
    call edgl_fill(mrk,edgl,crnr,0,nt,(nm+mv)*3)

c   Send edgl to the relevant nodes and receive edgr
c   Warning we are entering MPI country
    call pcom1 (edgl,edgr,crnr,buff,(nm+mv)*3,0,nt-1,1)

c   Fix edgr into the correct position in mrk
    call edgr_empty(mrk,edgr,crnr,0,nt,(nm+mv)*3)

c   Copy mrks right boundary into the arrays edgr and crnr.
    call edgr_fill(mrk,edgr,crnr,0,nt,(nm+mv)*3)

c   Send edgr to the relevant nodes and receive edgl
    call pcom2 (edgl,edgr,crnr,buff,(nm+mv)*3,0,nt-1,1)

c   Fix edgl into the correct position in mrk
    call edgl_empty(mrk,edgl,crnr,0,nt,(nm+mv)*3)

```

There are five buffers used in the parallel communication: $edgl(ii, id, kk, 1)$,
 $edgl(ii, id, kk, 2)$, $crnr(ii, id)$, $edgr(ii, id, kk, 1)$,

$\text{edgr}(ii, id, kk, 2)$. In the case of a left to right swap the $\text{edgr}(ii, id, kk, 1)$ stores the data in the top right edge of the subdomain, $\text{edgr}(ii, id, kk, 2)$ stores data in the bottom right edge of the subdomain, and crnr stores the data in the node at the right corner of the subdomain[†]. Parallel communication is then used to send this data to the processors that own the relevant neighbouring subdomains. The data being received by the processors is then stored in the $\text{edgl}(ii, id, kk, 1)$ (top left edge of the halo region), $\text{edgl}(ii, id, kk, 2)$ (bottom left edge of the halo region), and crnr arrays (the left corner of the halo region). These buffers are then copied back into the halo region. This process is illustrated in figure B.1.

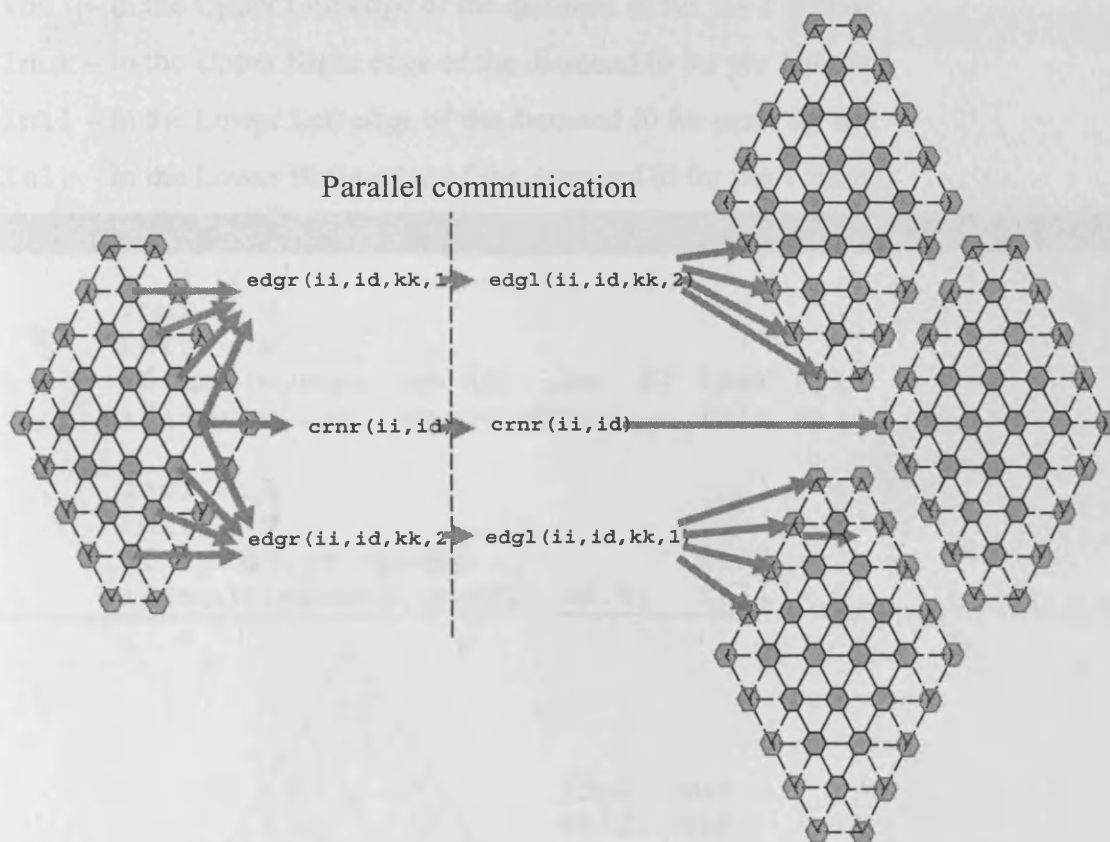


Figure B.1

A schematic of the three stages of left to right boundary communication (half a boundary swap). Nodes owned by the subdomain are stored in three buffers. These are then transmitted to the processors that own the relevant neighbouring subdomains. They are then stored in other buffers before being copied into the halo region of the subdomains.

[†] This is an example of the simplest case of subdomains that communicate only with subdomains in the same diamond. When information is required to cross into different diamonds the nodes copied into the buffers may be different, as will the nodes into which the data is copied at the subdomain receiving the data.

B.1 Position of a subdomain within a diamond

Being able to determine the position of a subdomain in a diamond is critical when performing parallel sends and received. Data must be handled differently for subdomains on the edge of diamonds to those in the centre. For these reasons a series of integers `inul`, `inur`, `inll` & `inlr` are stored in the `/edge/` common block. The subroutine `edgegen` is used to set-up these values. Figure B.2 shows how the values of `inul`, `inur`, `inll` & `inlr` change depending on the position of the subdomain within the diamond.

`Inul` – In the Upper Left edge of the diamond (0 for yes 1 for no)

`Inur` – In the Upper Right edge of the diamond (0 for yes 1 for no)

`Inll` – In the Lower Left edge of the diamond (0 for yes 1 for no)

`Inlr` – In the Lower Right edge of the diamond (0 for yes 1 for no)

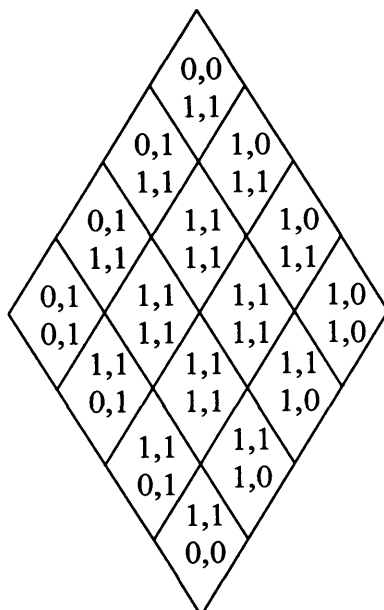
Setting up `inur`, `inur`, `inll`, `inlr`

```

inur = 0
inlr = 0
if(mod(mynum, npedg) .ne. 0) inur = 1
if(iproc .lt. mproc-npedg)   inlr = 1

inul = 0
inll = 0
if(iproc.ge.npedg)           inul = 1
if(mod(iproc+1,npedg).ne.0)  inll = 1

```



`inul, inur`
`inll, inlr`

Fig B.2
The values of `inul`, `inur`,
`inll` & `inlr` in a diamond

B.2 Knowing which diamond we are sending data to

During parallel communication, data is routinely passed between subdomains in different diamonds. This occurs when subdomains at the edge of diamonds exchange data. To account for the correction that must be made when pasting values back in to the correct arrays it is necessary to know the 'id' of the subdomain surrounding a node. These values are stored in `idul(nd)`, `idll(nd)`, `idur(nd)`, `idlr(nd)` in the `/edge/` common block. Their values are calculated during the initialisation of TERRA and are calculated in the `edgegen` subroutine. An example of the values of `idul(nd)`, `idll(nd)`, `idur(nd)`, `idlr(nd)` are shown in figure B.3.

```

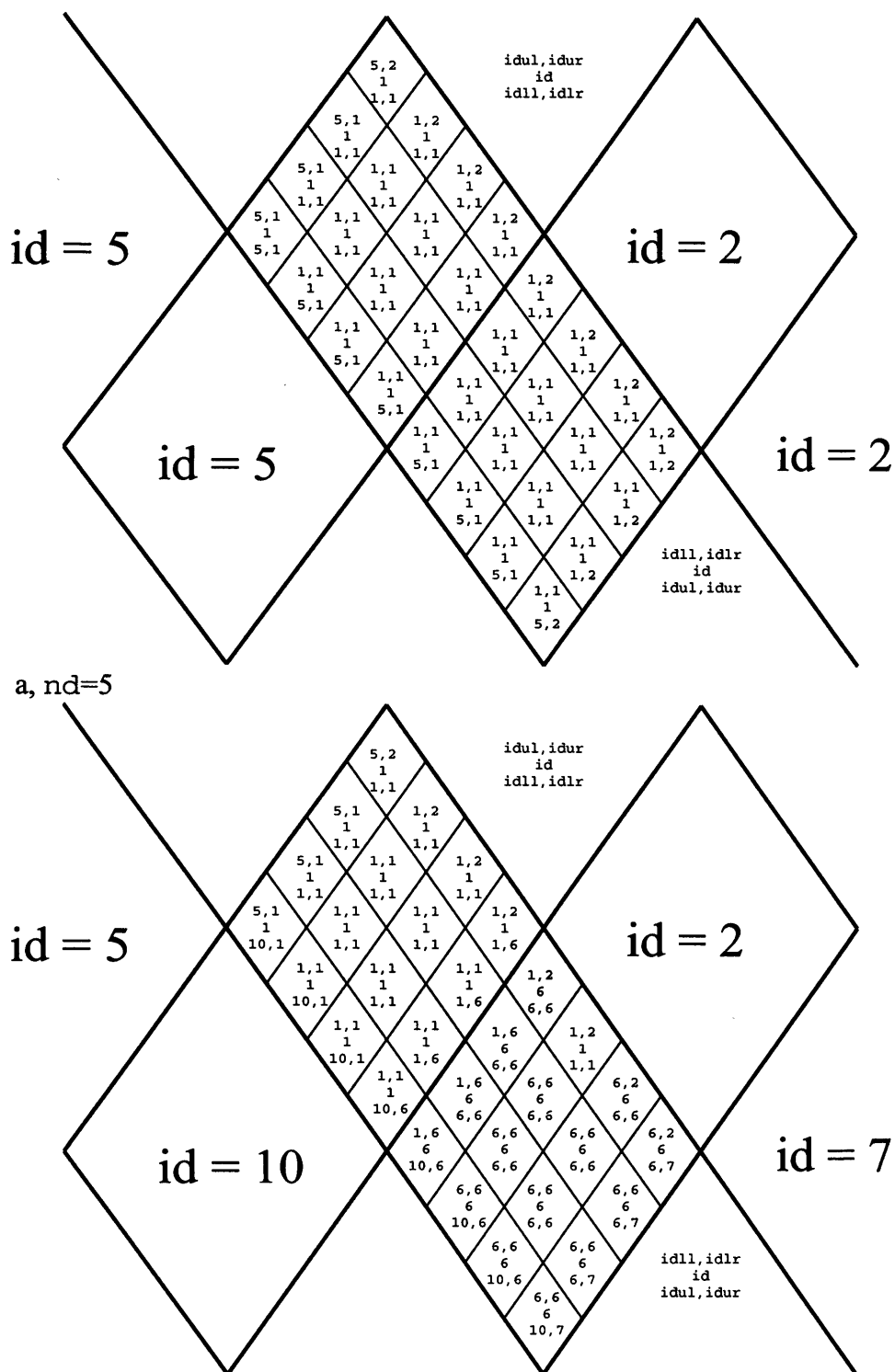
Setting up idul(nd), idll(nd), idur(nd), idlr(nd)
do id=1,nd ! Loop over diamonds

    idul(id) = mod(id+3,5) + 1
    idur(id) = mod(id ,5) + 1
    if (nd.eq.10) then
        idll(id) = idul(id) + 5
        idlr(id) = id + 5
        if (id.gt.5) then
            idll(id) = id - 5
            idul(id) = idul(id) + 5
            idlr(id) = idur(id)
            idur(id) = idur(id) + 5
        end if
    else if (nd.eq.5) then
        idll(id) = idul(id)
        idlr(id) = id
        if (mynum.ge.mproc) then
            idll(id) = id
            idlr(id) = idur(id)
        end if
    end if

    if (mod(mynum, npedg) .ne.0) idur(id) = id
    if (iprocc .lt. mproc-npedg ) idlr(id) = id
    if (iprocc.ge.npedg) idul(id) = id
    if (mod(iprocc+1,npedg).ne.0) idll(id) = id

end do !End loop over diamonds

```



b, $nd=10$

Fig B.3

An example of the values that $idul, idll, idur, idlr$ shall have for the subdomains in diamonds 1 & 6, for an $mt/nt = 4$ case. A, for the $nd=5$ case and b, for the $nd=10$ case. Thick black lines separate diamonds, while thinner lines separate the subdomains. Notice the values of the idu^* and idl^* are reversed in the southern hemisphere diamonds. This is consistent with the coordinate system used in TERRA.

B.3 Parallel communication – but where to?

Once halo data has been copied into buffers ready for a boundary swap we must know the MPI rank of the processor to which the data should be sent. These are saved in two arrays `iright()` which contains the rank of processors that own subdomains to the right of the processors on which data is being sent and `ileft()` which contains those to left. The values of `iright()` and `ileft()` are stored in the `/nbr1/` common block. The values of `iright`, and `ileft` are set-up during TERRA initialisation in the `neighborid` subroutine. The values of `iright` and `ileft` are set-up such that...

`iright(1)` – The rank of processor that owns the subdomain to the top right.
`iright(2)` – The rank of processor that owns the subdomain to the bottom right.
`iright(4)` – The rank of processor that owns the subdomain to the right.
`ileft(1)` – The rank of processor that owns the subdomain to the top left.
`ileft(2)` – The rank of processor that owns the subdomain to the bottom left.
`ileft(4)` – The rank of processor that owns the subdomain to the left.

Note: `iright(3)` & `ileft(3)` contain similar data to `iright(4)` & `ileft(4)` however this is used when a different type of boundary exchange is used and does not interest us.

```
Setting-up the values of iright() and ileft() in neighborid
c... npedg is the number of subdomains along a diamond edge.
c... kproc is the number of processors onto which each set of nd
c    diamonds is mapped.
c... iproc is the local process number relative to the set of kproc
c... processes.
c... kown is the increment in process number between mynum and iproc.
c... koth is the increment if process number for diamond located
c... in the other hemisphere.

kproc = npedg**2
iproc = mod(mynum, kproc)

if(nd .eq. 10) then
  kown = 0
  koth = 0
elseif(nd .eq. 5) then
  kown = mynum - iproc
  koth = kproc - kown
endif

c... Treat case of subdomain boundaries within the diamond interior.

iright(1) = mynum - 1
iright(2) = mynum + npedg
iright(3) = mynum + npedg - 1
iright(4) = iright(3)
ileft(1) = mynum - npedg
ileft(2) = mynum + 1
ileft(3) = mynum - npedg + 1
ileft(4) = ileft(3)
c... 1) Special case of upper right boundary of diamond:
```

```

if(mod(iproc,npedg) .eq. 0) then
  irect(1) = iproc/npedg + kown
  irect(2) = mynum      + npedg
  irect(3) = irect(1) + 1
  irect(4) = irect(1) - 1
endif

```

c... 2) Special case of lower right boundary of diamond:

```

if(iproc .gt. kproc-npedg-1) then
  irect(1) = mynum - 1
  irect(2) = (kproc - iproc)*npedg - 1 + koth
  irect(3) = irect(2) + npedg
  irect(4) = irect(3)
endif

```

c... 3) Special case of upper left boundary of diamond:

```

if(iproc .lt. npedg) then
  ileft(1) = iproc*npedg + kown
  ileft(2) = mynum + 1
  ileft(3) = ileft(1) - npedg
  ileft(4) = ileft(1) + npedg
endif

```

c... 4) Special case of lower left boundary of diamond:

```

if(mod(iproc+1,npedg) .eq. 0) then
  ileft(1) = mynum - npedg
  ileft(2) = kproc - (iproc + 1)/npedg + koth
  ileft(3) = ileft(2) + 1
  ileft(4) = ileft(3)
endif

```

c... 5) Special case of right corner node of diamond:

```

if(iproc .eq. kproc-npedg) then
  irect(1) = iproc/npedg + kown
  irect(2) = kproc - 1 + koth
  irect(3) = kown
  irect(4) = iproc/npedg - 1 + kown
endif

```

c... 6) Special case of pole:

```

if(iproc .eq. 0) then
  ileft(1) = kown
  ileft(2) = kown + 1
  ileft(3) = kown + (npedg - 1)*npedg
  irect(4) = npedg - 1 + kown
endif

```

c... 7) Special case of left corner node of diamond:

```

if(iproc .eq. npedg-1) then
  ileft(1) = iproc*npedg + kown
  ileft(2) = kproc - (iproc + 1)/npedg + koth
  ileft(3) = ileft(1) - npedg
  ileft(4) = kown
endif

```

B.4.1 Saving data in the left-hand side of the subdomains

Subdomain data is copied in to the `edgl` and `crnr` arrays prior to parallel communication by the `edgl_fill` subroutine. This is straightforward with no complications caused by the position of the subdomain within the diamond. This procedure is illustrated in figure B.4.

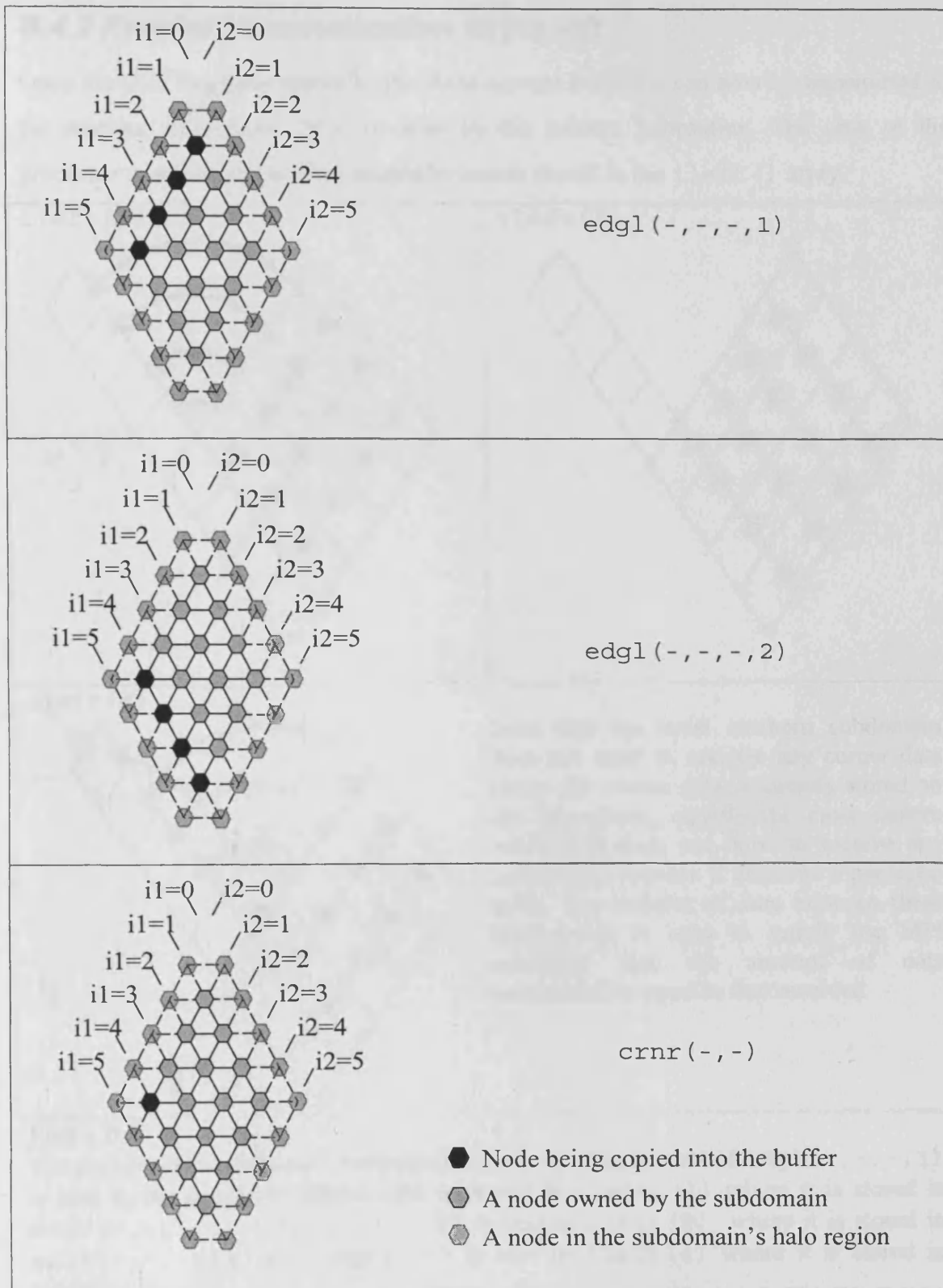


Figure B.4
 An illustration of the task performed by the `edg1_fill` subroutine. The diagrams on the left show the section of the grid that is copied into the buffer. The name of the buffer into which they are copied is displayed on the right.

B.4.2 Parallel communication to the left

Once the data has been stored in the three correct buffers it can now be transmitted to the relevant processors. This is done by the `pcom1` subroutine. The rank of the processor to which the buffers should be sent is stored in the `ileft()` array.

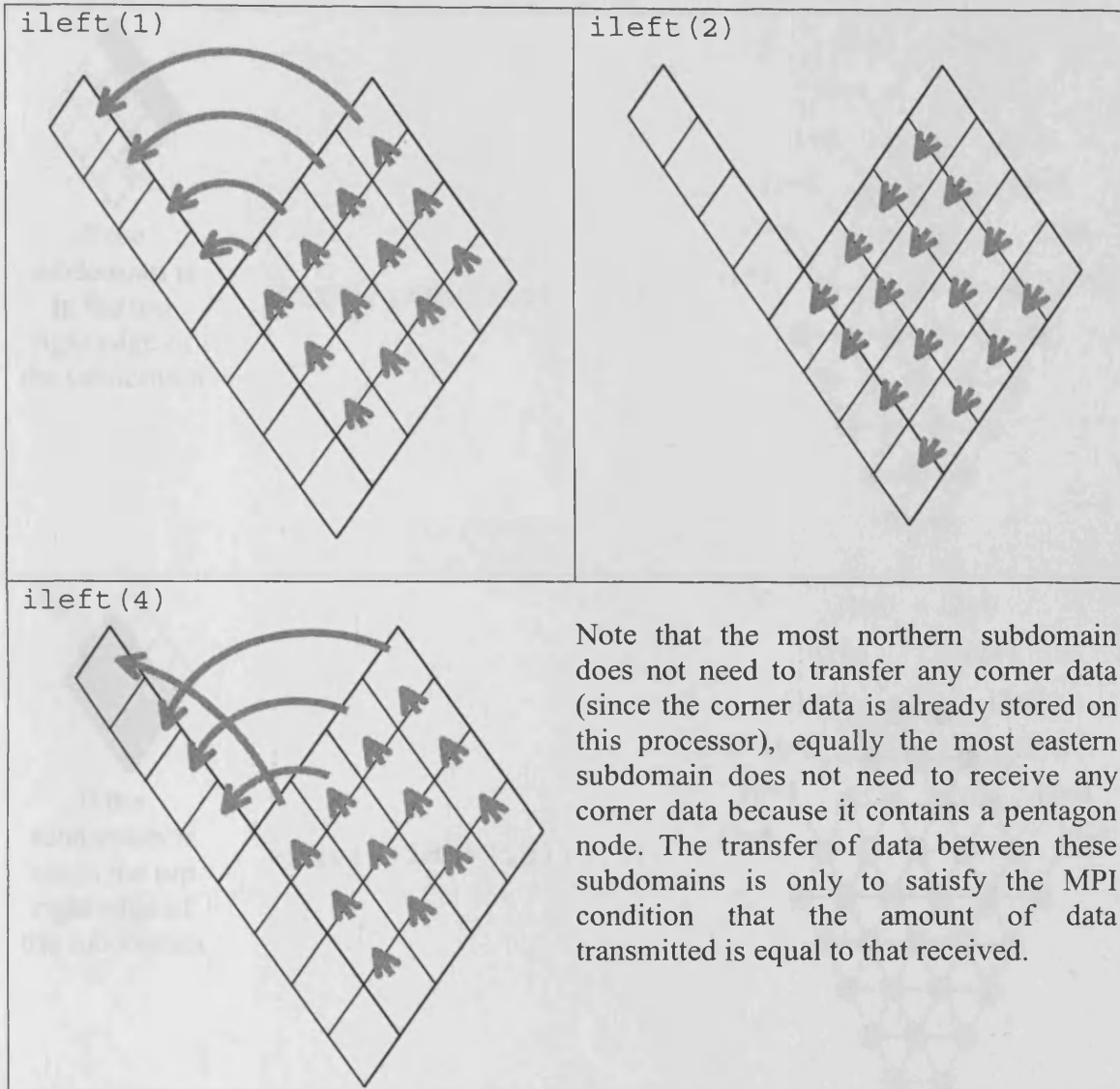


Figure B.5

The parallel communication performed by `pcom1`. The content of `edg1(-,-,-,1)` is sent to the processor whose rank is stored in `ileftt(1)` where it is stored in `edgr(-,-,-,2)`, `edg1(-,-,-,2)` is sent to `ileft(2)` where it is stored in `edgr(-,-,-,1)`, and `crnr(-,-)` is sent to `ileft(4)` where it is stored in `crnr(-,-)`.

Shown are subdomains in a $mt/nt = 4$ case. Thick black lines define the boundary between diamonds, thinner black lines are the boundary between subroutines. Grey arrows show the MPI communication of the buffer data.

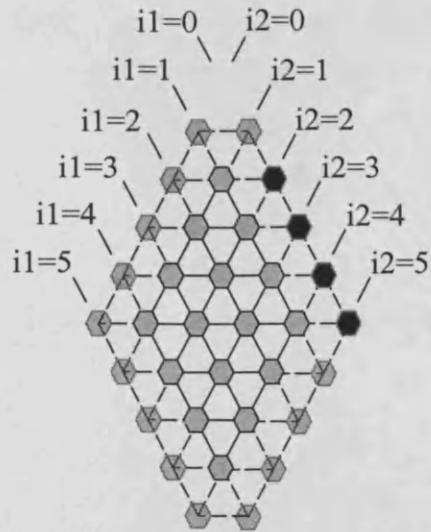
B.4.3 Saving the right edge data into the halo region

After parallel communication each processor has halo data stored in `edgr(-,-,-,1)`, `edgr(-,-,-,2)` and `crnr(-,-)`. These need to be copied into the halo region. This is done by the `edgr_empty` subroutine.



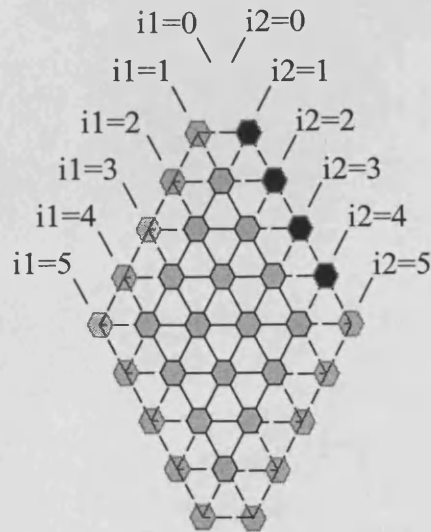
If the subdomain is in the top right edge of the subdomain

`edgr(-, idur(id), -, 1)`



If the subdomain is not in the top right edge of the subdomain

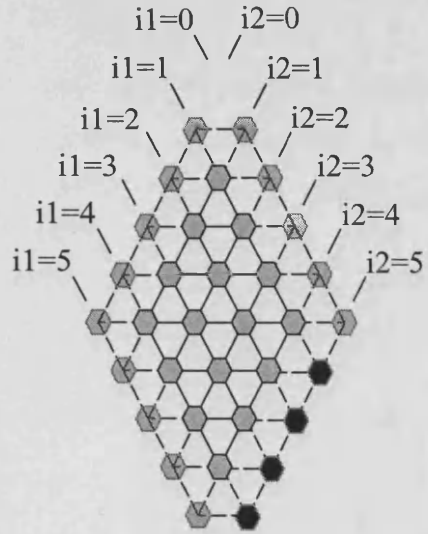
`edgr(-, idur(id), -, 1)`





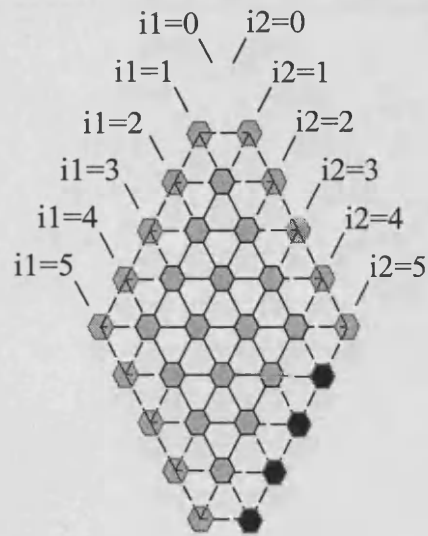
If the subdomain is not in the bottom right edge of the subdomain

`edgr(-, idlr(id), -, 2)`



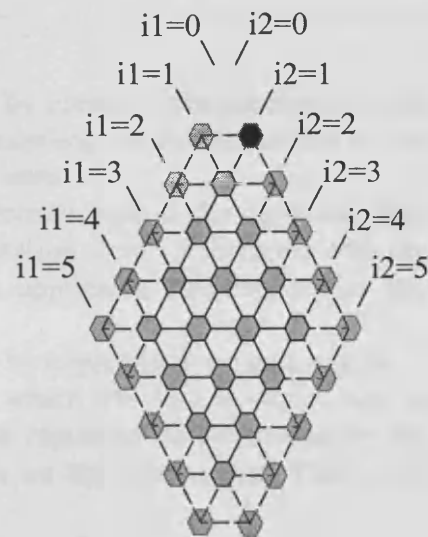
If the subdomain is in the bottom right edge of the subdomain

`edgr(-, idlr(id), -, 2)`
 This may seem identical to the above case; however we must account for the reversed coordinate system between the northern and southern diamonds.



If the subdomain is at the top of the diamond

`array(0, 1, 1, -, -)`
 This is the pole node case. We just copy from the $i1=0, i2=1, id=1$ element of the subdomain owned by the node.



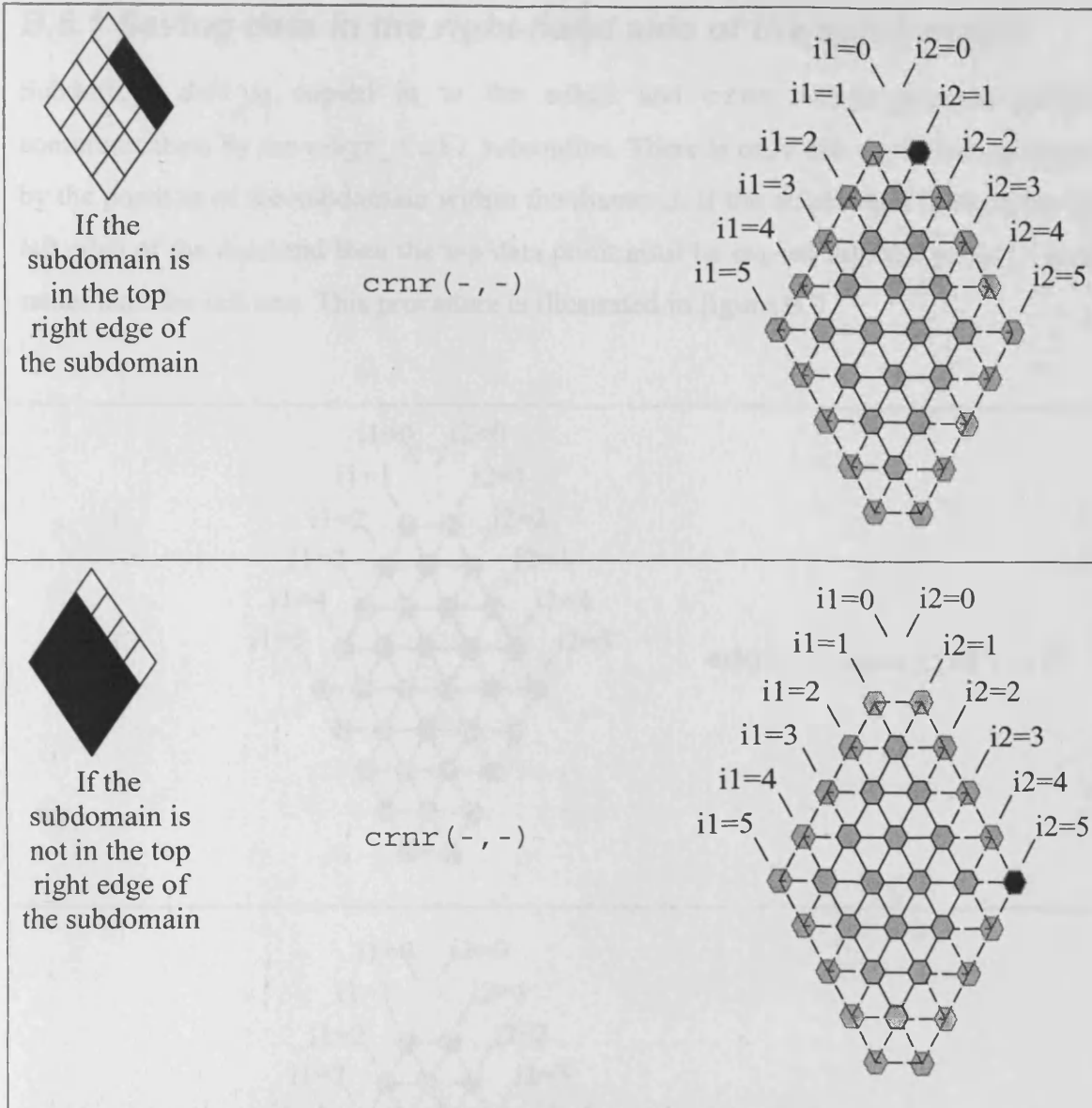


Figure B.6

The process of putting the halo region data received by parallel communication back into the array. There are a number of conditions depending on the placement of the subdomain with the diamond, all the cases are shown here.

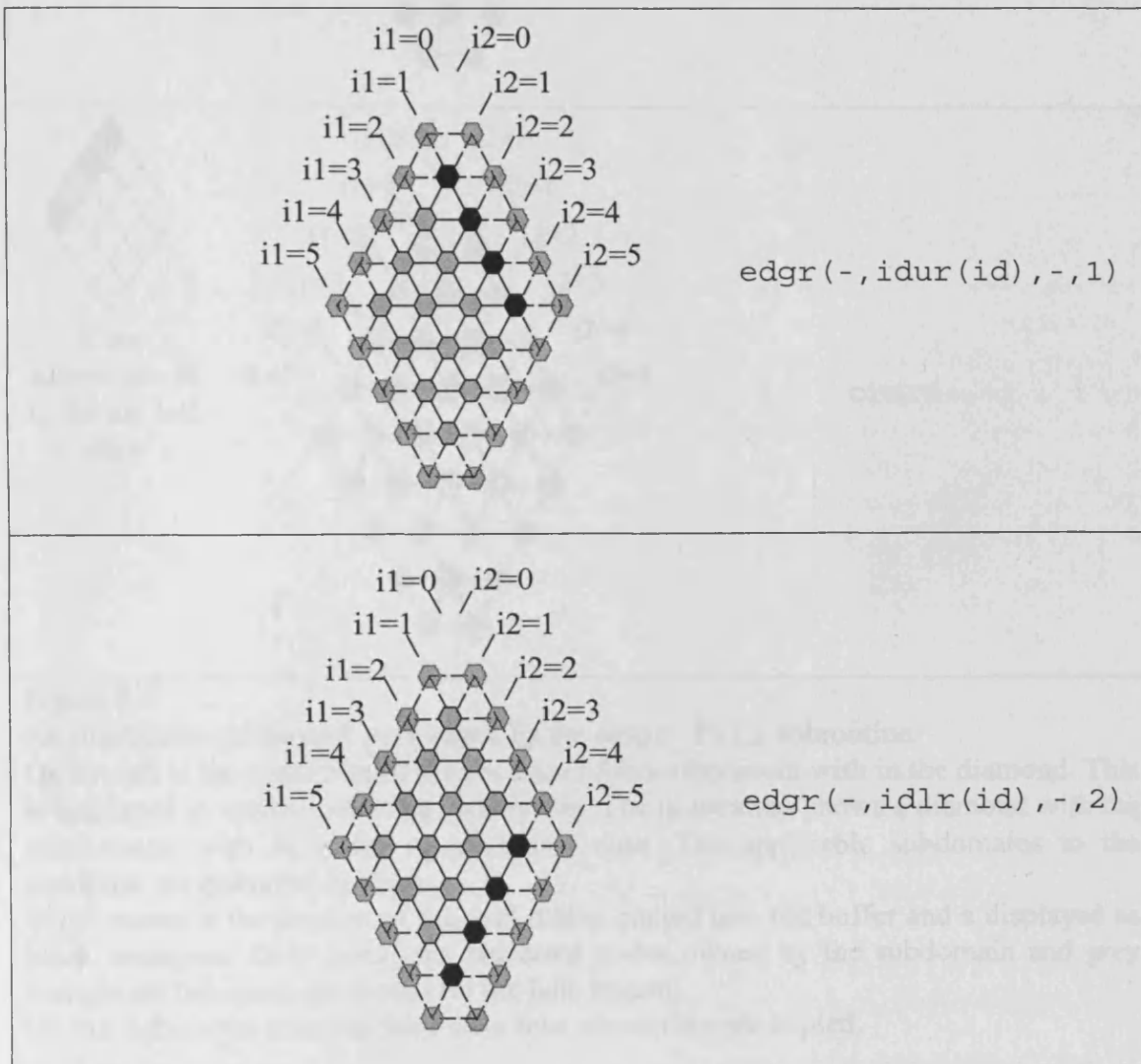
On the left is the condition of the location of the subdomain with in the diamond. This is displayed in words and in an illustration. The illustration shows a diamond with the subdomains within it for an $mt/nt=4$ case. The applicable subdomains to the condition are coloured in black.

In the centre of the figure is the buffer that is going to be copied into the halo region.

On the right is the location in the halo region into which the data is copied and is represented by black filled hexagons. Grey hexagons represent nodes owned by the subdomain and grey transparent hexagons are nodes on the halo region. The $mt=8$ case is shown as an example.

B.5.1 Saving data in the right-hand side of the subdomains

Subdomain data is copied in to the `edgr` and `crnr` arrays prior to parallel communication by the `edgr_fill` subroutine. There is only one complication caused by the position of the subdomain within the diamond. If the subdomain is along the top left edge of the diamond then the top data point must be copied into the `crnr()` array rather than the left one. This procedure is illustrated in figure B.7.



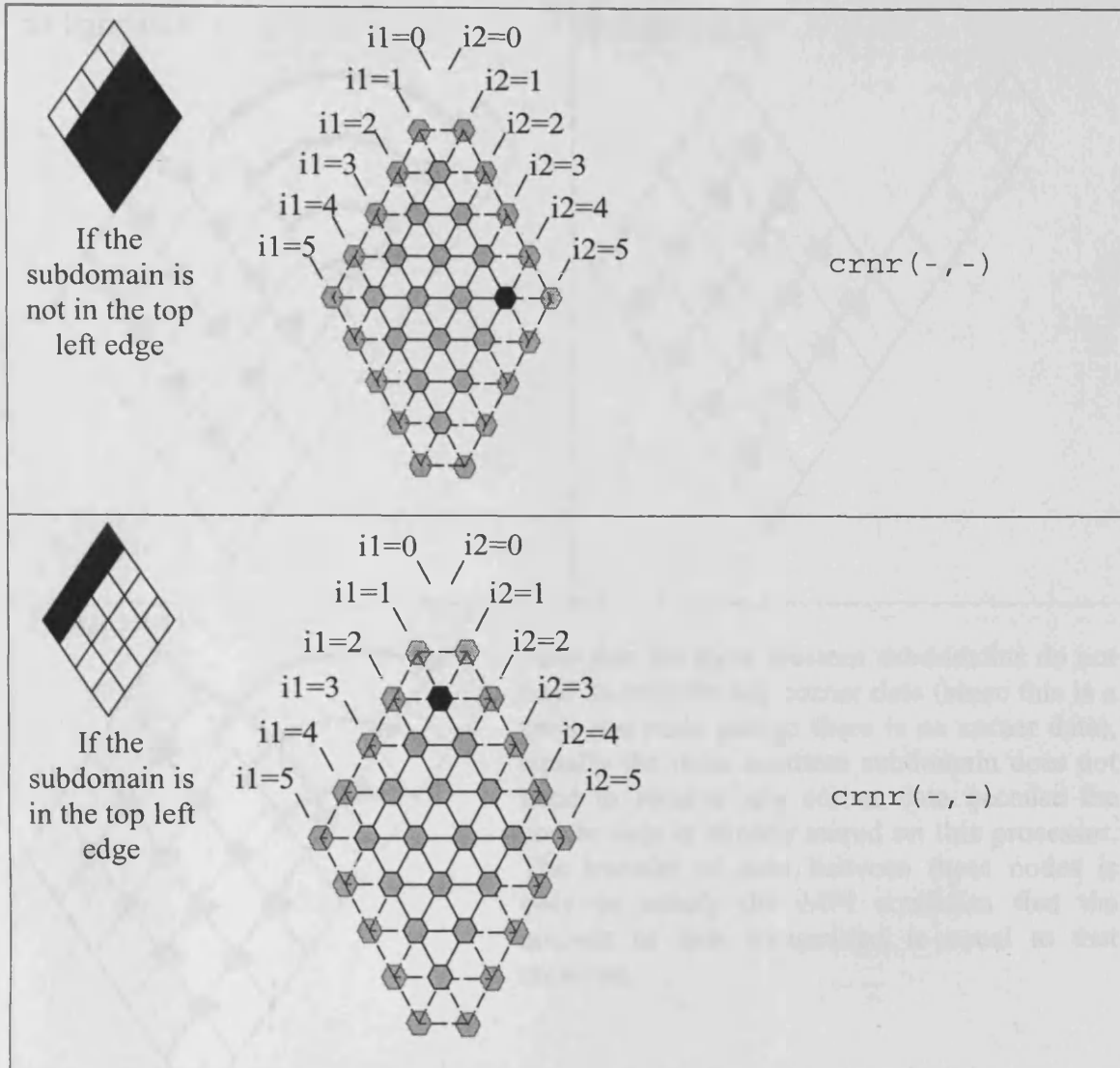


Figure B.7

An illustration of the task performed by the `edgr_fill` subroutine.

On the left is the condition of the location of the subdomain with in the diamond. This is displayed in words and in an illustration. The illustration shows a diamond with the subdomains with in it for an $mt/nt=4$ case. The applicable subdomains to the condition are coloured in black.

In the centre is the section of the grid that is copied into the buffer and a displayed as black hexagons. Grey hexagons represent nodes owned by the subdomain and grey transparent hexagons are nodes on the halo region.

On the right is the name of the buffer into which they are copied.

B.5.2 Parallel communication to the right

Once the data has been stored in the three correct buffers it can now be transmitted to the relevant processors. This is done by the `pcom2` subroutine. The rank of the processor to which the buffers should be sent is stored in the `iright()` array.

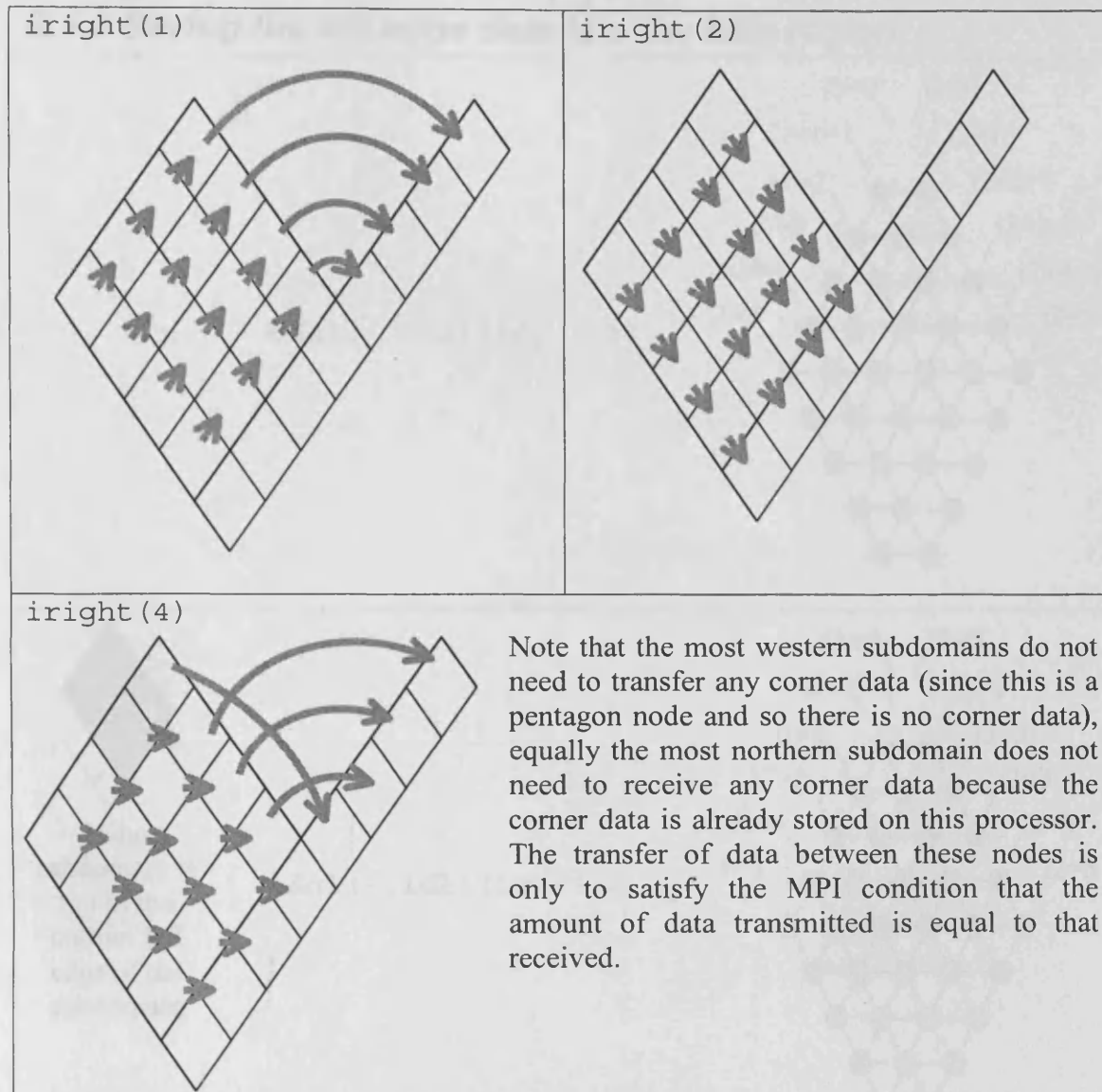

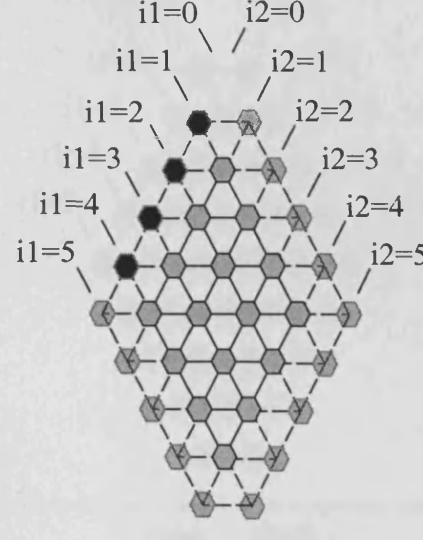

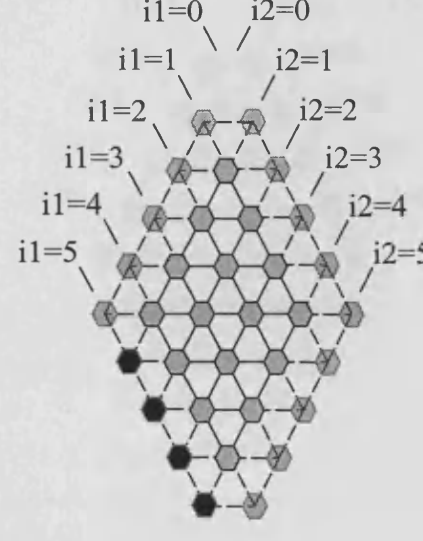
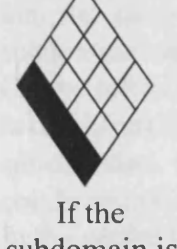
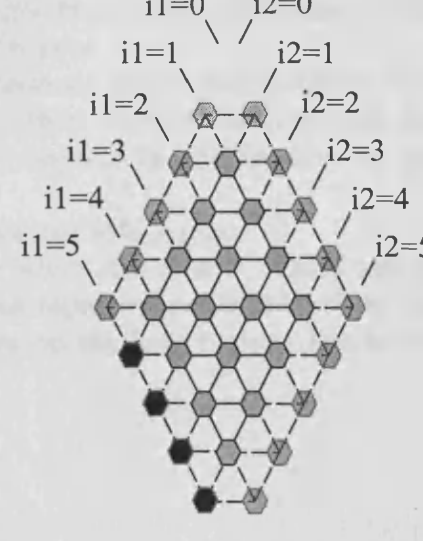


Figure B.8

The parallel communication performed by `pcom2`. The content of `edgr(-,-,-,1)` is sent to the processor whose rank is stored in `iright(1)` where it is stored in `edgl(-,-,-,2)`, `edgr(-,-,-,2)` is sent to `iright(2)` where it is stored in `edgl(-,-,-,1)`, and `crnr(-,-)` is sent to `iright(4)` where it is stored in `crnr(-,-)`.

Shown are subdomains in an $mt/nt = 4$ case. Thick black lines define the boundary between diamonds, thinner black lines are the boundary between subroutines. Grey arrows show the MPI communication of the buffer data.

B.5.3 Saving the left edge data into the halo region

	<p><code>edg1(-, idul(id), -, 1)</code></p>	
 <p>If the subdomain is not in the bottom left edge of the subdomain</p>	<p><code>edg1(-, idll(id), -, 2)</code></p>	
 <p>If the subdomain is in the bottom left edge of the subdomain</p>	<p><code>edg1(-, idll(id), -, 2)</code> This may seem identical to the above case; however we must account for the reversed coordinate system between the northern and southern diamonds.</p>	

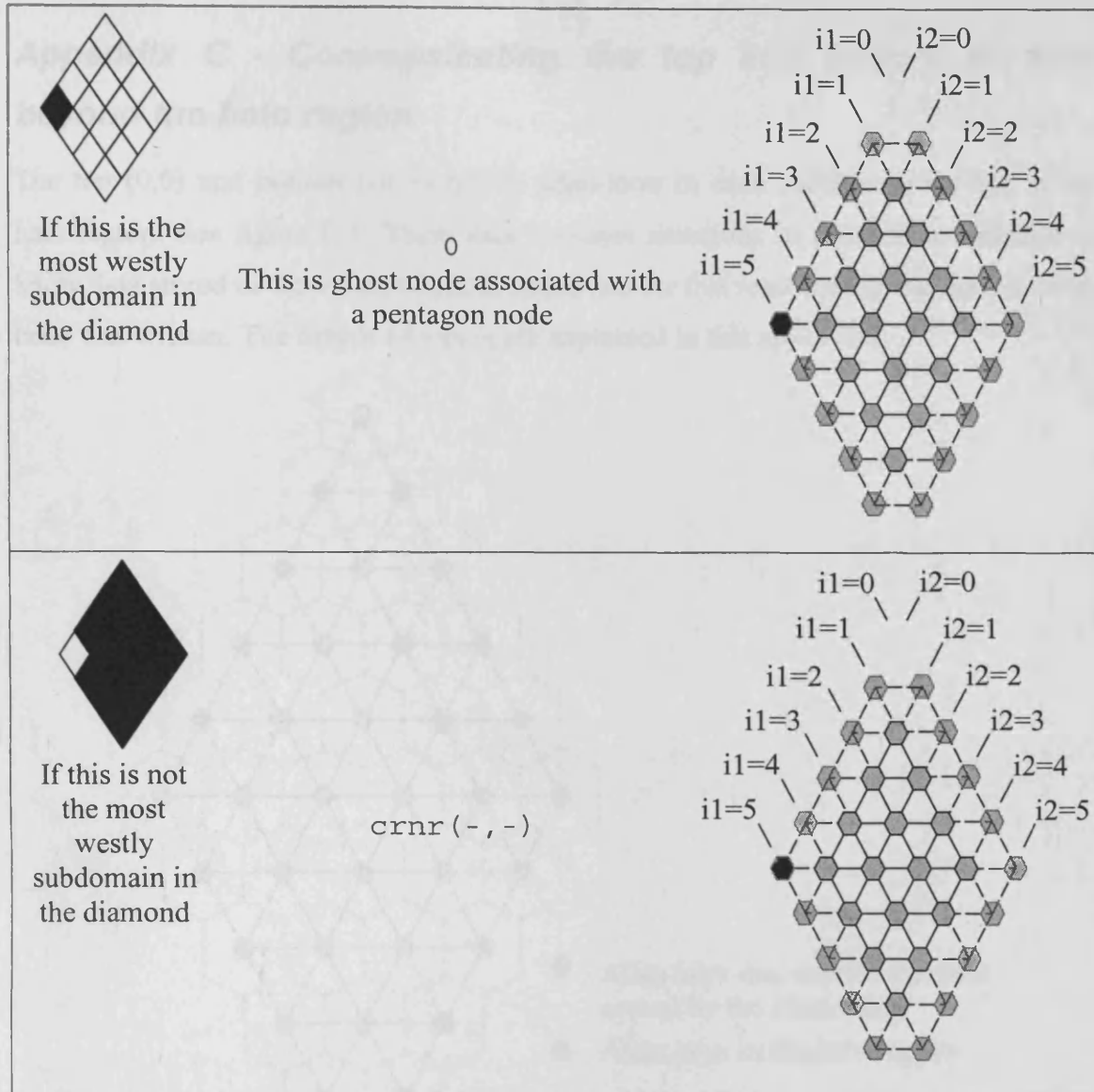


Figure B.9

The process of putting the halo region data received by parallel communication back into the array. There are a number of conditions depending on the placement of the subdomain within the diamond, all the cases are shown here.

On the left is the condition of the location of the subdomain within the diamond. This is displayed in words and in an illustration. The illustration shows a diamond with the subdomains within it for an $mt/nt=4$ case. The applicable subdomains to the condition are coloured in black.

In the centre is the buffer that is going to be copied into the halo region.

On the right is the location in the halo region into which the data is copied and is represented by black filled hexagons. Grey hexagons represent nodes owned by the subdomain and grey transparent hexagons are nodes on the halo region. The $mt=8$ case is shown as an example.

Appendix C - Communicating the top and bottom corners beyond the halo region

The top $(0,0)$ and bottom $(nt+1,nt+1)$ allan-keys in each subdomain are not in the halo region. See figure C.1. There may be some situations in which it is desirable to know data stored in the top and bottom nodes and for this reason a top and bottom swap code was written. The details of which are explained in this appendix.

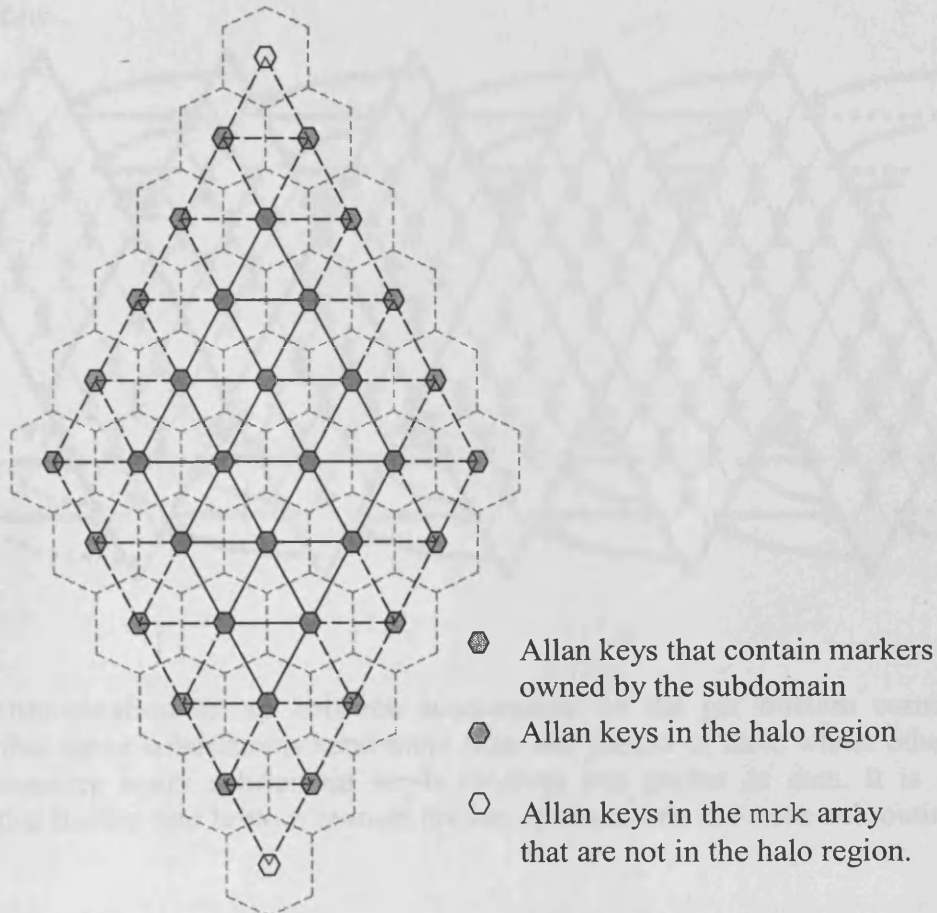


Figure C.1

The status of allan keys in the mrk array. The centre allan keys contain markers that are owned by the subdomain. The halo allan keys contain markers passed on from neighbouring subdomains and is used to see if markers have migrated to new owner allan key across a subdomain.

C.1 Configuring parallel communication

If it is only necessary to find the values of the bottom allan key, is there any need to communicate the top values as well? You would think not, however MPI is such that a parallel send must be accompanied with a parallel receive¹. If we consider the case of only sending data such that each subdomain only receives a bottom allan key, we find that although each subdomain receives one packet of data, some send two packets and others none.

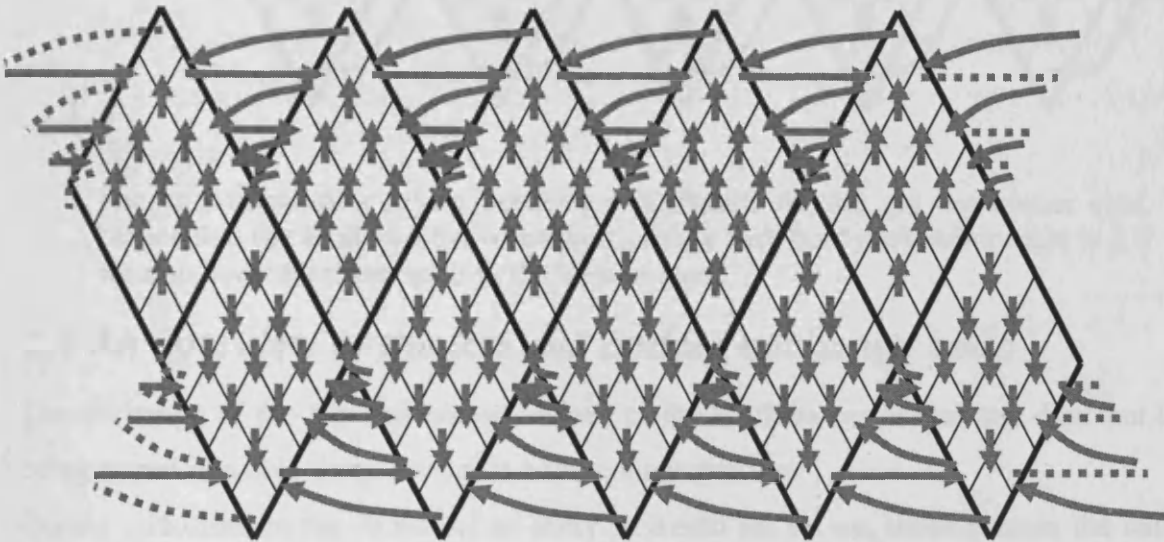


Fig C.2

The communication set-up between subdomains for the get **bottom** corner case. Notice that some subdomains send more than one packet of data, whilst others send none, however every subdomain sends receives one packet of data. It is for this reason that the top and bottom corners are incorporated into the same subroutine.

¹ This is strictly speaking not true. However parallel code with an uneven number of sends and receives at each processor is complex and is in general avoided when ever possible.

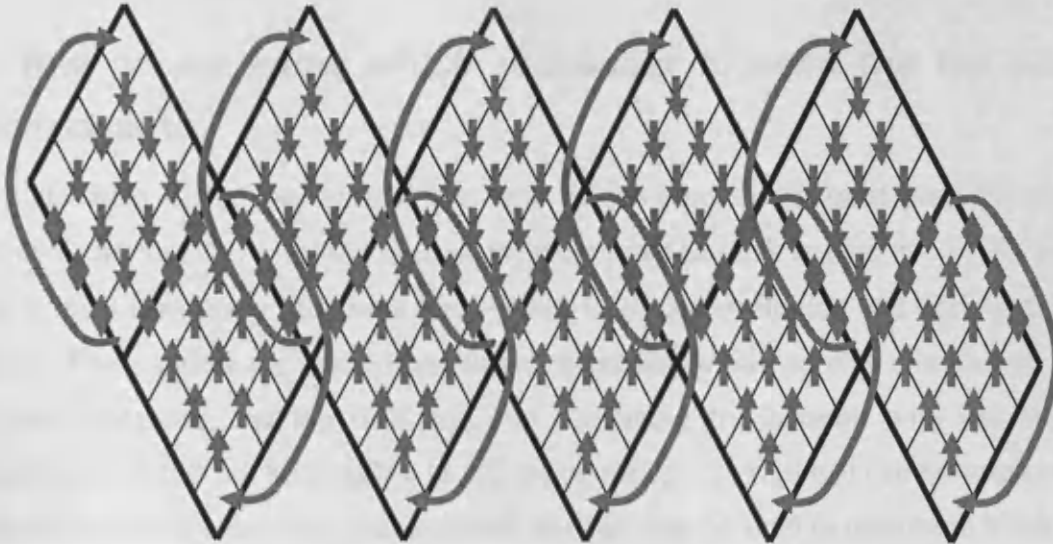


Fig C.3

The communication set-up between subdomains for the get **top** corner case. Notice that the total number of packets of data sent from each subdomain is 2 if we also consider those used in the bottom send.

C.2 An overview of the top and bottom exchange code

The exchange of the top and bottom values of the markers (or indeed any data that is being stored in a halo swap set-up) is a three-stage process.

During initialisation the values of an array `itandb` are set-up, these contain the rank of the processor that are used to either send data to or receive data from.

Firstly, the correct data is taken from the subdomain and stored in a buffer (`edgl`).

Secondly, the parallel communication is performed. Data stored in `edgl` is set to processor determined by `itandb`. The received data is stored in `edgr`.

Thirdly, the data store in `edgr` is copied into the correct array (in my case the `mrk` array). This is complicated by the fact that we must check to make sure that data has not been set from a different diamond and if so correct for it.

Below is section of the `mrktabcom` subroutine that performs the top and bottom swap.

Subroutine `mrktabcom`

```

c      Store the top and bottom markers in edgl
c      call tab_edgl_fill(mrk,edgl,0,nt,(nm+mv)*3)

c      Perform the parrallel communication
c      Send edgl to the relavent processors and recieve edgr
c      call pcom3(edgl,edgr,buff,(nm+mv)*3,0)

c      Store edgr into the relavent areas of the node
c      call tab_edgr_empty(mrk,edgr,0,nt,(nm+mv)*3)

```

C.3 How do we know which processor to send the top and bottom data to?

Each node must know four values. The rank of the processor it must send the data stored in `itandb(1, -)` to, the rank of the processors to send `itand(2, -)` to and finally it must also know the rank from which it is receive the top and bottom data. These final two values are needed because each processor will receive two packets of data, one containing the top data and one containing the bottom, with out more information it would not be possible to tell the two apart. An `mpi` call can be employed to find the rank of the sending processor and this can then be used to determine if this is top and bottom data.

These values are stored in `itandb(-, -)`.

`Itandb(1,-)` is an integer array that contains the ranks of processors that are used in the top and bottom corner communication.
`itandb(1,-)` – the rank of the processor to send `edgr(-,1)` to.
`itandb(2,-)` – the rank of the processor to send `edgr(-,2)` to.
`itandb(1,-)` – the rank of the processor to receive `edgl(-,1)` from: the top corner data
`itandb(2,-)` – the rank of the processor to receive `edgl(-,2)` from: the bottom corner data







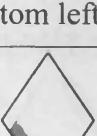
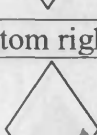
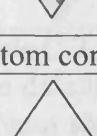
Middle subdomains	
	$\begin{aligned} \text{Itandb}(1,-) &= \text{Mynum} - \text{npedg} - 1 \\ \text{Itandb}(2,-) &= \text{Mynum} + \text{npedg} + 1 \\ \text{Itandb}(3,-) &= \text{Mynum} - \text{npedg} - 1 = \text{Itandb}(2,-) \\ \text{Itandb}(4,-) &= \text{Mynum} + \text{npedg} + 1 = \text{Itandb}(3,-) \end{aligned}$
Top corner subdomains	
	$\begin{aligned} \text{Itandb}(1,-) &= (\text{iprocc} + 1)\text{npedg} - \text{kown} \\ \text{Itandb}(2,-) &= \text{Mynum} + \text{npedg} + 1 \\ \text{Itandb}(3,-) &= \text{kown} - 1 \\ \text{Itandb}(4,-) &= \text{Mynum} + \text{npedg} + 1 = \text{Itandb}(2,-) \end{aligned}$
Top left subdomains	
	$\begin{aligned} \text{Itandb}(1,-) &= (\text{iprocc} + 1)\text{npedg} - \text{kown} \\ \text{Itandb}(2,-) &= \text{Mynum} + \text{npedg} + 1 \\ \text{Itandb}(3,-) &= \text{iprocc} * \text{npedg} + \text{kown} \\ \text{Itandb}(4,-) &= \text{Mynum} + \text{npedg} + 1 = \text{Itandb}(2,-) \end{aligned}$
Top right subdomains	
	$\begin{aligned} \text{Itandb}(1,-) &= (\text{iprocc} / \text{npedg}) + \text{kown} \\ \text{Itandb}(2,-) &= \text{Mynum} + \text{npedg} + 1 \\ \text{Itandb}(3,-) &= (\text{iprocc} / \text{npedg}) + \text{kown} - 1 = \text{Itandb}(2,-) - 1 \\ \text{Itandb}(4,-) &= \text{Mynum} + \text{npedg} + 1 = \text{Itandb}(2,-) \end{aligned}$
Left corner subdomains	
	$\begin{aligned} \text{Itandb}(1,-) &= (\text{iprocc} + 1)\text{npedg} - \text{koth} - 1 \\ \text{Itandb}(2,-) &= (\text{iprocc} + 1)\text{npedg} - \text{koth} - 2 \\ \text{Itandb}(3,-) &= \text{iprocc} * \text{npedd} + \text{koth} \\ \text{Itandb}(4,-) &= (\text{iprocc} + 1)\text{npedg} - \text{koth} - 2 = \text{Itandb}(2,-) \end{aligned}$
Right corner subdomains	
	$\begin{aligned} \text{Itandb}(1,-) &= (\text{iprocc} / \text{npedg}) + \text{kown} \\ \text{Itandb}(2,-) &= \text{iprocc} + \text{koth} - 1 \\ \text{Itandb}(3,-) &= (\text{iprocc} / \text{npedg}) + \text{kown} - 1 = \text{Itandb}(1,-) \\ \text{Itandb}(4,-) &= \text{Mynum} + \text{npedg} + 1 = \text{Itandb}(2,-) \end{aligned}$
Bottom left subdomains	
	$\begin{aligned} \text{Itandb}(1,-) &= \text{Mynum} - \text{npedg} - 1 \\ \text{Itandb}(2,-) &= \text{kproc} - (\text{iprocc} + 1 / \text{npedg}) + \text{koth} - 1 \\ \text{Itandb}(3,-) &= \text{Mynum} - \text{npedg} - 1 = \text{Itandb}(1,-) \\ \text{Itandb}(4,-) &= \text{kproc} - (\text{iprocc} + 1 / \text{npedg}) + \text{koth} - 1 \end{aligned}$
Bottom right subdomains	
	$\begin{aligned} \text{Itandb}(1,-) &= \text{Mynum} - \text{npedg} - 1 \\ \text{Itandb}(2,-) &= (\text{kproc} - \text{iprocc} - 1) \text{npedg} + \text{koth} - 1 \\ \text{Itandb}(3,-) &= \text{Mynum} - \text{npedg} - 1 = \text{Itandb}(1,-) \\ \text{Itandb}(4,-) &= (\text{kproc} - \text{iprocc} - 1) \text{npedg} + \text{koth} - 1 = \text{Itandb}(2,-) \end{aligned}$
Bottom corner subdomains	
	$\begin{aligned} \text{Itandb}(1,-) &= \text{Mynum} - \text{npedg} - 1 \\ \text{Itandb}(2,-) &= \text{kown} \\ \text{Itandb}(3,-) &= \text{Mynum} - \text{npedg} - 1 = \text{Itandb}(1,-) \\ \text{Itandb}(4,-) &= \text{npedg} + \text{koth} - 1 \end{aligned}$

Table C.1

The method/formula used to find itandb in each of the special cases on the edge of a diamond

C.4 Which data should we send?

The pattern used to transmit the top and bottom data across subdomains and processors is not a simple one. It has been generated such that the number of packets of data sent by each processor is two. However to do this we have had to cheat and in the subdomains in the top right of a diamond send data stored in the halo region. There are two reasons why this should not be a problem. This data is used to find the values of the top corner and since we are only concerned with data in the bottom corner then any inaccuracies will have no effect. Also as long as we always perform a top and bottom communication after a halo swap (as is the case in the current version of the code) then the results will be correct.

Each processor does not send one packet of data that will be used as top corner and one packet that will be used as bottom corner. For example the processor that owns the pole region will send out two corners, both of which will be used to acquire the top corners of a subdomain. Because of this the data that needs to be stored in `edg1` in different subdomains will vary depending on the position of the subdomain in the diamond. Table C.2 shows a break down of which allan keys/nodes should be copied in `edg1` for all the subdomains in a diamond.







Top left subdomains		
		$\text{edg1 } (-, 1) = \text{nt}-1, 1$ $\text{edg1 } (-, 2) = \text{nt}, \text{nt}$
Top right subdomains		
		$\text{edg1 } (-, 1) = 1, 0$ $\text{edg1 } (-, 2) = \text{nt}, \text{nt}$ <i>note: it is here that we are taking data from the halo region.</i>
The other subdomains		
		$\text{edg1 } (-, 1) = 1, 1$ $\text{edg1 } (-, 2) = \text{nt}, \text{nt}$

Table C.2

The data that needs to be stored in `edg1` ready for parallel communication. The first column shows the position of the subdomain relative to the diamond and the second column the position of the allan keys/ nodes in the subdomain that need to be stored in the transmission buffer `edgr`. This task is performed by the `tab_edg1_fill` subroutine.

C.5 Parallel communication: how do we know where to save the data?

The mpi calls are set up such that the first communication performed is to send the data stored in the buffer `edgl(-,1)` to the processor specified by the array `itandb(1,-)`. The processor will then wait until it receives a packet of data and store this before it goes on to send the final packets of data in `edgl(-,2)` to the processor with the rank stored in `itandb(2,-)`.

Since each of the processors is working independently and is sending data to two other processors is it not possible to determine the order in which a processor will receive data; either the top corner data could be received and then the bottom or vice versa.

To discover where to save data received, an mpi call is used to discover the rank of the processor that sent the data (there is an mpi call already written to do this). This is then compared with the values of `itandb(3,-)` and `itandb(4,-)`, which are set up to contain the ranks of the processors from which the top and bottom corner data were sent to the receiving processor. This is then used to determine whether to store the received data in `edgr(-,1)` (the top corner) or `edgr(-,2)` (the bottom corner).

The result of this method is that the top corner data is always stored in `edgr(-,1)` and the bottom corner data in `edgr(-,2)`.

Summary: the values of `itandb` are used to send data to the correct processors and to determine whether received data is either top of bottom corner data. Top corners are stored in `edgr(-,1)` and the bottom corner in `edgr(-,2)`.

C.6 Storing the received data: has the data moved into a new diamond?

Storing the data is not as simple as it first seems. We have an array of data in the form...

```
edgr(nd, kk, 2)
```

..where `kk` is the number of data points in each top and bottom corner, which for the markers is the total number of markers in each allan key multiplied by the three spatial co-ordinates of each marker. `nd` is the number of diamonds mapped onto each processor which can be either 5 or 10. Whilst copying the data from `edgr` into the relevant array we must check to see if communication of the data has passed over a diamond boundary, and if so, correct for it. This is done by using the values of the `idul(nd)`, `idll(nd)`, `idur(nd)`, `idlr(nd)`. These contain the values of the diamond number of the subdomain to the Upper Left, Low Right etc of each subdomain.





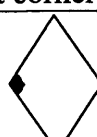
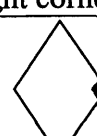

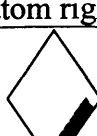
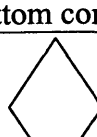
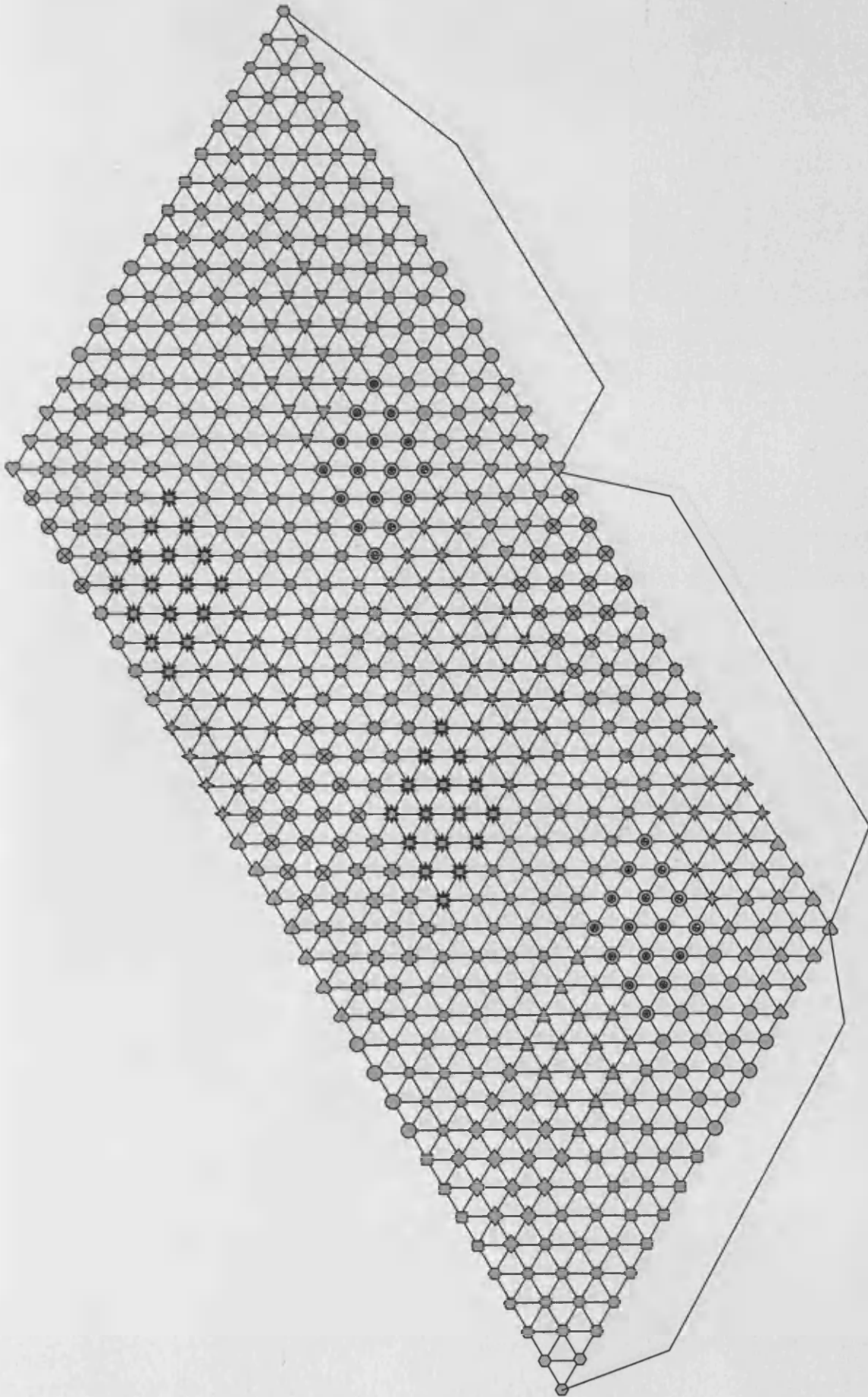
Middle subdomains	
	$u(0, 0, id, ii) = \text{edgr}(id, ii, 1)$ $u(nt+1, nt+1, id, ii) = \text{edgr}(id, ii, 2)$
Top corner subdomains	
	$u(0, 0, id, ii) = u(0, 0, idlp(id), ii)$ $u(nt+1, nt+1, id, ii) = \text{edgr}(id, ii, 2)$ <i>This is a special case where we do not use the data received in the parallel communication</i>
Top left subdomains	
	$u(0, 0, id, ii) = \text{edgr}(idul(id), ii, 1)$ $u(nt+1, nt+1, id, ii) = \text{edgr}(id, ii, 2)$
Top right subdomains	
	$u(0, 0, id, ii) = \text{edgr}(idur(id), ii, 1)$ $u(nt+1, nt+1, id, ii) = \text{edgr}(id, ii, 2)$
Left corner subdomains	
	$u(0, 0, id, ii) = \text{edgr}(idul(id), ii, 1)$ $u(nt+1, nt+1, id, ii) = \text{edgr}(idl1(id), ii, 2)$
Right corner subdomains	
	$u(0, 0, id, ii) = \text{edgr}(idur(id), ii, 1)$ $u(nt+1, nt+1, id, ii) = \text{edgr}(idlr(id), ii, 2)$
Bottom left subdomains	
	$u(0, 0, id, ii) = \text{edfr}(id, ii, 1)$ $u(nt+1, nt+1, id, ii) = \text{edgr}(idl1(id), ii, 2)$
Bottom right subdomains	
	$u(0, 0, id, ii) = \text{edgr}(id, ii, 1)$ $u(nt+1, nt+1, id, ii) = \text{edgr}(idlr(id), ii, 2)$
Bottom corner subdomains	
	$u(0, 0, id, ii) = \text{edgr}(id, ii, 1)$ $u(nt+1, nt+1, id, ii) = \text{edgr}(idlr(id), ii, 2)$

Table C.3

The method/formula used to store the data stored in edgr (the buffer that holds the data received during parallel communication).

Appendix D - Template for the icosahedron model

Instructions: Copy either of the two templates five times onto card and cut out and connect together to form an icosahedron. The colors/shapes of the nodes then make a useful tool for considering the halo swaps used in TERRA. The case shown in the models is $mt=16$, $nt=4$, $nd=10$.



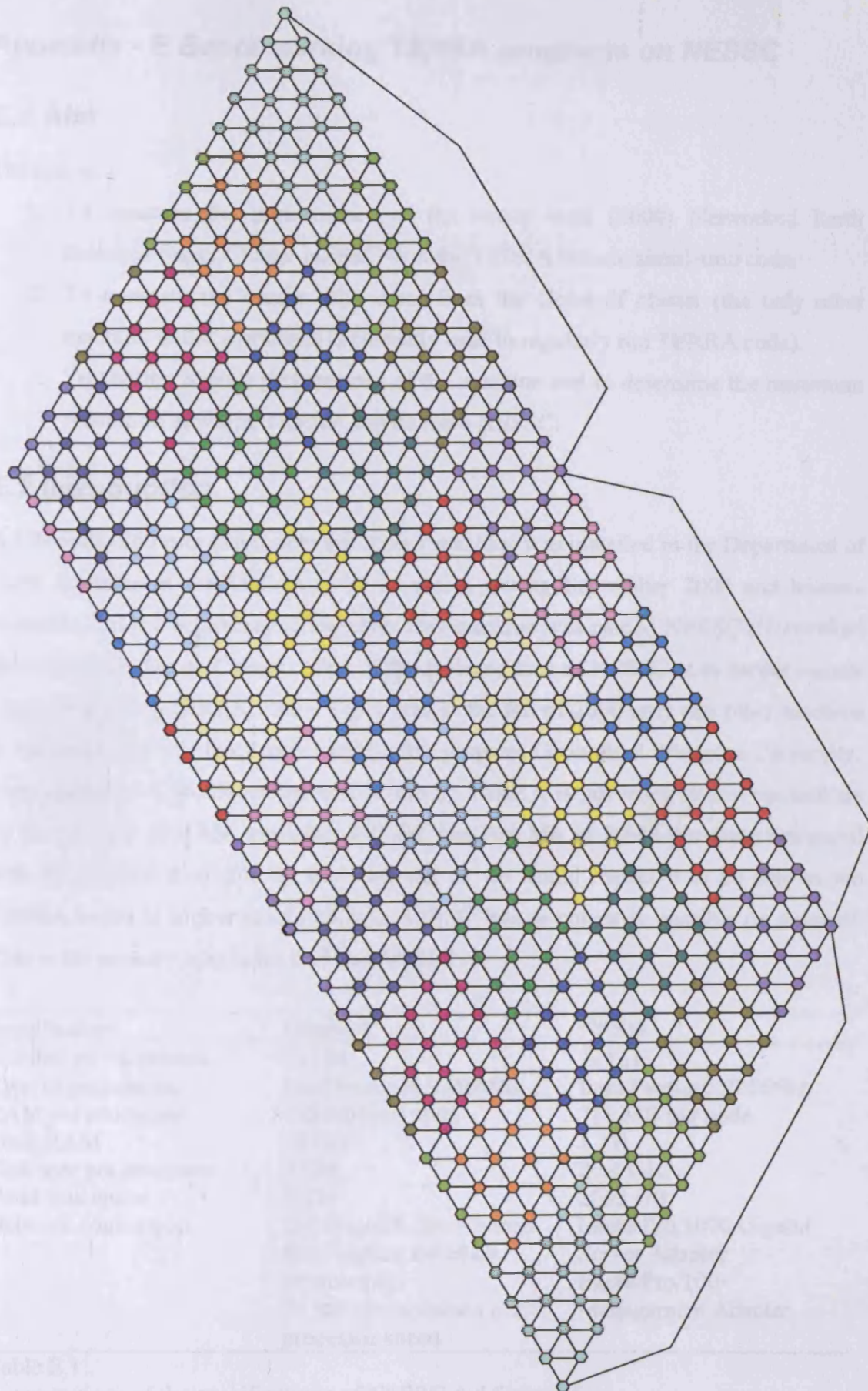


Table 5.1
A comparison of the applications of NLSIC at 4 GeV

Appendix - E Benchmarking TERRA programs on NESSC

E.1 Aim

The aim is...

1. To measure the performance of the newly built (2000) Networked Earth Sciences Super Cluster NESSC with the TERRA mantle simulation code.
2. To compare the results with those from the Geowulf cluster (the only other machine in the world that is currently used to regularly run TERRA code).
3. To test the overall performance of the machine and to determine the maximum resolution at which TERRA can be run a NESSC.

E.2 Introduction

A 130 node, 260 processor, network cluster machine was installed in the Department of Earth Sciences at the University of Liverpool during September 2000 and became operational at the beginning of October. This machine was named NESSC (Networked Earth Sciences Super Cluster). One of the primary uses of NESSC is to model mantle convection using TERRA code. There was in the fall of 2000 only one other machine in the world that was frequently used for this purpose: Geowulf at Princeton University. The resolution of problems that can be run by TERRA is governed almost exclusively by the amount of RAM available. NESSC has 768 Mb of RAM per node compared with the 128MB available on Geowulf and so we would expect it to be able to run TERRA codes at higher resolutions on NESSC than is currently possible on geowulf. This is the primary reason for building NESSC.

Specification	Geowulf	NESSC
Number of processors	2×136	2×131
Type of processors	Intel Pentium II350Mhz	Intel Pentium III 866hz
RAM per processor	128 MB per node	768 MB per node
Total RAM	18 GB	1 TB
Disk size per processor	8 GB	20.4 GB
Total disk space	1 TB	2652 GB
Network connection	100 BaseTX fast ethernet fully duplex switched interconnect	Intel®Pro/1000 Gigabit Server Adapter Intel®Pro/100+ Management Adapter
	70 Mflops sustained per processor speed	

Table E.1

A comparison of the specifications of NESSC and Geowulf.

E.3 Method

To perform Benchmarking the NESSC code was altered to minimise the amount of output files created. Thus the only alterations made were to comment out several lines of the subroutine vecout.

```

Utility.f lines 1083-1116
subroutine vecout(u,rshl,nj,kr,kt,mr,nf,ifmt)

c... This routine writes the nodal field u to logical
unit nf
c... using 1pe10.3 format when ifmt = 0 and f10.3 when
ifmt = 1.

      include 'size.h'
      real u(*), rshl(*)
      common /name/ titl(4,4)
      common /prty/ propr(20)
      character*8 titl

c      write(nf,10) kr, kt
c 10   format(2i5)

c      write(nf,20) titl
c 20   format(4a8)

c      write(nf,30) (rshl(i),i=1,kr+1)
c      write(nf,30) propr
c 30   format(1p10e15.8)

c      if(ifmt .eq. 0) then

c          write(nf,40) (u(ii),ii=1,(kt+1)**2*nd*nj*(mr+1))
c 40   format(1p15e10.3)

c      elseif(ifmt .eq. 1) then

c          write(nf,50) (u(ii),ii=1,(kt+1)**2*nd*nj*(mr+1))
c 50   format(15f10.3)

c      endif

      end

```

Benchmark programs were then run for a range of problem sizes and number of processors. This was done for both single and double processor use on each node.

These exercises were done to mimic those performed on the Geowulf cluster so that a direct comparison could be made.

Heterogeneous behaviour in the cluster was investigated by running a TERRA code that required 32 nodes over a series of distributions around NESSC. For example on nodes 1 to 32 and then on nodes 33 to 64. To get some idea of the scatter in the times the simulation was run five times at each array of nodes.

E.4 Results

The results shown below show the improvement in the time taken to calculate the last iteration of a 10 time step simulation. This has been done for a range of resolution (mt) and number of processors (np). A ratio of 1 would show that Geowulf and NESSC perform equally well, while a ratio greater than one would show an improved performance for NESSC and one less than one would suggest that Geowulf is performing better than NESSC.

Ratio of Geowulf/NESSC times				
Number of processors	Mt			
	16	32	64	128
1	1.84	1.56	1.58	1.42
4	2.00	1.85		
8		2.16	1.68	
16		1.66	1.62	
32		1.72	1.81	
64			1.73	1.51

For **Single** processor use i.e. only one processor is used per node

Ratio of Geowulf/NESSC times				
Number of processors	Mt			
	16	32	64	128
1	1.84	1.56	1.58	1.42
4	2.51	1.65		
8		1.16	1.14	
16		1.64	0.99	
32		0.65	0.81	
64			0.65	0.76
128				0.64

For **Double** processor use i.e. both processors are used on each node

E.4.1 Heterogeneous behaviour

Figure E.1 shows the mean and standard deviations of the times taken to perform the benchmarking program.

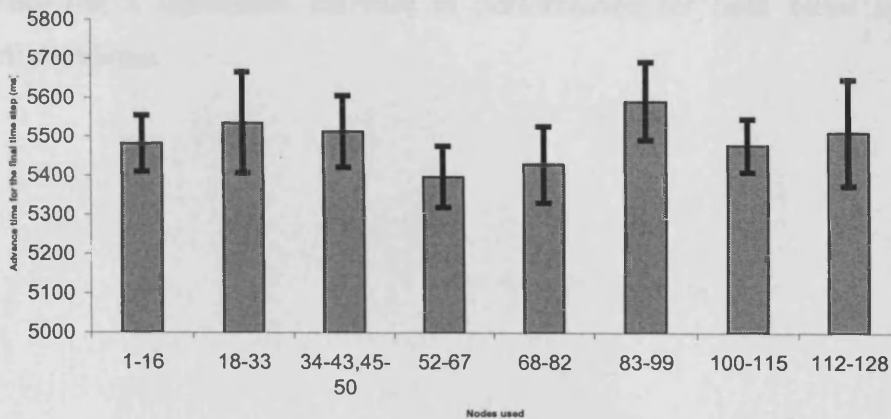


Figure E.1

The heterogeneous behaviour of NESSC. The bars show the mean time to perform the benchmarking problem over 5 runs and the standard deviation is represented by the error bars (plus and minus the s.d.).

E.5 Discussion

When only one processor is used per node the performance of NESSC shows a significant improvement to Geowulf, with this improvement becoming less pronounced with both increasing problem size and the number of nodes. This is, as we would expect since the parallel overhead in the TERRA calculation increases with problem size and domain decomposition¹. The fact that speed up is improved with problem size is also expected.

The results of the double processor runs are disappointing and we see that NESSC starts to show some decrease in performance for large processor use. We see similar problems in the speed-ups: this is currently being investigated. The most likely cause of the poor performance on the double processors is LAMMPI not using usysv communication.

The heterogeneous behaviour results (figure E.1) do show some variation, however these are very small, and given the size of the standard deviations of the computation time they are probably caused by natural scatter in the results.

E.6 Conclusions

NESSC is new networked cluster that has been purpose built to run code similar to TERRA. It is superior to the existing Geowulf cluster in almost all specifications and so we would expect it to show an improvement in performance. This is the case with NESSC showing a significant increase in performance for both serial and parallel benchmark problems.

Appendix F - Calculating the Rayleigh and Nusselt numbers

The following formulas show how TERRA calculates the Rayleigh number Ra and Nusselt number Nu:

For bottom heated cases...

$$Ra = \frac{\alpha g \rho^2 C_p (R_S^3 - R_{CMB}^3) (T_{CMB} - T_S) (R_S - R_{CMB})^3}{3 A k \eta}$$

$$Nu = \frac{Q_S (R_S - R_{CMB})}{12.56637 k R_S R_{CMB} (T_{CMB} - T_S)}$$

For internally heated cases...

$$Ra = \frac{\rho^3 \alpha g C_p q_{rad} (R_S - R_{CMB})^3}{A k^2 \eta}$$

$$Nu = q_{rad} \rho R_S^2 \left(1 - \left(\frac{R_{CMB}}{R_S} \right)^2 \left(3 - 2 \left(\frac{R_{CMB}}{R_S} \right) \right) \right) \div 6 k (T_{CMB} - T_S)$$

Where T_{CMB} & T_S is the temperature at the Core Mantle Boundary and Surface respectively; R_{CMB} & R_S are the radius of the Core Mantle Boundary and Surface respectively; α is the thermal expansivity; g is gravitational acceleration; η is the dynamic viscosity; C_p is the specific heat constant; k is the thermal conductivity; ρ is the reference density, Q_S is the total heat flowing across the surface; q_{rad} is the rate of radiogenic heat production per unit mass, and A is a constant defined as...

$$A = \sum_{ir=1}^{nr} \frac{\frac{1}{4} (R_{ir}^4 - R_{ir+1}^4) (\eta_{ir} - \eta_{ir+1}) + \frac{1}{3} (R_{ir}^3 - R_{ir+1}^3) (R_{ir} \eta_{ir+1} - R_{ir+1} \eta_{ir})}{R_{ir} - R_{ir+1}}$$

Appendix G - Solving $\phi = a \div (B^a - b^a)$

```

BandR.f
c   A program to calculate the predicted temperatures
c   of a layered mantle.

program BandR

real B(1000), R(1000), depth(1000)
real a,c,p,S, Smin
real abest, cbest, pbest
real amax, aincement
real cmax, cincrement
real pmax, pincrement

c   Load the values of the buoyancy ratio and the non-dimensional
c   area variable into array B and R
call GetBRN(B,R,depth,N)

c   Set up the range of values of a, b, & alpha we're going to try
amax=1.
aincrement=0.001
cmax=1.
cincrement=0.01
pmax=5.
pincrement=0.01

c   Loop over the values of a, b, & alpha
do i = 0, (amax/aincrement)
  a = (real(i))*aincrement
do j = 0, (cmax/cincrement)
  c = (real(j))*cincrement
do k = 0, (pmax/pincrement)
  p = (real(k))*pincrement

c   Calculate S^2
S=0.
do l=1,N
  S = S + ( R(l) - ( a / ( ( B(l)**p)-(c**p) ) ) )**2
end do

c   Check to see if this is the best result obtained
if (S.lt.Smin) then
  Smin = S
  abest = a
  cbest = c
  pbest = p
end if

end do
end do
end do

c   Output the results
write (*,'(
& "a from ", f7.3," to ", f7.3, " in steps of ", f7.3/,
& "b from ", f7.3," to ", f7.3, " in steps of ", f7.3/,
& "p from ", f7.3," to ", f7.3, " in steps of ", f7.3/,
& i20, " cases were compired* '))
& 0., amax, aincement, 0., cmax, cincrement, 0., pmax, pincrement,
& ((amax/aincrement)+1)*((cmax/cincrement)+1)*((pmax/pincrement)+1)

write (*,'("The best result was..."/,
& "sqrt(S) = ", f15.5/,
& "a      = ", f15.5/,
& "b      = ", f15.5/,
& "alpha  = ", f15.5)') sqrt(smin), abest, cbest, pbest

end

subroutine GetBRN(B,R,depth,N)

real B(*), R(*), depth(*)
integer N

N=44

B(1) = 0.80
B(2) = 1.00
B(3) = 0.60
B(4) = 0.80
B(5) = 1.00
B(6) = 0.60
B(7) = 0.80
B(8) = 1.00
B(9) = 0.60
B(10) = 0.80
B(11) = 1.00
B(12) = 0.80
B(13) = 0.82
B(14) = 1.05
B(15) = 1.39
B(16) = 1.72
B(17) = 0.93
B(18) = 1.29
B(19) = 1.72
B(20) = 2.13
B(21) = 1.08
B(22) = 1.52
B(23) = 2.03
B(24) = 2.54
B(25) = 1.01
B(26) = 1.56
B(27) = 2.09
B(28) = 2.65

```

Appendix G – Solving $\phi = a \div (B^y - b^y)$

B(29) = 1.36
 B(30) = 2.06
 B(31) = 2.71
 B(32) = 0.60
 B(33) = 0.80
 B(34) = 1.00
 B(35) = 0.60
 B(36) = 0.80
 B(37) = 1.00
 B(38) = 0.60
 B(39) = 0.80
 B(40) = 1.00
 B(41) = 0.60
 B(42) = 0.80
 B(43) = 1.00
 B(44) = 0.80

R(1) = 0.072373011
 R(2) = 0.055185324
 R(3) = 0.339926401
 R(4) = 0.134996385
 R(5) = 0.073594586
 R(6) = 0.686185118
 R(7) = 0.243540614
 R(8) = 0.109759252
 R(9) = 0.489804071
 R(10) = 0.163009005
 R(11) = 0.047917388
 R(12) = 0.221687278
 R(13) = 0.041809412
 R(14) = 0.016986613
 R(15) = 0.006837418
 R(16) = 0.006125546
 R(17) = 0.16059581
 R(18) = 0.049900703
 R(19) = 0.026716846
 R(20) = 0.014325566
 R(21) = 0.092924377
 R(22) = 0.024956456
 R(23) = 0.01023572
 R(24) = 0.005965631
 R(25) = 0.075623152
 R(26) = 0.021490072
 R(27) = 0.010989745
 R(28) = 0.006543749
 R(29) = 0.084028359
 R(30) = 0.034056222
 R(31) = 0.016696693
 R(32) = 0.384445618
 R(33) = 0.106899358
 R(34) = 0.029881591
 R(35) = 0.558729126
 R(36) = 0.190862758
 R(37) = 0.061951132
 R(38) = 0.754932135
 R(39) = 0.280215363
 R(40) = 0.088844261
 R(41) = 0.580799156
 R(42) = 0.17213412
 R(43) = 0.045266706
 R(44) = 0.18892076

Depth(1) = 500
 Depth(2) = 500
 Depth(3) = 1000
 Depth(4) = 1000
 Depth(5) = 1000
 Depth(6) = 1500
 Depth(7) = 1500
 Depth(8) = 1500
 Depth(9) = 2000
 Depth(10) = 2000
 Depth(11) = 2000
 Depth(12) = 2500
 Depth(13) = 500
 Depth(14) = 500
 Depth(15) = 500
 Depth(16) = 500
 Depth(17) = 1000
 Depth(18) = 1000
 Depth(19) = 1000
 Depth(20) = 1000
 Depth(21) = 1500
 Depth(22) = 1500
 Depth(23) = 1500
 Depth(24) = 1500
 Depth(25) = 2000
 Depth(26) = 2000
 Depth(27) = 2000
 Depth(28) = 2000
 Depth(29) = 2500
 Depth(30) = 2500
 Depth(31) = 2500
 Depth(32) = 500
 Depth(33) = 500
 Depth(34) = 500
 Depth(35) = 1000
 Depth(36) = 1000
 Depth(37) = 1000
 Depth(38) = 1500
 Depth(39) = 1500
 Depth(40) = 1500
 Depth(41) = 2000
 Depth(42) = 2000
 Depth(43) = 2000
 Depth(44) = 2500

end

Appendix H – Solutions to Davaille's equations with Earth-like parameters

```

entrain.f
  program entraincal
c   Calcultes the density contrast relative to a particular
c   rate of entrainment and depth for a kellogg layer.

  real c1, c2
  real depth, rmax, rmin, rmid
  real entrain, entrainms
  real dyviscu, dyviscl
  real alphau, alphas
  real tcmb, ts
  real tdiff, grav, rho, deltat
  real nocells, pi

  real Eup, Edown
  real Raup, Radownd
  real B, A1, A2, A3
  real tmp1, tmp2, entguess

  real dcon

  entrain = 150.
  depth   = 1500.

  c1      = 0.00012
  c2      = 0.0481
  rmax    = 6370e3
  rmin    = 3500e3
  dyviscu = 1e21
  dyviscl = 1e23
  alphau  = 5E-5
  alphas  = 1E-5
  tcmb    = 3000.
  ts      = 1000.
  tdiff   = 4.8E-7
  grav    = 10.
  rho     = 5e3
  deltat  = 2000.

  entrainms = 150 * 1E9 / (60**2*24*365.25)
  dcon = 0.00000002
  rmid = rmax - (depth*1000)
  pi = 3.141592653589793
  nocells = 4.*pi*rmid**2/((rmid-rmin)**2)
c   write(*,'(e12.4)') entrainms

  do j=1,28

    depth=real(j)*100.
    rmid = rmax - (depth*1e3)
    dcon = 200

  do i=1,10000000

    dcon = real(i)*0.0000001

    B = dcon/(alphas*deltat)

    Raup = alphau*rho*grav*deltat*(rmax-rmid)**3/(tdiff*dyviscu)
    Radownd = alphas*rho*grav*deltat*(rmid-rmin)**3/(tdiff*dyviscl)

    entguess =
& C1*tdiff*4*pi*rmid**2/((rmid-rmin)**3)
& *(
&   ((alphas*tcmb-alphas*ts)*(rmid-rmin)*Raup**(1./6.)/dcon)
&   -
&   (dyviscu*tdiff*Raup**(7./6.)/(dcon*rho*grav*(rmid-rmin)**2))

```

Appendix H – Solutions to Davaille's equations

```

& )**2
& +
& C2*tdiff*4*pi*rmid**2/((rmid-rmin)**2)
& *(
& (
& (alpha*tcmb-alpha*ts)*tdiff*(rmid-rmin)*Radown**(1./5.)
& /dcon
& )
& -
& (
& dyviscl*tdiff**2*Radown**(4./5.)
& /(dcon*rho*grav*(rmid-rmin)**2)
& )
& )

if (entguess.le.entrainms) then
  write(*,'(f12.3,"km ",f15.5,"%",2(f15.5))')
&   depth, dcon*100, entguess, entrainms
  goto 100
end if

end do

100 continue

end do

end

```

